



HAL
open science

Compaction banding in high-porosity limestones : Experimental observations and modelling

Youssef Abdallah

► **To cite this version:**

Youssef Abdallah. Compaction banding in high-porosity limestones : Experimental observations and modelling. Mechanics of materials [physics.class-ph]. Université Paris-Est, 2019. English. NNT : 2019PESC1024 . tel-02878898

HAL Id: tel-02878898

<https://pastel.hal.science/tel-02878898>

Submitted on 23 Jun 2020

HAL is a multi-disciplinary open access archive for the deposit and dissemination of scientific research documents, whether they are published or not. The documents may come from teaching and research institutions in France or abroad, or from public or private research centers.

L'archive ouverte pluridisciplinaire **HAL**, est destinée au dépôt et à la diffusion de documents scientifiques de niveau recherche, publiés ou non, émanant des établissements d'enseignement et de recherche français ou étrangers, des laboratoires publics ou privés.

Thèse

soumise pour l'obtention du grade de

Docteur de l'Université Paris-Est

Ecole Doctorale Sciences, Ingénierie et Environnement (SIE)

par

Youssouf Abdallah

Compaction Banding in High-porosity Carbonate Rocks

Experimental Observations and Modelling

Spécialité : *Géotechnique*

Thèse préparée au Laboratoire Navier - Ecole des Ponts ParisTech

Soutenue le 2 décembre 2019 devant un jury composé de :

Prof. Christopher Spiers	Utrecht University	Rapporteur
Prof. Patrick Baud	Université de Strasbourg	Rapporteur
Dr. Pierre Bésuelle	Université de Grenoble Alpes	Examineur
Dr. Jérôme Fortin	Ecole Normale Supérieure - Paris	Examineur
Dr. Michel Bornert	Ecole des Ponts ParisTech	Co-encadrant
Dr. Siavash Ghabezloo	Ecole des Ponts ParisTech	Co-encadrant
Prof. Ioannis Stefanou	Ecole Centrale de Nantes	Co-encadrant
Prof. Jean Sulem	Ecole des Ponts ParisTech	Directeur de thèse
Prof. Muhsin-Elie Rahhal	Université Saint-Joseph de Beyrouth	Invité

Thèse

soumise pour l'obtention du grade de

Docteur de l'Université Paris-Est

Ecole Doctorale Sciences, Ingénierie et Environnement (SIE)

par

Youssef Abdallah

Compaction Banding in High-porosity Carbonate Rocks

Experimental Observations and Modelling

Spécialité : *Géotechnique*

Thèse préparée au Laboratoire Navier - Ecole des Ponts ParisTech

Acknowledgement

Ce travail a été réalisé au sein du Labex MMCD (Multiscale Modelling and Experimentation of Materials for Sustainable Construction) et a bénéficié d'une aide de l'état gérée par l'ANR au titre du programme des Investissements d'Avenir ANR-11-LABX-022-01. Je remercie le Labex MMCD pour avoir financé cette thèse.

Je tiens à remercier chaleureusement les membres de mon jury de thèse. Je remercie particulièrement les professeurs Patrick Baud et Christopher Spiers d'avoir accepté de rapporter ce travail. Vos commentaires très positifs, ainsi que vos remarques et suggestions m'ont encouragé et aidé à mieux préparer la soutenance. Je remercie également le professeur Pierre Bésuelle d'avoir présidé mon jury de thèse. De plus, je remercie le docteur Jérôme Fortin d'avoir examiné mon travail. Au cours de ces trois années, on a eu plusieurs occasions pour échanger et discuter à propos de mon travail. Je tiens à remercier ton doctorant Cédric Bailly, qui m'a aidé dans la réalisation des observations microscopiques au sein de votre laboratoire à l'ENS. De plus, je tiens à remercier professeur Muhsin-Elie Rahhal qui est venu depuis le Liban pour assister à ma soutenance. Je le remercie également pour son encouragement et son aide depuis l'époque où j'étais son étudiant en 2013 à l'Ecole Supérieure d'Ingénieurs de Beyrouth (ESIB).

Je tiens à adresser les plus sincères remerciements à mon directeur de thèse, professeur Jean Sulem, qui a eu confiance en moi et m'a accordé cette thèse. J'ai beaucoup appris de vous, non seulement sur le plan scientifique mais aussi sur le plan humain. Je vous remercie surtout pour votre patience, votre aide et votre gentillesse. Je tiens à remercier chaleureusement mon encadrant, docteur Michel Bornert, qui m'a appris énormément de choses sur les techniques d'imagerie et de traitement d'images. De plus, je remercie vivement mon encadrant, professeur Ioannis Stefanou, qui était toujours prêt à m'accompagner dans le travail de modélisation. Ta personnalité et ton enthousiasme m'ont toujours marqué. Finalement, je tiens à remercier du fond du cœur mon encadrant, docteur Siavash Ghabezloo, qui m'a accompagné depuis mon stage de master. Je te remercie Siavash pour tes conseils et ton aide précieuse, surtout en ce qui concerne le volet expérimental. J'apprécie beaucoup la relation d'amitié qu'on avait toujours entre nous, et les discussions fructueuses qu'on a eues. C'était un plaisir et un honneur pour moi de travailler avec vous les quatre. Je vous remercie tous, parce que vous m'avez toujours poussé à partir jusqu'au bout dans mes analyses et à

ne pas se limiter à des interprétations superficielles. Je vous remercie aussi pour la liberté que vous m'avez accordée et pour les facilités que vous avez mises à ma disposition pour tester et réaliser beaucoup de mes propositions.

Je remercie chaleureusement l'équipe technique du laboratoire Navier – Cermes, qui ont été toujours à mon service. En particulier, je remercie le chef de l'équipe Emmanuel De Laure et je salue la façon dont il gère le déroulement des expériences au laboratoire. Je remercie Baptiste Chabot et Xavier Boulay qui m'ont aidé et appris à la manipulation de la machine triaxiale, la Sanchez. Je remercie également Marine Le Maire, qui s'occupait surtout des systèmes d'acquisitions et des outils de mesures. De plus, je remercie Loic Lesueur qui m'a aidé surtout dans le carottage et la préparation des échantillons à différentes échelles. Finalement, je remercie Patrick Aïmedieu, pour sa gentillesse tout d'abord et son aide précieuse dans la réalisation des observations tomographiques.

Je tiens à remercier l'ensemble de l'équipe géotechnique (Cermes) du laboratoire Navier. C'est un laboratoire, où l'ambiance est très favorisant pour le travail et la créativité. Je remercie les assistantes, Sabrina Chartier et Catherine Noor, pour leur gestion impeccable et leur travail formidable. Je tiens à remercier du fond de mon cœur, mes amis les doctorants. Votre connaissance est une richesse pour moi. Chacun d'entre vous a sa propre personnalité et souvent sa propre culture. Je considère que j'ai gagné des amis et que j'ai formé des relations qui me seront utiles tout au long de ma vie. Je vous remercie pour les bons moments qu'on a passés ensemble et pour les souvenirs inoubliables. Je remercie notamment, mes amis Hussein Bakri, May Awarkeh, Radja Andaloussi, Ibrahim Fawaz, Nour Awarkeh et Fayad Bou Saleh qui m'ont aidé à la préparation d'un pot magnifique.

Je remercie également les familles Jebara et Kemakem, qui m'ont accueilli dès mon arrivée en France. Je vous considère comme ma deuxième famille. Je vous aime !

Finalement, je tiens à remercier ma famille. Les mots ne suffiront pas pour exprimer mes sentiments. Je remercie mes parents, qui m'ont encouragé depuis mon enfance à être brillant et ont mis à ma disposition toutes les facilités pour que j'arrive à ce que je suis aujourd'hui. J'espère que j'ai réalisé leur rêve d'obtenir le grade de doctorat, dans l'un des meilleurs laboratoires au sein d'une des meilleures écoles en France, l'ENPC. Je remercie, mon épouse Amira, qui m'a toujours encouragé et supporté tout au long de ces trois années. Je te remercie beaucoup pour ta patience, ton amour et ton soutien ! Je vous aime tous !

Résumé

La déformation des roches sédimentaires donne lieu dans certains cas à la formation de bandes de compaction qui peuvent affecter considérablement le rendement des géosystèmes. L'objectif de cette thèse est d'identifier la formation des bandes de compaction dans les roches carbonatées poreuses à travers des essais de compression triaxiale et de proposer un modèle de comportement basé sur la théorie de plasticité du second-gradient pour prendre en compte l'effet des hétérogénéités locales.

Les essais de compression axisymétrique sont combinés avec des observations tomographiques aux rayons X. Les échantillons sont scannés avant et après différents paliers de chargement et sous différents niveaux de pression de confinement. La construction de cartes de déformation 3D en utilisant la technique de corrélation d'images volumiques permet d'identifier les zones de localisation de déformation. Une méthode simple basée sur des considérations cinématiques est proposée pour identifier le type des bandes de localisation. Des bandes de compaction sont identifiées sous forts confinements, des bandes de cisaillement pur sont obtenues à des faibles confinements, tandis que des bandes de cisaillement compactant sont observées dans le régime de transition. En revanche, une compaction diffuse a lieu sous chargement isotrope. D'autre part, des cartes de porosité 3D à une certaine méso-échelle intermédiaire sont construites et superposées sur les cartes de déformation. Il est observé que l'hétérogénéité de la porosité contrôle la structure des bandes de compaction qui s'étendent à l'intérieur des zones les plus poreuses et contournent les zones les plus denses. Il est également observé que l'écrasement des grains est le mécanisme dominant à l'échelle microscopique qui accompagne le mode de déformation. Des particules très fines remplissent ainsi les pores et induisent une réduction de l'espace poreux. Dans les zones assez denses, les grands pores protégés par une structure quasi-rigide de grains cimentés restent intacts. Quand la composante de cisaillement est présente dans la bande de localisation, l'hétérogénéité de la porosité contrôle le comportement volumique. Le long d'une bande de cisaillement pur/compactant, une fissuration du ciment intergranulaire apparaît dans les zones denses, tandis que des phénomènes d'écrasement de grains et de remplissage des pores sont observés dans les endroits les plus poreux. Ces mécanismes sont responsables d'une coexistence complexe de compaction et de dilatation locales.

Les modèles de comportement élasto-plastiques standards pour les milieux homogènes ne permettent pas de modéliser précisément la formation des bandes de compaction, car ils prévoient des bandes de localisation de déformation d'épaisseur nulle. Pour régulariser ce problème, des milieux continus d'ordres supérieurs (micromorphes) peuvent être considérés, où des longueurs internes en relation avec la microstructure sont introduites dans les lois de comportement. Une problématique particulière de ces modèles est la détermination des paramètres d'ordres supérieurs. Dans le cadre de la théorie de plasticité du second-gradient,

la surface de charge dépend d'une variable interne d'écroutissage et de son second gradient. L'effondrement plastique de la porosité est considéré ici comme la variable interne. Une procédure de calage des paramètres d'ordres supérieurs supplémentaires basée sur les données mécaniques macroscopiques et les données fournies par les images obtenues par microtomographie aux rayons X est proposée. Une analyse de stabilité linéaire en conditions axisymétriques triaxiales est appliquée pour prévoir la formation des bandes de compaction. Le modèle de comportement est ensuite implémenté dans un logiciel de calcul aux éléments finis, *Numerical Geolab*, afin de réaliser une simulation numérique des essais. On montre que les résultats numériques sont cohérents avec les observations expérimentales quant à l'initiation des bandes de compaction, leur épaisseur et évolution.

Mots-clés: Roches carbonatées; Bandes de compaction; Corrélation d'images volumiques; Plasticité du second-gradient.

Abstract

The mechanical deformation of sedimentary rocks gives rise in some cases to the formation of compaction bands which can significantly affect the performance of geosystems. The objective of this thesis is to identify the formation of compaction bands in porous carbonate rocks in laboratory experiments and to propose a constitutive model based on gradient-dependent plasticity theory to account for the effect of local heterogeneity.

Axisymmetric compression tests are combined with X-Ray Computed Tomography observations. Samples are imaged before and after several loading steps and at different confining pressure levels. Digital Volume Correlation technique is applied on consecutive images to build 3D deformation maps at a millimetric gauge length, which permit to identify strain localization zones. A simple method based on kinematic considerations is proposed to classify these zones. Compaction bands have been identified at high confining pressures, pure shear bands are obtained for low confinements whereas compactive shear bands are observed in the transitional regime. In contrast, a diffuse compaction occurs in hydrostatic loading conditions. 3D porosity maps are constructed at some intermediate meso-scale and superimposed on deformation maps. The heterogeneity of porosity is found to control the pattern of compaction bands, as they lay inside high-porosity zones and avoid denser zones. Grain crushing is identified as the main micromechanism of the deformation. Very fine particles fill the pores and induce a pore space reduction. Large pores are observed to remain intact in denser zones, as they are protected by a surrounding rigid lattice of cemented grains. When shear strain is identified in deformation bands, porosity heterogeneity is found to control the volumetric behavior. Along a compactive/pure shear band, some cracks are observed in denser zones, whereas grain crushing and pore filling are observed in the more porous ones. These mechanisms are responsible for a complex co-existence of local contractancy and dilatancy along shear bands.

Standard constitutive elastic-plastic laws of homogeneous media are insufficient to model correctly compaction banding, as a zero-thickness band is obtained for rate-independent materials in a Cauchy continuum. To regularize this problem, higher-order continua (micro-morphic media) can be considered, where internal lengths in relation with the microstructure are introduced in the constitutive relations. A particular issue of these models is to calibrate the higher-order parameters. In the framework of gradient-dependent plasticity theory, the yield surface depends on a hardening parameter, related to the plastic strain and its second gradient. The plastic porosity reduction is taken here as the hardening parameter. A calibration procedure of the additional higher-order parameters based on macroscopic mechanical data and the data provided by X-Ray images is proposed. Once the model is calibrated, a linear stability analysis in axisymmetric triaxial loading is applied to predict the formation of compaction bands. The calibrated model is subsequently implemented in a

finite element code, *Numerical Geolab*, to perform numerical simulations of the experiments. We show that the numerical results are consistent with experimental observations in terms of compaction banding onset, band thickness and evolution.

Keywords: Carbonate rocks; Compaction bands; Digital volume correlation; Gradient-dependent plasticity.

List of Abbreviations

DVC	Digital Volume Correlation
XRCT	X-Ray Computed Tomography
SML	Saint-Maximin Limestone
MIP	Mercury Intrusion Porosimetry
SEM	Scanning Electron Microscopy
LVDT	Linear Variable Differential Transformer
NSP	Normalized Scalar Product
BSE	BackScattered Electrons
FFT	Fast Fourier Transformation
REV	Representative Elementary Volume

Contents

1	General introduction	1
1.1	Context	1
1.2	Knowledge gaps and objectives	3
1.3	Thesis structure	4
2	Literature review	5
2.1	Rock types - Geological framework	6
2.2	Typical behavior of limestones and sandstones	7
2.3	Compaction bands in sedimentary rocks	10
2.3.1	In-situ observations	11
2.3.2	Laboratory testing	13
2.3.3	Micromechanisms of deformation	20
2.3.4	Discussion on the laboratory techniques for compaction banding identification	22
2.3.5	Microstructural features and compaction banding	24
2.4	Compaction bands modelling	28
2.4.1	Bifurcation theory	28
2.4.2	Linear stability analysis - The limitation of the Cauchy continuum	32
2.4.3	Micromorphic media	35
2.4.4	Non local models	37
2.4.5	Discussion on the internal length calibration	37
3	Material description	39
3.1	Material selection - The Saint-Maximin limestone	40
3.2	Sample preparation and global porosity measurements	42
3.3	Microstructure characterization	44
3.3.1	Observations at the sub-millimetric scale	44
3.3.2	Observations at the centimetric scale	45
3.3.3	X-Ray Computed Tomography and MIP tests on millimetric cubic specimen	46
3.3.4	Porosity maps analysis	51
3.3.5	Microscopic observation on thin sections	51
3.4	Summary of SML microstructural attributes	55

4	Experimental equipments and methods	57
4.1	Triaxial tests	58
4.2	X-Ray Computed Tomography	58
4.3	Digital volume correlation	60
4.3.1	Principle of the technique	60
4.3.2	Computation of local strain fields	63
4.3.3	Error estimation	63
4.4	Deformation bands type	65
4.4.1	Kinematics of strain localization	65
4.4.2	Deformation bands classification method	66
4.5	Porosity maps	68
4.5.1	Grey level adjustment	68
4.5.2	Grey level and porosity	69
4.5.3	Quartz and calcite attenuation coefficients	71
4.5.4	Porosity maps computation	72
4.5.5	The choice of the subvolume size	72
4.6	Second gradient evaluation	74
4.6.1	The 1D problem	74
4.6.2	The 3D problem	75
5	Experimental observations	77
5.1	Definitions	78
5.2	Preliminary tests	78
5.3	Hydrostatic loading test	81
5.3.1	Initial state	82
5.3.2	First loading stage	83
5.3.3	Second loading stage	83
5.3.4	Thin section observations	88
5.4	Triaxial test under high confining pressure	91
5.4.1	Initial state	92
5.4.2	First loading stage	92
5.4.3	Second loading stage	95
5.4.4	Thin section observations	100
5.5	Triaxial test under low confining pressure	104
5.5.1	Initial state	104
5.5.2	First loading stage	104
5.5.3	Second loading stage	109
5.5.4	Thin section observations	113
5.6	Triaxial test under intermediate confining pressure	115
5.6.1	Initial state	115
5.6.2	First loading stage	115
5.6.3	Second loading stage	120

5.6.4	Thin section observations	122
5.7	Conclusions	123
6	A gradient-dependent plasticity model for compaction banding	127
6.1	Gradient-dependent plasticity model	128
6.2	Micromorphic continuum	129
6.2.1	Internal power density	129
6.2.2	Equilibrium equation	130
6.2.3	Boundary conditions	131
6.2.4	Gradient-dependent plasticity model interpreted as a restricted micro- morphic continuum	132
6.2.5	Constitutive modelling	133
6.3	Calibration of the constitutive model	134
6.3.1	Calibration of the Cauchy component	135
6.3.2	Internal length identification	139
6.3.3	Enhanced hardening laws	142
6.3.4	Linear stability analysis - Calibration of the parameter B	149
6.4	Numerical implementation	155
6.4.1	Cauchy continuum	156
6.4.2	Micromorphic medium implementation	156
6.4.3	High confinement triaxial loading	161
6.4.4	Comparison with the experimental results	168
6.5	Conclusions	171
7	Conclusions and Perspectives	173
7.1	General conclusions	173
7.2	Suggestions for future research	176
8	Appendices	179
A	Limestones classifications	179
A.1	Dunham classification	179
A.2	Folk classification	180
B	Microstructural features of several limestones	181
B.1	Lavoux limestone	181
B.2	Anstrude limestone	181
B.3	Estailades limestone	182
B.4	Euville limestone	182
B.5	Chamesson limestone	182
B.6	Lens limestone	182
B.7	Vilhonneur limestone	182
B.8	Chauvigny limestone	183
B.9	Other limestones	183
C	Thin rod preparation	184

D	Python script to calculate the porosity and its second gradient	185
E	m-grade of micromorphic continuum of degree n	188
F	Calculation of P_v	190
G	Calculation of P_c	192
H	Calculation of P_i	196
I	Penalty moduli identification	198
Bibliography		201
List of Figures		211
List of Tables		223

General introduction

1.1 Context

Understanding the inelastic compaction of sedimentary rocks is highly important to enhance the operation performance of many geosystems. From the millimetric scale to lengths over kilometers, the compaction of sedimentary rocks may occur homogeneously or in the form of strain localization bands. A reduction in the pore space is generally observed due to many possible mechanisms, such as grain crushing, pore collapse, grain-rearrangement, crystal plasticity, pressure solution, etc. Moreover, the strain localization may occur with or without any sign of shearing. Deformation bands are thus called compactive shear bands in the former case and pure compaction bands in the latter one.

The inelastic compaction may occur in water-saturated aquifers exploited for geothermal energy. Since the risks of pollution and the consumption of energy have been rapidly increasing over the last decades, the need of clean and renewable resources of energy is overwhelming. In addition, these needs are expected to expand because of the world population growth and the human activities development. Thus, geothermal energy which is one of the competitive resources for producing electricity and heating could be a considerable alternative. It consists in exploiting the heat inside the Earth (for full description and some key statistics, see Barbier (2002), Bertani (2016) and Melikoglu (2017)). The rainwater infiltrates through permeable rocks and accumulates inside aquifers, where it is heated under high-pressure conditions (Figure 1.1). Hot water is extracted, heat is explored and the circuit is then closed by re-injecting the cold water in the aquifer at some distance from the extracting location (1 kilometer in case of the Parisian basin as reported by Laplaige and Lemale (2008)). In France, two main sedimentary basins exist: the Parisian and the Aquitanian basins. In 2007, 65 geothermal wells were exploited to produce energy equivalent to 166,000-housing needings to fossil energy. They allow to get rid of 400,000 tonnes of CO₂ emission per year (Laplaige and Lemale, 2008).

Another related application concerns the CO₂ capture and storage in deep geological formations, which is a promising approach to face the global climate change (Rutqvist, 2012 and the references herein). The most suitable geological media for these operations are deep sedimentary rocks, especially the depleted oil and gas reservoirs. These formations are sufficiently porous to provide the capacity of storage and have the permeability required

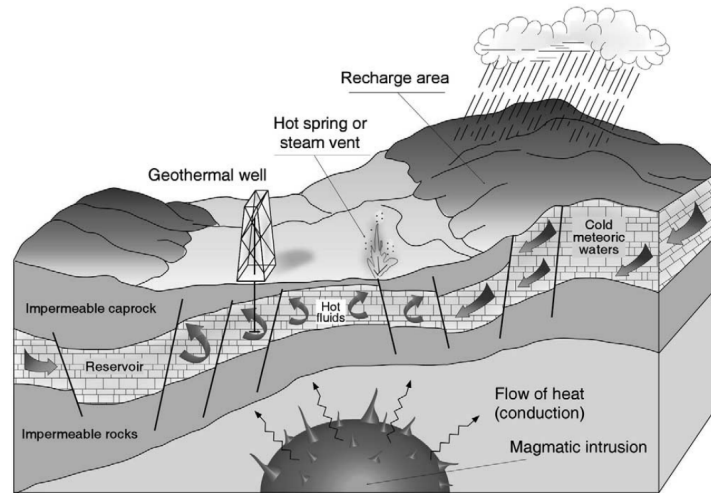


Figure 1.1: A schematic of a geothermal system (from Barbier, 2002).

for CO₂ injectivity. The reservoir should be confined by low permeability geological formations to prevent the migration and leakage of the supercritical fluid to shallow potable groundwater or to the surface. In order to make noticeable reduction of atmospheric CO₂, billion metric tons must be stored annually and the reservoir rocks permeability should be maintained to have better capacities of injection at lower costs. Therefore, a solid scientific characterization of sedimentary rocks behavior and inelastic compaction is required to fulfill these needs.

During these geosystem operations, the pore pressure is modified and the stress state is consequently affected. In addition, the temperature conditions may change due to the injection of fluids in the reservoir. The modification of the stress and temperature conditions can lead to an inelastic compaction of the rock and a surface subsidence. For instance, four meters and a half of land subsidence have been measured in the Wairakei geothermal field in New Zealand during ten years of exploitation (Allis et al., 1998). Moreover, inelastic compaction in the form of shear/pure compaction bands can form in the reservoir rock, accompanied by intense pore space reduction. Permeability inside these bands can consequently drop to over 4 orders of magnitude (Rath et al., 2011), where the bands act as barriers to fluid transport and affect drastically the performance of the geosystem. On the other hand, a fluid over-pressurization can be generated due to the pore space collapse inside the bands and instabilities can be triggered. A micro-seismicity can be induced by fault reactivation or formation. In general, geothermal systems are implemented at the tectonic plaques boundaries where hot reservoirs are found. A plastic compaction can perturbate the equilibrium and release the accumulated tectonic stresses. Furthermore, the fluid is usually rich in minerals and is acid in case of CO₂ storage. Therefore, it can chemically interact with the rock. The specific surface between the two phases can be increased (after a grain crushing for example) and the alteration reaction can be thus accelerated. A positive feedback can occur leading to instabilities in the geosystem (Stefanou and Sulem, 2014).

The inelastic compaction behavior is also an interesting phenomenon in oil and gas engineering (Olsson et al., 2002). Similarly, the changes in the effective stresses during production induce a compaction which can lead to casing failures and seafloor subsidences having a significant impact on the structure performances. The rock compaction can also squeeze oil from the rock to the borehole. A significant decrease in permeability due to strain localization is an important issue, as well as the risk of induced micro-seismicity as mentioned before.

1.2 Knowledge gaps and objectives

Carbonate rocks represent a large category of sedimentary rocks. According to Flügel (2013), carbonate rocks hold 40% to 60% of oil and gas reserves around the world. Contrary to sandstones, the inelastic deformation and compaction banding have been less studied in carbonate rocks over the last decades. This is partly due to the great variety of carbonate rock microstructures (Dunham, 1962, Choquette and Pray, 1970). Moreover, the experimental characterization of compaction bands on carbonate rock samples is generally more challenging than on sandstone samples (Fortin et al., 2006, Baud et al., 2017a). Many developed techniques have successfully identified compaction bands in sandstones, but have failed in carbonate rocks. Therefore, one objective of this thesis is to identify compaction bands in laboratory tested carbonate rock samples. The Digital Volume Correlation (DVC) technique is applied on X-Ray Computed Tomography (XRCT) images recorded before and after several loading stages. Strain localization bands can be identified on 3D deformation maps and are classified based on their deformation kinematics.

The effect of the microstructure features on compaction banding remains unclear. At the sample scale, compaction bands are identified in some sedimentary rocks and homogeneous cataclastic flow occurs for others (Cheung et al., 2012). Thus, understanding the effect of the microstructure heterogeneity on strain localization - and compaction bands in particular - is one of the thesis objectives. Based on XRCT images recorded at different deformation states, 3D maps of the local porosity evaluated at some meso-scale in the initial state of the rock and of its evolution are computed and superimposed on the deformation maps. In addition, thin sections at the initial and deformed states are prepared and observed using optical and scanning electron microscopy in order to investigate the local microstructural features and deformation mechanisms involved in the localization bands.

Modelling compaction bands have been a primordial topic over the last decades (e.g. Rudnicki and Rice (1975), Vardoulakis and Sulem (1995)). The standard constitutive laws in a homogeneous Cauchy continuum oversimplifies the strain localization mechanism since they neglect the microstructure scale in their formulations. Observations show that deformation bands have comparable thicknesses to the grain size diameter. To overcome

this limitation, macroscopic constitutive laws can be enriched by introducing some internal lengths that account for the microstructure, at least partially. However, the difficulty lays in the calibration of the additional parameters introduced in such formulations. In this work, a gradient-dependent plasticity model is considered, where the porosity and its second-gradient are identified as two independent hardening parameters. A method to compute the second gradient of porosity from a XRCT image is proposed. The additional parameters are calibrated based on XRCT images recorded at several deformation states, on DVC strain maps and on a linear stability analysis performed at the plasticity onset to predict the formation of compaction bands. Then, the constitutive model is implemented in the finite element code, *Numerical Geolab*, where triaxial loading at high confining pressures is performed. Finally, the numerical results are compared with the experimental data to validate the model.

1.3 Thesis structure

In addition to this introductory chapter, the manuscript is organized into six chapters:

- Chapter 2 presents a literature review on compaction bands in sedimentary rocks (both sandstones and limestones) in field and laboratory observations. A synthesis of the microstructure effects on compaction banding is presented and some criteria are given to choose an appropriate rock for the study. In addition, the principles of some modelling approaches of strain localization are presented.
- Chapter 3 describes the microstructure of the selected rock: the Saint-Maximin limestone. Several complementary techniques are used to characterize the microstructure.
- Chapter 4 introduces the experimental equipments and methods used in the study. A method to identify the types of deformation bands based on kinematic considerations is developed. The procedure of porosity maps computation is also described. Finally, a method to evaluate the porosity second-gradient from XRCT images is proposed.
- Chapter 5 illustrates the experimental results. Four loading cases are considered: a hydrostatic loading and three axisymmetric triaxial loadings under relatively high-, low- and intermediate confining pressures.
- Chapter 6 presents a gradient-dependent plasticity model for compaction banding. Based on experimental data, the additional parameters are calibrated. Finally, a numerical modelling is performed and compared with the experimental results.
- Chapter 7 discusses the major findings of this work and the possible perspectives for future studies.

Literature review

Résumé Dans ce chapitre, on présente une étude bibliographique sur les bandes de compaction dans les roches sédimentaires et en particulier dans les roches carbonatées. Les observations in-situ et sur des échantillons testés au laboratoire mettent en évidence que les micromécanismes impliqués dans la formation des bandes de compaction dans les carbonates diffèrent de ceux dans les grès. De plus, il s'avère que leur identification au laboratoire est moins facile. Des outils de modélisation de la localisation des déformations qui tiennent compte de la microstructure du matériau et introduisent des longueurs internes dans leur formulation sont également présentés.

Abstract In this chapter, a literature review on compaction bands in sedimentary rocks, and in particular in carbonate rocks, is presented. In-situ and laboratory observations show that micromechanisms involved in compaction banding in carbonate rocks and in sandstones are different. Moreover, laboratory identification of compaction bands in carbonate rocks is more challenging. On the other hand, some strain localization modelling approaches are presented. Constitutive models accounting for the material microstructure and introducing internal lengths in their formulation are necessary for robust modelling of strain localisation.

2.1 Rock types - Geological framework

The characterization of rock mechanical responses is essential to any deep underground project. However, a large variety of rocks exist and each category has a specific behavior. Based on their texture, the mineral composition and the mode of formation, 3 families of rocks can be distinguished (Homand and Duffaut, 2000):

1. **Igneous rocks:** These rocks are formed through the solidification of magma. They are rich in silicates such as quartz, feldspar and mica. They are present at the crust's surface (extrusive rocks) or in depth (intrusive rocks). Due to the rapid cooling, extrusive rocks are composed of small crystals whereas intrusive rocks have larger ones. Granite and Basalt are the most famous types. The Earth crust is mostly formed by granite rocks, generally covered by sedimentary rocks. The microstructure of these rocks is usually homogeneous.
2. **Sedimentary rocks:** The physical and/or chemical erosions of pre-existing rocks and marine organisms, then the transport of the small particles followed by diagenesis mechanisms lead to the formation of these rocks. According to Wilkinson et al. (2009), they cover around 73% of the Earth land surface and are usually found under oceans. Based on their mineral composition and textures, they are classified into several main subgroups:
 - **Sandstones:** formed after the diagenesis of sand grains. They have usually a homogeneous microstructure, where quartz is the main mineral.
 - **Carbonate rocks:** composed of different skeletal fragments of marine organisms and rich in carbonate minerals. Limestones are rich in calcium carbonate minerals such as calcite and aragonite (two crystal forms of CaCO_3), whereas dolomites are rich in $\text{CaMg}(\text{CO}_3)_2$.
 - **Shales:** fine-grained rocks rich in clay minerals.
 - **Evaporites:** formed from the precipitation of sediments through evaporation of an aqueous solution, like gypsum.
 - **Coals:** combustible rocks rich in carbon.

The microstructure of these rocks is widely diversified because of their various fragment origins and the different conditions accompanying their diagenesis.

3. Metamorphic rocks: These rocks have undergone a transformation in their textures at high temperature and pressure conditions. Because of the anisotropy of the stress field during their crystallization, a foliation can be observed inside these rocks. The most known types are: Gneiss, marble, schist, and quartzite.

2.2 Typical behavior of limestones and sandstones

In the previous section, it is shown that sedimentary rocks cover the majority of the shallowest portion of the Earth crust. In addition, due to their high permeability comparing to other types of rocks (Lion, 2004; Dautriat et al., 2011; Zinsmeister, 2013; Baud et al., 2015), sandstones and carbonate rocks are considered as potential reservoirs for geothermal and petroleum engineering. Contrary to sandstones, carbonate rocks present a large variety of microstructure types. However, the macroscopic mechanical behavior of these rocks are very similar (Wong and Baud (2012)). In this section, the mechanical behavior of carbonate rock samples tested in triaxial loading conditions are presented.

In case of hydrostatic loading (Figure 2.1), the plot of the mean pressure with respect to the volumetric deformation is composed of 3 distinct parts:

1. A non-linear elastic behavior in the form of a positive convex curve corresponding to the closure of the pre-existing cracks in the rock.
2. A linear elastic behavior up to a critical effective mean pressure P^* .
3. A plastic deformation regime where the volumetric compaction is accelerated.

Walsh (1965) has demonstrated that the intercept on the horizontal axis of the linear part (second stage) of the curve extrapolated back to zero pressure corresponds to the initial crack-porosity. This crack-porosity is independent of the shape and the distribution of cracks, and constitutes when added to the pore-porosity the total porosity.

As for triaxial loading, two extreme cases can be distinguished: At relatively low confining pressures, the rock has a dilatant brittle behavior, characterized by a sharp softening after the peak stress (Figure 2.2). The dilatancy onset, designed by an effective mean pressure C' , is usually observed to be a precursor to failure. Shear bands are generally observed in the samples, through which failure surfaces occur. For relatively higher confinements, a transition from brittle to ductile behavior is observed and the stress-strain curves exhibit an overall hardening of the material. The plot of the mean stress with respect to the volumetric strain coincides with the hydrostatic-loading curve up to a critical mean pressure C^* where

shear-enhanced compaction takes place (Wong et al., 1997). Beyond the value of C^* , dilatancy can be observed again from a new critical mean pressure designed by $C^{*'}$.

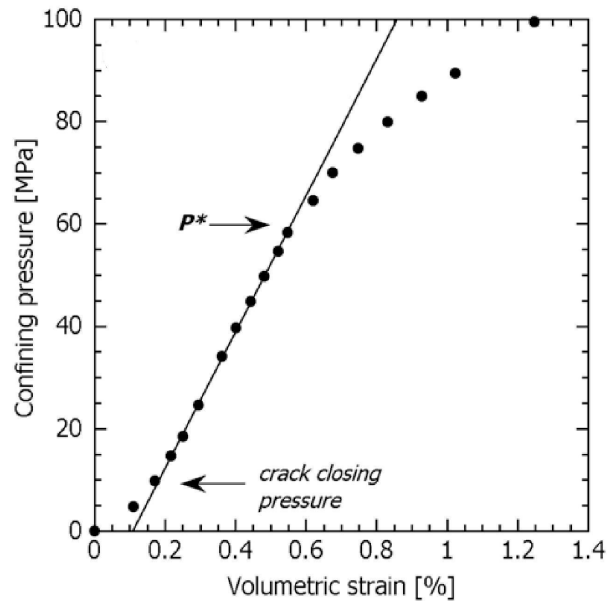


Figure 2.1: Typical Mean pressure vs Volumetric strain plot for a hydrostatic loading (Vajdova et al., 2004).

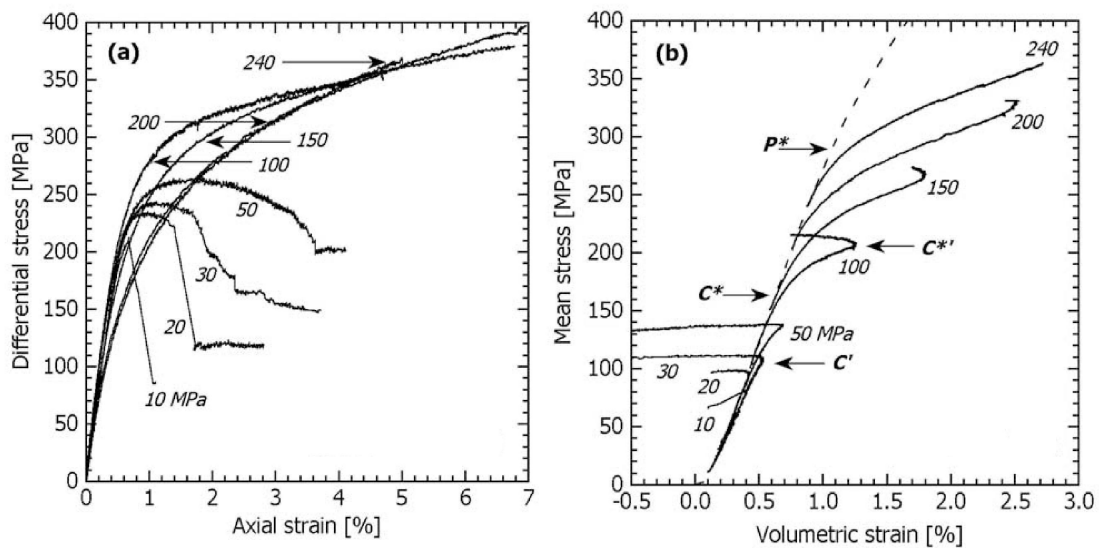


Figure 2.2: Typical results for triaxial loading at different confining pressures. **a)** Differential stress versus axial strain; **b)** Mean stress versus volumetric strain (Vajdova et al., 2004).

From previous data, yield stresses can be plotted and the yield surface is generally composed of two parts: a linear yield and a cap surface for low and high confining pressures respectively (black squares and black circles in Figure 2.3). A positive correlation exists between the confining pressure and the differential stresses corresponding to the dilatancy

onset thresholds C' and C^{*} . However, a negative correlation relates the confining pressure to the differential stress corresponding to the shear-enhanced compaction onset C^* . The brittle failure criterion is linear and can be described by a Mohr-Coulomb yield surface. At high confining pressures, a homogeneous deformation can take place. However, heterogeneous deformation in the form of compaction bands can be observed in some cases. This point will be discussed later in detail.

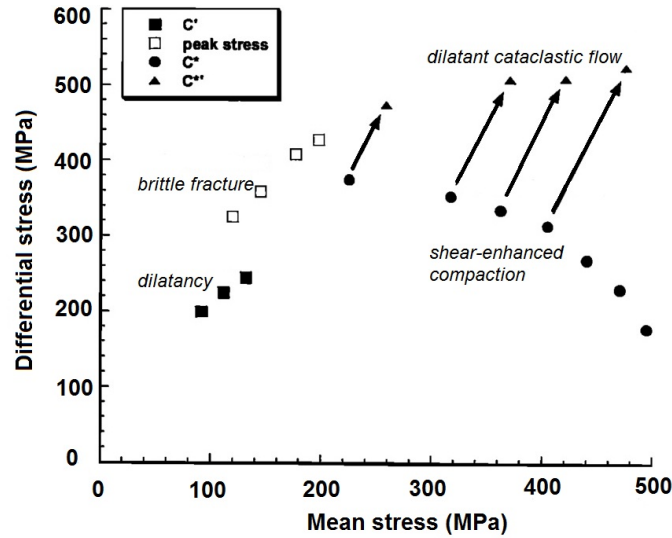


Figure 2.3: Typical yield stresses (black squares and circles), dilatancy thresholds (black squares and triangles) and brittle failure envelope (hollow squares) of carbonate rocks (From Baud et al. (2000)).

The microstructure of sedimentary rocks is a key factor to determine its mechanical behavior. High porosity induces a rock weakening and a yield surface shrinkage (Figure 2.4). Wong et al. (1997) have verified that the Hertzian fracture model is in good agreement with experimental data on sandstones, where the critical effective mean pressure P^* is proportional to the product of the porosity by the mean grain radius raised to the exponent $-3/2$:

$$P^* \propto (\phi \cdot R)^{-3/2} \quad (2.1)$$

They have also proposed an empirical relation linking the critical mean pressure C^* at the brittle-ductile transition and the critical hydrostatic mean pressure: $C^*_{transition} \approx 0.15 \times P^*$. Thus, a high porosity reduces P^* and the transition to ductile behavior occurs earlier. For very high-porosity rocks, the brittle phase can no longer exist. Recently, Baud et al. (2017b) verified the good agreement between Equation (2.1) and their experimental data on Leitha limestone. For different porosities of the same grainstone, they have found that P^* is increased from 28 MPa to 125 MPa when porosity decreases from 31% to 18%.

The brittle-ductile transition depends on extrinsic variables such as confinement, pore pressure, temperature, fluid chemistry and the strain rate (Wong and Baud (2012) and the

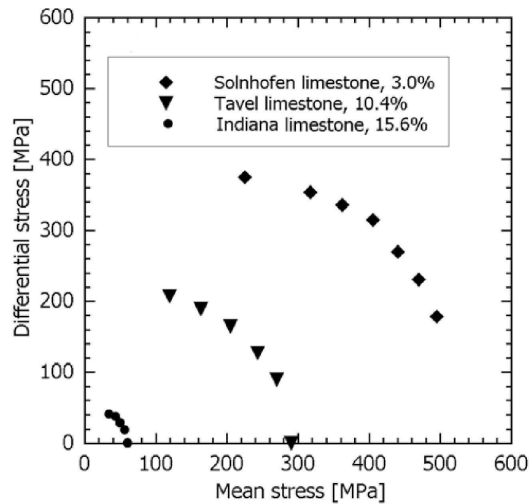


Figure 2.4: Porosity effect on yield stresses of limestones (From Vajdova et al. (2004)).

references herein). A high temperature leads to a ductile behavior even at low confining pressures (Paterson and Wong, 2005) and the transition pressure is lowered. Moreover, intrinsic variables such as porosity and grain diameter play a major role as shown previously (e.g. the hertzian fracture model expressed by Equation (2.1)). The mineral composition is also a very important factor in the transition. Experiments on relatively compacted granite show a brittle behavior up to a confining pressure of 3 GPa at room temperature (Shimada et al., 1983). In contrast, limestones and sandstones show a brittle-ductile transition at room temperature at lower confining pressures (15 to 75 MPa).

Despite the similar macroscopic mechanical behavior of sandstones and limestones, the micro-mechanisms of deformation are not the same (Zhu et al., 2010). The micromechanisms involved in both rocks deformation will be discussed in section 2.3.3. On the other hand, the dilatancy onset C^{*2} beyond shear-enhanced compaction C^* is not always seen in laboratory testing on sandstone samples because it requires higher stresses, unlike limestones which are often softer (Wong and Baud, 2012).

2.3 Compaction bands in sedimentary rocks

Strain localization is a widespread phenomenon in geomaterials. Deformation bands are observed over a large range of size scales, from the grain scale level up to faults which correspond to the scale of hundreds of kilometers (Bésuelle and Rudnicki, 2004). The concentrated deformation is generally accompanied by intense cracking, grain crushing, pore collapse, mechanical twinning or pressure solution, etc. These micromechanisms can induce an inelastic evolution of volumetric strain by either a dilatancy or compaction. When no evidence of shear is observed, the deformation band is called a pure compaction/di-

lation band. Strain localization bands are generally associated to instability phenomena in geomaterials. In fact, they may induce a strength reduction as a result of the material degradation. In addition, when fluids are present, the volume changes may affect the pore pressure and subsequently the effective stress state. Moreover, some chemical interactions can occur between the fluid and the solid matrix, such as the dissolution/precipitation of quartz and calcite minerals in water (Grgic, 2011). The material comminution inside the bands leads to an increase of the specific surface of the solid phase, which causes the acceleration of the chemical reaction and contributes in a further degradation of the material. A positive feedback process takes place and leads to a mechanical instability of the geomaterial (Ciantia and Hueckel, 2013; Stefanou and Sulem, 2014). On the other hand, deformation bands in general and compaction bands in particular are associated with a drastic permeability decrease across the band, that can reach several orders of magnitude (Rath et al., 2011; Rustichelli et al., 2012). Nonetheless, although that these bands may act as barriers to fluid transport, flow in the parallel direction to the band can be facilitated. Therefore, deformation bands can heavily affect geosystems performance, such as reservoirs for oil production, geothermal energy and CO₂ storage (Olsson et al., 2002; Holcomb et al., 2007; Rutqvist, 2012).

The identification of these bands in sedimentary rock fields and in laboratory testing is essential to understand how these bands are formed and to characterize the factors that enhance or prohibit their development and propagation. The first part of this section is devoted to in-situ observations of deformation bands and compaction bands in particular. Second, a review of the characterization of these bands on laboratory tested samples is presented. Finally, a synthesis of the microstructural attributes that affect the compaction banding in sedimentary rocks is presented.

2.3.1 In-situ observations

Field deformation bands are observed in both sandstone and limestone rocks and are documented in several publications (e.g. Antonellini et al., 1994; Aydin et al., 2006; Tondi et al., 2006; Tondi, 2007; Eichhubl et al., 2010 ; Fossen et al., 2011; Rath et al., 2011; Rustichelli et al., 2012; Cilona et al., 2014; Rotevatn et al., 2016; Araujo et al., 2018; Nicchio et al., 2018; Pontes et al., 2019). Due to their high resistance to weathering and their low porosity, these bands can have a positive relief and a lighter color with respect to the host rock, which facilitates their recognition. Various types have been detected: shear bands, pure compaction/dilation bands and compactive/dilatant shear bands. As already mentioned, these bands extend on a vast range of scales. Figure 2.5 gathers some photos of shear/compaction bands, in limestone/sandstone fields at different scales. Shear bands of millimetric thickness have been observed in the Navajo sandstone field, Utah, USA (Fossen et al., 2011). Nonetheless, shear zones of 3 meters of thickness have been reported by Antonellini et al. (1994) in the same field (Figures 2.5 a-b). Similarly, shear bands at various

scales have been reported by Tondi et al. (2006) in a porous carbonate grainstone, Majella, Italy (Figures 2.5 c-d). In addition, pure compaction bands of millimetric to centimetric scale have been observed by Eichhubl et al. (2010) and Sternlof et al. (2005) respectively in the Aztec sandstone field, Nevada, USA (Figures 2.5 e-f). Compaction bands have also been found in limestone units. Tondi et al. (2006) were the first to identify compaction bands in a carbonate rock field (Majella grainstone, Italy) with a thickness varying between 1 to 5 mm. In this field, compaction bands have been linked to coarse grained layers having porosities higher than 24% (Rustichelli et al., 2012). Rath et al. (2011) have documented thicker compaction bands in the Saint-Margarethen carbonate field, Austria (Figures 2.5 g-h). A gradual porosity reduction is often observed by these authors, where a compaction band is limited from the two sides by zones of intermediate porosity with respect to the host rock. Permeability inside compaction bands is reduced up to 4 orders of magnitude in comparison with the host rock. Moreover, a porosity reduction up to 10% has been assessed. On the other hand, the coexistence between shear and volumetric strain changes is very common in field deformation bands. Antonellini et al. (1994) have measured a dilation of 8% inside some shear bands and a porosity reduction of around 10% inside others in the same rock unit. Therefore, understanding the development of deformation bands can be fundamental to study the geological formation history of these fields, as their thicknesses can be indicators of the stress state history. All these observations make evidence of the complex nature of deformation bands. The role of microstructure in their formation will be discussed later in section 2.3.5.

A rare type of localized deformation is pure dilation bands. The scarcity of this type of bands in field observations is due to the fact that underground stresses are in general of compactive type. Dilation bands have been first observed by Du Bernard et al. (2002) in a poorly consolidated granular media (Figure 2.6) in the vicinity of developed shear bands. They have measured a 7% reduction of grain abundance inside the band in comparison with the host rock. Clay cement (in dark color) was formed between the 200 μm in diameter grains, resulting to a diagenetic phase of mineral alteration and infiltration that occurred after the band formation. The thickness is evaluated to be in the range of 1 to 2 mm which is equivalent to 5 to 10 times the grain size.

The formation of field compaction bands is a process that happens over years. Since the onset and development of these bands is unclear and because of the potential contribution of many factors (such as the stress state, pore pressure, fluid chemistry, temperature, time of formation, etc.), experimental testing on sedimentary rocks is useful to explore the micro-mechanisms of localization and the influence of the microstructure on deformation bands formation.

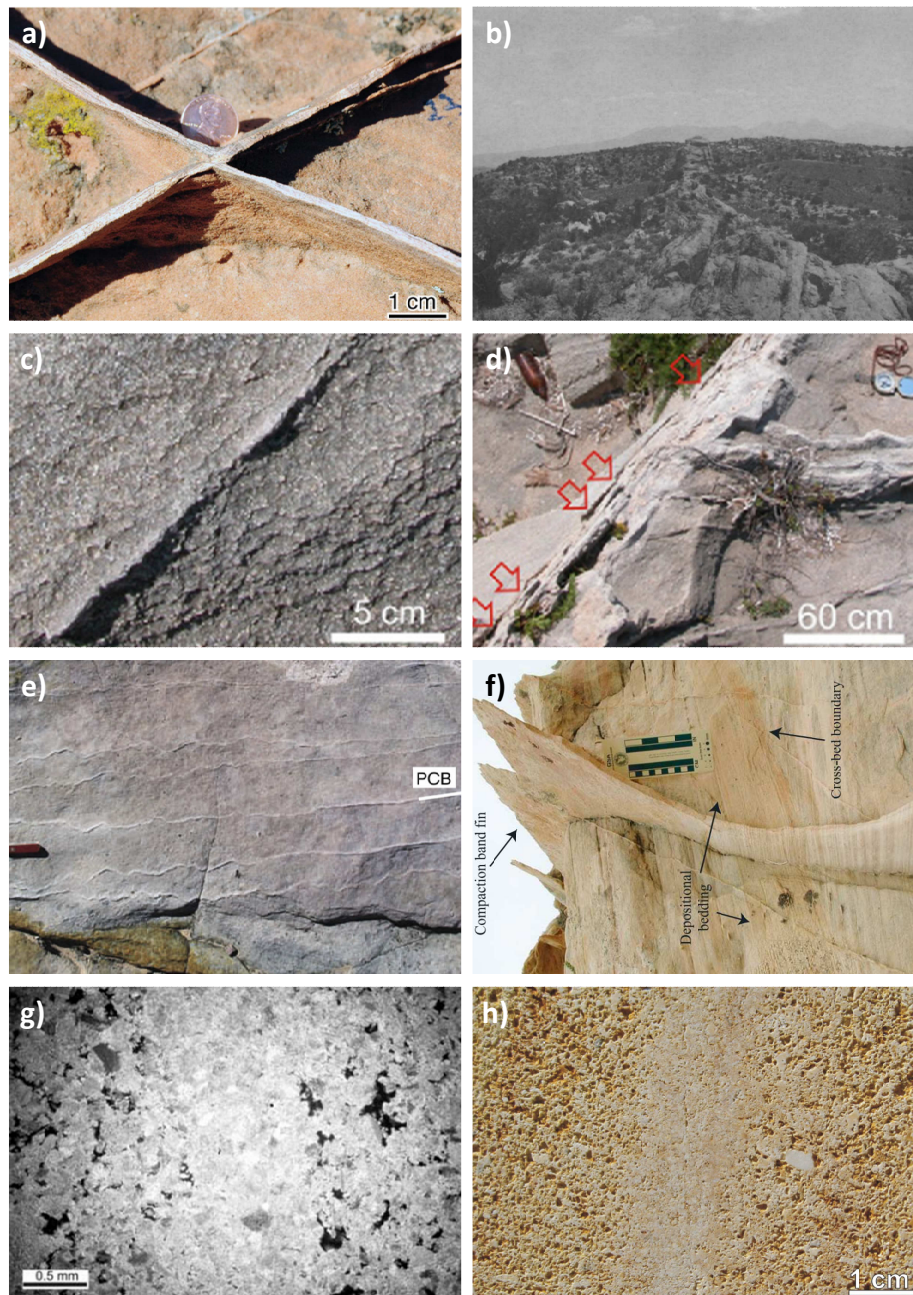


Figure 2.5: Field observations of: **a)** Conjugated shear bands at the millimetric scale in the Navajo sandstone (Fossen et al., 2011); **b)** Shear band of 3 meters thickness in the Navajo Sandstone (Antonellini et al., 1994); **c)** A single shear band at the millimetric scale in a porous carbonate grainstone (Tondi et al., 2012); **d)** Thick zone of shear bands in the same carbonate rock field (Tondi et al., 2012); **e)** Pure compaction bands in Aztec sandstone (Eichhubl et al., 2010); **f)** Pure compaction band at the centimeter scale in Aztec sandstone (Sternlof et al., 2005); **g)** Pure compaction band of millimetric thickness in Majella limestone (Tondi et al., 2006); **h)** Pure compaction band of centimetric thickness in Saint Margarethen limestone (Rath et al., 2011).

2.3.2 Laboratory testing

Many experiments have been conducted on sedimentary rock samples in order to characterize the deformation modes and to identify the strain localization bands (e.g. Mair et al.,

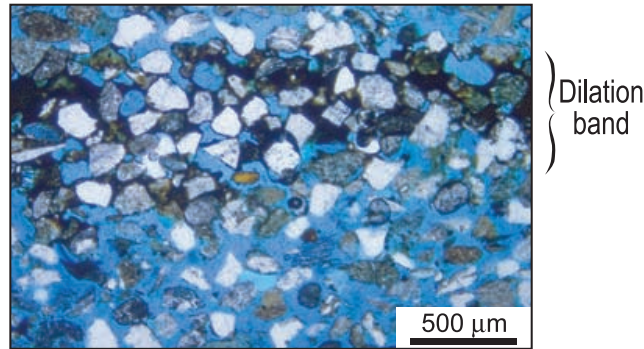


Figure 2.6: Field observation of a dilation band in a poorly consolidated sand where pore space is impregnated by blue epoxy and clay cement has a dark color (from Du Bernard et al., 2002).

2000; Baud et al., 2000; El Bied et al., 2002; Baud et al., 2004; Sulem and Ouffroukh, 2006; Baud et al., 2006; Fortin et al., 2006; Baxevanis et al., 2006; Baud et al., 2009; Fortin et al., 2009a; Vajdova et al., 2010; Zhu et al., 2010; Cilona et al., 2014; Ji et al., 2014; Baud et al., 2015; Baud et al., 2017a; Baud et al., 2017b; Papazoglou et al., 2017). Reproducing deformation bands in laboratory is essential to detect the stress conditions at which they are triggered and to understand how the microstructural attributes enhance or prohibit their propagation.

At low confining pressures, shear bands preceding the failure are generally observed. Mair et al. (2000) have performed triaxial tests on Locharbriggs sandstone at a relatively low confinement (34.5 MPa) and have identified grain crushing inside the shear band. The Fontainebleau sandstone has also been studied at relatively low confinements (El Bied et al., 2002; Sulem and Ouffroukh, 2006), where shear bands have been observed in the brittle regime (loading is stopped just after the peak). The orientation of these bands with respect to the maximum (in absolute value) principal stress direction is found to increase with the confining pressure. In addition, an evolution from dilatant shear bands to compactive shear bands is reported when confinement is increased. In drained conditions, bands of crushed grains can be identified (Figure 2.7a), with thicknesses in the order of several grain sizes. In undrained conditions, similar results are obtained, but connected channels are observed inside the bands, marking local fluid exchanges inside the sample (Figure 2.7b).

When considering relatively higher confinements, a transition from brittle to ductile regime occurs. A positive correlation is found between the angle of shear bands and confinement (Vajdova et al., 2004; Cilona et al., 2014). The samples in the ductile regime are found to deform either in a homogeneous way (called homogeneous cataclastic flow) or by developing compaction bands perpendicular to the maximum principal stress direction. However, despite the similarities in the macroscopic behaviors of sandstone and limestone rock samples (as presented in section 2.2), identifying compaction bands in carbonate rock samples is more challenging.

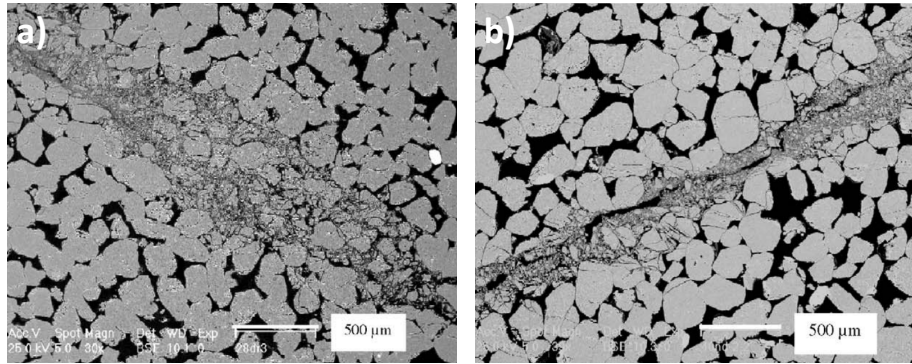


Figure 2.7: Photomicrographs of shear bands formed in Fontainebleau sandstone samples tested at relatively low confinements: **a)** in drained conditions; **b)** in undrained conditions (from Sulem and Ouffroukh, 2006).

Sandstones When compaction bands are formed in laboratory tested sandstones, a simple eye inspection of the sample is sufficient in some cases to identify their formation (see the compaction bands formed in a Bleurswiller sandstone sample tested at 80 MPa of effective confining pressure in Figure 2.8a). This is due to the quite homogeneous initial microstructure of sandstones as explained in section 2.1. From acoustic emission measurements on Bleurswiller sandstone samples, Fortin et al. (2006) have located their hypocenter distributions, which leads to the detection of compaction bands formation (Figure 2.8b). Later, Baud et al. (2015) have performed a series of triaxial experiments on Bleurswiller sandstone which has 25.2% of porosity and a mean grain radius of 112 μm (Table 2.1) and have documented the development of compaction bands in the ductile regime. Figure 2.9 compiles the photos of tested samples at different levels of confinement. At $\sigma_3 = 10$ MPa and 20 MPa, high angle shear bands are formed and brittle failure occurs. Inclination of these bands is evaluated at 30° with respect to the axial loading direction. In the transitional regime ($30 \text{ MPa} < \sigma_3 < 50 \text{ MPa}$), shear and compaction bands co-exist and a mixed mode of failure is observed. At high confinements (higher than 70 MPa), tortuous compaction bands are formed, perpendicular to the axial direction.

Baud et al. (2004) have conducted a series of triaxial tests on 5 sandstones (Table 2.1) and have visualized compaction bands at relatively high confining pressures. Bentheim sandstone samples have been deformed to different axial strain levels, then thin sections have been prepared from the unloaded samples. Microscopic observations show the formation of sub-horizontal compaction bands at the boundaries of the samples for effective confinements ranging from 90 to 395 MPa (Figure 2.10). While applying further loading, these bands propagate towards the center of the samples. Although the obvious evidence of boundary effects on bands formation, compaction bands are clearly observed. Acoustic emission has been recorded along the loading process. The differential stress curve with respect to the axial strain is marked by several stress drops which correspond to acoustic emission rate surges (Figure 2.11). Diemelstadt sandstone has a similar behavior, but with smaller stress drops. In contrast, Darley Dale sandstone (Figure 2.12c) shows the narrowest range of

Table 2.1: Petrophysical properties of some sandstones

Sandstone	Porosity(%)	Grain Radius (μm)	References
Darley Dale	14.5	170	Wong et al., 1997; Baud et al., 2004
Rothbach	19.9	230	Wong et al., 1997; Baud et al., 2004
Kayenta	21.0	150	Wong et al., 1997
Berea	21.0	130	Wong et al., 1997; Baud et al., 2004
Adamswiller	22.6	90	Wong et al., 1997
Benheim	22.8	110	Baud et al., 2004
Diemelstadt	24.3	80	Baud et al., 2004
Bleurswiller	25.2	110	Fortin et al., 2006; Baud et al., 2015
Boise	35	280	Wong et al., 1997

effective confinement where samples have two conjugate shear bands (between 80 and 95 MPa). Beyond 95 MPa, the sample undergoes a hardening phase, but no localization is observed. Berea and Rothbach sandstones show intermediate behavior. A "plateau" is observed after the peak for high confining pressures (Figures 2.12 a-b). Conjugate shear bands are formed up to 90 MPa of confinement, beyond which mosaic compaction bands appeared (Figure 2.13 a-b).

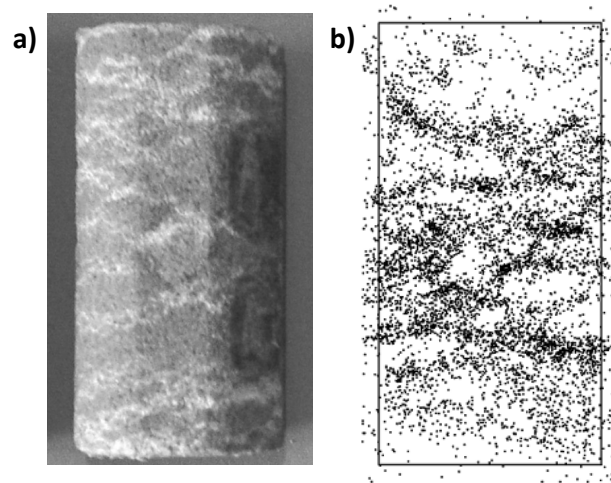


Figure 2.8: Sub-horizontal compaction bands formed in Bleurswiller sandstone sample tested at 80 MPa of effective confining pressure (from Fortin et al., 2006): **a)** Eye inspection of the sample surface; **b)** Inferred from acoustic emission measurements.

Limestones As for limestones, less studies have been done. Baud et al. (2000) have worked on a low porosity rock: the Solnhofen limestone (Table 2.1). The brittle regime is extended up to a confining pressure of 50 MPa (Figure 2.3). Dilatancy is observed as a precursor of shear band localization. Beyond 50 MPa, the behavior is ductile with a compactive cataclastic flow. For intermediate confining pressures, dilatancy occurs again, but for higher pressures (>300 MPa) dilatancy does not occur probably due to the limited

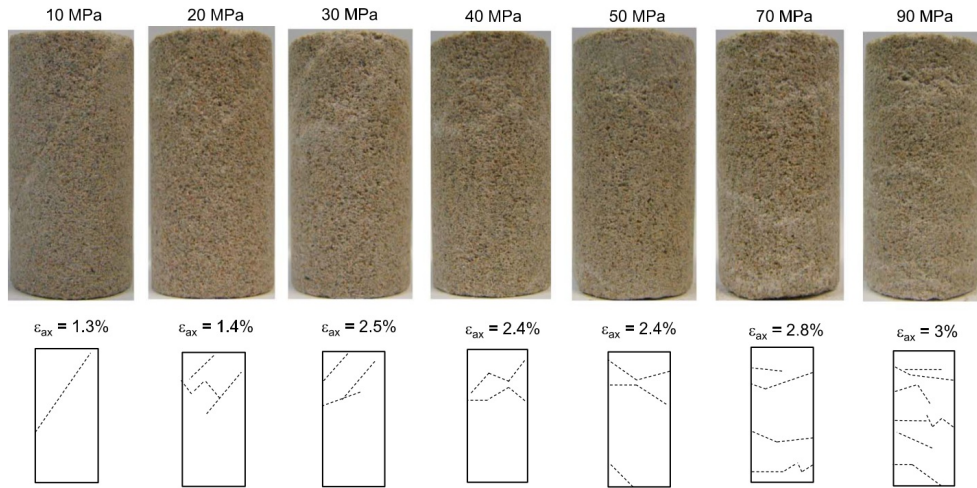


Figure 2.9: Photographs of deformation bands on tested Bleurswiller sandstone samples at different confinements (from Baud et al., 2015).

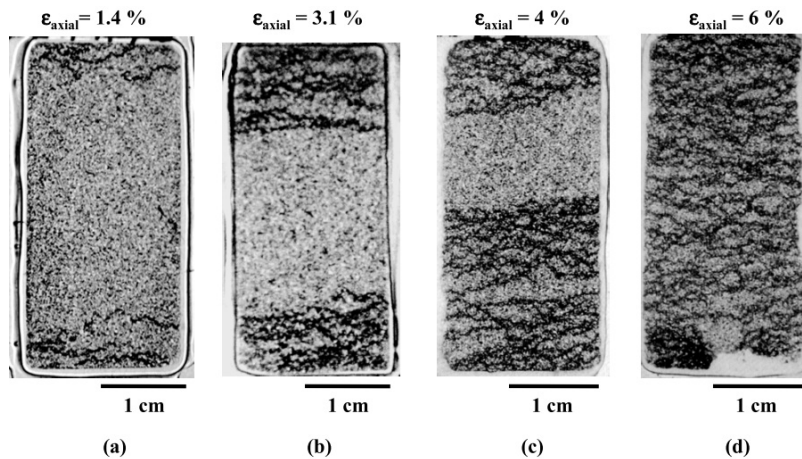


Figure 2.10: Sub-horizontal compaction bands formed at the boundaries and propagating towards the center of Bentheim sandstone samples (from Baud et al., 2004).

capacity of the experimental equipment. No localization is observed by visual inspection in the ductile regime.

Tavel and Indiana limestones (Table 2.2) have been studied by Vajdova et al. (2004). Despite having higher porosities (10.4% and 16% respectively), they have shown similar behavior to Solnhofen, but with lower yield stress states (Figure 2.4). The brittle regime is characterized by shear localization band formed by the coalescence of cracks, as shown by microscopic observations on thin sections (Fredrich et al., 1989). However, visual examination of the deformed samples in the ductile regime suggest that homogeneous compactive cataclastic flow occurs. Later, a dilatancy is observed. Vajdova et al. (2010) have observed, by scanning electron microscopy on thin sections, the appearance of new cracks sub-parallel to the direction of the maximum principal stress direction after the critical stress C^{*} . Shear bands may form at this stage by the coalescence of these new cracks.

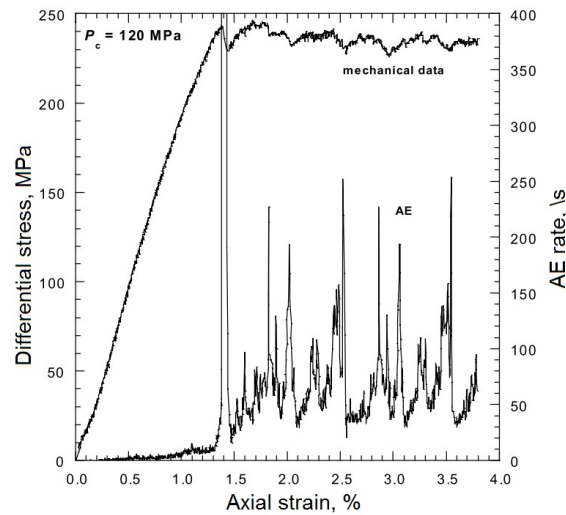


Figure 2.11: Differential stress and acoustic emission rate plots versus the applied axial strain for a Bentheim sandstone sample tested at 120 MPa of confining pressure (from Baud et al., 2004).

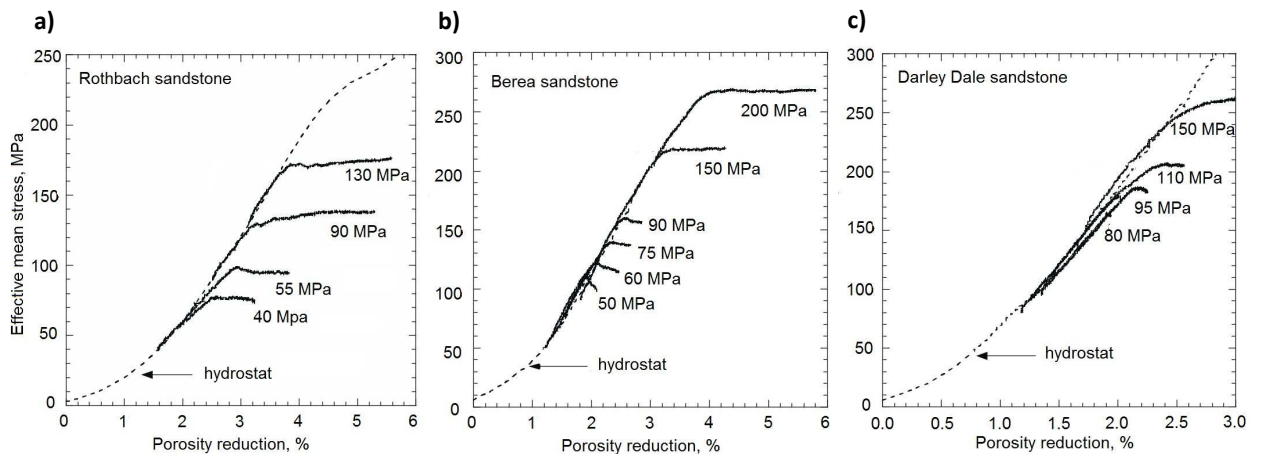


Figure 2.12: Effective mean pressure vs porosity change for: a) Rothbach sandstone samples; b) Berea sandstone samples; c) Darley Dale sandstone samples. (from Baud et al., 2004).

Field compaction bands have been observed in high-porosity Majella limestone (Table 2.2) in Italy (see the section 2.3.1). Cilona et al. (2014) and Ji et al. (2014) have documented laboratory compaction bands on Majella samples even at low confining pressures. Note that for this high porosity limestone, the brittle-ductile transition regime occurred between 10 and 15 MPa of confinement (Figure 2.14a). At 5 MPa, single shear bands are formed at 30° to 40° with respect to the vertical axis (Figure 2.15). At 12.5 MPa, conjugate shear bands formed at 53° and 77° of orientation. By increasing the confinement to 15 and 20 MPa, the angle of shear bands increased to 55° and 72° respectively. Sub-horizontal bands, designed by compaction bands are formed at 25 MPa of confining pressure and no localization is observed at 35 MPa.

The Leitha limestone is a porous grainstone explored in many quarries at the margins of the Vienna Basin. Baud et al. (2017b) have studied two facies of this rock: One having a

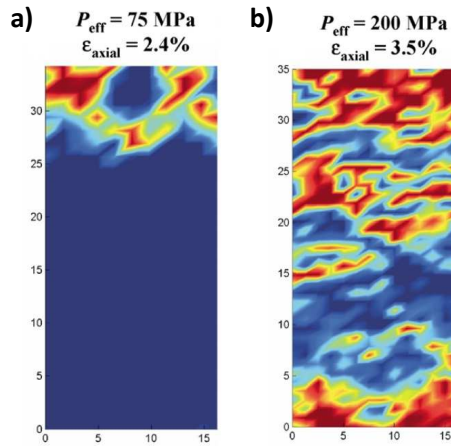


Figure 2.13: Spatial distribution of specific surface area (due to grain crushing) in Berea sandstone samples: **a)** Conjugate shear bands at 75 MPa of confinement; **b)** Compaction bands at 200 MPa of confinement. (from Baud et al., 2004).

Table 2.2: Petrophysical properties of many limestones.

Limestone	Porosity(%)	Grain Radius (μm)	Reference
Solnhofen	3.0	2.5	Baud et al., 2000
Tavel	10.4	2.5	Vajdova et al., 2004
Indiana	16.0	150	Vajdova et al., 2004
Majella	30	27	Cilona et al., 2014
Leitha	18-31	240	Baud et al., 2017b
Saint Maximin	37	70	Baud et al., 2009
Tuffeau de Maastricht	Not provided	Not provided	Baxevanis et al., 2006

porosity of 21% and another having a porosity of 31%. The lack of cementation in the latter facies causes this high porosity with respect to the former one. Two families of macro-pore diameters are found : 30 and 500 μm , and micro-porosity is found to be negligible. For samples with $\phi = 31\%$, no brittle behavior is observed even at 5 MPa of confinement and stress drops are present in all experiments. Compaction bands are observed in triaxial tests at $\sigma_3 = 5, 10$ and 15 MPa. At higher confinements, distributed cataclastic flow is observed (Figure 2.16). In contrast, samples with $\phi = 21\%$ show less pronounced stress drops. A brittle regime with a compactive shear band formation is observed at 10 MPa. At 20 MPa, conjugate shear bands are obtained. For higher confinements, distributed cataclastic flow is observed (Figure 2.16).

The Saint-Maximin rock is a high-porosity limestone ($\phi = 37\%$) found in the north of Paris. Stress drops are found on the mechanical data of the triaxial experiments (Figure 2.14b) and compactive shear bands are observed at high angles (80° with respect to the maximum principal stress direction). Based on thin section observations, the thickness of the bands is estimated around 3 to 4 times the grain diameter.

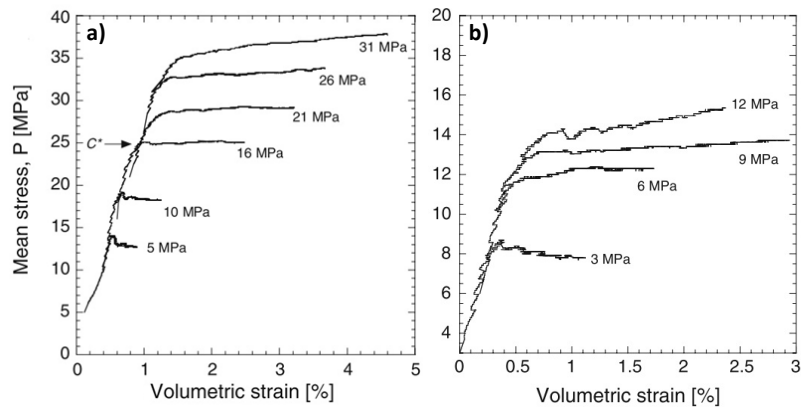


Figure 2.14: Mean stress vs volumetric strain for samples tested under several confining pressures: **a)** Majella limestone; **b)** Saint-Maximin limestone (from Baud et al., 2009).

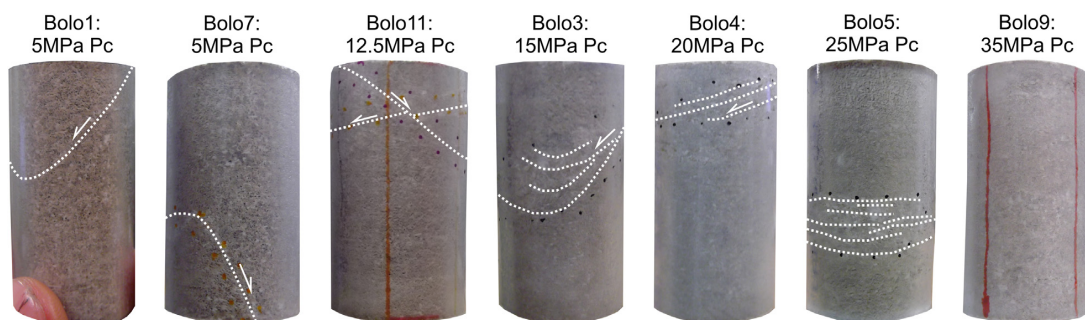


Figure 2.15: Photographs of deformation bands on Majella limestone samples tested under several confining pressure (from Cilona et al., 2014).

Baxevanis et al., 2006 have worked on a high-porosity limestone called "Tuffeau de Maastricht". By means of computed tomography scans, they have observed a zone of sub-horizontal cracks, which has been interpreted as a compaction band at relatively low confinements in the transitional regime. At 0.5 MPa of confinement only, the rock undergoes a brittle behavior whereas compaction bands and conjugate shear bands are obtained between 2 and 5 MPa.

2.3.3 Micromechanisms of deformation

Several micromechanisms are involved in compaction banding. In sandstones, **grain crushing** is commonly observed inside the bands (see also Bésuelle and Lanatà (2017) who have studied samples of the Vosges sandstone). It results from a stress concentration at grain boundaries and from a formation of hertzian cracks towards the center (Figure 2.17a). The comminuted material may consequently fill the pores. In addition, in poorly cemented sandstone rocks, micro-cracks can be formed in the cement leading to a loss of cohesion and allowing a **grain movement/rotation** without crushing (Cashman and Cashman, 2000).

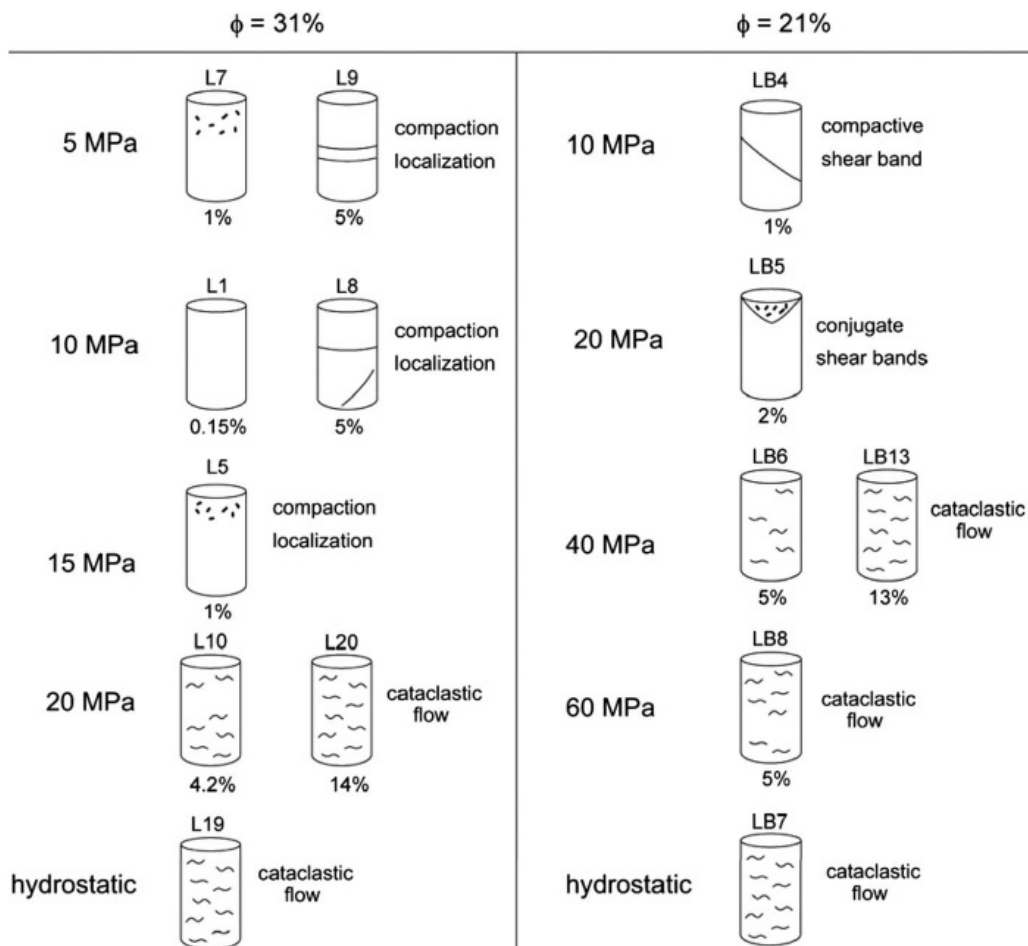


Figure 2.16: Deformation modes of two facies of Leitha limestone (from Baud et al., 2017b).

As for limestones, the same mechanisms can be identified. In high-porosity grainstones, calcite **grain crushing** is observed in compaction bands (e.g. in Saint-Maximin limestone from Baud et al., 2017a). Moreover, **grain re-arrangement** is reported inside compaction bands of the Majella limestone units. Figure 2.17b shows a zone of compacted grains without signs of breakage in a Majella field, which has been interpreted as a compaction band (see also Rath et al., 2011). However, particularly in limestones, additional micromechanisms can be involved. Due to the low shear strength of calcite in comparison with other minerals such as quartz and feldspar (Turner et al., 1954), crystal plasticity may be activated in limestones, even at room temperature. A **calcite grain twinning** can be observed in compaction bands (Figure 2.17e). Zhu et al. (2010) have reported that a halo of cataclastic damage can be observed around the pores (Figure 2.17c), leading to a **pore collapse** as shown in Figure 2.17d. Larger pores are weaker than micropores and are subject to collapse first. Furthermore, long-term **pressure solution** processes have been observed in limestones. A chemical dissolution of calcite in water can occur. Once the water is fully saturated by calcite minerals, a precipitation can take place. Figure 2.17f shows a flat grain contact indicating a pressure solution phenomenon.

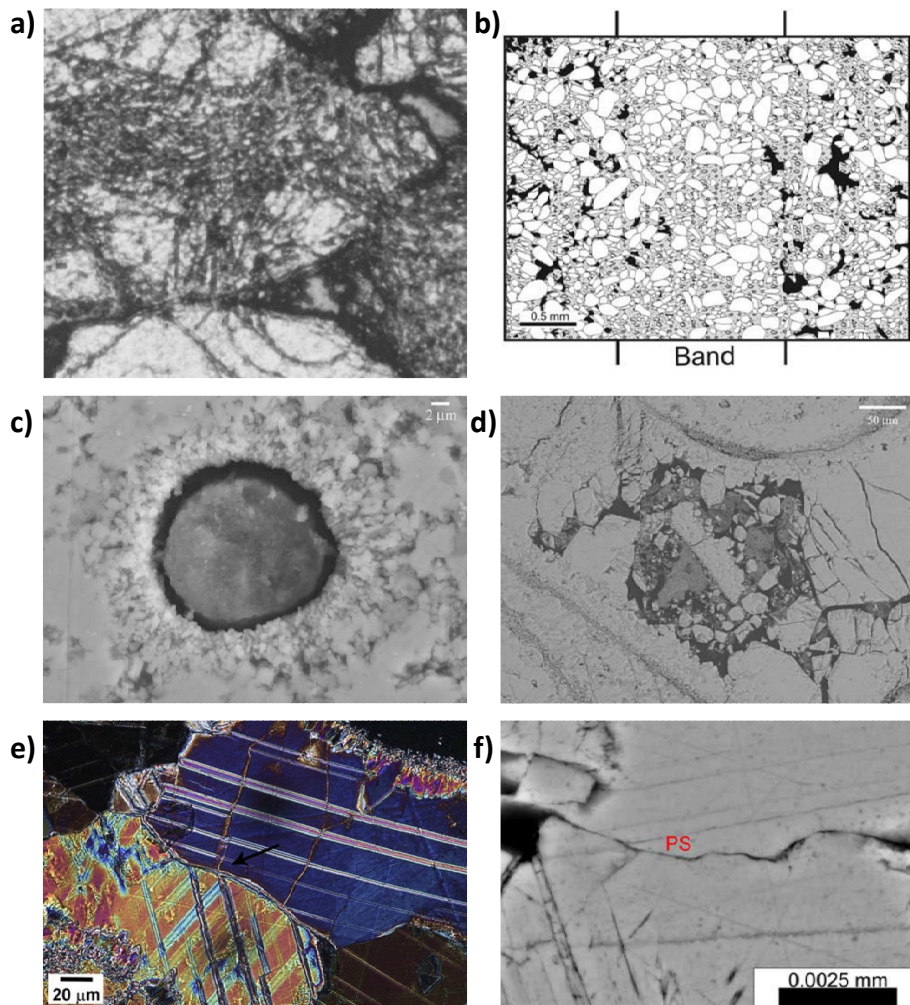


Figure 2.17: a) Radiated cracks from a grain contact in Boise sandstone (Zhang et al., 1990); b) Grain sliding and rotation in a Majella limestone field compaction band (Tondi et al., 2006); c) A pore surrounded by a halo of cataclastic damage in Tavel limestone (Zhu et al., 2010); d) Pore collapse in Indiana limestone (Zhu et al., 2010); e) Twin lamellae observed in a triaxially deformed sample of Indiana limestone (Wong and Baud, 2012); f) Pressure solution process at the grain contacts in the Majella limestone field (Cilona et al., 2012).

2.3.4 Discussion on the laboratory techniques for compaction banding identification

Identifying the formation of compaction bands on laboratory tested limestone samples is a challenging task. Due to the various diagenesis conditions, limestones have a wide variety of microstructural attributes and a more complex pore geometry than sandstones (Choquette and Pray, 1970; Lucia, 1995). Identifying deformation bands by eye inspection of sample surfaces or thin sections is not obvious, unlike for sandstones (Figures 2.8a and 2.10). For instance, Baud et al. (2017b) have recorded stress drops in many samples of Leitha limestone whereas visual inspection does not show any evidence of localization. Moreover, observations on thin sections give a qualitative description of the strain localization and do not allow to characterize the 3D pattern of compaction bands, neither their evolution with

loading, since a sample is no longer eligible for testing once they are prepared. The same configuration cannot be inspected in a reference and deformed states.

As presented in section 2.3.3, grain crushing is pervasive in sandstones. Therefore, a stereological technique has been proposed by Wu et al. (2000). It consists in evaluating quantitatively the crack densities on 2D images, where a zone of high crack density is supposed to correspond to a deformation band. A test array of 10 parallel lines, spaced at a distance of around the third of the grain size, are superimposed to a 2D image at a specific deformation state. This allows to count the number of crack intersections in a specific direction. Supposing that grain cracking is significant in deformation bands, they can be identified based on an analysis of the crack density. Baud et al. (2004) have applied this method to identify deformation bands in Berea sandstone as shown in Figure 2.13. An additional technique in relation with X-Ray imaging has been developed by Otani et al. (2005). The method assumes that a grain crushing would homogenize the spatial distribution of X-Ray attenuation. Thus, the relative dispersion inferred from the grey level statistics in a multiple-voxel elemental volume is an indicator of deformation bands. This technique has been successfully applied on sandstones (Louis et al., 2006; Charalampidou et al., 2011; Charalampidou et al., 2014). However, since grain crushing is not the only micromechanism involved in limestones compaction banding, these techniques cannot be adapted for carbonate rocks. Moreover, the technique that evaluates the spatial distribution of crack density has the same drawback explained for thin section observations: the same configuration cannot be followed before and after loading.

In addition, acoustic emission measurements allow to characterize compaction banding in sandstones (Figure 2.8b). However, this technique is not convenient for limestones, as no acoustic emission activity is in general measured (Vajdova et al., 2004). Recently, Baud et al. (2017a) have recorded acoustic emission activities on laboratory tested Saint-Maximin limestone samples and have explained that it could be attributed to the cracking of quartz grains only. Anyway, it turns out that this technique is not adapted for limestones, which are generally formed of pure calcite.

For all these considerations, the Digital Volume Correlation technique is adopted in this study. It is a recent extension of the 2D image correlation and a non destructive technique that allows to build 3D incremental deformation maps by comparing a configuration before and after its deformation. This technique has been successfully applied to many materials such as bone materials (Follet et al., 2005), argillaceous rocks (Lenoir et al., 2007) and carbonate rocks (Zinsmeister, 2013; Ji et al., 2014 and recently Papazoglou et al., 2017) (Figure 2.18). It allows to characterize the 3D pattern of a strain localization band, follow its evolution with loading and describe the kinematic of deformation inside. The principles of this technique are described later in Chapter 4.

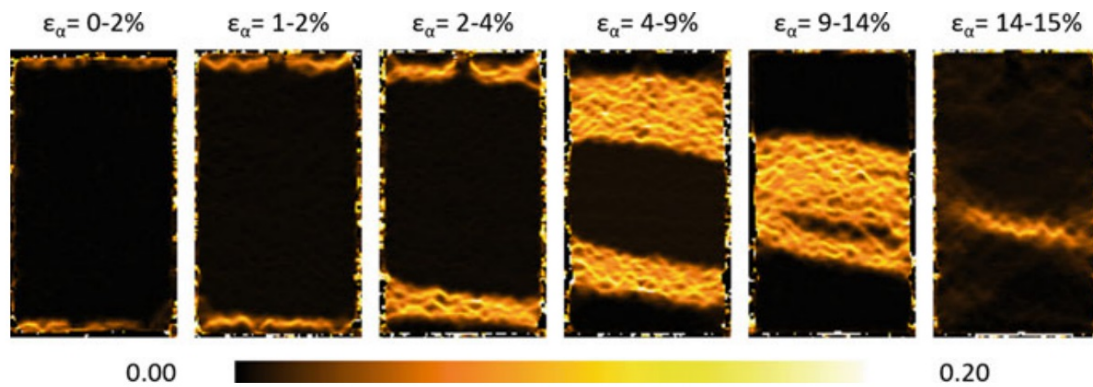


Figure 2.18: Strain localization in a Maastricht carbonate sample obtained from Digital Volume Correlation (Papazoglou et al., 2017).

2.3.5 Microstructural features and compaction banding

As mentioned in sections 2.3.1 and 2.3.2, the deformation mode in the ductile regime may correspond to homogeneous cataclastic flow for many rocks and to localized deformation in the form of compaction bands for others. It is therefore interesting to explore the dominant features of the microstructure that could enhance compaction banding. In the following paragraphs, the role of porosity, grain shape, cementation and mineral composition in compaction banding are discussed.

Porosity

Porosity plays a key role on the deformation mode in the ductile regime. By inspecting the values of porosity in Tables 2.1 and 2.2, one can observe that higher porosity enhances the formation of compaction bands. In laboratory tested sandstones, a homogeneous deformation is observed for low-porosity Darley Dale samples in the ductile regime ($\phi = 14.5\%$). In contrast, discrete compaction bands have been detected in three high-porosity sandstones: Bleuswiller, Bentheim and Diemelstadt whose porosities are around 24%. Berea and Rothbach sandstones with intermediate porosities have shown a mixed behavior (section 2.3.2). Thus, compaction is homogeneous in low-porosity sandstones, whereas a transition to a localized behavior is observed for high-porosity sandstones. However, no compaction bands have been observed in Boise sandstone samples ($\phi = 35\%$), which suggest that high-porosity is a necessary but not sufficient condition for compaction banding. Similarly, low-porosity limestones (e.g Solnhofen, Tavel and Indiana with $\phi < 16\%$) do not show any evidence of localization whereas Majella ($\phi=30\%$) and Saint Maximin ($\phi=37\%$) limestone samples have developed compaction bands. However, a cataclastic flow is reported on porous Leitha limestone ($\phi = 31\%$) as shown in Figure 2.16. These observations corroborate the conclusion made from sandstone results.

Table 2.3: Petrophysical properties of Majella limestone facies studied by Rustichelli et al. (2012). The presence of compaction bands is investigated by naked eye and thin section observations.

Facies	Grain size (mm)	Sorting	ϕ 2D	ϕ_{macro} 2-D	ϕ 3-D	Compaction Bands
A	Medium-coarse (0.52)	Moderate-poorly	16.6	10.8	23.9	Yes
B	Medium (0.3)	Moderate-well	24.6	19.4	32.1	Yes
C1	Fine (0.15)	well-very well	6.5	3.9	10.2	No
C2	Very fine (0.14)	well-very well	0.5	0	3.9	No
E	Mudstone-wackestone (-)	-	1.1	0	29.9	No

Field observations are consistent with laboratory experiment results. Fossen et al. (2011) have noticed that pure compaction bands are only formed in zones where the porosity of the Navajo sandstone host-rock is higher than 29%. In addition, Rustichelli et al. (2012) have explored several facies of Majella limestones whose data are summarized in Table 2.3. According to the authors, a minimum porosity of 15% is needed to generate compaction bands, but it is not sufficient. They have found compaction bands only in facies A and B (porosities 23.9% and 32.1% respectively). These bands are longer, thicker and less-spaced in facies B, whose porosity is higher. In low porosity facies, no localization is found. However, facies E which have high porosity (29.9%) do not reveal any sign of localization. Therefore, from field and laboratory observations, it can be concluded that high porosity is a necessary but not sufficient condition for compaction banding.

Moreover, although facies B and E of the Majella limestone have comparable porosities (around 30%), macro-porosity is dominant in B whereas micro-porosity constitutes the totality of facies E porosity. Thus, a positive effect of macro-porosity on localization is identified. Furthermore, the 2-D micro-porosities of facies A and B are very similar (around 5.5%), but the macro-porosity of facies A is smaller than that of facies B (Table 2.3). According to Rustichelli et al. (2012), compaction bands are more developed in facies B than in A. This result makes evidence of the role played by macro-porosity in order to generate compaction bands. Zhu et al. (2010) have reported that large pores are the first to collapse during loading in triaxial tests. In addition, micro-porosity has been found the same in both the host rock and inside compaction bands of the Saint Margarethen carbonate field (Rath et al., 2011). Baud et al. (2017b) have also shown that macro-pores having diameters larger than 400 μm are collapsed whereas micro-porosity remains intact under triaxial compression. From these observations, a second conclusion can be reached: High macro-porosity enhances compaction banding whereas micro-porosity does not affect the deformation mode.

Grain shape and sorting

The grain shape and sorting play also a role in compaction banding. The Navajo sandstone is formed by rounded, very well sorted grains of 200 to 500 μm in diameter (Fossen et al., 2011). However, compaction bands are formed in zones where grain diameter is higher than 400 μm . Moreover, it is found that poorly sorted grains prevent localization in the Entrada sandstone (Antonellini et al., 1994). Large sized grains surrounded by smaller grains remain intact and act as barriers to the band propagation. The effect of the grain size distribution has been studied by Cheung et al. (2012), who have investigated two samples of Boise and Bleurswiller sandstones having the same porosity (25%) and mineralogy. As aforementioned, compaction bands are formed in three sandstones (Bleurswiller, Bentheim and Diemelstadt) whereas no localization is observed in Boise sandstone, despite its high porosity (Wong et al., 1997). Boise sandstone has a broader range of grain sizes whereas all the others have narrow grain size distributions up to only 300 μm (Figure 2.19a). Although Boise and Bleurswiller sandstones have very close yield stresses (Figure 2.19b), the deformation modes are different in the ductile regime. Figure 2.20 shows a discrete compaction band in a Bleurswiller sandstone sample tested at an effective confining pressure of 40 MPa and a homogeneous cataclastic deformation where localization is prohibited in a Boise sample tested at 60 MPa. In the Boise sample, large grains of quartz and feldspar are found to remain intact and are identified as barriers to the band propagation.

This observation is also common for limestones. In Majella limestone, Tondi et al. (2006) have identified compaction bands only in coarse-grained beds where grains represent 53% of the rock volume and have sizes ranging between 50 and 400 μm . Later, Rustichelli et al. (2012) have reported that compaction bands are the most developed in facies B (Table 2.3) which contain well sorted grains of 300 μm of diameter. No localization is found in fine grained facies such as C1, C2 and E even though grains are very well sorted. In facies A, large and elongated grains represent obstacles to the compaction bands propagation. From these observations, it can be concluded that well sorted, large and rounded grains enhance compaction banding, whereas poorly sorted and elongated grains act as barriers to the band propagation.

Cementation

Other parameters may affect the deformation mode. The presence of cement around grains prohibits stress concentration and plays a role in attenuating strain localization. In addition, cement prevents grain movements and rotations. According to Aydin et al. (2006), the abundance of cement prohibits grain size reduction and pore collapse. This result is clearly shown in Figure 2.21, where pore collapse occurs only in non-cemented granular media. In contrast, the absence of cement in the Saint Margarethen carbonate lead

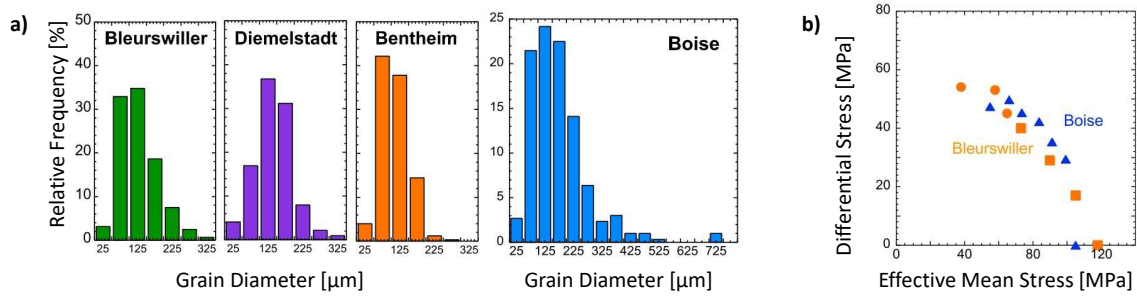


Figure 2.19: a) Grain size distribution in Bleurswiller, Bentheim, Diemelstadt and Boise sandstones; b) Yield stresses for Boise and Bleurswiller sandstones (Cheung et al., 2012).

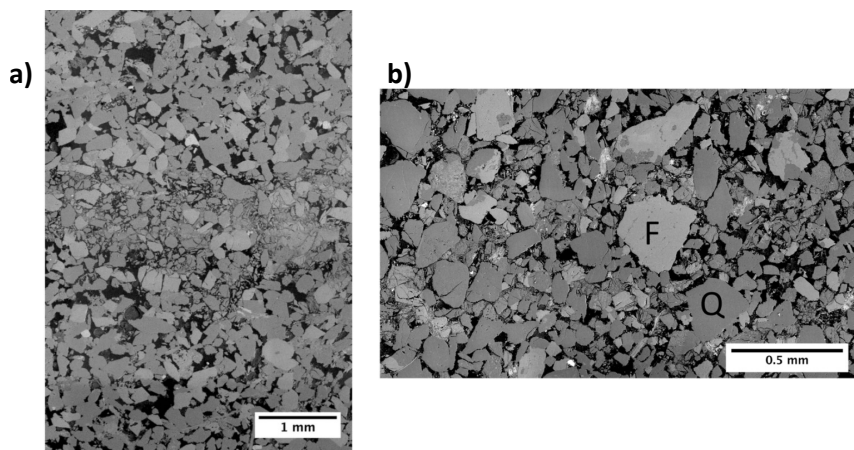


Figure 2.20: Backscattered scanning electron micrograph of: a) a discrete compaction band in a Bleurswiller sample; b) cataclastic deformation without localization in a Boise sample (Cheung et al., 2012).

to the formation of compaction bands by a mechanism of intergranular sliding and grain re-arrangement (Rath et al., 2011). Tondi (2007) have also reported that cement constitutes only 22% of the Majella host rock volume where compaction bands take place. Furthermore, in their paper, Baud et al. (2017b) studied two facies of Leitha limestone having the same composition and similar grain size and macro-pore distributions. Compaction bands are observed in samples showing a lack of cementation as it plays a similar role to small grains around larger ones in a rock constituted of non-homogeneous grain size distribution. This leads to the following conclusion: abundance of cement may prevent the occurrence of compaction bands.

Mineral composition

Rocks can be composed of several minerals, each one has its own resistance and behavior. Although Bentheim sandstone, is composed essentially by quartz (95%), Bleurswiller and Diemelstadt have two main minerals: Quartz (61 to 68 %) and Feldspar (around 27 %). All

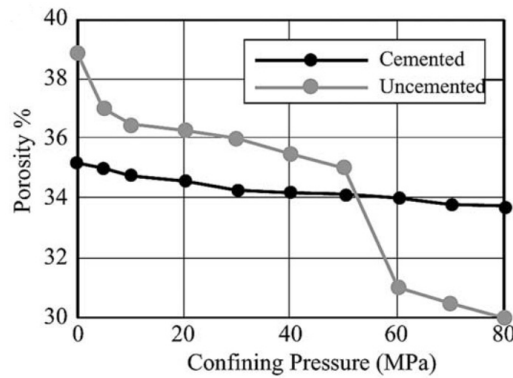


Figure 2.21: Porosity change vs confining pressure for a cemented and non-cemented granular media (Yin and Dvorkin, 1994).

of these three sandstones show compaction bands. Bentheim and Diemelstadt sandstones have the same porosity and grain size distribution, but the difference of mineral composition does not lead to a change in the deformation mode. Furthermore, the Saint-Maximin limestone is not monomineral like Majella limestone, but compaction bands are seen in both rocks. In fact, Majella limestone is composed of almost pure calcite (99%), but the Saint Maximin limestone contains 61% of calcite and 39% of quartz. For all of these reasons, the next conclusion can be taken: Mineral composition of the constitutive grains of sedimentary rocks does not seem to affect the formation of compaction bands.

Figure 2.22 summarizes all the conclusions obtained in this section. It has been shown that a high macro-porosity combined with a well sorted, spherical and large grains enhance the formation of compaction bands in the ductile regime. In contrast, poorly sorted and elongated grains could block the band propagation. In addition, high amount of cement prohibits localization. Moreover, micro-porosity and mineral composition of sedimentary rocks do not seem to have an influence on the deformation mode. A study of the microstructure of many limestones in France has been done in order to choose the one which obeys to the criteria cited above. This will be discussed in Chapter 3.

2.4 Compaction bands modelling

2.4.1 Bifurcation theory

In the framework of the bifurcation theory, strain localization is seen as an equilibrium bifurcation from a homogeneous to a non-homogeneous deformation state, where the deformation is localized in the form of a planar band as shown in Figure 2.23 (Bésuelle and Rudnicki, 2004). The objective is thus to find at which stress condition the band is triggered, the orientation and type of the deformation band. This threshold corresponds to a state for

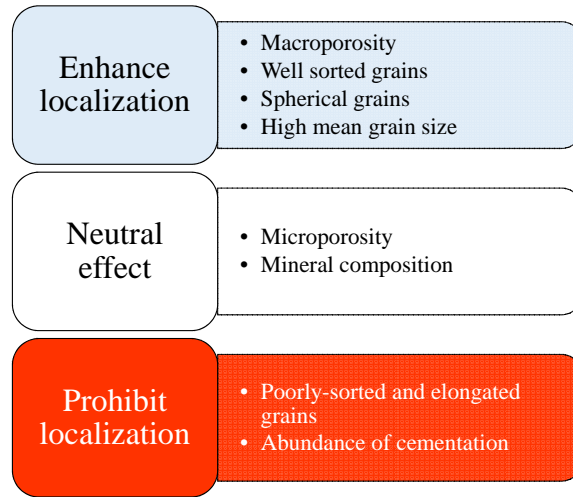


Figure 2.22: Factors that prohibit, allow and are neutral to compaction banding in sedimentary rocks.

which the acoustic tensor becomes singular (Rudnicki and Rice, 1975). The development of the theory will be briefly presented below.

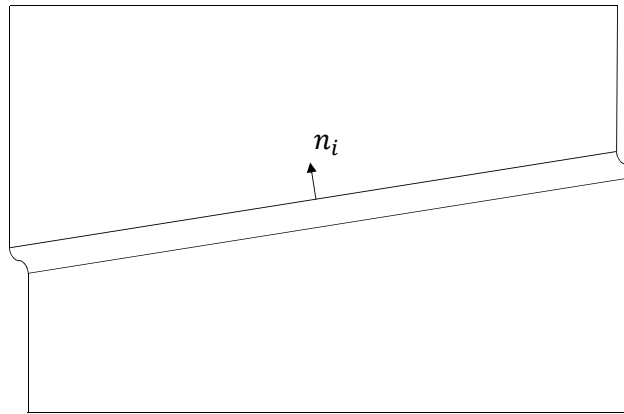


Figure 2.23: A planar deformation band.

Constitutive relations for rate-independent solids

Consider a rate-independent homogeneous solid for which the linear incremental constitutive equations are written as:

$$\Delta\sigma_{ij} = L_{ijkl}\Delta\epsilon_{kl} \quad (2.2)$$

where σ_{ij} and ϵ_{kl} are the Cauchy stress and the strain tensors respectively, whereas L_{ijkl} is a fourth-order tensor. Because of the symmetry of both the stress and strain tensors ($\sigma_{ij} = \sigma_{ji}$ and $\epsilon_{kl} = \epsilon_{lk}$), one should have:

$$L_{ijkl} = L_{jikl} = L_{ijlk} = L_{jilk} \quad (2.3)$$

Consider a homogeneous deformation of the solid subjected to quasi-static increments of deformation. The existence of discontinuous deformation modes is sought, as possible continuations of homogeneous deformation (Vardoulakis and Sulem, 1995).

Kinematic condition

Let denote by n_i the unit vector normal to the band. The rate of deformation is assumed to remain homogeneous outside the band. In addition, the incremental displacement field Δu_k is assumed to be continuous across the band. Therefore, according to Maxwell theorem, only the normal derivative of the displacement field may be discontinuous across the band. The following kinematic compatibility conditions hold:

$$[[\Delta u_k]] = 0 \quad \text{and} \quad [[\partial_k \Delta u_l]] = g_l n_k \quad (2.4)$$

where $[[.]]$ denotes the discontinuity of a quantity across the band boundaries and the vector g_i describes the direction of the discontinuity. The inner product of g_i with the normal direction n_i allows to determine the deformation band type:

$$\left\{ \begin{array}{ll} n_i \cdot g_i = 1 & \text{Pure dilation band} \\ 0 < n_i \cdot g_i < 1 & \text{Dilatant shear band} \\ n_i \cdot g_i = 0 & \text{Pure shear band} \\ -1 < n_i \cdot g_i < 0 & \text{Compactive shear band} \\ n_i \cdot g_i = -1 & \text{Pure compaction band} \end{array} \right. \quad (2.5)$$

In the case of a simple shear band, the relative movement is tangent to the band (Figure 2.24). Shearing can be accompanied by volumetric changes: either compactant or dilatant. In case of little or no shear offset, a pure extension or shortening occurs.

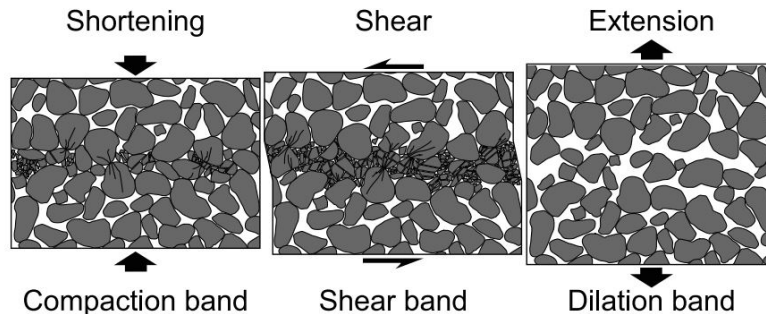


Figure 2.24: Three reference types of strain localization: compaction, shear and dilation bands (from Du Bernard et al., 2002).

Equilibrium condition

To ensure equilibrium, the stress vector t_i should remain continuous across the band boundary:

$$[[\Delta t_i]] = [[\Delta \sigma_{ij}]] n_j = 0 \quad (2.6)$$

From Equation 2.2, it follows:

$$\left[L_{ijkl}^b \Delta \epsilon_{kl}^b - L_{ijkl}^o \Delta \epsilon_{kl}^o \right] n_j = 0 \quad (2.7)$$

where the superscripts $..^b$ and $..^o$ denote quantities inside and outside the band respectively. Two cases can be considered: The first case is to suppose an elastic unloading outside the band while inelastic loading occurs inside it, which implies a discontinuity of the fourth-order tensor L_{ijkl} across the band boundaries. The second case is to consider a continuous tensor $L_{ijkl}^b = L_{ijkl}^o$. The two cases are called *discontinuous bifurcation* and *continuous bifurcation* respectively. Rice and Rudnicki (1980) have demonstrated that discontinuous bifurcation is always preceded by the continuous one. Therefore, the latter assumption is considered for simplicity. By combining Equations 2.4 and 2.7 and with noticing the symmetry conditions (Equation 2.3), the discontinuity condition becomes as follows:

$$\left[n_j L_{ijkl} n_l \right] g_k = 0 \quad (2.8)$$

The acoustic tensor is thus defined as $\Gamma_{ik} = n_j L_{ijkl} n_l$. Non trivial solutions exist for g_k when the acoustic tensor becomes singular.

$$\det(\Gamma_{ik}) = 0 \quad (2.9)$$

the system bifurcates and the homogeneous deformation is no longer the unique solution. The discontinuity of the strain tensor over a band becomes possible, since g_k can take non-zero values. The bifurcation condition (Equation 2.9) is valid no matter the material constitutive behavior is.

Rudnicki and Rice (1975) have applied this theory to predict the formation of shear bands. Later, Olsson (1999) has noted that the approach can also predict the formation of compaction bands perpendicular to the most compressive stress direction. The theoretical considerations have been then extended by Issen and Rudnicki (2000). They have considered an elastic-plastic constitutive law depending on the first and second stress invariants ($p = \frac{\sigma_{ii}}{3}$ and $q = \sqrt{\frac{1}{2} s_{ij} s_{ij}}$ respectively, where $s_{ij} = \sigma_{ij} - p \delta_{ij}$ is the deviatoric stress). Under axisymmetric triaxial compression, the bifurcation theory provides a critical hardening modulus h_{cr} in terms of the yield surface F slope $\mu = \frac{\partial F / \partial p}{\partial F / \partial q}$ and the dilatancy parameter $\beta = \frac{\partial g / \partial p}{\partial g / \partial q}$, where g is the plastic potential (Figure 2.25). The critical hardening modulus cor-

responds to the maximum value calculated over all the orientations (n_i). Strain localization occurs when the hardening modulus $h = \partial q / \partial \gamma^p$ becomes smaller than the critical modulus $h < h_{cr}$ for given values of μ and β (γ^{pl} represents the plastic shear strain as defined by Isсен and Rudnicki (2000)). Compaction bands are observed to take place at the lower left part of the plot which mainly corresponds to highly compactive materials. The values of the critical hardening modulus are given by Isсен and Rudnicki (2000). According to the authors, a non-associative material ($\mu \neq \beta$) is more prone to compaction bands formation, as the critical hardening modulus is larger.

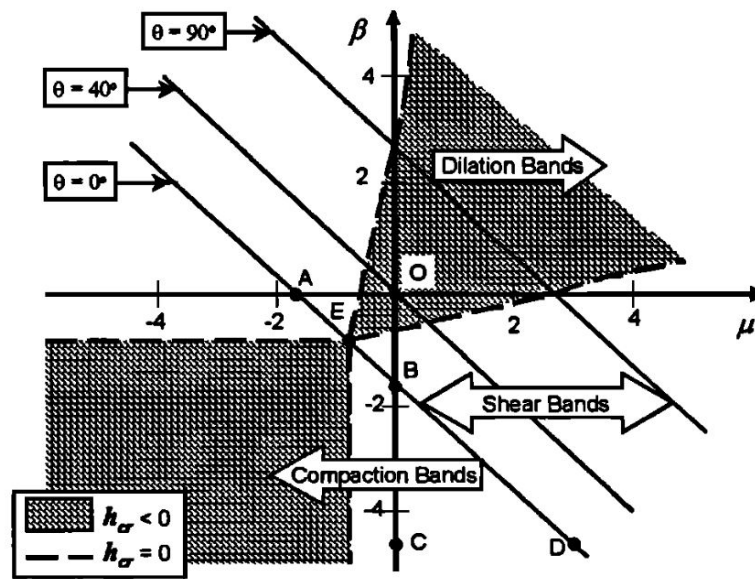


Figure 2.25: Critical hardening modulus h_{cr} for deformation bands onset in terms of the yield surface slope μ and the dilatancy parameter β . The angle θ represents the orientation of band normal vector with respect to the most compressive principal stress direction (from Isсен and Rudnicki (2000)).

The bifurcation theory as applied here allows to predict the stress conditions at which localization of deformation occurs, the orientation and the type of the band. However, the band thickness is not predicted, neither the post-localization behavior.

2.4.2 Linear stability analysis - The limitation of the Cauchy continuum

Deformation bands formation can be seen as an instability problem. A system is unstable in the sense of Lyapunov (1992) when its response to a perturbation is unbounded (simple examples are given in Stefanou and Alevizos (2016)). The momentum balance equation can be written by considering the inertial terms:

$$\sigma_{ij,j} = \rho \ddot{u}_i \quad (2.10)$$

where ρ is the material density and the double dot \ddot{u}_i represents the second time derivative. Before any perturbation, the homogeneous solution σ_{ij}^* respects the following equilibrium equation:

$$\sigma_{ij,j}^* = 0 \quad (2.11)$$

For a small increment (or perturbation) $\Delta\sigma_{ij} = \sigma_{ij} - \sigma_{ij}^*$, the constitutive law can be linearized around the homogeneous solution and one can get:

$$\Delta\sigma_{ij} = L_{ijkl}\Delta u_{k,l} \quad (2.12)$$

where $\Delta u_i = u_i - u_i^*$ is a perturbation around the homogeneous solution u_i^* and the notation $(\cdot)_{,l}$ represents the derivative in terms of the coordinate x_l . Going back to Equation (2.10), one can get a new relation for the displacement field perturbation:

$$L_{ijkl}\Delta u_{k,lj} = \rho\Delta\ddot{u}_i \quad (2.13)$$

The latter differential equation can be solved by separation of the variables, where the perturbation is decomposed in the product of two functions $\Delta u_i(x_k, t) = X(x_k)U_i(t)$:

$$L_{ijkl}X_{,lj}U_k = \rho X\ddot{U}_i \quad (2.14)$$

The solution of this equation is decomposed in Fourier modes under the following form: $\Delta u_i = g_i e^{ikn_i x_i + st}$, where k is the wave number of the perturbation and n_i is the unit vector normal to the band. Since the displacement field is continuous across the band boundaries, the wavelength $\lambda = \frac{2\pi}{k}$ defines the band thickness, as $\Delta u_i = 0$ at the boundary. The stability condition corresponds to negative values of the growth coefficient s as this corresponds to perturbations which vanish in time. However, if the real part of s is ≥ 0 , the system is unstable and a localization band forms with a normal vector n_i . By replacing the proposed solution into Equation 2.13, one can obtain after some algebraic manipulations:

$$\left[n_j L_{ijkl} n_l - \rho \left(\frac{\lambda s}{2\pi} \right)^2 \delta_{ik} \right] g_k = 0 \quad (2.15)$$

By setting $c = \frac{\lambda s}{2\pi}$ (which has the dimension of a velocity), one can obtain the Hadamard equation on the propagation of acceleration waves in a solid body along the direction n_i (Hadamard, 1903, Lemaitre et al., 2009). These waves represent weak discontinuities of the mechanical fields across wave-fronts propagating with a speed c , which corresponds to a square root of an eigenvalue of the acoustic tensor. Noticing that $s = 2\pi \frac{c}{\lambda}$, if the real part of an eigenvalue is positive, the homogeneous solution is unstable and a deformation band with normal direction n_i is formed.

In case of rate-independent materials in a Cauchy continuum, the eigenvalues of the acoustic tensor are independent on the perturbation wavelength λ neither on the growth

coefficient s . Therefore, the velocity c can only take constant values. Moreover, if an eigenvalue with positive real part exists, the perturbation which propagates faster has zero wavelength since $s \rightarrow \infty$ when $\lambda \rightarrow 0$. A minor imperfection in size will thus dominate any imperfection of larger wavelength. Consequently, the deformation band has a zero thickness and occurs over a mathematical plane. In Finite Element simulations, plastic strains, energy dissipation are mesh-dependent because the band thickness itself is mesh-dependent. Figure 2.26 shows an example of the mesh-dependency of a shear band formed in a rate-independent constitutive law in a Cauchy continuum, where the band is always spread over 1 to 2 elements.

In the presented analysis, the constitutive behavior is supposed to be uniform for a homogenized material at the scale of the representative elementary volume. The limitation of the rate-independent constitutive laws in a Cauchy continuum must be corrected by taking into consideration the microstructure. In other words, when localization occurs, the mechanisms at the microscale are no longer negligible and should be considered in the constitutive laws.

To describe the microstructure, at least one internal length must be introduced in the constitutive relations. Thus, the linear stability analysis performed on the enriched continuum allows to determine a finite band thickness and to get rid of the mathematically ill-posed governing equations in the post-localization regime. Micromorphic media are higher-order continua which contain additional degrees of freedom allowing to control the deformation band thicknesses and regularize the problem of localization. The principle of these media is presented in next section.

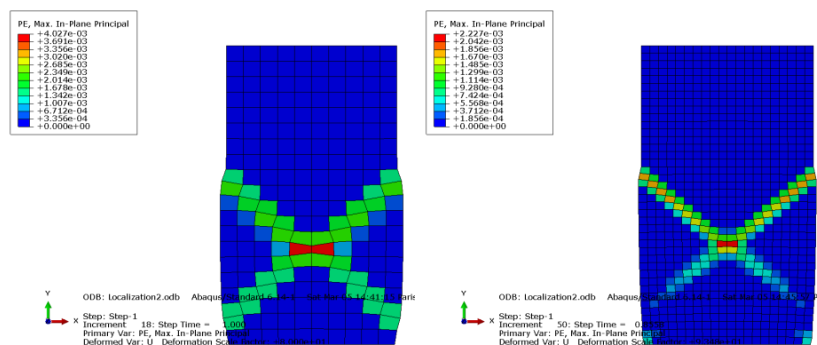


Figure 2.26: An example of mesh-dependent shear band in a rate-independent constitutive law in Cauchy continuum (from Stefanou and Alevizos, 2016).

2.4.3 Micromorphic media

Unlike Cauchy continuum, micromorphic media are general continua that represent heterogeneous solids with microstructure of non-negligible size. Following the work of Mindlin (1964), Germain (Germain, 1973a; Germain, 1973b) has developed the complete formulation of micromorphic media based on the principle of virtual power.

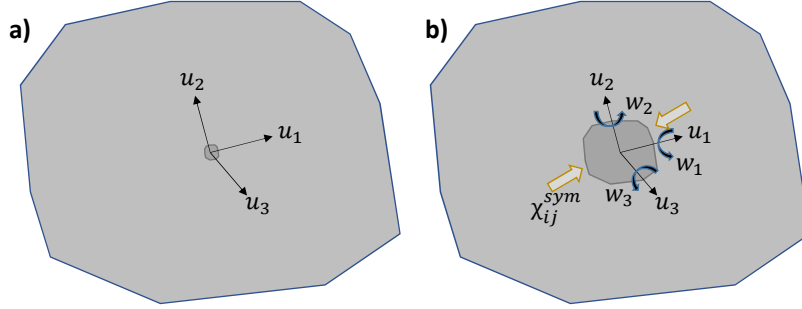


Figure 2.27: A schematic of the degrees of freedom considered for: **a)** a material point in the Cauchy continuum; **b)** a microvolume in the micromorphic continuum of degree 1.

In a model with microstructure, each particle is no longer represented by a point that has only 3 translational degrees of freedom ($u_1; u_2; u_3$ - see Figure 2.27a). In contrast, a microvolume is attached to each material point and is considered as a continuum of small extent. The description of the microvolume kinematics is enhanced by the introduction of additional degrees of freedom.

Let M be the center of mass of the subvolume and u_i its displacement vector. For a point M' of the subvolume of coordinate x'_j with respect to M , its displacement can be approximated using the Taylor expansion by:

$$u'_i = u_i + \chi_{ij}x'_j + \chi_{ijk}x'_jx'_k + \chi_{ijkl}x'_jx'_kx'_l + \dots \quad (2.16)$$

where χ_{ij} is a first gradient of relative displacement, χ_{ijk} is a second gradient and so on. If $u'_i = u_i$, a Cauchy continuum is obviously obtained. However, if the expansion is cut after the term $\chi_{ij}x'_j$, the medium is called a micromorphic continuum of degree 1. A sufficient description of the relative motion of the subvolume points can be obtained if the fields u_i and χ_{ij} are given. The symmetric part of χ_{ij} represents the micro-strain tensor, whereas its antisymmetric part represents the micro-rotation tensor. Thus, the microvolume can rotate ($w_1; w_2; w_3$) or deform (χ_{ij}^{sym}) (Figure 2.27b). The internal power density δw is assumed to have a linear form on u_i , $u_{i,j}$, χ_{ij} and $\chi_{ij,k}$, or equivalently on u_i , $u_{i,j}$, $\eta_{ij} = u_{i,j} - \chi_{ij}$ and $\kappa_{ijk} = \chi_{ij,k}$:

$$\delta w = K_i \cdot u_i + \sigma_{ij} \cdot u_{i,j} + s_{ij} \cdot \eta_{ij} + \nu_{ijk} \cdot \kappa_{ijk} \quad (2.17)$$

where K_i , σ_{ij} , s_{ij} and ν_{ijk} are the dual parts of the kinematic quantities. δw should remain unchanged whatever the cartesian frame is. Thus, $K_i = 0$ and σ_{ij} should be symmetric (Germain, 1973b). σ_{ij} , s_{ij} and ν_{ijk} are the Cauchy stress, relative stress and the second microstress tensors respectively. After some integration by parts, the internal power can be written as:

$$P_i = - \int_{\mathcal{D}} \delta w dv = \int_{\mathcal{D}} \left[(\sigma_{ij,j} + s_{ij,j}) u_i + (s_{ij} + \nu_{ijk,k}) \chi_{ij} \right] dv - \int_{\partial \mathcal{D}} \left[(\sigma_{ij} + s_{ij}) n_j u_i + \nu_{ijk} \chi_{ij} n_k \right] dS \quad (2.18)$$

where \mathcal{D} and $\partial \mathcal{D}$ represent a subvolume and its surface respectively. The virtual power of external forces is defined by analogy and is decomposed in volumic and contact forces powers:

$$P_e = P_v + P_c = \int_{\mathcal{D}} \left[f_i u_i + \Psi_{ij} \chi_{ij} \right] dv + \int_{\partial \mathcal{D}} \left[T_i u_i + M_{ij} \chi_{ij} \right] dS \quad (2.19)$$

with f_i and T_i as volumic and traction forces respectively, Ψ_{ij} as a volumic double force and M_{ij} as a double surface traction. By applying the principle of virtual power ($P_i + P_e = 0$) and isolating the volumic from the surface integrals, two equilibrium conditions are obtained:

$$\begin{aligned} \tau_{ij,j} + f_i &= 0 \\ s_{ij} + \nu_{ijk,k} + \Psi_{ij} &= 0 \end{aligned} \quad (2.20)$$

where $\tau_{ij} = \sigma_{ij} + s_{ij}$ is the total stress tensor. In addition, the following boundary conditions are obtained:

$$\begin{aligned} T_i &= \tau_{ij} n_j \\ M_{ij} &= \nu_{ijk} n_k \end{aligned} \quad (2.21)$$

Two interesting particular cases of a micromorphic medium of degree 1 can be examined:

- If the subvolume is considered as a rigid body. Therefore, the gradient of the relative displacement is purely antisymmetric. The subvolume is allowed to move and rotate only. The medium is nothing else than the Cosserat continuum (Cosserat and Cosserat, 1909). This model seems to be appropriate for localization of deformation in sands and sandstones (Mühlhaus and Vardoulakis, 1987; Vardoulakis and Sulem, 1995; Rattetz et al., 2018).
- If the subvolume is assumed to deform identically to the general continuum, the micromorphic medium degenerates to a second gradient theory. In this case, the restriction $\chi_{ij} = u_{i,j}$ should be applied (Chambon et al., 2001).

The models described in this section are considered as local models, since the introduction of dual terms of the micro kinematic variables is done in the expression of the

energy. The equilibrium equations and boundary relations are thereafter generalized to take into consideration the additional terms. However, non-local approaches provide other models that allow to take microstructure into account and regularize the problem of strain localization.

2.4.4 Non local models

Non local models constitute another strategy to assess deformation bands thickness. In classical continuum theory, physical quantities are defined locally at a point (stress state, deformation tensor and internal variables). However, these quantities can be affected by the material heterogeneities at the vicinity (pores, cracks..). In this case, physical quantities are averaged over a subvolume centered at the material point, which leads to the introduction of an internal length. For instance, a non local internal variable $\xi(\bar{\kappa}^P)$ can be considered and on which the yield surface depends:

$$F(\sigma_{ij}, \xi(\bar{\kappa}^P)) = 0 \quad (2.22)$$

κ^P is a hardening parameter (it could be the plastic shear strain, plastic volumetric strain..) and $\bar{\kappa}^P$ is the average over a volume V_x centered over x (Bazant and Pijaudier-Cabot (1988)):

$$\bar{\kappa}^P(x) = \frac{1}{V_r} \int_{V_x} \alpha(s-x) \kappa^P(s) dV \quad (2.23)$$

where $\alpha(x)$ is a weighting function and V_r is defined as:

$$V_r = \int_{V_x} \alpha(s-x) dV \quad (2.24)$$

Consider a uniform weighting function ($\alpha(x) = 1$). After developing the Taylor expansion of κ^P around the position x up to the second order, $\bar{\kappa}^P$ can be expressed in terms of:

$$\bar{\kappa}^P = \kappa^P + l^2 \nabla^2 \kappa^P \quad (2.25)$$

where l is proportional to the size of the subvolume V_x (the proportionality coefficient depends on the shape of the subvolume V_x) and ∇^2 is the second gradient operator. A gradient-dependent elastic-plastic model is thus constructed (Vardoulakis and Aifantis, 1991; De Borst and Mühlhaus, 1992; Pamin, 1996).

2.4.5 Discussion on the internal length calibration

In classical constitutive models, material parameters are calibrated using experimental laboratory tests such as triaxial, oedometer, plane strain loading experiments, etc., assuming samples are loaded homogeneously during such experiments. However, the additional

parameters introduced in micromorphic media require the development of new calibration procedures which are able to capture the effects of heterogeneous behaviors. For this purpose, global measurements of stress state, strain tensor and other state variables are not sufficient, and local measurements at the scale of the microstructure are required. In the last two decades, several imaging and post-processing techniques which enable to get data at the micro-scale level have been developed (Hall et al., 2012). Nonetheless, few works have been dedicated to the calibration of higher order continua based on local measurements (e.g. for Cosserat continuum: Wang et al., 2016; Esin et al., 2017). An indirect attempt to calibrate the additional parameters is by numerical identification procedure (e.g. El Moustapha, 2014; Raude et al., 2015). Back analysis of the thickness of deformation bands as observed in element tests can give access to the internal length of the underlying constitutive model. However, this procedure can be poorly constrained as other additional parameters can be involved in the constitutive models of micromorphic media. Consequently, it is of high importance to exploit imaging technique in the calibration of higher order continuum parameters.

Material description

Résumé Dans ce chapitre, les propriétés microstructurales de la roche de Saint-Maximin sont présentées. Des observations tomographiques au synchrotron sur un échantillon de section millimétrique sont montrées. A plus grande échelle, une hétérogénéité de porosité est mise en évidence grâce à des images aux rayons X de laboratoire. Pour caractériser la microstructure dans ces zones, des petits échantillons sont préparés, imagés et testés à l'aide de la porosimétrie par intrusion de mercure. De plus, des lames minces de la roche sont préparées et observées aux microscopes optique et électronique à balayage. Toutes ces observations mettent en évidence une dissolution éventuelle des grains de calcite dans les zones les plus poreuses, qui est responsable d'une fluctuation à l'échelle centimétrique de la porosité variant entre 30% et 45% d'une zone à l'autre.

Abstract In this chapter, the microstructural properties of the Saint-Maximin limestone are presented. Tomographic synchrotron observations on a rod of millimetric size cross-section are shown. On a larger scale, a porosity heterogeneity is brought out by means of laboratory X-Ray microtomography images. To characterize the microstructure inside these zones, small samples are prepared, imaged and tested by Mercury Intrusion Porosimetry. In addition, thin sections are prepared and observed by means of optical and scanning electron microscopy. All these observations allow to conclude that a possible calcite grain dissolution in the more porous zones is responsible for fluctuations at centimetric scale of the porosity which varies between 30% and 45% from a zone to the other.

3.1 Material selection - The Saint-Maximin limestone

As presented in Section 2.3.5, the microstructure of sedimentary rocks has a major impact on the formation of compaction bands. Limestones exhibit a wide range of microstructural features (Flügel, 2013). The diagenetic reaction conditions control the shape, size and amount of grains, cement and pores. Limestones are characterized by complex pore geometries where porosity can go from 2% to more than 40%. According to Mutti (1995), a lack of cementation induces a high porosity in sedimentary rocks. Furthermore, several families of porosity are found in general, with inter-particle and intra-particle pores usually referred as macro-porosity and micro-porosity respectively. Thus, grains in carbonate rocks can be dense or micro-porous. Two main classifications of carbonate rocks exist: The Dunham (1962) and Folk (1962) classifications (summarized in Appendix A). They highlight the wide range of microstructural features of carbonate rocks. From the criteria listed in Figure 2.22, it appears that grainstones (in Dunham classification) or sparry allochemical limestones (in Folk classification) are the most appropriate for the purpose of this study. In these rocks, a structure of large grains is observed, macro-porosity is dominant and cementation is rare.

The microstructural features of many limestone rocks are gathered in Table 3.1 (empty cells correspond to non provided data). A more detailed description is given in Appendix B. It can be seen that:

- Solnhofen and Tavel limestones have low porosities as well as small grains.
- Vilhonneur and Euville limestones contain an abundant amount of cement in the macro-pores and around the grains. In addition, Lens limestone does not contain macro-pores.
- Pillar and Bouye limestones are considered as mudstones according to the Dunham classification. Grains are rare and macro-porosity does not exist.
- Indiana limestone does not seem to have a sufficient macro-porosity to enhance compaction bands (Vajdova et al., 2004).
- Chameçon, Chauvigny and Anstrude limestones have dominant micro-porosities in comparison with macro-porosity.
- Estailades limestone present an inconvenience because of its elongated grains.

Limestone	D_{grains} (μ m)	D_{pores} (μ m)	ϕ_{total} (%)	ϕ_{micro} (%)	ϕ_{macro} (%)	Sorting	Grain shape	Cement amount	References
Solnhofen	5		3						Baud et al., 2000
Tavel	5		10.4						Vajdova et al., 2004
Vilhonneur	1000		11.0				sphere	abundant	Saad, 2011
Lens	< 1000	0.22-0.85	13.9	13.9	0.0		sphere		Saad, 2011
Pillar	-		9-22		$\simeq 0$	-	-	abundant	Lezin et al., 2009
Bouye	-		<14		$\simeq 0$	-	-	abundant	Lezin et al., 2009
Indiana	300		16						Vajdova et al., 2004
Euville	100-1000	0.5-20	17.0	7.5	9.5		sphere	around grains	Nguyen, 2012
Chamesson	< 1000	0.2	17.0	17.0	0.0		sphere	fills macropores	Saad, 2011
Chauvigny	400		17.0	13.0	6.0		sphere		Fortin et al., 2009b
Anstrude	100-1000	0.4	20.0	20.0	0.0		sphere	fills macropores	Lion, 2004
Lavoux CG	500	0.7-30	23.5	12.9	10.6	good	sphere	rare	Zinsmeister, 2013
Lavoux FG	10-50	0.5-5	24.5	13.5	11.0	not well		homogeneous	Zinsmeister, 2013
Estailades	300-500	0.2-10	24-30	9.0	18.0		elongated	rare	Dautriat, 2009
Majella	54	16.2	30		Dominant			Rare	Ji et al., 2014
Leitha	480	30-500	18-31	$\simeq 0$	18-31			Rare	Gilona et al., 2014
Saint-Maximin	140	26.4	37		Dominant	good		Rare	Baud et al., 2009
								Rare	Baud et al., 2017b
								Rare	Baud et al., 2009

Table 3.1: Summary of several limestones microstructural properties.

For all these reasons, none of the previous rocks is retained. On the other hand:

- Lavoux is a grainstone which has a bimodal porosity of 25%. Coarse grained facies contains spherical grains and a rare amount of cement. However, fine grained facies contains higher amounts of cement and wider particle size distribution. Thus, coarse grained facies could be a good choice.
- Majella and Leitha limestones have presented for some confinements the formation of compaction bands. The high porosity facies are grainstones of rare cementation. Thus, they could be also good choices in this study.
- Saint-Maximin limestone is a grainstone, having the highest macro-porosity among all the rocks. An advantage of this rock with respect to other grainstones is that it contains one family of pores as well as a good sorting and homogeneous microstructure.

In conclusion, Saint-Maximin limestone seems to be an appropriate rock for the purpose of this study and is finally selected.

3.2 Sample preparation and global porosity measurements

The Saint-Maximin limestone (SML) is a porous rock from the Parisian basin (Fronteau et al., 2010). It belongs to the Lutetian stage of the Eocene epoch, which spans the time between 47.8 and 41.2 million years (Jenkins and Luterbacher, 1992). Parallelepipedic blocks of $30 \times 30 \times 13 \text{ cm}^3$ have been provided from the Rocamat quarry in Saint-Maximin-sur-Oise in the North of Paris. For the mechanical tests, cylindrical samples of 4 cm diameter and 8 cm height are cored. The samples faces are ground to ensure that they are flat and parallel.

Then, the interconnected porosity is measured by the hydrostatic weighing method. The sample is put in a bowl filled with water around two thirds of its volume. A glass bell covers the bowl and isolates the system from the outside (Figure 3.1). Vacuum is thereafter applied by means of a pump. Air inside pores is thus pushed away. Two hours later, more water is added to completely cover the sample and vacuum is applied for a second time. After four hours, the mass of the sample is observed to remain constant, which means that open pores are totally filled with water. The water-saturated mass m_s is recorded and the sample is

then dried in an oven at 60°. After one day, it is observed that the mass becomes constant. The dry mass m_d is thus evaluated. The interconnected porosity ϕ is finally measured as:

$$\phi = \frac{m_s - m_d}{\rho_w V_{cyl}} \quad (3.1)$$

where V_{cyl} is the total volume of the sample computed from its overall dimensions, and ρ_w is the density of water

72 samples are cored from two parallelipedic blocks and their porosities are evaluated. Figure 3.2 shows that these blocks are rather homogeneous: the porosity of the samples ranges between 35% and 40%, with a mean value of 37.85%. The samples having porosity lower than 37.25% or greater than 39.25% are excluded throughout the study.

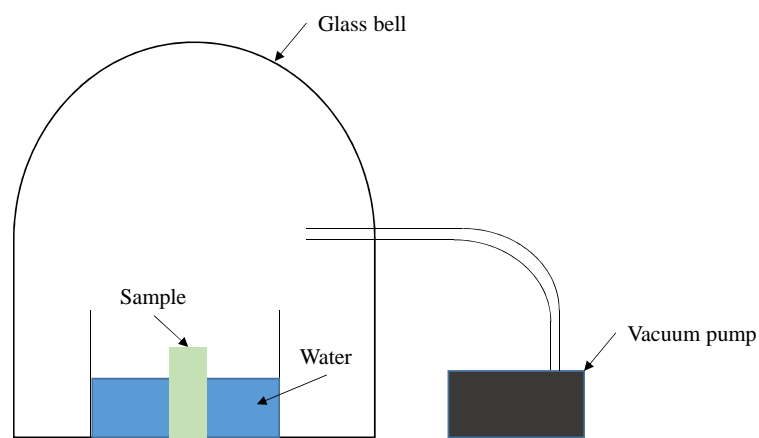


Figure 3.1: A schematic of the sample water saturation procedure.

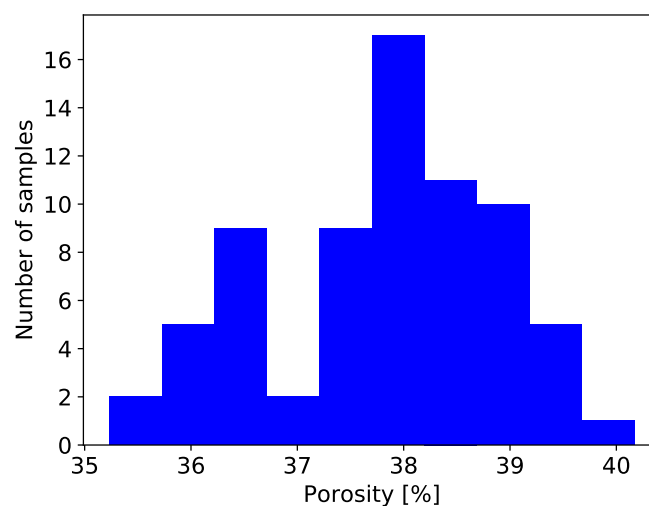


Figure 3.2: Histogram of the global porosity distribution evaluated for 72 samples.

3.3 Microstructure characterization

After characterizing the global porosity of the SML samples, it is important to understand the features of its microstructure. Thus, various complementary techniques are used.

3.3.1 Observations at the sub-millimetric scale

In order to characterize the rock microstructure, XRCT images are recorded using the ANATOMIX beamline at Synchrotron SOLEIL¹. The use of such radiations allows for both fast and high-resolution microtomography (Weitkamp et al., 2017). However, the low photon energy (from 5 to 25 keV) does not allow the transmission of incident emission across a large specimen. Therefore, the size of the specimen in the beam direction should be at most 2 mm. A rod of SML - in as-received conditions - is thus prepared using a diamond wire saw (Details of the preparation are presented in Appendix C). The rod, which has a square cross-section of 1.3 mm in side length is imaged at a voxel size of $0.65 \mu\text{m}$ (Figure 3.3). The principles of laboratory X-Ray imaging will be explained later in Section 4.2. 2000 projections are recorded over 80 rotations. After reconstructions with the pyhst software, volumes of 2048^3 voxels are re-obtained, covering a physical volume of $1.35 \times 1.35 \times 1.35 \text{ mm}^3$. The total duration of the complete scan is 45 minutes.

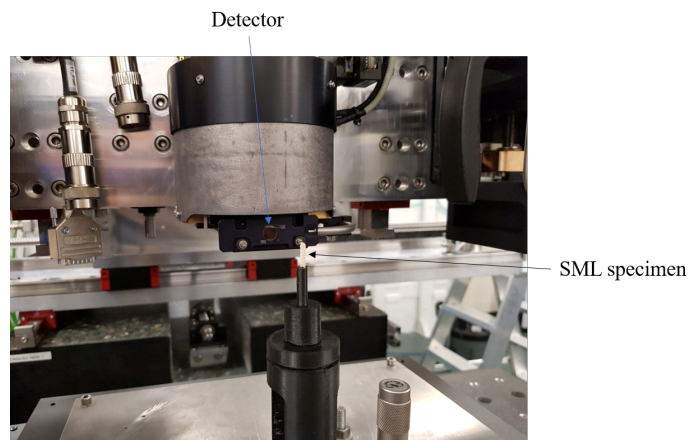


Figure 3.3: A SML rod specimen imaged by XRCT at SOLEIL synchrotron.

Figure 3.4 presents a transverse cross-section of a XRCT image of the SML specimen. Microporous angular grains of calcite are observed with a diameter range between 150 and $300 \mu\text{m}$, whereas smaller limited number of quartz grains² are found with a diameter range between 50 and $100 \mu\text{m}$. These observations are consistent with those of Baud et al. (2017a) who have reported that SML contains around 80% of calcite and 20% of quartz as indicated by X-Ray diffraction analysis. Figure 3.4 also shows the existence of a

¹Images have been recorded in April 2017 within the context of the proposal 20171213

²The quartz grains appear somewhat darker because of the lower X-Ray absorption of the quartz mineral with respect to calcite.

non-negligible proportion of calcareous *Miliolidae*, which are shells of spherical shape and represent a feature of the Lutetian stage (Flügel, 2013). On the other hand, two families of porosity can be distinguished: polydisperse inter-granular pores of diameters ranging between 1 and 100 μm and intra-granular pores inside calcite grains having a comparable size to the image resolution or even lower ($<0.65 \mu\text{m}$). In addition, the large pores are sometimes linked to the porosity inside *Miliolidae* shells. These observations give a first understanding of the microstructure of SML. However, looking at a larger scale, additional complexities are found.

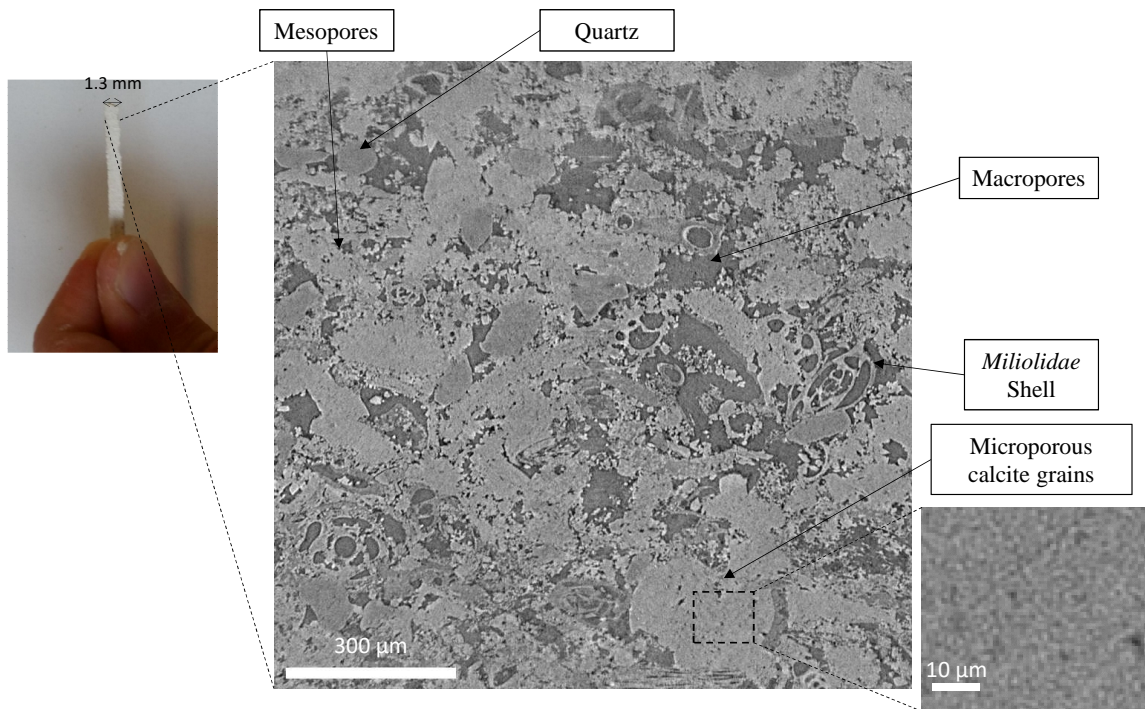


Figure 3.4: A transverse cross-section of XRCT image of the SML specimen.

3.3.2 Observations at the centimetric scale

Laboratory XRCT images recorded on cylindrical SML samples of 4 cm in diameter show a heterogeneity of microstructure at the scale of the centimeter. The details of the imaging technique will be presented later in Section 4.2. Figure 3.5 shows a typical transverse cross-section of a XRCT image taken at a voxel size of 24 μm . An alternation between high-porosity and low-porosity zones is observed. These zones correspond to darker and brighter zones respectively in the image. Consequently, observations made in previous subsection are not sufficient, since the rod has a millimetric cross-section and porosity is found to fluctuate at a larger scale. It is worth mentioning that this heterogeneity of porosity is commonly observed for all samples cored from different positions in the provided SML blocks. In addition, isolated large pores (up to 2 mm diameter) are commonly observed in low-porosity zones in the XRCT images (Figures 3.5 and 3.6). In order to characterize and

compare the microstructure at a smaller scale inside both zones, smaller specimen included totally in single zones are prepared. Moreover, in order to complete the characterization, thin sections impregnated with blue epoxy resin are prepared and observed with optical and scanning electron microscopy. The results are shown in next subsections.

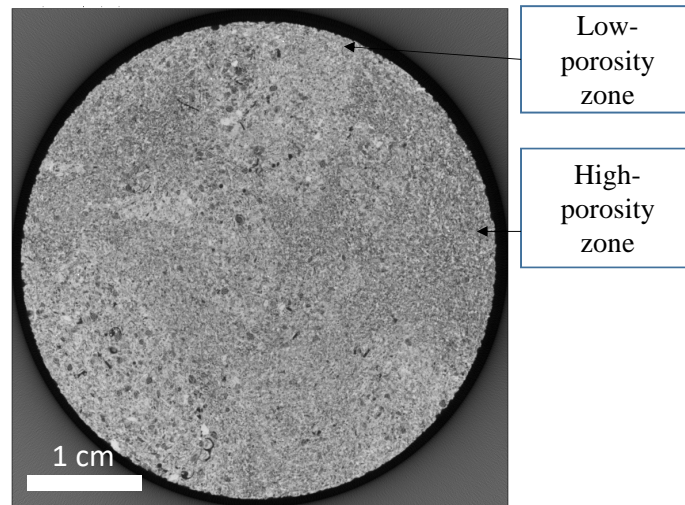


Figure 3.5: A typical transverse cross-section of XRCT image recorded on cylindrical SML samples.

3.3.3 X-Ray Computed Tomography and MIP tests on millimetric cubic specimen

Specimens preparation

First, a large cylindrical sample of SML is imaged with XRCT at a voxel size of $24\ \mu\text{m}$. High-porosity and low-porosity zones are identified inside the sample. It is observed that the larger cube that can totally lay inside a single zone has 6 mm in side length. Thus, four cubic domains are selected on the reconstructed image. Figure 3.6 shows many cross-sections of the four specimens before being cored: D1, D2 and D3 are three specimens laying inside denser zones, whereas P1 is a specimen laying inside a high-porosity zone.

Similarly to the rod specimens preparation presented in Appendix C, the diamond wire saw is used again here to extract the four specimens. Before cutting, the position of each specimen is defined at a millimeter accuracy. Note that the orientation of the SML cylinder with respect to the X-Ray beam direction needs to be specified on the sample in order to define a common frame for the sample and its 3D image. These specimens are then imaged by XRCT at a voxel size of $6\ \mu\text{m}$, before being subjected to Mercury Intrusion Porosimetry (MIP). Figure 3.7 shows the path of a specimen from the preparation until the MIP test, passing through the X-Ray observations.

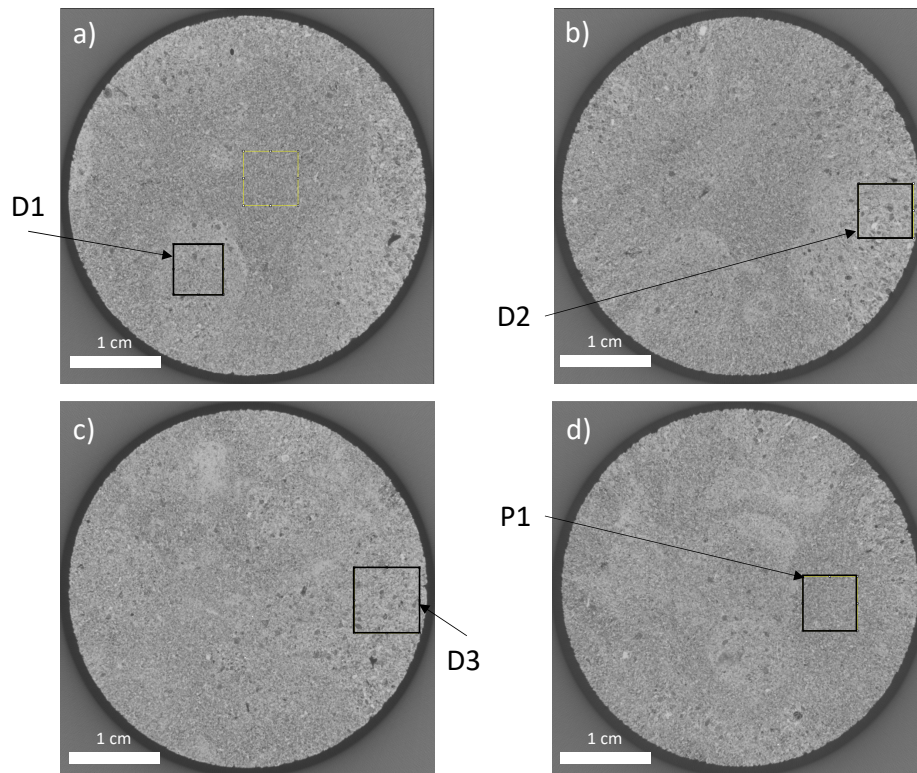


Figure 3.6: Transverse cross-sections of the XRCT image recorded on a SML sample in initial condition showing: **a)** a section of the specimen D1; **b)** a section of specimen D2; **c)** a section of specimen D3; **d)** a section of specimen P1.

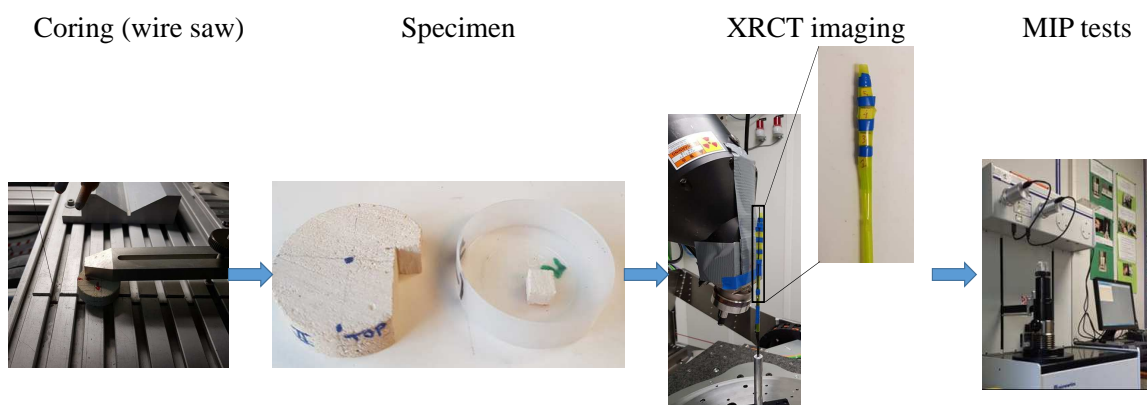


Figure 3.7: SML Specimens: From coring to MIP tests.

XRCT images

The four specimens are put inside a straw as shown in Figure 3.7 and imaged all together by XRCT at a voxel size of $6\ \mu\text{m}$. Typical transverse cross-sections in high-porosity and low-porosity zones are shown respectively in Figures 3.8a and 3.8c. Large and more cemented grains are observed in denser zones, whereas smaller grains with more apparent pores are observed in high-porosity zones. Figure 3.8b shows a zoom inside a more porous zone, where grains have diameters ranging between 100 and $250\ \mu\text{m}$ and macropores of diameters around $100\ \mu\text{m}$ (inter-granular pores presented in section 3.3.1) are abundant. Note that for the used X-Ray source energy, it is almost impossible to distinguish quartz and calcite grains because they share almost the same grey level. This will be discussed in the next chapter (Section 4.5.3). As for the low-porosity zone, a zoomed image shown in Figure 3.8d emphasizes the fact that grains are larger (diameters above $250\ \mu\text{m}$ and can reach $1\ \text{mm}$ in some cases). Regarding the macropores, they are still observed between the grains despite being less abundant and cementation is more present. However, because of the limited resolution of images, no conclusion can be made on smaller macropores neither on micropores. That's why MIP tests are conducted on the specimens.

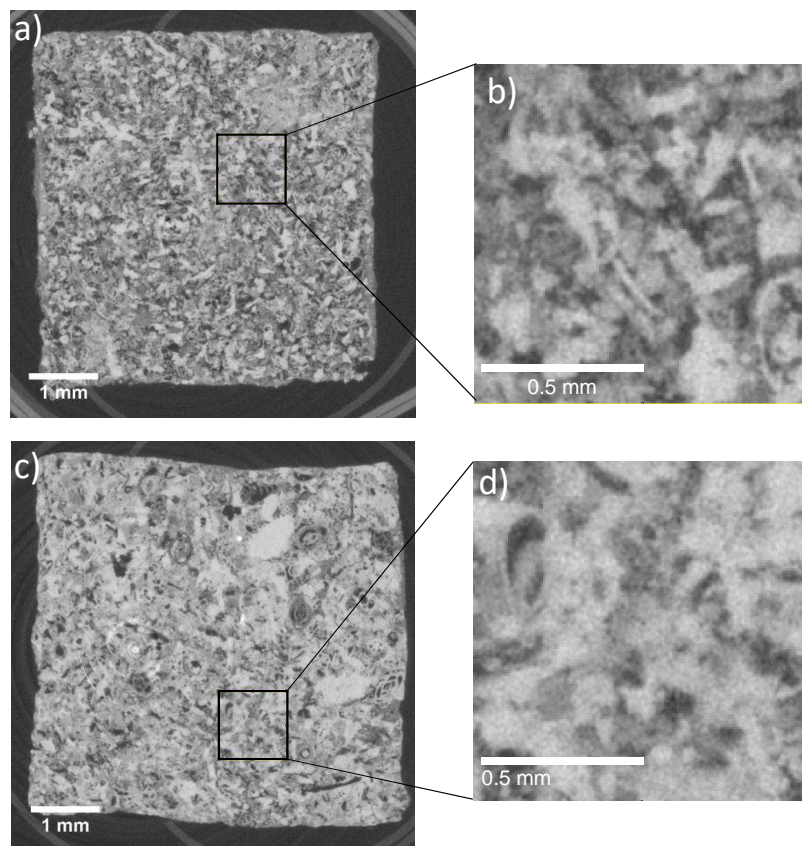


Figure 3.8: a) Typical transverse cross-section of the specimen P1 in a high-porosity zone; b) Zoomed image showing grains and intergranular pores in high-porosity zones; c) Typical transverse cross-section of a specimen in a low-porosity zone; d) Zoomed image showing grains and intergranular pores in low-porosity zones.

MIP tests

MIP is a common method used to study a material porous structure. Due to its high surface tension, mercury is a non-wetting fluid usually used to assess the pore throat diameter distribution. Assuming a cylindrical pore geometry, the Washburn equation relates the applied pressure P_{Hg} to an equivalent pore diameter D (Washburn, 1921):

$$P_{Hg} = -\frac{4\gamma \cdot \cos(\theta)}{D} \quad (3.2)$$

with γ as the surface tension of mercury (0.485N/m) and θ the contact angle between mercury and the pore surface, commonly considered as 140° for limestones (Dixon and Marek, 1990; Zhu et al., 2010; Saad, 2011). The procedure consists in applying vacuum at the beginning, then inject mercury with increasing pressure. The measured incremental entry volume allows to characterize the connected pore size distribution. In this study, the porosimeter used is an AutoPoreIV 9500 from Micrometrics that can reach a maximum pressure of 230 MPa corresponding to a pore size of 6 nm.

Since the synchrotron observation, presented in section 3.3.1, has a limited voxel size ($0.65\ \mu\text{m}$), MIP turns out to be a complementary technique to characterize the microstructure of SML regarding the smaller pores. In order to study the pore size distribution in both zones, MIP tests are conducted on the four specimens and the results are shown in Figure 3.9. The three specimens in low-porosity zones exhibit a common microporosity (as defined in section 3.3.1). These pores have diameters ranging from 100 nm to around $0.6\ \mu\text{m}$, with a peak in their distribution around $0.2\ \mu\text{m}$. They can be attributed to the microporosity inside calcite grains, the larger pores of which could be seen in the synchrotron microporosity image (Figure 3.4).

In addition, inter-granular mesopores of diameters ranging between 1 and $20\ \mu\text{m}$ but with a strong predominance of pores around $10\ \mu\text{m}$ are identified with MIP. These pores are significantly more abundant in high-porosity zones, consistently with the conclusion made about inter-granular macropores based on XRCT images (Figure 3.8). However, intergranular pores are as well present in low-porosity zones. Their lower proportion corroborates the statement of a more present cementation in low-porosity zones. Finally, concerning the macropores (pores larger than $100\ \mu\text{m}$), no significant values are obtained by MIP, as the pore sizes are comparable to the upper limit of the MIP method.

The micro- and macro-porosities of the four specimens have been evaluated, assuming that $0.6\ \mu\text{m}$ is the pore size limit between the two families. The values are presented in Table 3.2. It is observed that the micro-porosity ranges between 8.4% and 9.7% in both zones and that the variation of the total porosity is essentially due to the macro-porosity heterogeneity.

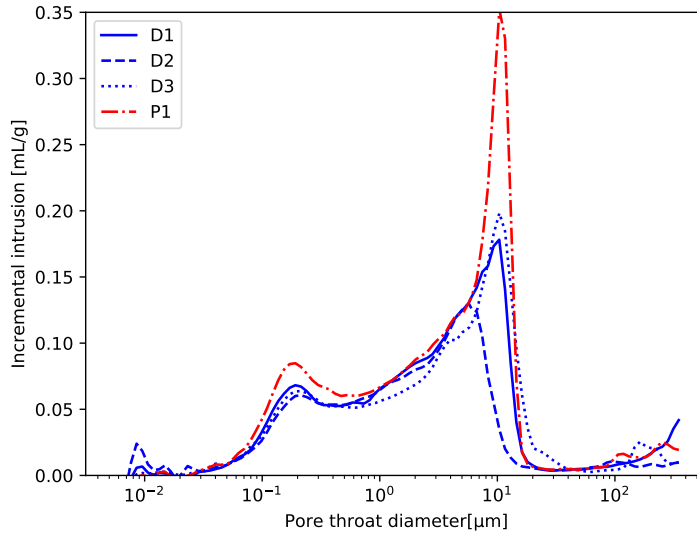


Figure 3.9: Pore throat diameter distribution for the four cored specimens: D1, D2, D3 in denser zones and P1 in more porous zones.

In conclusion, micropores of diameters around $0.2 \mu\text{m}$ lay inside calcite grains, which are present in both zones. These grains have smaller sizes and their proportion is lower in high-porosity zones, leading to higher mesoporosity (around $10 \mu\text{m}$ in diameter) and macroporosity (around $100 \mu\text{m}$) with respect to low-porosity zones. The microporosity seems to be uniform in both zones.

Porosity evaluation

The porosity of the four cubic samples is measured using different techniques. The porosity is first evaluated from the MIP results. Since porosity is defined as the ratio of the void volume V_v over the total volume V_{tot} , one can write:

$$\phi = \frac{V_v}{V_{tot}} = \frac{V_v}{V_v + V_s} = \frac{1}{1 + \frac{V_s}{V_v}} = \frac{1}{1 + \frac{m_s}{\rho_s V_v}} \quad (3.3)$$

where ρ_s , V_s and m_s are the solid matrix density, volume and mass respectively ($m_s = \rho_s V_s$). The mass of each sample m_s is measured before the MIP tests. In addition, the total volume of injected mercury V_{Hg} corresponds to the void volume V_v . It has been shown that calcite ($\rho_{calcite} = 2.70 \text{ g/cm}^3$) forms the majority of SML solid matrix, with a small amount of quartz grains ($\rho_{quartz} = 2.65 \text{ g/cm}^3$). However, due to their close densities, it can be assumed that $\rho_s \simeq 2.7 \text{ g/cm}^3$. The values of the porosity evaluated from MIP results are given in Table 3.2. The porosity in more porous zones is around 40%, whereas it drops to less than 35% in denser zones. On the other hand, the mean grey value over the images recorded by XRCT for each sample is evaluated by using the FIJI open-source software (Schindelin

et al., 2012). Since the grey value evolves linearly with the density, the porosity of the four cored samples can be deduced by taking the evaluated porosity from MIP of the P1 sample as a reference (Table 3.2). The procedure to quantitatively evaluate the porosity from the grey levels of XRCT images will be detailed later in Section 4.5.4. These results corroborate the values obtained from MIP results. Moreover, the total volume of each sample can also be evaluated from the XRCT images of the whole specimen using other image processing routines available in the FIJI software (Schindelin et al., 2012). Thus, knowing the samples masses and considering $\rho_s = 2.7 \text{ g/cm}^3$, the porosity is again evaluated and the previous values are corroborated (Table 3.2). The porosity values obtained from the various methods are consistent. Porosity in more porous zones is around 40% while it can reach 30% in denser zones. A porosity fluctuation of 10% is thus identified, varying at a scale of one centimeter, when considering rock volumes at millimetric size

Table 3.2: Porosity of the four cored samples estimated from: the MIP tests, the mean grey level (GL) and the mass to volume ratio (M/V) evaluations. The micro- and macro-porosities are evaluated from the MIP tests, considering that $0.6 \mu\text{m}$ is the threshold size between the two families.

Zone	Sample	ϕ_{micro} (MIP)	ϕ_{macro} (MIP)	ϕ (MIP)	ϕ (GL)	ϕ (M/V)
Low-porosity	D1	8.8%	26.5%	35.3%	35.4%	34.2%
Low-porosity	D2	9.1%	21.4%	30.5%	30.8%	31.3%
Low-porosity	D3	8.4%	26.8%	35.2%	36.5%	34.6%
High-porosity	P1	9.7%	30.9%	40.6%	40.6%	38.9%

3.3.4 Porosity maps analysis

From the XRCT images recorded in the initial state of many SML samples, 3D porosity maps can be computed (the full procedure will be given later in Section 4.5). In these maps, porosity is evaluated over a spherical subvolume of 1 mm diameter. Histograms of the porosity distribution in 4 different cylindrical samples, presented in Figure 3.10, show that it varies from around 30% to about 45%.

3.3.5 Microscopic observation on thin sections

To characterize the microstructural attributes at the grain scale in both zones, thin sections of samples impregnated with blue epoxy resin are prepared in Lithologie Bourgogne laboratory³. Optical microscopy observations are firstly performed in the Laboratoire de Géologie of the Ecole Normale Supérieure. An observation at a large scale of the interface between more porous and denser zones is shown in Figure 3.11. Pores are marked with blue colors, quartz grains have bright color, whereas calcite grains are green. In the more porous zones, many clusters of pores are observed. This observation could suggest a dissolution of some microstructural components or a precipitation in the denser zones. Looking further,

³<http://www.lithologie-bourgogne.com/>

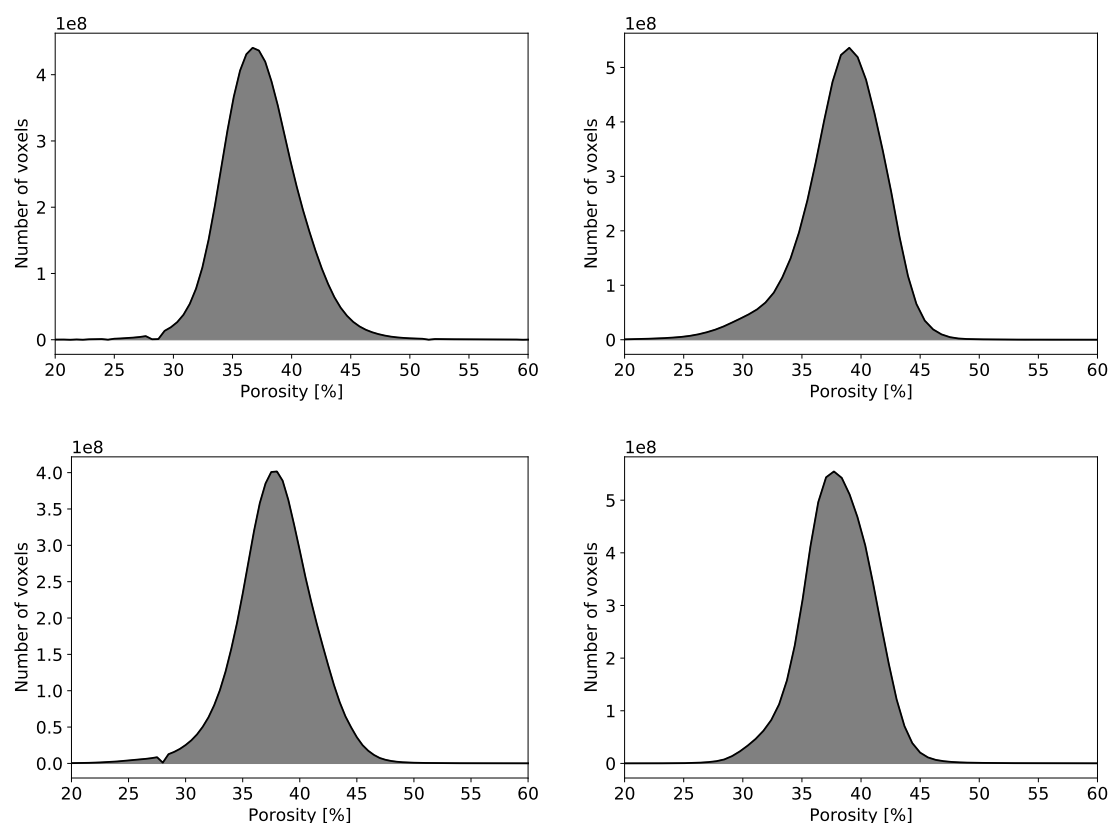


Figure 3.10: Porosity distribution over 4 cylindrical samples of 4 cm diameter and 8 cm height.

images show that calcite grains are smaller and less abundant in high-porosity zones (Figure 3.12), as they have diameters ranging from $100\ \mu\text{m}$ to $250\ \mu\text{m}$ in low-porosity zones in accordance with XRCT observations. Pores have diameters in the order of 100 to $300\ \mu\text{m}$ in high-porosity zones. On the other hand, quartz grains are present in both zones. Moreover, calcareous *Miliolidae* shells are commonly observed in both zones.

To characterize the microstructure at a finer scale, the thin sections are then coated with carbone to ensure electric conduction and are observed with a Scanning Electron Microscope (SEM) in the Laboratoire de Géologie of the Ecole Normale Supérieure. Figure 3.13 shows an interface between more porous and denser zones. Grains in the latter zone are more cemented and larger than those of high-porosity zones. Their diameters are in majority higher than $250\ \mu\text{m}$. In contrast, calcite grains have diameters lower than $250\ \mu\text{m}$ in more porous zones. In the latter zones, some SEM observations focusing on a single calcite grain suggest a dissolution at their boundaries (*i.e.* Figure 3.14). The grain is intact at the center, but the borders are extremely altered. In addition, Figure 3.15 shows a mesopore and a macropore (diameter of $10\ \mu\text{m}$ and $100\ \mu\text{m}$ respectively) surrounded by altered calcite. Thus, new pores of 10 to $20\ \mu\text{m}$ may be formed as shown from MIP results (Figure 3.9). These observations suggest that not only new pores are created in high-porosity zones, but also already existing pores are expanded due to a possible calcite dissolution.

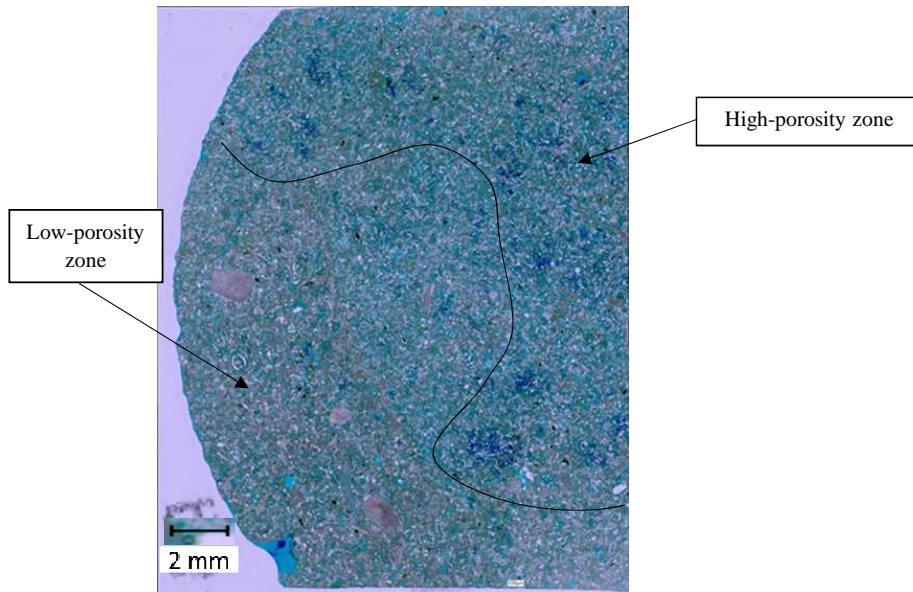


Figure 3.11: Optical microscopic observation showing the contrast between more porous and denser zones.

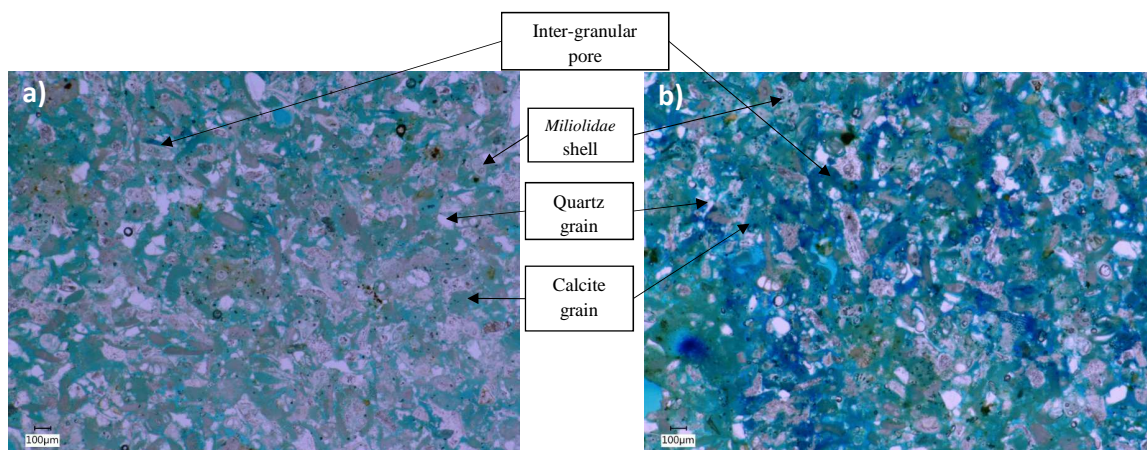


Figure 3.12: a) Optical microscopy observation showing a low-porosity zone; b) Optical microscopy observation showing a high-porosity zone.

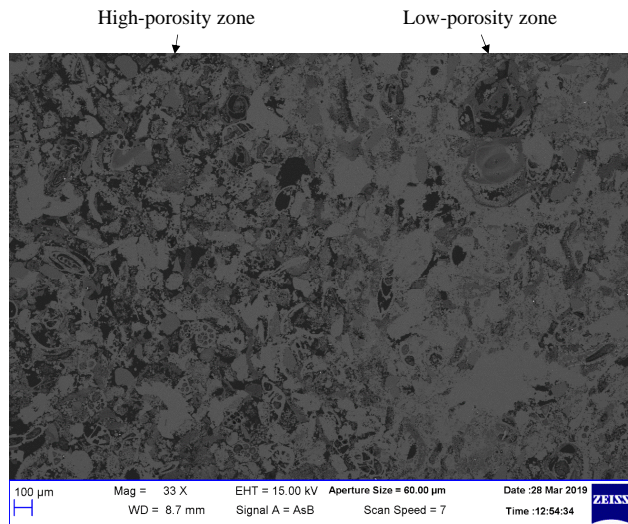


Figure 3.13: Backscattered Electron Microscopy observation showing the contrast between low- and high-porosity zones.

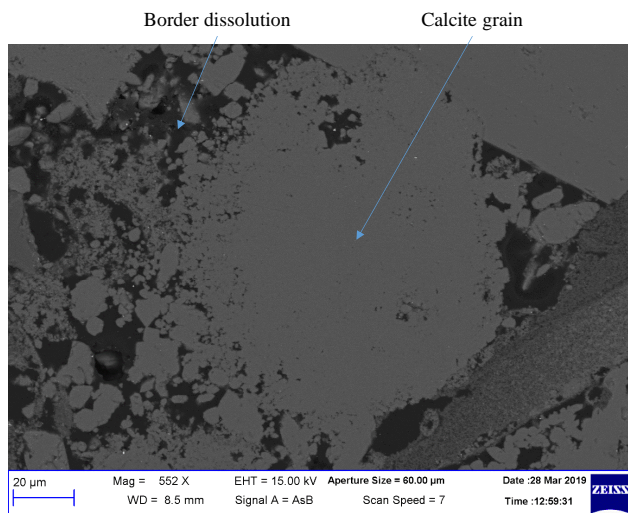


Figure 3.14: Backscattered Electron Microscopy observation showing a calcite grain, intact at the center and dissolved at the boundaries in a high-porosity zone.

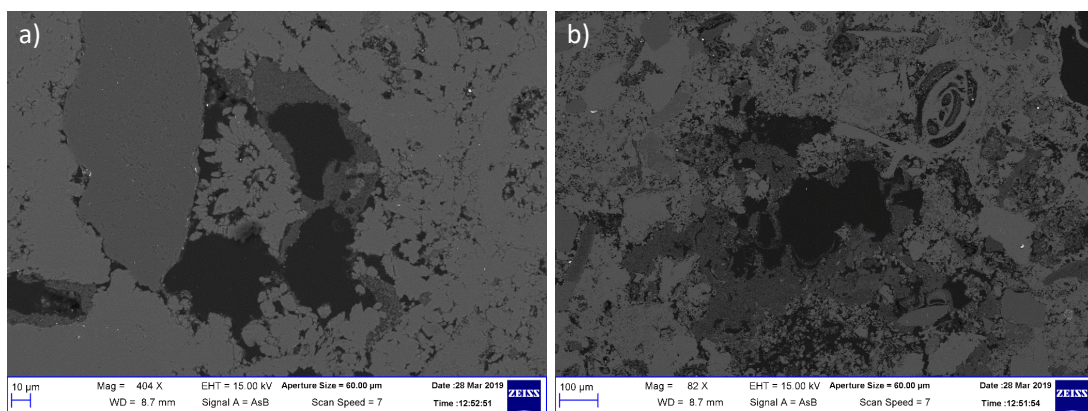


Figure 3.15: Backscattered Electron Microscopy observations showing: a) a mesopore surrounded by altered calcite; b) A macropore surrounded by altered calcite in high-porosity zones.

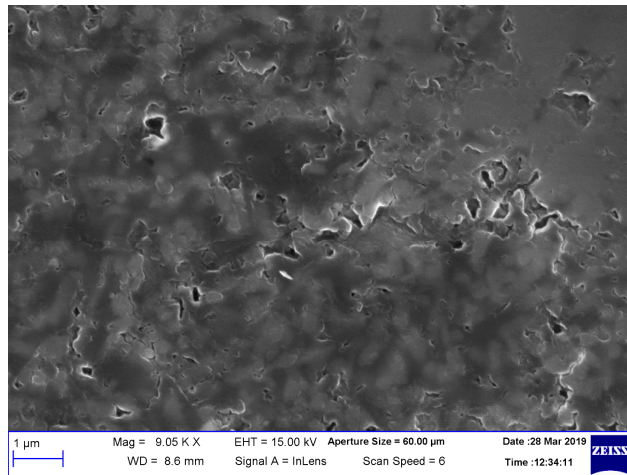


Figure 3.16: Microporosity inside calcite grains.

From the MIP tests performed on millimetric cubic samples, microporosity is found to be redundant in both zones. A SEM observation shows that calcite grains contain a family of micropores of mean diameter around $0.2 \mu\text{m}$ (Figure 3.16). In addition, *Miliolidae* shells have a similar family of microporosity (Figure 3.17). These components are present in both zones and SEM observations thus corroborate the MIP results.

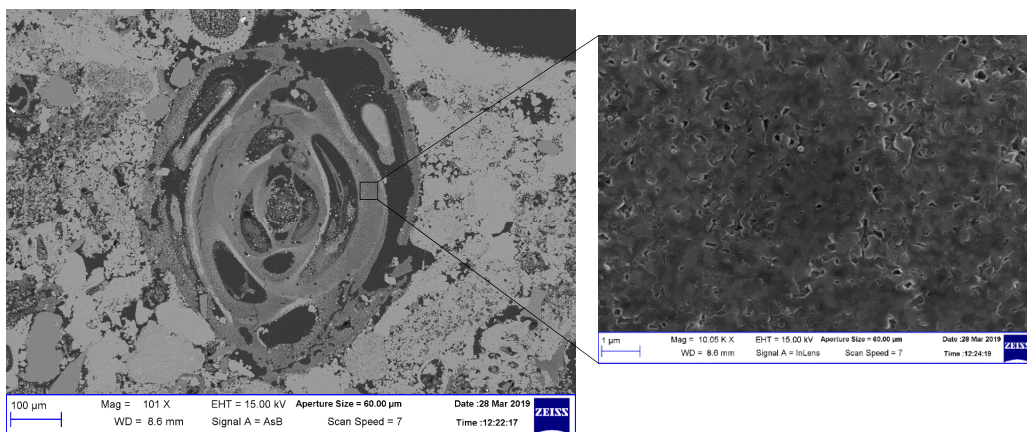


Figure 3.17: Backscattered Electron Microscopy observation showing a microporous miliolidae.

3.4 Summary of SML microstructural attributes

Finally, from all the previous observations and experiments, the SML microstructure presents an alternation between two types of zones due to a possible calcite mineral dissolution: high-porosity and low-porosity zones. The main features of each zone are gathered in Table 3.3.

Table 3.3: Microstructural main features of high- and low-porosity zones.

	High-porosity zone	Low-porosity zone
Porosity	>40%	<35%
Micropores	Present in both zones, with similar proportions Inside calcite grains and <i>Miliolidae</i> $D = 0.1 - 0.6 \mu\text{m}$	
Mesopores	more present $D = 0.6 - 20 \mu\text{m}$	less present
Macropores	more present $D > 100 \mu\text{m}$	less present
Calcite grains	$D = 100 - 250 \mu\text{m}$	$D > 250 \mu\text{m}$
Quartz grains	present in both zones - $D = 50 - 100 \mu\text{m}$	
<i>Miliolidae</i> shells	present in both zones	

Experimental equipments and methods

Résumé L'objectif de ce chapitre est de présenter la procédure expérimentale suivie dans cette étude et d'expliquer les principes des méthodes développées et utilisées. Comme les essais triaxiaux sont combinés à des observations tomographiques aux rayons X, la machine triaxiale est d'abord présentée. Ensuite, les caractéristiques des observations de tomographie sont détaillées. Puis, les principes de la technique de corrélation d'images volumiques et de l'évaluation des champs de déformation sont décrits. Les erreurs et incertitudes inhérentes à cette technique sont discutées. Une fois les cartes de déformation obtenues, les zones de localisation de la déformation peuvent être identifiées. Une nouvelle méthode basée sur la cinématique de la déformation permettant la classification des bandes est présentée. D'autre part, des cartes de porosité calculées à partir des images de tomographie au travers d'une calibration de leurs niveaux de gris, sont utilisées pour évaluer le rôle de l'hétérogénéité de la porosité sur la formation et le développement des bandes de localisation de la déformation. Finalement, une nouvelle méthode de post-traitement des cartes de porosité est proposée pour évaluer le second gradient de la porosité sur des volumes élémentaires cubiques au sein des domaines d'analyse, dans l'objectif de calibrer un modèle de plasticité de type second-gradient.

Abstract The purpose of this chapter is to present the experimental methodology followed in this study and to explain the basics of the developed and used methods. Since triaxial experiments are combined to X-Ray Computed Tomography, the triaxial apparatus is at first presented. Then, the characteristics of X-Ray observations are detailed. The principle of the Digital Volume Correlation technique and of the evaluation of the deformation fields are thereafter described. Errors and uncertainties inherent to this technique are discussed. Once deformation maps are obtained, strain localization zones can be identified. A new method is developed to identify the type of deformation bands based on kinematics of deformation. On the other hand, porosity maps evaluated from the 3D images through appropriate calibration of their grey levels, are used to assess the role of porosity heterogeneities in the onset and development of localized deformation. Finally, in order to calibrate the gradient-dependent plasticity model, a new post-processing method of the porosity maps is proposed to evaluate second gradient of porosities on cubic volumes throughout the investigated domains..

4.1 Triaxial tests

Cylindrical samples of 4 cm in diameter and 8 cm in height are cored and placed inside a rubber membrane. Triaxial tests are then performed using a high-pressure & high-temperature triaxial machine Tri X 150/200 designed by Sanchez Technologies (Figure 4.1). It is equipped by 4 servo-controlled pressure generators with possible control of pressure, volume or flow rate: two generators to apply confining pressure (up to 150 MPa) and deviatoric loading (up to 1 GPa) respectively and two others to apply pore pressure (up to 100 MPa) with water from the top and bottom of a sample respectively. However, as water affects the mechanical properties of SML, all experiments are performed in dry conditions. Samples are dried at a constant temperature of 60°C for 48 hours before testing. The triaxial cell contains a system of hydraulic self-compensated piston, where the loading piston is equilibrated during the hydrostatic loading and can apply directly deviatoric pressure. The machine is also equipped with a heating system that can prescribe a temperature up to 200°C. However, temperature effects are out of the scope of this study and all the experiments are conducted at a constant temperature of 25°C. Strains are measured by means of 6 linear variable differential transformers (LVDT). 2 axial and 4 radial LVDTs are disposed at the mid-height of the sample. Axial strain is measured on a height of 5 cm (Figure 4.1). Deviatoric loading rate is imposed by controlling the injection flow rate in the axial loading pump. This flow rate is identified in such a way that a constant axial strain rate of about 10^{-5} /sec is applied on the SML samples in the elastic regime. Circular pieces of teflon with 1 mm in thickness are disposed at the interface between the sample and the loading pistons and grease is added in order to reduce friction boundary effects and to allow slippage on the top and bottom of the sample.

4.2 X-Ray Computed Tomography

The XRCT is a non-destructive technique that allows to record 3D images of an object. The sample is put between a X-Ray source and a detector, which measures the ratios between incident and transmitted radiation intensities. The Beer law (Equation 4.1) relates the incident intensity I_0 to the transmitted intensity $I(x)$ through a pure material of length x where μ is the linear attenuation coefficient of this material.

$$I(x) = I_0 \exp(-\mu \cdot x) \quad (4.1)$$

The attenuation coefficient μ depends on the energy of the incident ray, on the atomic number of the elements that compose the material and their relative proportions as given by the chemical composition (Thiery, 2013). Finally, grey levels in a reconstructed image correspond to X-Ray attenuation, which reflects the proportion of X-Rays absorbed or scattered through the material in the physical volume associated with each voxel.

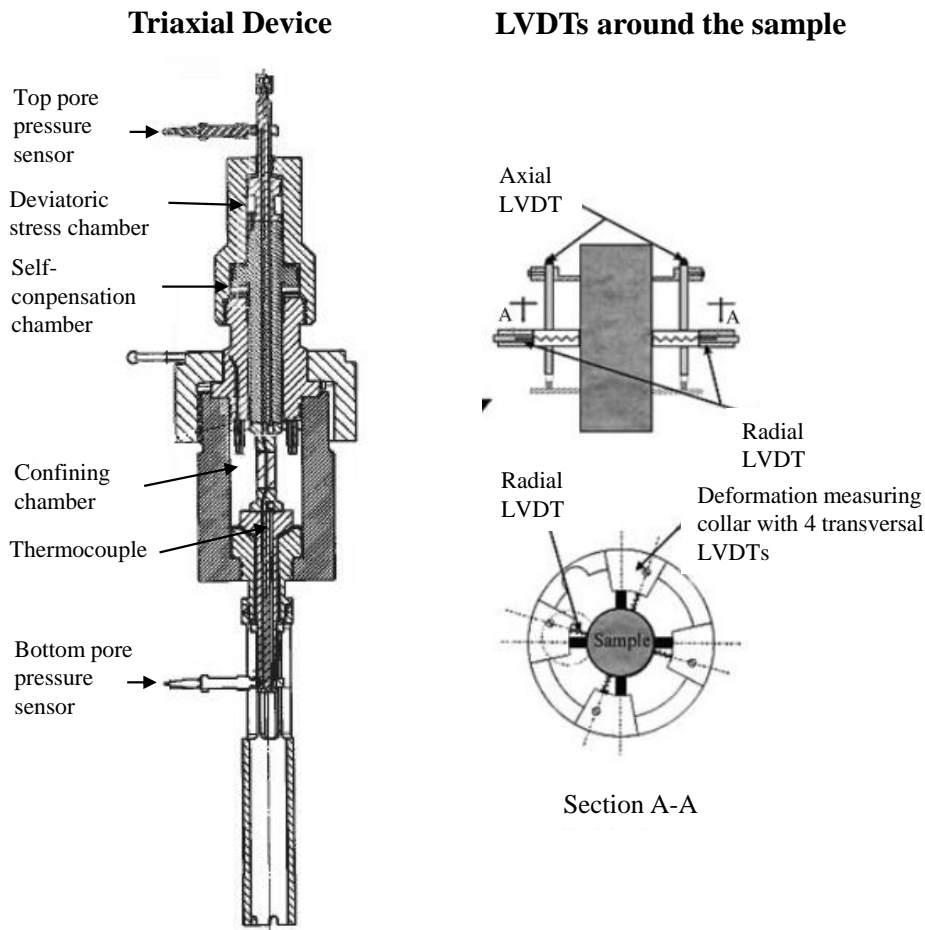


Figure 4.1: Schematic of the triaxial machine and LVDTs disposition.

In this study, samples are imaged before and after each loading step, using an UltraTom microtomograph (RX-Solutions, Chavanod, France), equipped with a 230KV Microfocus Hamamatsu L10801 X-Ray source associated with a PaxScan 2520V flat panel detector used at full resolution (Varian, Palo Alto, USA) (Figure 4.2). A copper filter of 0.5 mm in thickness is placed on the beryllium window of the source since large samples are imaged and because calcite, the main mineral of the SML, is opaque to low energy X-Ray radiations. In order to have good contrast images, the main source parameters have been chosen as: an accelerating voltage of 100 kV and an electron beam intensity of 500 μA . The XRCT observations are conducted using stack mode since an image of the full sample is sought, with the best possible resolution: the sample rotates around itself, whereas the source and detector are translated vertically, step by step. At the beginning of a scan, the source is in front of the upper part of the sample. After a 360° rotation, the source and detector move downward, then the process is repeated. Finally, the image is composed of 6 levels. For each level, 1440 mean projections are recorded, each one is obtained by averaging 18 radiographies at a fixed rotation angle (a projection corresponds to an increment of rotation of 0.25°). Averaging allows to reduce random image noise. The 3D images are reconstructed using a voxel size of 24 μm by means of X-Act software (RX-Solutions, Chavanod, France), based

on the standard filtered back projection algorithm for conical projection (Feldkamp et al., 1984). A cylindrical reference sample of the same material is systematically imaged together with all unloaded samples. This sample, of 4 cm in diameter and height, is conserved in constant temperature and humidity conditions and is supposed to remain unmodified. The imaging of the reference sample is therefore useful to calibrate the images of consecutive observations and to measure the error of the correlation method.

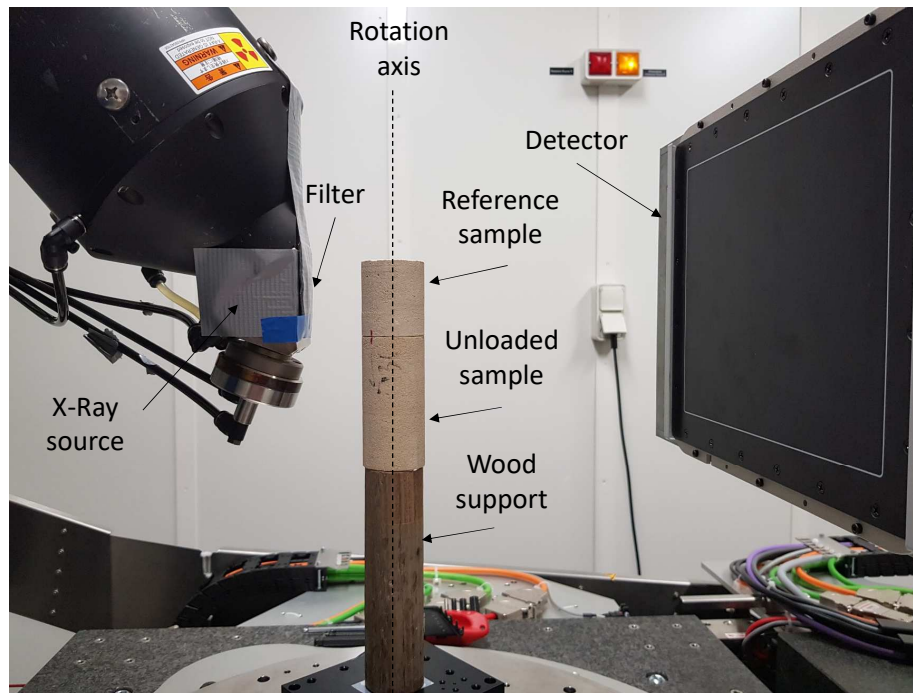


Figure 4.2: Details of a XRCT scanning of a SML sample.

4.3 Digital volume correlation

4.3.1 Principle of the technique

The main objective of the Digital Volume Correlation (DVC) technique is to identify the three-dimensional displacement field of a deformed sample on the basis of 3D imaging. The technique operates on volume images recorded in reference and deformed states of a material, and requires a local contrast associated to the material. In case of XRCT images, the local contrast is obtained by variation of material density. Carbonate rocks are among the materials that present natural contrasts due to their heterogeneous microstructures and are thus adapted for correlation without any addition of markers at a millimetric gauge length (Zinsmeister, 2013). The reconstructed 16-bit images are rescaled to 8-bit images via a linear transformation. The DVC is performed on images using the in-house developed software CMV3D (Bornert et al., 2004; Lenoir et al., 2007), using recent extensions of Gaye

(2015). Images of a sample before and after a loading step will be henceforth referred as reference and deformed images respectively (Figure 4.3).

The procedure is simply an extension of the 2D digital image correlation. The principle of the method is to set a regular mesh of points \underline{X}_i in the reference image and to find their homologous positions \underline{x}_i in the deformed image. To do so, the grey-level distribution in a subvolume D_{X_i} centered over a point \underline{X}_i in the reference image is considered. The position \underline{x}_i in the deformed image is simply defined as the center of a domain D_{x_i} , that most closely resembles to D_{X_i} . Hence, a displacement vector can be associated to each point of the regular mesh. Obviously, the subdomain cannot be a single voxel because the problem would be ill-posed. Therefore, in our case, D_{X_i} is set to be of cubic shape with a size of $40 \times 40 \times 40$ voxel³. The spacing between mesh points is also set to be 40 voxels (=960 μm).

Let the scalars f and g denote the grey levels of voxels in reference and deformed images respectively. From the two images, a local mechanical transformation Φ_i is sought as:

$$\underline{x}_i = \Phi_i(\underline{X}_i) \quad (4.2)$$

assuming that Φ_i is a homogeneous translation:

$$\Phi_i(\underline{X}_i) = \underline{X}_i + \underline{u}_i(\underline{X}_i) \quad (4.3)$$

that varies from a correlation point to another. To find \underline{x}_i , the grey level distribution in the domain D_{x_i} in the deformed image must be the closest to the grey level distribution in the domain D_{X_i} in the reference image. Thus, a correlation coefficient must be defined and its optimum would correspond to the best local transformation $\Phi_i(\underline{X}_i)$. Calculations are done in three steps:

-First, $\Phi_i(\underline{X}_i)$ is supposed to have integer values of translation with respect to voxels. A correlation coefficient $C(\Phi_i)$ is calculated between the domains D_{X_i} and D_{x_i} , where $C(\Phi_i)$ is the *zero centered normalised cross-correlation coefficient*:

$$C(\Phi_i) = 1 - \frac{\sum_{\underline{X} \in D_{X_i}} (f(\underline{X}) - \bar{f}_D) \cdot (g(\Phi(\underline{X})) - \bar{g}_D)}{\sqrt{\sum_{\underline{X} \in D_{X_i}} (f(\underline{X}) - \bar{f}_D)^2 \cdot \sum_{\underline{X} \in D_{X_i}} (g(\Phi(\underline{X})) - \bar{g}_D)^2}} \quad (4.4)$$

with \bar{f}_D and \bar{g}_D are the mean grey values over D_{X_i} and D_{x_i} respectively. This coefficient should be interpreted as one minus a scalar product of the grey level distributions in both configurations, giving 0 for a perfect matching ($g(\Phi(\underline{X})) = f(\underline{X})$ for all $\underline{X} \in D_{X_i}$) and 2 for an antisymmetric configuration. When no correlation is found, the value of $C(\Phi_i)$ should be equal to 1. The normalization of the coefficient with respect to the mean values and standard deviations makes it insensitive to brightness and contrast variations between the

images in both configurations. The coefficient is minimized while moving x_i in a *search domain* that has a size of $5 \times 5 \times 5$ voxel³ in this study. If the minimal value of $C(\Phi_i)$ over a domain D_{x_i} exceeds a criterion value (0.25 in this study), the position of its central point will not be found at this step of calculation. Thus, the code will skip it and move to the next domain defined in the reference configuration.

-Second, since the transformation $\Phi_i(\underline{X}_i)$ can have non integer values in terms of voxels, a subvoxel optimization is applied. The grey level in the deformed image $g(\Phi_i(\underline{X}_i))$ is interpolated using a trilinear function. The grey level at a point $\underline{x}_i = \Phi(\underline{X}_i) = (x, y, z)$ is evaluated as:

$$\begin{aligned}
 g(x, y, z) = & g(i, j, k) + a(x - i) + b(y - j) + c(z - k) \\
 & + d(x - i)(y - j) + e(x - i)(z - k) + f(y - j)(z - k) \\
 & + h(x - i)(y - j)(z - k)
 \end{aligned} \quad (4.5)$$

where $(x, y, z) \in [i, i + 1] \times [j, j + 1] \times [k, k + 1]$ and the interpolation coefficient (a to h) are such as the interpolated functions coincides with the grey level of the eight nearest voxels. Then, the new vector position \underline{x}_i is obtained by finding the minimum of the correlation coefficient $C(\Phi_i)$ using a gradient-based descent minimization (Doumalin and Bornert, 2000; Bornert et al., 2004).

-Finally, an interpolation is done to locate the points that do not have a sufficient correlation coefficient (> 0.25 in this study). It consists in fitting a local gradient of transformation using the position of 15 nearest found points. Details of the method can be found in the PhD thesis of Gaye (2015).

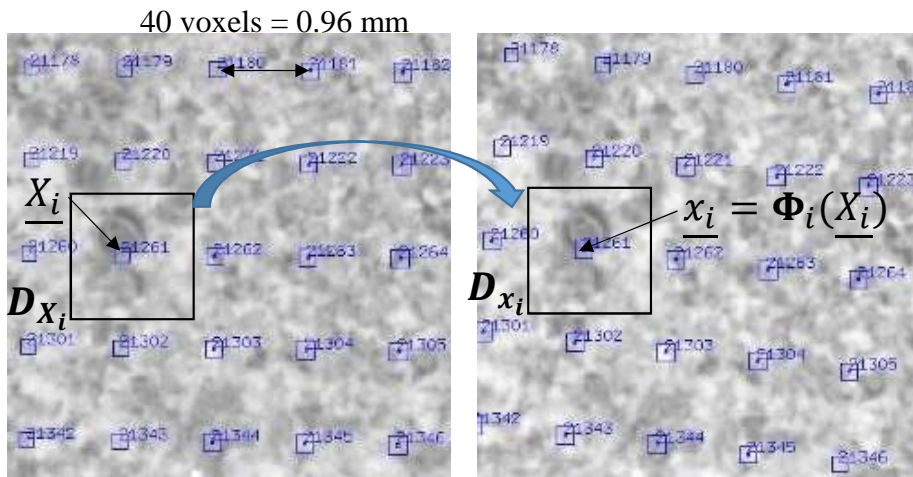


Figure 4.3: DVC principles: Mesh points on the reference image (on the left) and their homologous points on the deformed image (on the right).

4.3.2 Computation of local strain fields

To compute the deformation field, one must first evaluate the displacement gradient. Since DVC predicts discrete values of the displacement field, a measure of its gradient would be an average value over a characteristic dimension called *the gauge length*. To do so, a regular mesh of finite elements is defined where the nodes coincide with the correlation domains centers of known displacement. Each element of the mesh is a cube with 8 nodes, the size of which coincides with the spacing of the correlation grid (40 voxels in all 3 directions in our case). This distance defines the gauge length of the local strain measurement. Indeed the local strain is defined as the average strain over such elements, assuming a trilinear continuous interpolation of the DVC evaluation at the nodes over the whole mesh. In practice, the calculation of this average is performed by a Gaussian integration, which provides the exact average in the case of such a linear interpolation and such a regular mesh. This operation and then the evaluation of the linearized strain tensor are performed by means of the Paraview software, using the "compute derivative" filter (Ayachit, 2015).

The strain field is thus evaluated between two states (before and after a loading stage). For a new loading stage, the deformed image is considered as the new reference image. Therefore, it is the same initial regular mesh which is followed along one experiment of several loading stages. Once the incremental¹ strain tensor of an element $\underline{\underline{\epsilon}}$ is calculated, the volumetric deformation ($\epsilon_v = tr(\underline{\underline{\epsilon}})$) can be assessed. In addition, it is possible to evaluate the shear strain magnitude ($\gamma = \sqrt{2\underline{\underline{e}} : \underline{\underline{e}}}$) where $\underline{\underline{e}}$ is the deviatoric strain tensor $\underline{\underline{e}} = \underline{\underline{\epsilon}} - \frac{1}{3}tr(\underline{\underline{\epsilon}})\underline{\underline{I}}$. Paraview is also used for plotting the 3D deformation maps, which might be superimposed on the reference image or any other local quantity, whenever usefull. In addition, the mean deformation of the sample can be calculated and compared to the data provided by the LVDTs disposed around the samples.

4.3.3 Error estimation

The uncertainties of the evaluation of the strain field from the DVC applied on XRCT images may be due to many factors, among which:

1. The random noise of XRCT images.
2. The artefacts of images reconstruction, which might be local in the images (e.g. ring artefact), or global (variation of magnification between images of two configurations).

¹One increment corresponds to one loading stage.

3. The size of the correlation domain which determines also the spatial resolution of the measurement.
4. The scale at which strain is measured: the smaller the gauge length, the higher the errors due to random image noise.
5. The grey level interpolation in the subvoxel optimization step of the DVC.
6. The interpolated positions of the points with non-sufficient contrast.
7. The discretization of the displacement field, the assumption of local translation at the scale of a correlation window and then its interpolation using the shape functions.

To evaluate the DVC strain field uncertainties and assess the order of magnitude of the induced errors, the DVC technique is thus applied on the reference sample. The microstructure and geometry of the reference sample remains unchanged for all XRCT observations. Ideally, a zero deformation tensor should be obtained for all the elements, as well as for the average strain. Figure 4.4 shows typical volumetric strain and shear strain magnitude maps obtained from a DVC applied on the reference sample. The maximum local volumetric strain (at the scale of an element) is at most of the order of 0.5%. As for shear strain magnitude, the maximum local value obtained for the reference sample is also of similar amplitude. An average of the strain tensor components over all the elements of the mesh permits to assess the error of the global deformation measured over the reference sample (Equation 4.6). The mean volumetric deformation is thus $\langle \epsilon_v \rangle = Tr(\langle \underline{\underline{\epsilon}} \rangle) = 2.16 \times 10^{-4}$, whereas the mean shear strain magnitude is $\langle \gamma \rangle = \sqrt{2\langle \underline{\underline{\epsilon}} \rangle : \langle \underline{\underline{\epsilon}} \rangle} = 2.74 \times 10^{-4}$.

$$\langle \underline{\underline{\epsilon}} \rangle = \begin{bmatrix} 0.56 & 0.35 & -0.68 \\ 0.35 & 0.67 & -1.12 \\ -0.68 & -1.12 & 0.93 \end{bmatrix} \times 10^{-4} \quad (4.6)$$

Figure 4.5 presents histograms of the probability densities of the volumetric strain and the shear strain magnitude of a typical DVC applied on the reference sample. To obtain these densities, the counts are normalized in such a way that the area under a histogram sums to 1. It is observed that the volumetric strain density follows a normal distribution of the form $f(x) = \frac{1}{\sqrt{2\pi}\sigma} \cdot \exp\left\{-\frac{(x-\mu)^2}{2\sigma^2}\right\}$ centered over $\mu = 1.1 \times 10^{-6}$ with a standard deviation of $\sigma = 8.2 \times 10^{-4}$. This shows that errors on positive and negative volumetric deformation are equiprobable, since the distribution is symmetrical. In addition, 90% of the volumetric strain errors range between -1.35×10^{-3} and 1.35×10^{-3} . Regarding the shear strain magnitude, it can only take positive values by definition. Thus, it is fitted with a lognormal distribution, where its logarithm follows a normal distribution of mean value

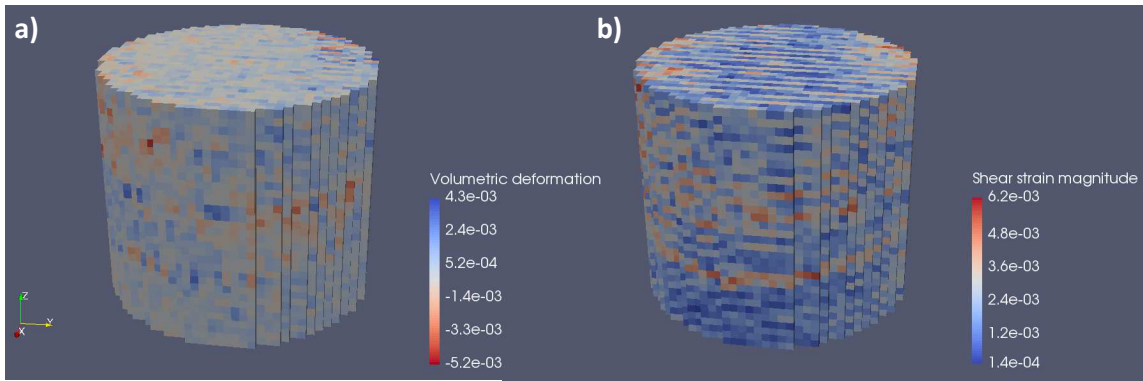


Figure 4.4: Typical DVC applied on the reference sample: (a) Volumetric deformation map; (b) Shear strain magnitude map.

$\mu = -6.28$ and a standard deviation $\sigma = 0.48$. 90% of shear strain magnitudes are lower than 3.48×10^{-3} . From these analyses, one can conclude that the order of magnitude of the error on the deformation field obtained from the DVC evaluated for a local gauge length of 40 voxels or $\simeq 1$ mm, is of the order of 10^{-3} . For average strain over a cylindrical domain of 4 cm diameter times 4 cm height, the accuracy is one order of magnitude better.

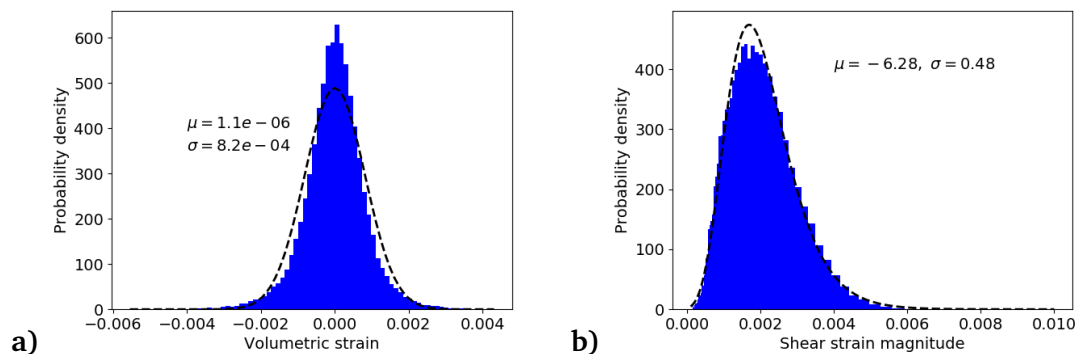


Figure 4.5: Typical DVC applied on the reference sample: (a) The probability density of volumetric strain with a fitted normal distribution; (b) The probability density of shear strain magnitude with a fitted log-normal distribution.

4.4 Deformation bands type

4.4.1 Kinematics of strain localization

As described previously in Section 2.4.1, the macroscopic description of deformation bands is as they are thin layers bounded by two parallel material discontinuity surfaces of the incremental strain tensor (Hill, 1962). A schematic representation of the kinematics of strain localization is presented in Figure 4.6. When the homogeneity of the deformation field

is lost, the displacement field remains continuous at the band boundaries but its gradient does not:

$$[[u_i]] = 0 \quad \text{and} \quad \left[\left[\frac{\partial u_i}{\partial x_j} \right] \right] = g_i \cdot n_j \quad (4.7)$$

where $[[\alpha]]$ denotes the discontinuity of a physical quantity α across the band boundary, n_j is the outward unit normal vector of the band, u_i represents the displacement field and g_i is a vector that describes the discontinuity direction (i and j can take the values 1, 2 and 3 in the three-dimensional space). Depending on the kinematics of strain localization, several types of deformation bands can be distinguished (see Section 2.4.1): Pure shear bands when $g_i \cdot n_i = 0$; pure compaction bands when $n_i \cdot g_i = -1$; pure dilation band when $n_i \cdot g_i = +1$; compactive shear bands when $-1 < n_i \cdot g_i < 0$ and dilatant shear bands when $0 < n_i \cdot g_i < +1$. These types of bands have been identified in many field and laboratory observations (see Section 2.3), based on band orientation to the maximum principal stress direction and observations on microstructural properties variation such as grain movement or rotation, grain crushing, pore collapse and cracks opening. Identification of deformation band types has been made indirectly, since the observations rely only on the analyses of the state after strain localization, as the initial state is usually unknown, and thus the displacement field also. In the next subsection, a simple and original method to classify the bands is described. The method is based on kinematic considerations and an analysis of deformation maps obtained from DVC.

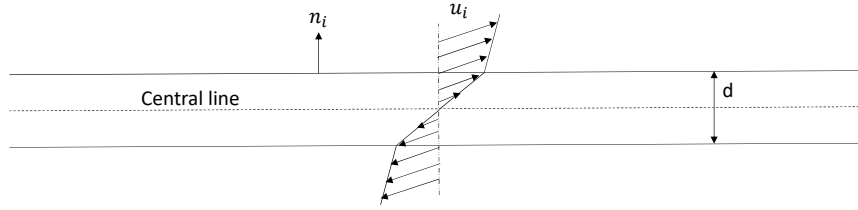


Figure 4.6: A schematic representation of the displacement gradient discontinuity across a deformation band (or equivalently, the strain tensor discontinuity).

4.4.2 Deformation bands classification method

Intense deformation occurs inside a strain localization band, whereas much lower deformation takes place outside the band (e.g. see Figure 4.7). This statement will be validated in the next chapter when deformation maps are presented. Thus, the discontinuity of the strain tensor across the band $[[\underline{\underline{\epsilon}}]]$ can be approximated by neglecting the strain outside the band:

$$[[\underline{\underline{\epsilon}}]] = \underline{\underline{\epsilon}}^b - \underline{\underline{\epsilon}}^o \simeq \underline{\underline{\epsilon}}^b \quad (4.8)$$

where $\underline{\underline{\epsilon}}^b$ and $\underline{\underline{\epsilon}}^o$ represent the strain tensors inside and outside a band respectively.

The procedure consists in defining manually a tangent plane to a deformation band detected on a strain map as shown in Figure 4.7. This plane is chosen at the middle of the

Table 4.1: Band types depending on the normalized scalar product value.

Band type	Pure compaction band	Compactive shear band	Pure shear band	Dilatant shear band	Pure dilation band
<i>NSP</i>	-1	$-1 < .. < 0$	0	$0 < .. < 1$	1

band and a unique unit outward normal vector \underline{n} is thus defined along the band. Then, the strain tensor of each element inside the band, which has a cubic shape of 1 mm of side length, permits to calculate the displacement vector:

$$\underline{u}^{\text{element}} = \underline{\epsilon}^{\text{element}} \cdot \underline{n} \times GL \quad (4.9)$$

where GL is the gauge length. Notice that the global rigid displacement does not intervene in the calculated displacement. The normalized scalar product NSP^{element} of the outward unit normal vector \underline{n} and the displacement vector $\underline{u}^{\text{element}}$ for an element inside the band can be calculated as:

$$NSP^{\text{element}} = \frac{\underline{n} \cdot \underline{u}^{\text{element}}}{\|\underline{u}^{\text{element}}\|} = \frac{\underline{n} \cdot \underline{\epsilon}^{\text{element}} \cdot \underline{n}}{\|\underline{\epsilon}^{\text{element}} \cdot \underline{n}\|} \quad (4.10)$$

NSP^{element} is thereafter calculated for each element through which passes the central line of the band. Finally, the normalized scalar product of the band NSP^{band} is evaluated as the mean value over all the considered elements:

$$NSP^{\text{band}} = \langle NSP^{\text{element}} \rangle_{\text{band}} \quad (4.11)$$

allowing to define the band type as summarized in Table 4.1. A pure compaction and dilation bands are identified for $NSP^{\text{band}} = -1$ and $NSP^{\text{band}} = +1$ respectively. In case of orthogonal vectors ($NSP^{\text{band}} = 0$), a pure shear band is defined. Compactive and dilatant shear bands are intermediate categories for which $-1 < NSP^{\text{band}} < 0$ and $0 < NSP^{\text{band}} < 1$ respectively.

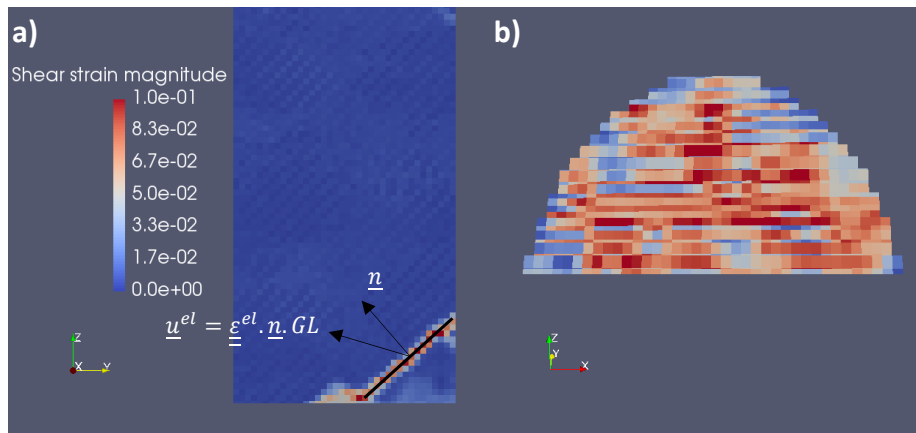


Figure 4.7: a) Definition of the plane of a localization band. The displacement vector for each element along the black solid line is evaluated, where GL is the gauge length; b) Cross-section of the DVC map in the plane of the band.

4.5 Porosity maps

From XRCT observations, one can obtain 3D images of the microstructure at successive states of deformation. These images show a heterogeneity of porosity. Thus, it is interesting to build 3D porosity maps and compare them to 3D deformation maps provided from DVC. These maps are useful to:

1. Characterize the heterogeneity of porosity in the initial state and understand its effect on strain localization process.
2. Follow the porosity evolution after the loading stages.
3. Measure the second gradient of porosity over a selected domain.

The main objective of this section is to explain how can one compute 3D porosity maps from XRCT images.

4.5.1 Grey level adjustment

To compute the porosity maps in various states of deformation, the consecutive 16-bit XRCT images of the same sample at different levels of deformation should be calibrated. Since CMV3D runs on 8-bit images, a linear transformation of the grey level should be made as described in Equation 4.12, where g_{8-bit} and g_{16-bit} represent the grey levels of a same voxel in the 8-bit and 16-bit images respectively. a and b are the transformation unknowns.

$$g_{8-bit} = a \times g_{16-bit} + b \quad (4.12)$$

The reference image is transformed to an 8-bit image by considering values for a and b that avoid a grey level saturation. However, the values of a and b corresponding to the deformed image should be adjusted. At first, one should consider a typical transverse cross-section of the reference sample in the 8-bit reference image (State i in Figure 4.8a). Then, the same section should be considered in the 16-bit image (State $i + 1$ in Figure 4.8c). Using FLJI, the grey level distributions in both states are plotted as shown in Figures 4.8b-d. Assuming a conservation of brightness and contrast levels between two images in consecutive deformation states, the parameters a and b can be evaluated as:

$$a = \sqrt{\frac{Var[g_{8-bit}]}{Var[g_{16-bit}]}} \quad (4.13)$$

$$b = \bar{g}_{8-bit} - a \times \bar{g}_{16-bit} \quad (4.14)$$

where \bar{g}_{8-bit} and \bar{g}_{16-bit} are the mean values of the grey level distributions in the 8-bit and 16-bit images respectively, whereas $Var[g_{8-bit}]$ and $Var[g_{16-bit}]$ are the variances of the grey level distributions in the 8-bit and 16-bit images respectively. The transverse cross-section after rescaling is shown in Figure 4.8e, with equivalent brightness and contrast properties to the section in the reference image (Figure 4.8a). The histogram of the grey level distribution of the rescaled image (Figure 4.8f) is too close to the reference histogram (Figure 4.8b). The same procedure is done to the 16-bit images of the following states.

4.5.2 Grey level and porosity

The grey level of a voxel g_v of an ideal XRCT image is an affine function of the average linear attenuation coefficient of the physical volume associated with this voxel μ_v . In case of a material made of several pure phases, this coefficient can be computed as

$$\mu_v = \sum_{i, phases} \rho_v^i \left(\frac{\mu}{\rho} \right)_i \quad (4.15)$$

where ρ_v^i is the local density of phase i in voxel v and $\left(\frac{\mu}{\rho} \right)_i$ is the mass attenuation coefficient of pure phase i , which is an intrinsic quantity of this phase. ρ_v^i itself can be written as: $\rho_v^i = f_v^i \rho_i$ where f_v^i is the volume fraction of phase i in voxel v and ρ_i is the density of pure phase i , such that $\rho_i \cdot \left(\frac{\mu}{\rho} \right)_i = \mu_i$, where μ_i is the lineic attenuation coefficient of pure phase i . When averaging over all the voxels of the sample, one gets:

$$\langle \mu_v \rangle = \sum_{i, phases} f_i \mu_i \quad (4.16)$$

with $f_i = \langle f_v^i \rangle$ is the overall volume fraction of phase i . As the grey levels are affine functions of the attenuation coefficient, a similar result can be obtained for the grey levels:

$$\langle g \rangle = \sum_{i, phases} f_i g_i \quad (4.17)$$

where g_i is the grey level associated to pure phase i . Since three phases are present in SML, the previous equation can be written as:

$$\langle g \rangle = \phi \times g_{pore} + f_{quartz} \times g_{quartz} + f_{calcite} \times g_{calcite} \quad (4.18)$$

where ϕ is the global porosity, f_{quartz} and $f_{calcite}$ are the volume fractions of quartz and calcite minerals respectively (with $\phi + f_{quartz} + f_{calcite} = 1$). The global porosity can be evaluated using the water saturation method. The grey level of a pore is evaluated directly using FIJI by selecting a sufficiently set of voxels strictly within a large pore. In addition, it is possible to calculate the global grey level of the sample $\langle g \rangle$ using FIJI by excluding all the voxels outside the sample (a cylindrical geometry fitted to the sample is defined for that purpose). On the other hand, Baud et al. (2017a) have reported that calcite constitutes 80%

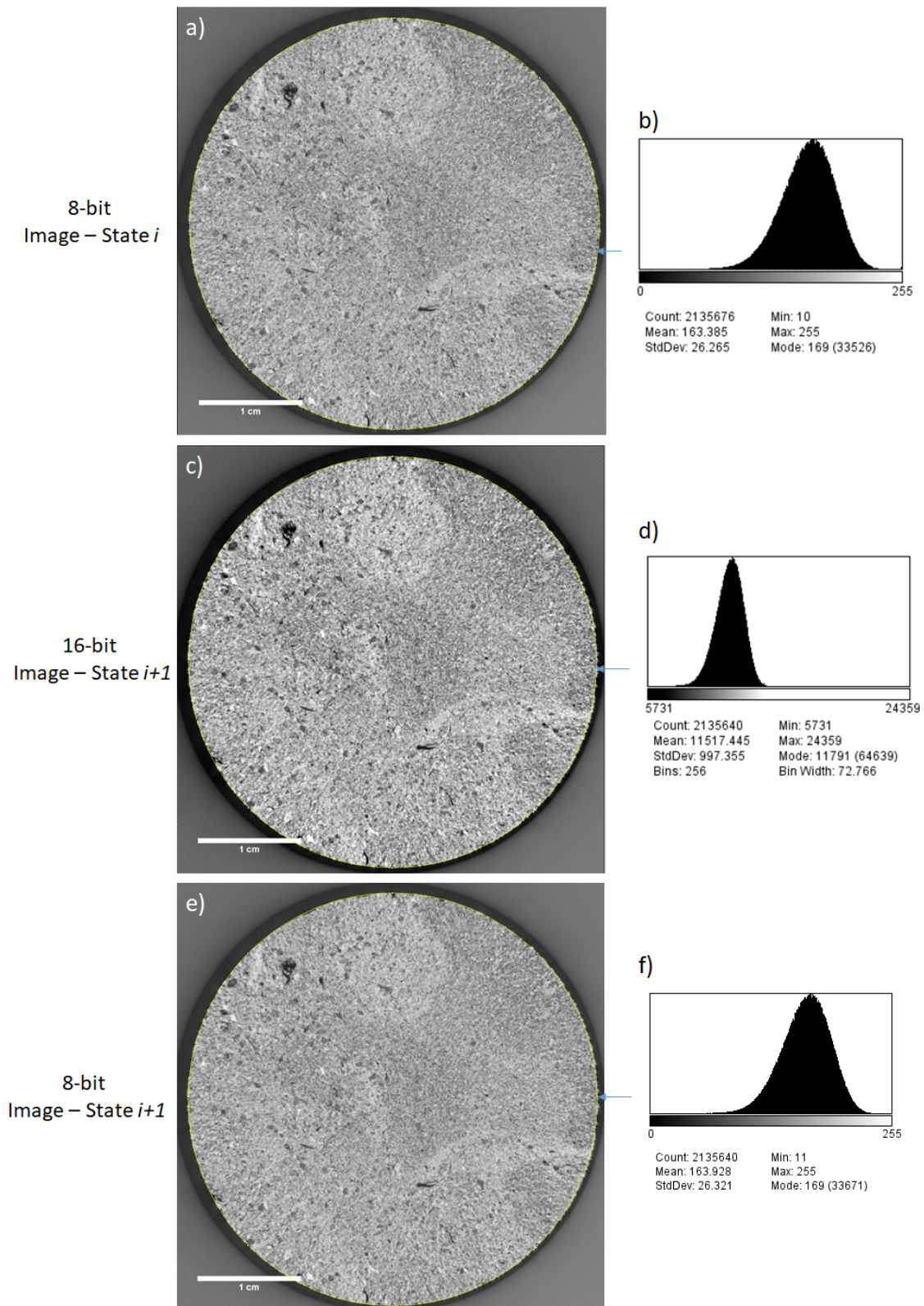


Figure 4.8: a) A typical transverse cross-section of the reference sample in the 8-bit reference configuration; b) Histogram of the grey level distribution inside the selection in the 8-bit image; c) The same cross-section in the 16-bit deformed configuration before calibration; d) Histogram of the grey level distribution inside the selection in the 16-bit image; e) The same cross-section after adjusting the grey levels; f) Histogram of the grey level distribution inside the selection in the rescaled 8-bit image.

of the weight of the solid phase whereas quartz forms the remainder. Despite supposing that the former mineral composition is valid for all our samples, Equation 4.18 is still insufficient because g_{quartz} and $g_{calcite}$ are both unknown. However, the calculation of quartz and calcite attenuation coefficients can simplify the problem.

4.5.3 Quartz and calcite attenuation coefficients

All the data concerning the attenuation coefficient of both pure phases calcite and quartz are provided on the website of the *National Institute of Standards and Technology*². The XRCT observations are done at a source energy of 100 KV. The transmittance coefficients $e^{-\mu \cdot x}$ of pure quartz and calcite minerals with respect to the source energy for a material length of $x = 0.96$ mm are depicted in Figure 4.9 (the effect of the copper filter is taken into account). The choice of the length x corresponds to the diameter of the subvolume over which the porosity will be evaluated in the forthcoming analysis (Section 4.5.5). Therefore, it is observed that the variability of the local mineral proportion has a negligible effect on the homogenized solid matrix grey value. Hence, an assumption can be made on the grey values of quartz and calcite, such as:

$$g_{calcite} \simeq g_{quartz} \simeq g_{solid\ phase} \quad (4.19)$$

where $g_{solid\ phase}$ corresponds to the grey level of the homogenized solid matrix. By noticing that $f_{quartz} + f_{calcite} = 1 - \phi$, the combination of Equations 4.18 and 4.19 leads to a simpler relation:

$$g_{av} = g_{pore} \times \phi + g_{solid\ phase} \times (1 - \phi) \quad (4.20)$$

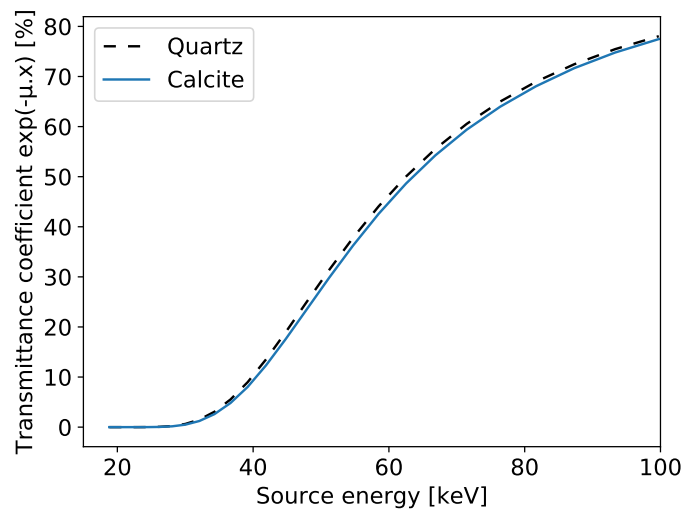


Figure 4.9: The transmittance coefficient evolution with respect to the source energy over a material length of 0.96 mm for both quartz and calcite minerals.

²<https://physics.nist.gov/PhysRefData/FFast/html/form.html>

4.5.4 Porosity maps computation

For a given sample of known global porosity ϕ , the quantities $\langle g \rangle$ and g_{pore} are easily measured with FIJI as explained in Section 4.5.2. Thus, the grey level of the homogenized solid phase $g_{solid\ phase}$ can be deduced. Equation 4.20 is valid not only at the scale of the sample, but also at the scale of any subvolume. Over each voxel, a spherical subvolume of radius R is defined in a given XRCT image (Figure 4.10). The sphere is composed of discrete voxels, the center of which have a distance smaller than R with respect to the sphere center. FIJI can smooth the images and give a mean value $\langle g \rangle_{sub}$ of the grey levels of all voxels inside the subvolume. Local porosity is finally deduced when applying Equation 4.20 over the subvolume. Figure 4.10 illustrates the steps of a porosity map computation. Paraview is then used to visualize the porosity maps.

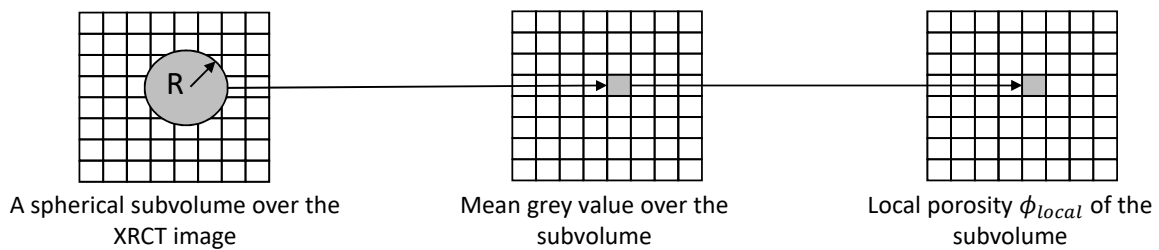


Figure 4.10: From XRCT image to porosity map computation: Local porosity evaluation over a subvolume of radius R .

4.5.5 The choice of the subvolume size

The diameter $2 \times R$ of the subvolume over which porosity is evaluated must be defined (Figure 4.10). The objective here is to describe the microstructure through the porosity notion, regardless of the local structure (grains, micro- and macro-pores, etc.). Therefore, this diameter should be sufficiently larger than the microstructure characteristic size. Microscopic observations presented in Chapter 3 show that grains and pores have diameters smaller than 0.3 mm. Hence, this size presents a lower bound of the subvolume diameter. On the other hand, a porosity heterogeneity is observed at the scale of the centimeter. If the subvolume diameter is comparable to or larger than this scale, the heterogeneity of porosity will be erased in porosity maps after the smoothing process. Since one purpose of this study is to understand the effect of this observed porosity heterogeneity on strain localization, the subvolume diameter should be sufficiently smaller than 10 mm.

To illustrate this analysis, let us consider a transverse cross-section of a XRCT image (Figure 4.11). The porosity is calculated for 4 different subvolume diameters: 0.24 mm (10 voxels); 0.48 mm (20 voxels); 0.96 mm (40 voxels) and 1.44 mm (60 voxels). Using FIJI, a line crossing many high- and low-porosity zones is added and over which the porosity profile can be plotted (Figure 4.12). It is observed that for a diameter of 0.24 mm, a porosity fluctuation of small wave length (<1 mm) is observed, which could be interpreted as the

signature of the alternation of grains and pores. The variation of porosity ranges from 20 to 55%. However, it is difficult to identify the fluctuations at centimetric scale which we are interested in. As for the diameter 0.48 mm, the variation range of the porosity is lower and the fluctuation at the centimetric scale becomes more clear. Regarding the diameters 0.96 and 1.44 mm, they act as frequency low-pass filters. The porosity fluctuation due to grain and pore sizes is almost fully erased. In addition, it is remarkable that these two last profiles are very similar, which suggests that there is not much information at a scale between 0.96 and 1.44 mm. Thus, since we are interested in the larger centimetric wave length, a diameter of 0.96 mm is judged as the appropriate diameter for porosity evaluation. Finally, the porosity map is computed and visualized using Paraview. Figure 4.13 illustrates an example of a cross-section of the computed porosity map.

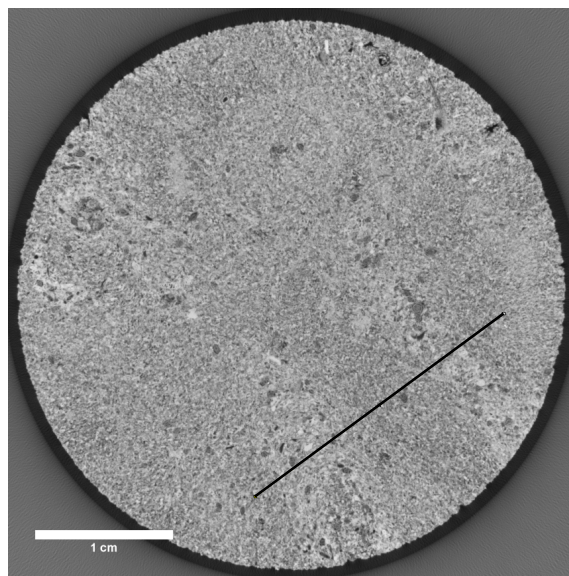


Figure 4.11: A transverse cross-section of a XRCT image.

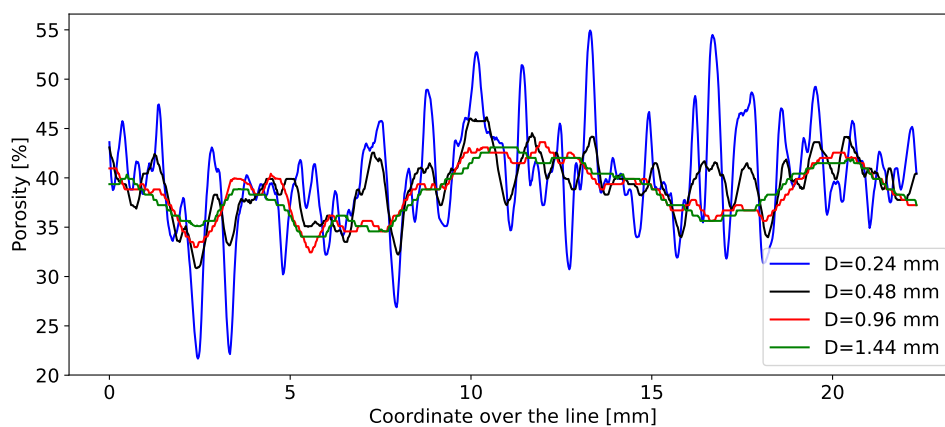


Figure 4.12: The profile of the porosity evaluated for different subvolume diameters over the line shown in Figure 4.11.

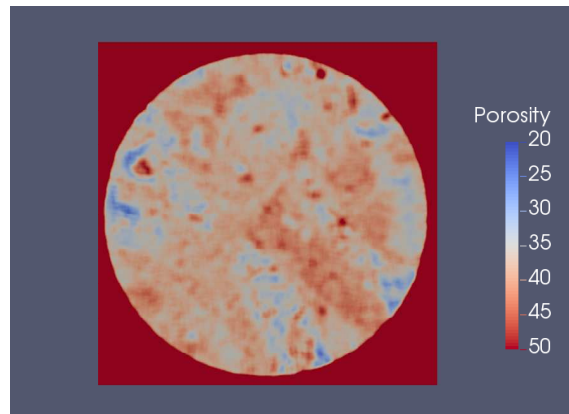


Figure 4.13: A transverse cross-section of the porosity map corresponding to the section shown in Figure 4.11.

4.6 Second gradient evaluation

Gradient-dependent constitutive laws will be used to model the strain localization in this study. This category of models constitutes a subfamily of general micromorphic models that take into account the microstructural features of the material and introduce an internal length that permits to regularize the problem of localization of deformation (Vardoulakis and Aifantis, 1991; De Borst and Mühlhaus, 1992). In this type of model, the hardening law of the plasticity formulation depends on a plastic strain measure but also on its second gradient. Compaction bands are generally accompanied with a pore collapse phenomenon (Cilona et al., 2014). Thus, it is natural to consider that the hardening law depends upon the plastic volumetric strain which is equal to the irreversible porosity change if it is assumed that the solid grains remain elastic (See Coussy, 2004). In the framework of gradient-dependent plasticity models, we choose the porosity and its second gradient as independent hardening parameters that control the evolution of the yield surface. Therefore, the second gradient of the porosity has to be evaluated from the images of the sample in order to calibrate the model. The purpose of this section is to present a new method that relies on XRCT observations to evaluate the second-gradient of the porosity. The method operates on 3D porosity maps computed as described previously in Section 4.5.

4.6.1 The 1D problem

For simplicity, the development of the procedure is firstly presented in the 1D problem. Let us consider a simple line divided into n intervals having each a grey value linearly related to the local porosity (Figure 4.14). The line is centered on x_0 and has a length of L . The latter dimension defines the size of the domain over which the second gradient of the porosity should be evaluated. Notice that, identifying this length is not the purpose of this section. In this paragraph, we seek to fit a quadratic function to the porosity distribution. Therefore, the Taylor series expansion of the porosity up to the second order is presented in Equation

4.21, where $\phi(x_0)$ represents the porosity at the center, $\phi'(x_0)$ and $\phi''(x_0)$ represent the first and the second derivative of the porosity with respect to x respectively.

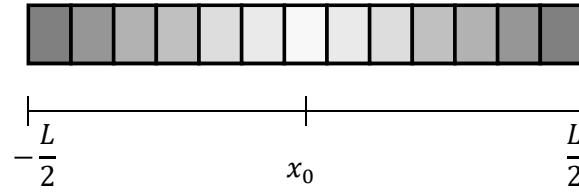


Figure 4.14: A line of pixels over which the second gradient of the porosity is evaluated.

$$\phi(x) = \phi(x_0) + \phi'(x_0) \times (x - x_0) + \phi''(x_0) \times \frac{(x - x_0)^2}{2} \quad (4.21)$$

The porosity mean value over the line can be written in terms of the central porosity and its second derivative:

$$\langle \phi \rangle = \frac{1}{L} \int_{-L/2}^{L/2} \phi(x) dx = \phi(x_0) + \frac{L^2}{24} \cdot \phi''(x_0) \quad (4.22)$$

However, a second equation is needed to assess $\phi(x_0)$ and $\phi''(x_0)$. For that, the mean value of the second order statistical moment is evaluated:

$$\langle d^2 \cdot \phi \rangle = \frac{1}{L} \int_{-L/2}^{L/2} (x - x_0)^2 \cdot \phi(x) dx = \frac{40 \cdot L^2 \cdot \phi(x_0) + 3 \cdot L^4 \cdot \phi''(x_0)}{480} \quad (4.23)$$

where d represents the distance of a pixel to the center $d = x - x_0$. Thus, once $\langle \phi \rangle$ and $\langle d^2 \cdot \phi \rangle$ are calculated, the identification of $\phi(x_0)$ and $\phi''(x_0)$ is straightforward.

4.6.2 The 3D problem

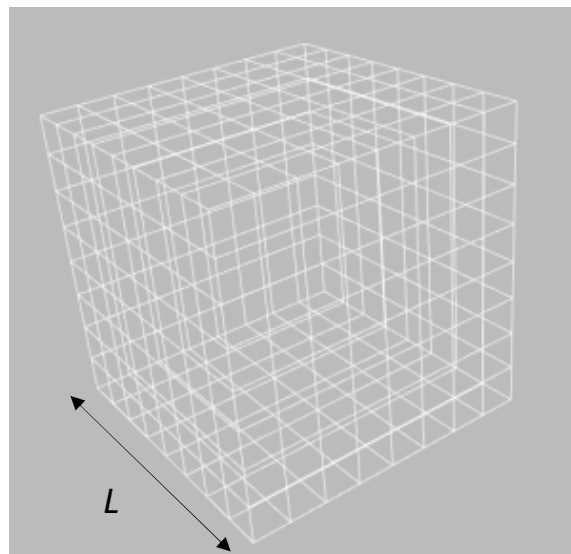


Figure 4.15: A grid of voxels over which the second gradient of the porosity is evaluated.

For 3D porosity maps, the above equations (4.21, 4.22 and 4.23) can be generalized. The considered domain has now a cubic shape of side length L , centered on a point (x_0, y_0, z_0) (Figure 4.15). Again, it is worthwhile to mention that the purpose of this section is not to propose how to define this length (this will be discussed later in Chapter 6). The Taylor series expansion up to the second order can be written as:

$$\begin{aligned}
\phi(x, y, z) = & \phi)_{x_0, y_0, z_0} \\
& + \frac{\partial \phi}{\partial x})_{x_0, y_0, z_0} \times (x - x_0) + \frac{\partial \phi}{\partial y})_{x_0, y_0, z_0} \times (y - y_0) + \frac{\partial \phi}{\partial z})_{x_0, y_0, z_0} \times (z - z_0) \\
& + \frac{\partial^2 \phi}{\partial x \partial y})_{x_0, y_0, z_0} \times (x - x_0) \times (y - y_0) + \frac{\partial^2 \phi}{\partial y \partial z})_{x_0, y_0, z_0} \times (y - y_0) \times (z - z_0) \\
& + \frac{\partial^2 \phi}{\partial x \partial z})_{x_0, y_0, z_0} \times (x - x_0) \times (z - z_0) \\
& + \frac{\partial^2 \phi}{\partial x^2})_{x_0, y_0, z_0} \times \frac{(x - x_0)^2}{2} + \frac{\partial^2 \phi}{\partial y^2})_{x_0, y_0, z_0} \times \frac{(y - y_0)^2}{2} \\
& + \frac{\partial^2 \phi}{\partial z^2})_{x_0, y_0, z_0} \times \frac{(z - z_0)^2}{2}
\end{aligned} \tag{4.24}$$

Similarly, the expressions of the mean value of the porosity and its second order statistical moment are expanded in Equations 4.25 and 4.26 in terms of the porosity at the cube center $\phi)_{x_0, y_0, z_0}$ and its second gradient $\nabla^2 \phi)_{x_0, y_0, z_0}$, where $\nabla^2 \phi = \frac{\partial^2 \phi}{\partial x^2} + \frac{\partial^2 \phi}{\partial y^2} + \frac{\partial^2 \phi}{\partial z^2}$.

$$\begin{aligned}
\langle \phi \rangle &= \frac{1}{L^3} \int_{-L/2}^{L/2} \int_{-L/2}^{L/2} \int_{-L/2}^{L/2} \phi(x, y, z) dx \cdot dy \cdot dz \\
&= \phi)_{x_0, y_0, z_0} + \frac{L^2}{24} \cdot \nabla^2 \phi)_{x_0, y_0, z_0}
\end{aligned} \tag{4.25}$$

$$\begin{aligned}
\langle r^2 \cdot \phi \rangle &= \frac{1}{L^3} \int_{-L/2}^{L/2} \int_{-L/2}^{L/2} \int_{-L/2}^{L/2} [(x - x_0)^2 + (y - y_0)^2 + (z - z_0)^2] \cdot \phi(x) dx \cdot dy \cdot dz \\
&= \frac{L^2}{4} \cdot \phi)_{x_0, y_0, z_0} + \frac{19 \cdot L^4}{1440} \cdot \nabla^2 \phi)_{x_0, y_0, z_0}
\end{aligned} \tag{4.26}$$

where $r = \sqrt{(x - x_0)^2 + (y - y_0)^2 + (z - z_0)^2}$ represents the distance of a voxel to the center of the cube. A script in Python language that operates on porosity maps has been written to evaluate $\langle \phi \rangle$ and $\langle r^2 \cdot \phi \rangle$. Thus, the porosity and its second gradient of the cubic domain can be obtained. For the sake of simplicity, the second gradient $\nabla^2 \phi)_{x_0, y_0, z_0}$ will be henceforth denoted by $\nabla^2 \phi_0$. The script is presented in Appendix D.

Experimental observations

Résumé Dans ce chapitre, les résultats d'essais de compression isotrope et de compression triaxiale sous différents confinements sont présentés. La technique de Corrélation d'Images Volumiques est appliquée pour suivre la localisation de la déformation à différents paliers de chargements. La construction de cartes de porosité permet d'étudier l'effet de l'hétérogénéité de la porosité sur le mode de déformation des échantillons. Finalement, des observations sur des lames minces permettent de caractériser les micromécanismes impliqués dans la déformation.

Abstract In this chapter, the results of hydrostatic and triaxial compression tests performed on samples of Saint-Maximin limestone are presented. The Digital Volume Correlation technique is used in order to follow the strain localization after different loading stages. The computation of porosity maps allows to study the effect of its heterogeneity on the deformation modes. The experimental observations permit to characterize the micromechanisms involved in the deformation of the material.

5.1 Definitions

The convention of negative compressive stresses is adopted in this study. The mean stress is defined as:

$$p = \frac{\text{Tr}(\underline{\underline{\sigma}})}{3} \quad (5.1)$$

whereas the shear stress intensity is defined as the square root of the second invariant of the deviatoric part, $\underline{\underline{s}}$, of the stress tensor:

$$q = \sqrt{\frac{1}{2}\underline{\underline{s}} : \underline{\underline{s}}} \quad (5.2)$$

with $\underline{\underline{s}} = \underline{\underline{\sigma}} - p\underline{\underline{I}}$ and $\underline{\underline{I}}$ is the identity matrix. Let σ_1 and σ_3 denote the maximum and minimum principal stresses in absolute value respectively ($|\sigma_1| > |\sigma_3|$). In axisymmetric triaxial compression, the stress state is diagonal with $\sigma_1 < \sigma_2 = \sigma_3 < 0$. Therefore, the mean stress and the shear stress intensity are expressed as:

$$p = \frac{\sigma_1 + 2\sigma_3}{3} \quad \text{and} \quad q = \frac{\sigma_3 - \sigma_1}{\sqrt{3}} \quad (5.3)$$

Equivalently, negative strain values refer to compaction while positive values indicate dilation. The volumetric and shear strain magnitudes are given by:

$$\epsilon_v = \text{tr}(\underline{\underline{\epsilon}}) \quad \text{and} \quad \gamma = \sqrt{2\underline{\underline{\epsilon}} : \underline{\underline{\epsilon}}} \quad (5.4)$$

where $\underline{\underline{\epsilon}}$ represents the deviatoric strain tensor $\Delta\underline{\underline{\epsilon}} = \underline{\underline{\Delta\epsilon}} - \frac{1}{3}\Delta\epsilon_v\underline{\underline{I}}$. In the DVC deformation maps, the sample axis is oriented along the axis z . The axes x and y are defined in the transversal plane, such that (x, y, z) is an orthogonal system.

5.2 Preliminary tests

The confining pressure in triaxial loading plays a major role in the rock behavior and deformation mode. To avoid water effect on the SML strength as reported by Baud et al. (2017a), all samples are dried at 60°C for 48 hours and all the experiments are performed in dry condition. A preliminary series of triaxial tests is conducted in order to characterize the confining pressure ranges which control the behavior regimes and to inspect the modes of localization by eye observation of the sample surface when possible. Then, some confining pressure conditions are selected, under which new samples are tested.

In a first stage, hydrostatic loading is applied up to a given pressure, then deviatoric loading is applied with an axial strain rate of about 10^{-5} s^{-1} (see Section 4.1). Figure

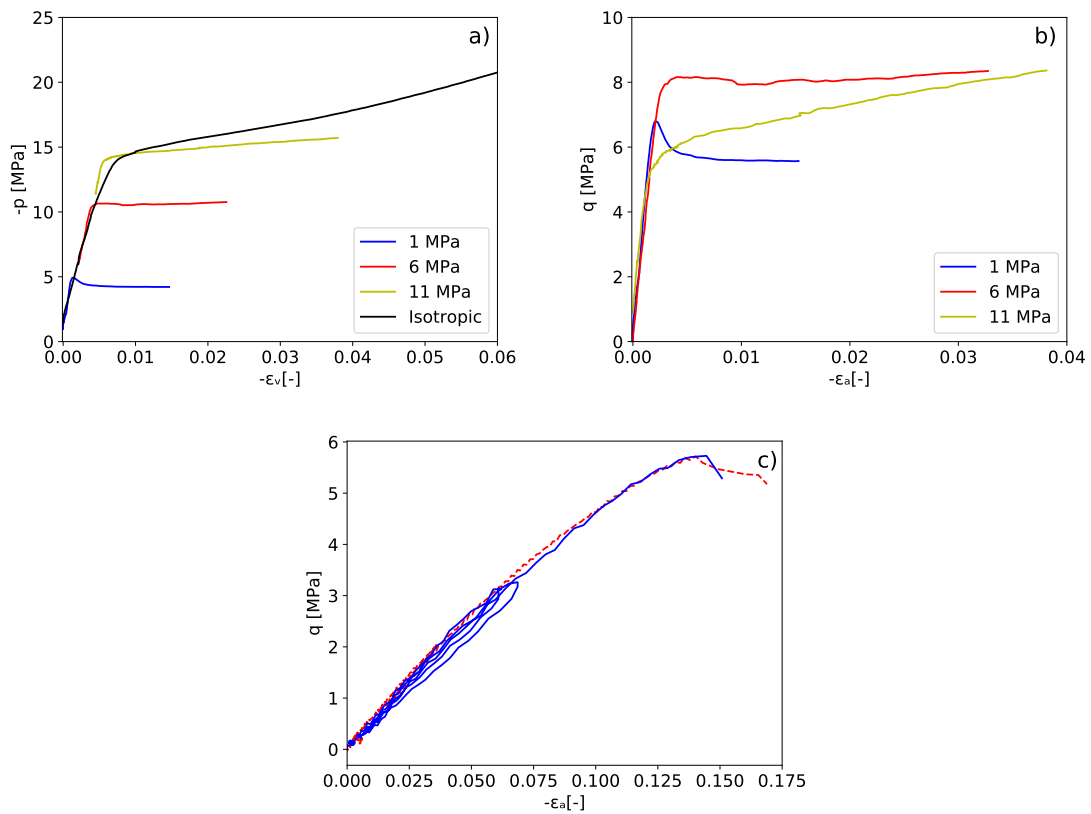


Figure 5.1: Typical triaxial test results in dry conditions for several confining pressures (a) Mean pressure vs volumetric deformation; (b) Shear stress intensity vs axial strain; (c) Two SML samples tested under uniaxial loading.

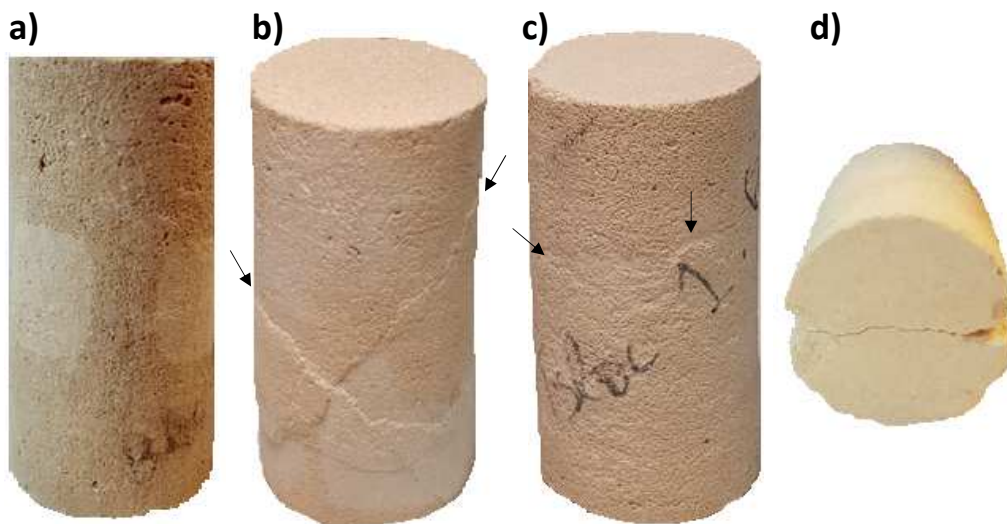


Figure 5.2: a) SML sample tested under hydrostatic condition; b) Conjugate shear bands on the surface of a sample tested at low confinement $\sigma_3 = -1\text{MPa}$; c) Deformation bands observed on the surface of a sample tested at high confinement $\sigma_3 = -11\text{MPa}$; d) Brazilian test performed on a sample.

5.1 shows the deviatoric loading stage of typical axisymmetric triaxial experiments and a full hydrostatic loading experiment in terms of stress-strain response, where ϵ_a and ϵ_v represent the axial and volumetric strains measured by the LVDTs respectively. Following the definition of Wong et al. (1997), plasticity onset is detected on the p vs ϵ_v plot (Figure 5.1a) and is denoted by P^* and C^* in isotropic and triaxial loading respectively. Under hydrostatic loading, the SML sample seems to deform homogeneously, as no barrel-shaped mode is obtained after more than 6% of compressive volumetric strain (Figure 5.2a). The yield stress P^* is evaluated at -14.5 MPa. The differential load causes an earlier compaction ($P^* < C^* < 0$). Two extreme responses can be distinguished. Under low confining pressure ($\sigma_3 = -1$ MPa), a peak stress is observed (Figure 5.1b), followed by a softening regime. After around 2% of axial strain, it is observed that two conjugate shear bands are formed as shown in Figure 5.2b. At relatively high confinements ($\sigma_3 = -11$ MPa), an overall hardening regime is observed after the elastic limit. Beyond 4% axial strain, one may detect the formation of deformation bands which are however difficult to observe with naked eye on the surface (Figure 5.2c). Due to the high porosity of SML, no dilatancy is measured by the LVDTs, even at low confining pressure. This result can be an indicator that all bands have a compactant behavior (pure compaction or compactive shear bands). The nature of the deformation bands will be studied later. The transitional regime occurs at $\sigma_3 = -6$ MPa and is characterized by a perfectly plastic response (plateau beyond the yield stress). A visual inspection of the sample surface after deformation reveals some signs of strain localization, similarly to the sample tested at high confinement. To complete the characterization of the yield surface shape, two additional uniaxial tests are performed in dry condition (Figure 5.1c). The uniaxial compressive stress is obtained at around 10 MPa. Moreover, the tensile strength σ_t is evaluated at 1.2 MPa by means of two brazilian tests (Figure 5.2d), as $\sigma_t = \frac{2P}{\pi DL}$, where P is the maximum applied load, D is the diameter and L is the height of the cylinder. Finally, all the data are gathered and yield stresses of SML are plotted in Figure 5.3. The results are consistent with Baud et al. (2009) and Baud et al. (2017a) data. Four different loading conditions are then selected to be studied by DVC and each section below is devoted to one of these loading cases:

1. Hydrostatic loading test.
2. High confining pressure test (11 MPa).
3. Low confining pressure test (1 MPa).
4. Intermediate confining pressure test (6 MPa).

The yield stresses corresponding to these samples are represented with solid triangles in Figure 5.3. Since X-Ray imaging is done ex-situ, samples must be unloaded after each loading stage, then extracted from the triaxial machine to be imaged. Thereafter, they are put back inside the machine where further loading is applied. This procedure becomes

increasingly difficult when it is repeated several times, since the samples become weaker after being tested, as some pieces may be broken, especially near the boundaries. For each confinement condition cited above, only two stages of loading are presented.

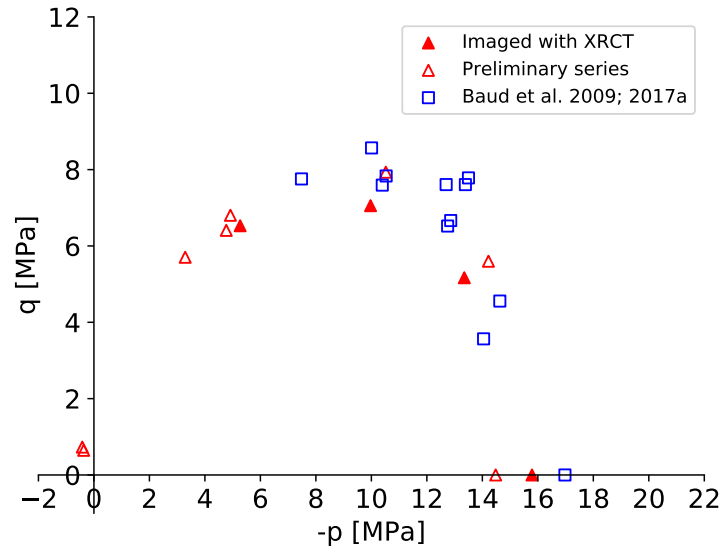


Figure 5.3: Yield stresses of SML samples: solid red triangles for samples studied with XRCT, empty red triangles for the preliminary experiments & blue squares for data from Baud et al. (2009); Baud et al. (2017a).

In addition to the XRCT images for which the resolution is limited to a voxel size of $24 \mu\text{m}$, SEM observations have been performed on thin sections (prepared as described in Section 3.3.5). These thin sections have been prepared on samples after the second stage of loading and observations have been performed at the *Laboratoire de Géologie* of the *Ecole Normale Supérieure* and at the *Laboratoire de Mécanique des Solides* of the *Ecole Polytechnique*.

5.3 Hydrostatic loading test

A SML sample with an overall porosity of 38.2% has been tested under hydrostatic loading conditions. The sample is imaged by XRCT in the initial state before any applied load. Figure 5.4 presents the volumetric response in terms of the mean stress vs volumetric strain plane measured by means of the six LVDTs disposed around the sample. Loading is applied in two stages; after each, the sample is imaged by XRCT. In total, three images are recorded in three different deformation states and DVC is applied twice (one after each loading stage).

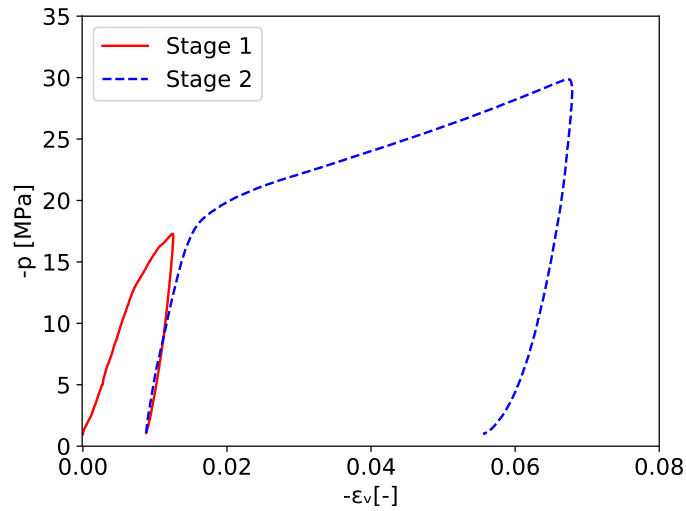


Figure 5.4: A SML sample tested in dry condition under hydrostatic loading.

5.3.1 Initial state

The porosity map of the sample in the initial state is computed following the steps presented in section 4.5. Figure 5.5 shows a vertical cross-section of the 3D XRCT image and its porosity map. Porosity is observed to fluctuate from about 30% to about 45%. High-porosity and low-porosity zones are observed to alternate at the centimetric scale. These results corroborate the material description analysis done in section 3.3.2.

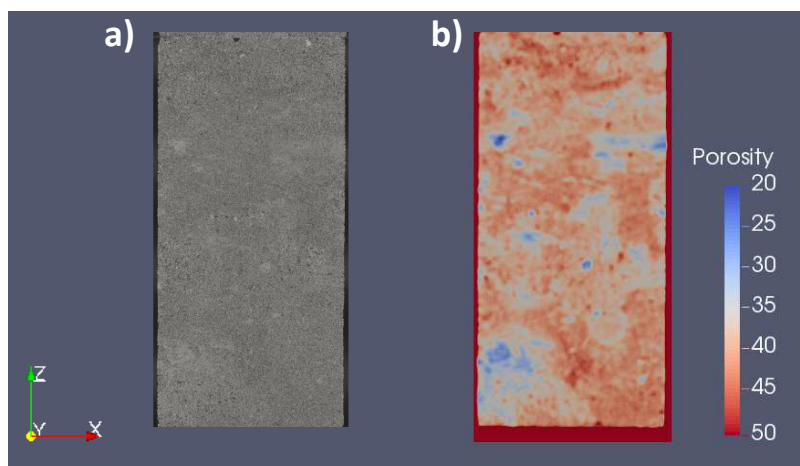


Figure 5.5: A SML sample in the initial state before being tested under hydrostatic loading conditions: a)-b) XZ middle cross-section of the XRCT image and the corresponding computed porosity map.

5.3.2 First loading stage

In the first stage, loading is stopped when the p vs ϵ_v curve slope begins to change. This state corresponds to the critical hydrostatic pressure P^* , which is found equal to 15.9 MPa in the current experiment. After unloading the sample, a residual volumetric strain of 0.8%, evaluated from LVDTs, is obtained. On the other hand, the volumetric strain is averaged over all the elements of the computed DVC map using Paraview and a mean compaction of 0.5% is obtained. This value is comparable to the measurement given by the LVDT. The inspection of the incremental volumetric strain map shows the onset of a plastic deformation at the right bottom part of the sample (Figure 5.6). The compactive strain evaluated inside this zone is around 2%, whereas the remaining zones of the sample are nearly undeformed.

The DVC strain map is compared with the porosity maps in order to understand the role of the porosity in the strain heterogeneity, as shown in Figure 5.7. The plastic compaction is observed to occur in a zone of high-porosity in comparison to other zones inside the sample (Figure 5.7a). The porosity distribution is investigated in this zone before and after loading and the histograms¹ are given in Figure 5.8. The porosity is observed to decrease from a mean value of 41.5% to around 39.5%. On the other hand, the mean plastic volumetric strain is evaluated at 2.6% in the same zone from the DVC map (Figure 5.7b), a comparable value to the porosity reduction.

A transverse cross-section corroborates the fact that plastic compaction occurs at first in high-porosity zones (Figure 5.9 a, b and c). Looking further into the microstructure evolution, a local densification is observed in the compacted zone (Figure 5.9 f and g). However, due to the limited resolution of the image, no conclusion can be made about the dominant micromechanism involved in the compaction. On the other hand, despite the presence of many large pores (having sizes up to 1 mm) in the denser zones (Figure 5.9d), these pores do not collapse (Figure 5.9e). According to Zhu et al. (2010), in a pore collapse mechanism, larger pores are weaker and are subjected to a collapse prior to smaller ones. Since some large pores lay inside denser zones, the rigid matrix of cemented grains appears to protect these "weak" pores.

5.3.3 Second loading stage

In the second stage, isotropic loading is applied and a linear overall hardening is observed up to a pressure of 30 MPa (Figure 5.4). A residual volumetric strain of 5.5%, evaluated

¹Notice that the considered zone in the deformed state does not perfectly correspond to the one considered in the initial state. Therefore, the comparison is not very accurate. The image subtraction method must be used to obtain more rigorous results (Chateau et al., 2018)

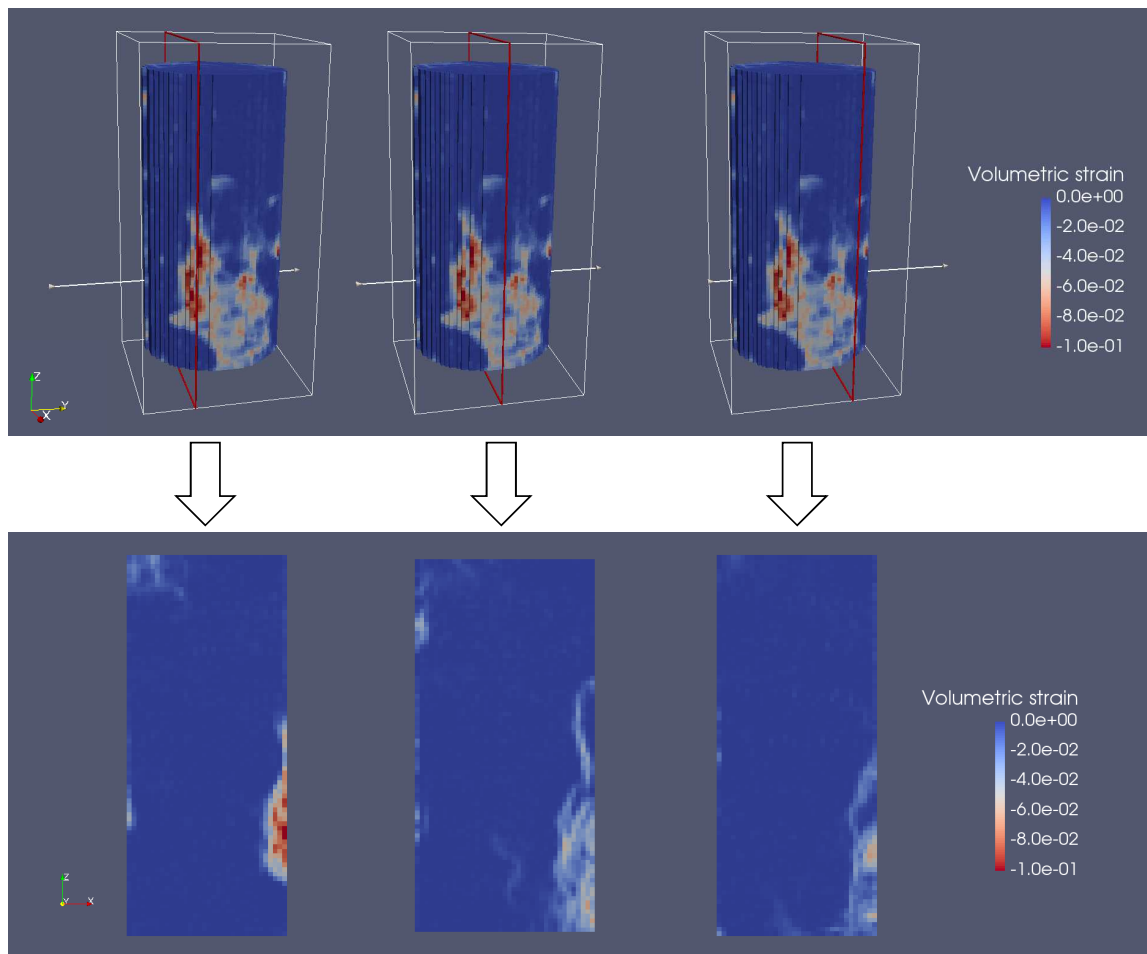


Figure 5.6: The incremental volumetric strain map for the first loading stage of the SML sample tested under hydrostatic loading conditions: 3D view and three vertical cross sections parallel to the XZ plane.

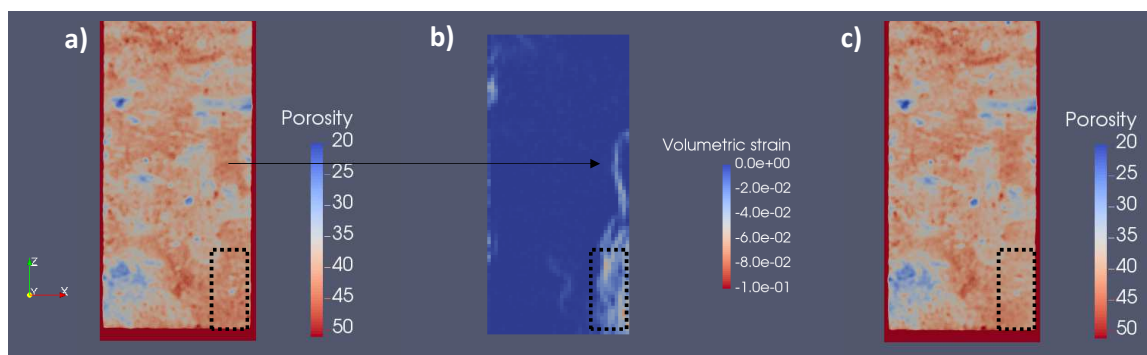


Figure 5.7: Vertical cross-sections at the middle of the sample of: a) the porosity map in the initial state; b) the incremental volumetric strain; c) the porosity map after the first stage of loading.

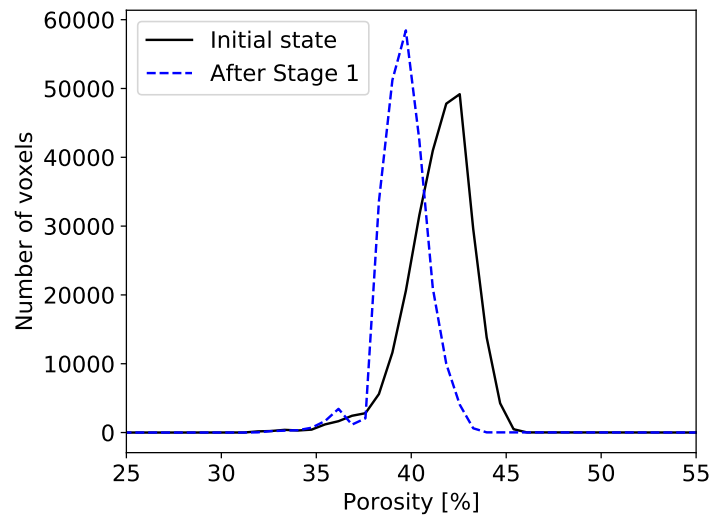


Figure 5.8: Histograms of porosity for the selected zones in Figure 5.7.

from LVDT measurements, is obtained². The incremental volumetric strain map computed after the DVC shows a diffuse compaction in the sample, without any sign of deformation bands (Figure 5.10). Inside the compacted zones, a negative volumetric strain up to 10% in some cases, is assessed (for instance the zone indicated by a black arrow on the central section in Figure 5.10). However, some zones are observed to remain undeformed (more precisely, the local strain is in the order of the DVC uncertainty: 0.1%).

In addition to the volumetric strain map, the shear strain magnitude map is compared now with the porosity maps computed before and after the second loading stage (Figure 5.11). Three zones can be distinguished: High-porosity zones (zones A) where porosity is higher than 40%; Low-porosity zones (zones B) where porosity is less than 35% and Interface zones (zones C). Compaction seems to happen without evidence of shear strain inside zones A, whereas zones B form stiff inclusions and remain relatively undeformed. Moreover, a significant shear strain takes place in zones C due to the stiffness contrast between zones A and B, as the stress at the local scale is not homogeneous. The incremental plastic shear strain intensity can go up to 10% in the interface zones. Nevertheless, volumetric compaction is also observed inside zones C, in the same range of the shearing intensity (10%), as shown in Figure 5.11c. For instance, porosity variation and strain quantities are evaluated on three domains selected on Figure 5.11a. Histograms of porosity are shown in Figure 5.12 and mean values of volumetric and shear strain magnitudes are presented in Table 5.1. A porosity decrease of about 5.5% is observed in the domain of the zone A, with a compactive strain of 6.8%. However, the domain in zone B seems to remain undeformed.

²The average value of the incremental plastic volumetric strain corresponding to this loading stage and evaluated over all the elements of the DVC map is 4.3%. When added to the value calculated for the first loading stage, a cumulative volumetric strain of 4.8% is obtained. This value is comparable to the measurement of the LVDTs.

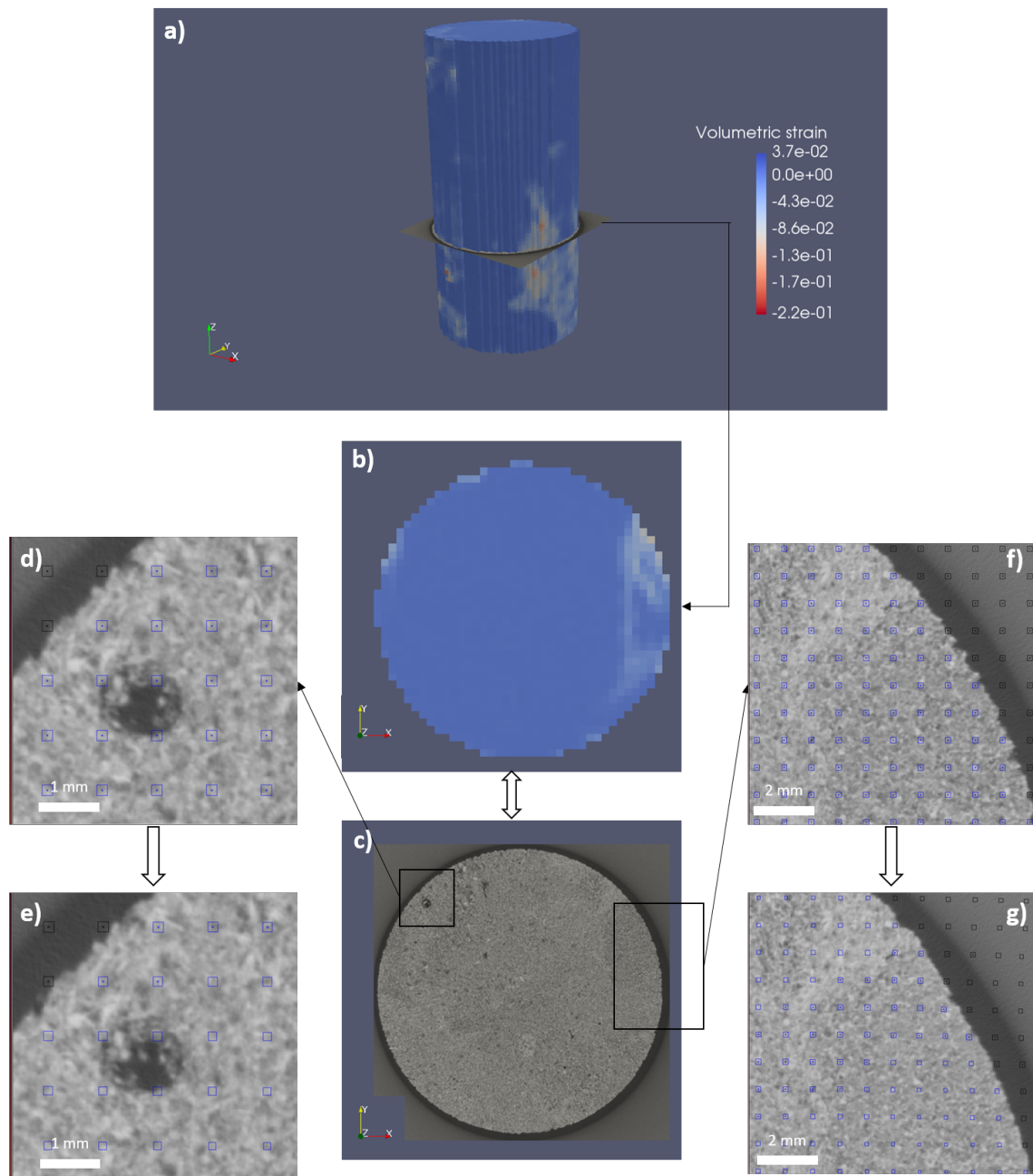


Figure 5.9: The SML sample, tested under hydrostatic loading conditions: **a)** Volumetric strain map after the first stage of loading; **b)** A transverse cross-section showing a heterogeneity of deformation; **c)** A transverse cross-section at the corresponding plane of the XRCT image in the initial state; **d)-e)** A large pore laying inside a low-porosity zone in the initial state and after the first loading stage; **f)-g)** A high-porosity zone at the initial state which is compacted after the first loading stage.

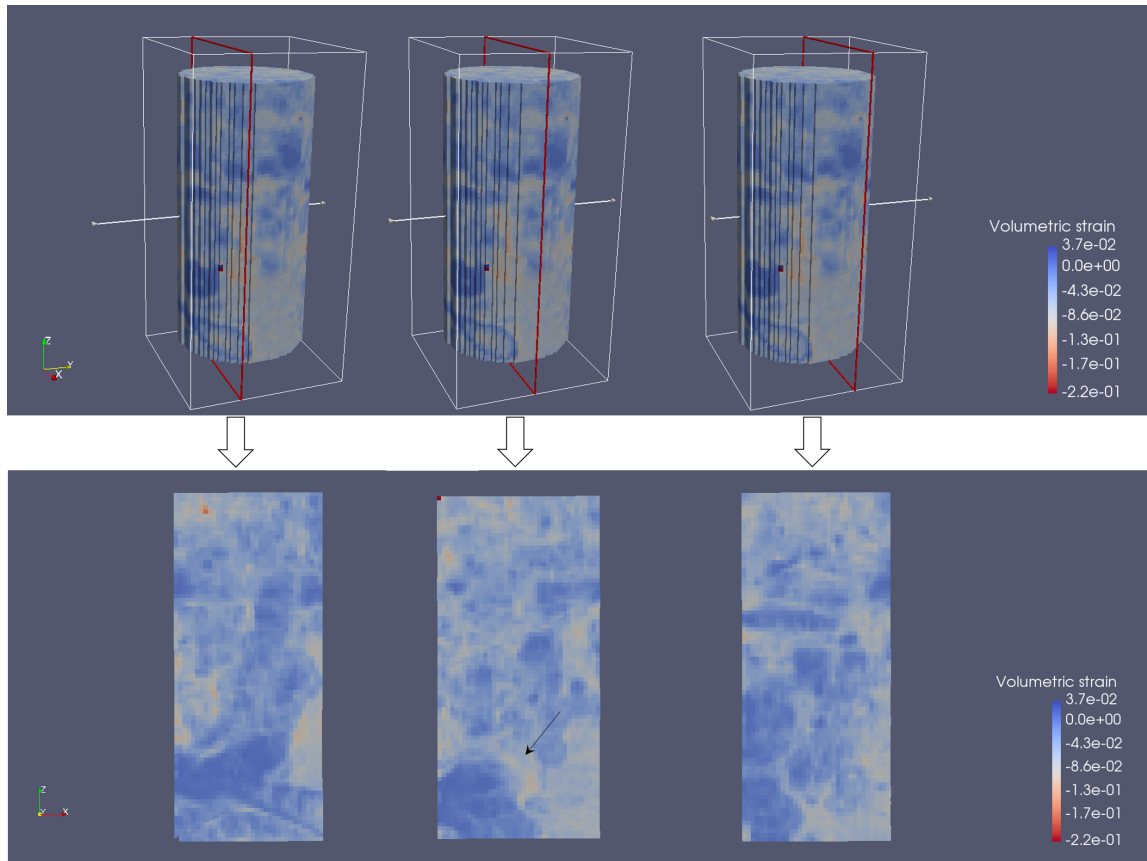


Figure 5.10: Incremental volumetric strain map after the second loading stage: three vertical cross sections parallel to the XZ plane.

In zone C, a porosity reduction of around 5.2% occurs and the shear strain intensity (5.1%) is much more present.

Table 5.1: Mean values of volumetric and shear strain magnitude of the 3 domains selected in Figure 5.11 during the second loading stage.

Zone	Mean shear strain magnitude [%]	Mean volumetric strain [%]
A	1.6	-6.8
B	0.9	-0.8
C	5.1	-6.9

Similarly to the observations made in the first stage, XRCT images make evidence of a densification inside zones A (Figure 5.14). Again, large pores laying in denser zones remain undeformed even after 5.5% of total volumetric strain (Figure 5.13). However, a slight pore size reduction is observed in pores near the high-porosity zones (Figure 5.14 e and f). In contrast, pores in high-porosity zones are completely closed after the deformation (Figure 5.15). The observed pore size reduction can occur due to a pore collapse or because of a pore filling by powders formed by grain crushing. At this stage, none of the two assumptions can be confirmed due to the limited resolution of the images. Post-mortem SEM observations on thin sections are needed. In conclusion, the observations performed for the two stages make

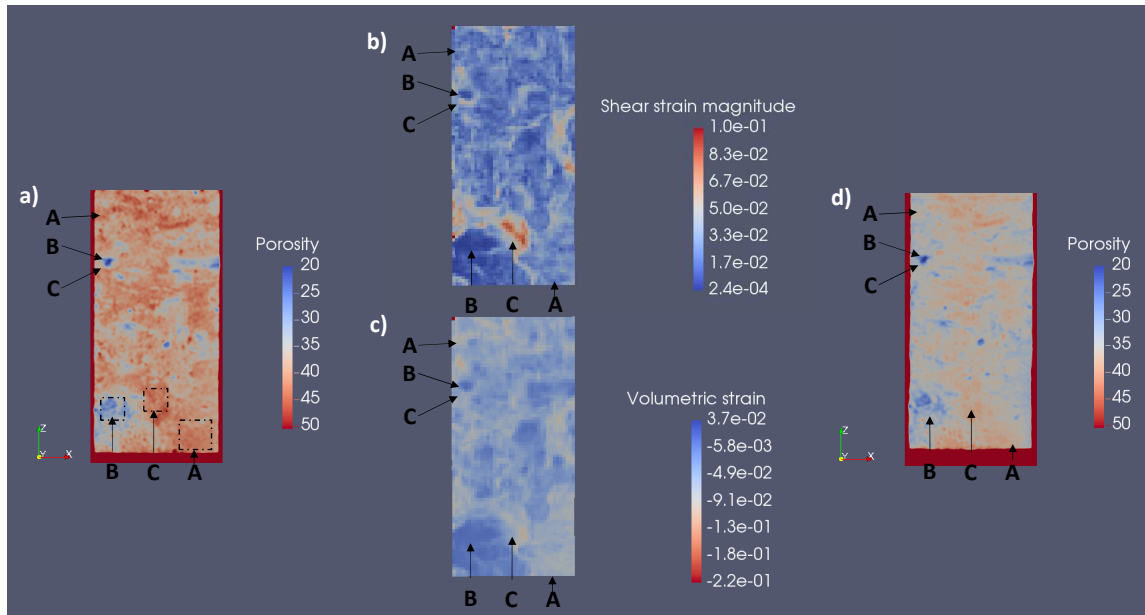


Figure 5.11: Vertical cross-sections at the middle of the sample of: **a)-d)** the porosity maps before and after the second loading stage; **b)-c)** the incremental shear strain magnitude and volumetric strain maps during the second loading stage. Zones A correspond to high-porosity zones ($\phi > 40\%$), zones B are low-porosity zones ($\phi < 35\%$) and zones C correspond to interface regions between zones A and B.

evidence that porosity heterogeneity at the scale of one centimeter controls the deformation heterogeneity pattern, whereas the pore diameter size is not observed to have a dominant effect on the strain heterogeneity.

5.3.4 Thin section observations

After the second loading stage, a thin section prepared in the vertical cross-section is prepared and observed in the SEM, using Backscattered Electrons contrast (BSE). Figures 5.16a and 5.17b show the contrast between deformed high-porosity zones and intact low-porosity zones. Large cemented calcite grains are observed to remain intact in the latter zones, whereas pervasive grain crushing occurs in high-porosity zones (Figure 5.16b). Indeed, the observations performed on high-porosity zones of the SML in the undeformed state do not show the presence of such amounts of small grains surrounded by powders (see Figure 3.13). In addition, quartz grains appear to remain intact as opposed to calcite grains, which are in many cases completely pulverized (Figure 5.17a), in accordance with Baud et al. (2017a) observations. In addition, *Miliolidae* shells are fractured in high-porosity zones (Figure 5.17a), but remain intact in low-porosity zones (Figure 5.17c), as the cementation seems to reduce stress concentration. As a consequence of grain crushing, powders are formed and fill subsequently the pores, contributing in a porosity reduction (Figure 5.16b).

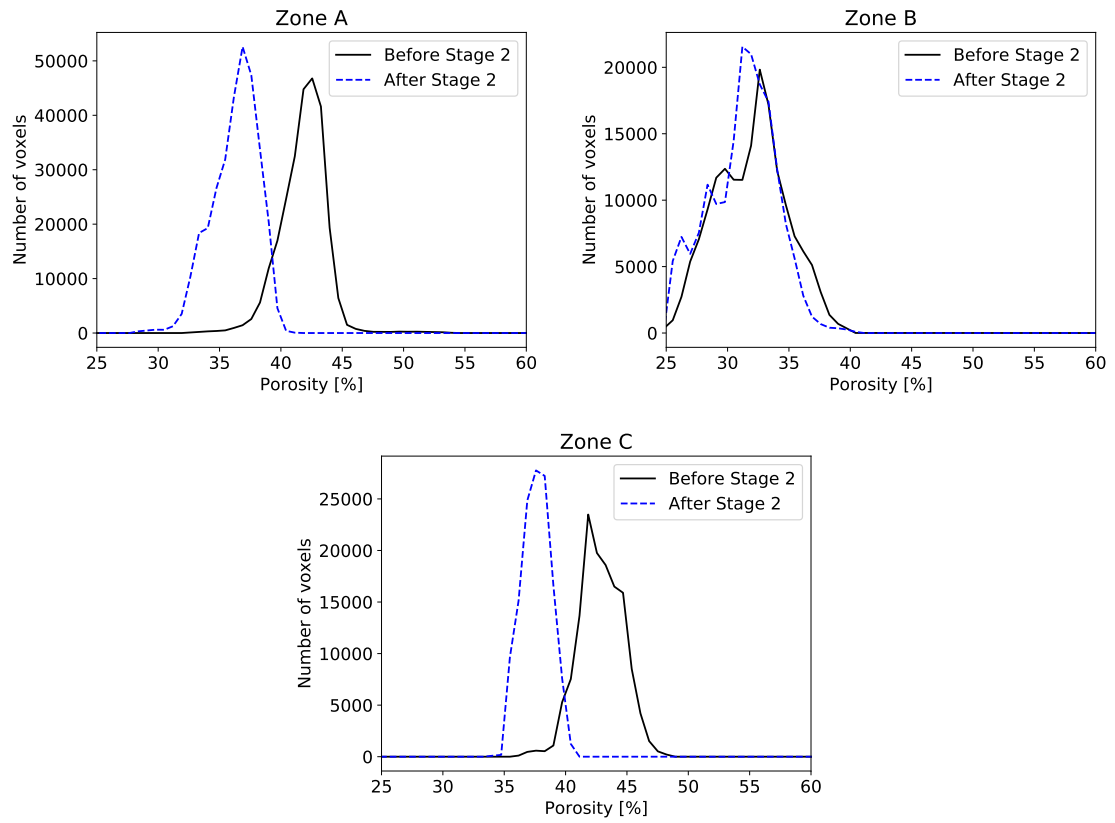


Figure 5.12: Porosity histograms of the three zones (A; B & C) selected in Figure 5.11a before and after the second loading stage.

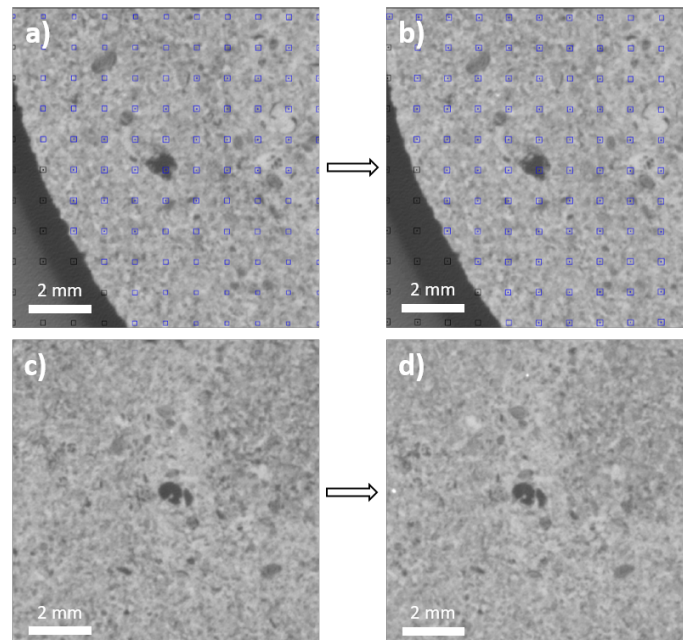


Figure 5.13: The SML sample, tested under hydrostatic loading condition: examples of two undeformed large pores observed before the second loading stage (a & c) and after the second loading stage (b & d).

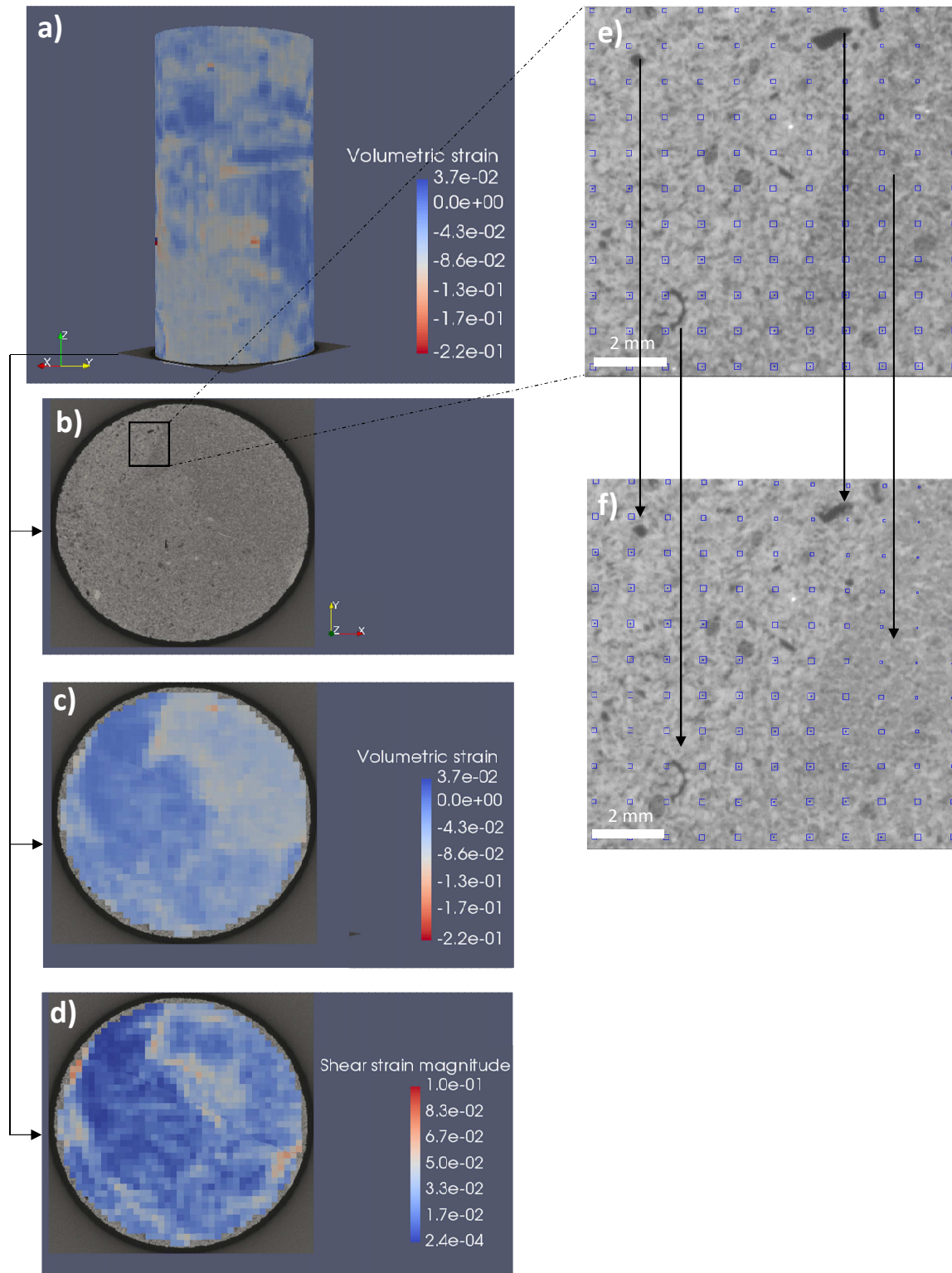


Figure 5.14: The SML sample, tested under hydrostatic loading condition: **a)** Volumetric strain map during the second stage of loading; **b)-c)-d)** A transverse cross-section of the XRCT image before loading and the corresponding planes of the volumetric strain & shear strain magnitude maps; **e)-f)** A zoom on the XRCT image showing the contrast between high- and low-porosity zones before and after the second loading stage.

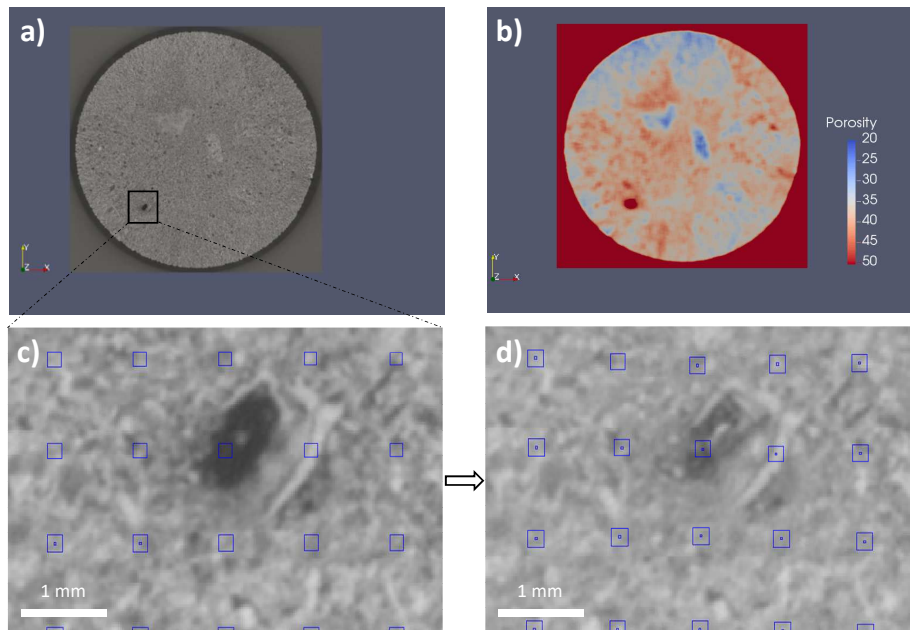


Figure 5.15: Large pore laying in a high porosity zone (41%): **a)-b)** XRCT image and the porosity map in the initial state; **c)-d)** A zoom on the pore before and after the second loading stage.

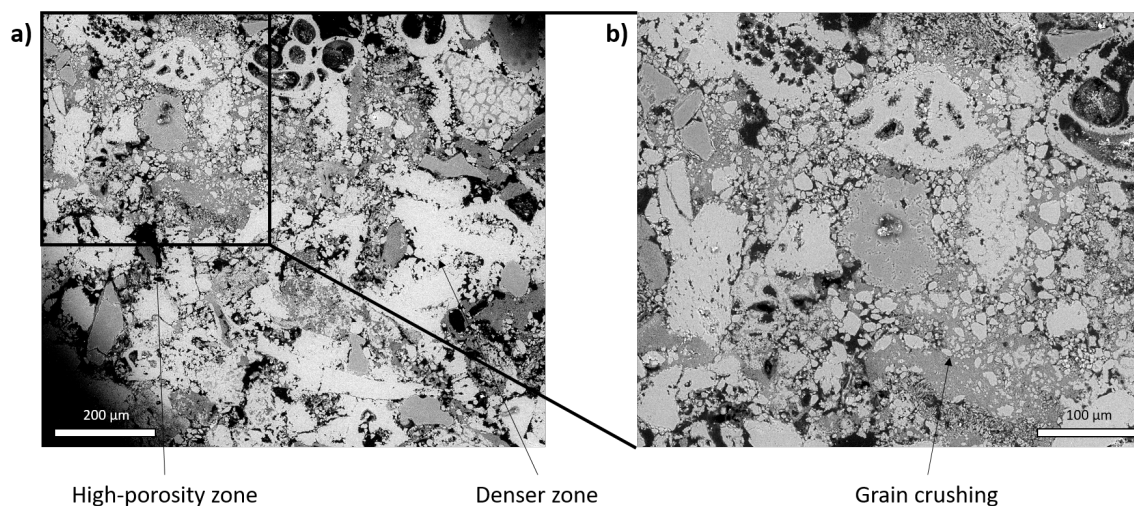


Figure 5.16: BSE image of the SML sample, tested under hydrostatic loading: **a)** Contrast between high- and low-porosity zones; **b)** Pervasive calcite grain crushing and pore filling.

5.4 Triaxial test under high confining pressure

A SML sample with an overall porosity of 37.7% has been tested under a relatively high confining pressure of 10.5 MPa. Again, the sample is imaged by XRCT three times. Figure 5.18 presents the shear stress intensity vs axial strain measured by means of the two axial LVDTs disposed around the sample.

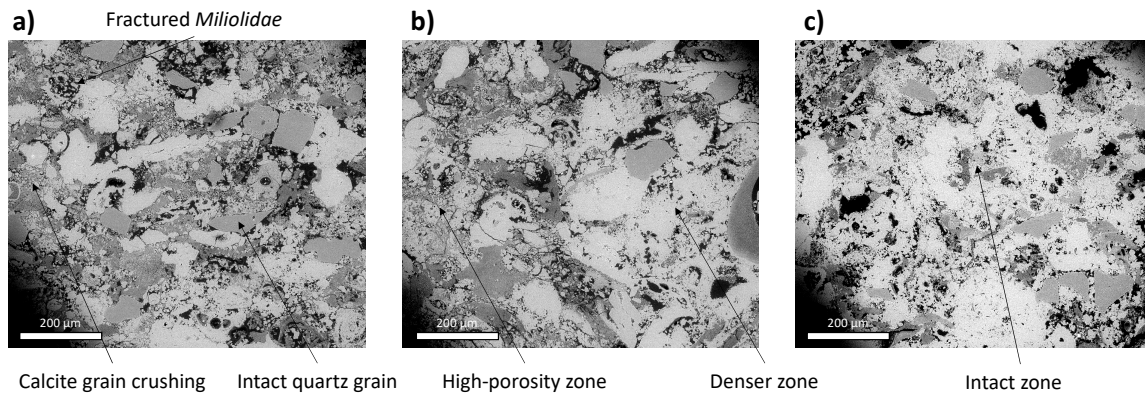


Figure 5.17: BSE image of the SML sample, tested under hydrostatic loading: **a)** Pervasive calcite grain crushing and pore filling with intact quartz grains in high-porosity zones; **b)** Contrast between high-porosity and low-porosity zones; **c)** Undeformed microstructure in low-porosity zones.

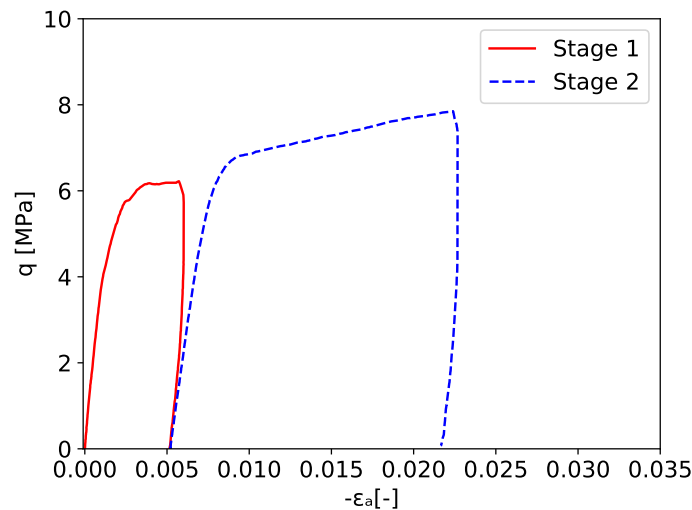


Figure 5.18: A SML sample tested in triaxial conditions under 10.5 MPa of confining pressure.

5.4.1 Initial state

Figure 5.19 shows a vertical cross-section of the 3D XRCT image and its porosity map in the initial state. The porosity fluctuates between around 30% and 45% at the scale of one centimeter in consistency with the previous observations on the sample tested under hydrostatic loading (Figure 5.5) and the results of the section 3.3.2. Several large pores (with sizes up to 2 mm) can be identified inside the denser zones (on the left part in Figure 5.19).

5.4.2 First loading stage

In the first stage, loading is stopped just after the plasticity onset (Figure 5.18). This state corresponds to the critical mean pressure C^* , which is found equal to 13.35 MPa in the

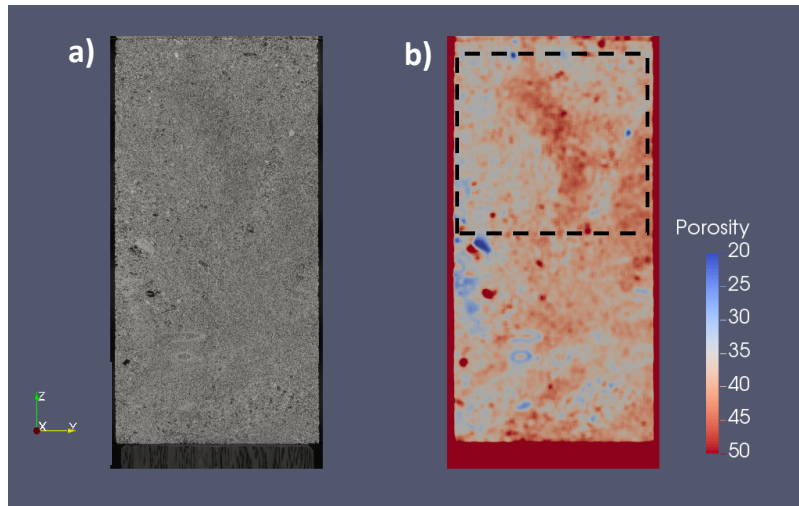


Figure 5.19: The SML sample imaged before being tested in axisymmetric triaxial loading under 10.5 MPa of confining pressure: YZ middle cross-section of the XRCT image and the porosity map. The dashed window represents the zone over which the porosity histogram will be computed in next chapter.

current experiment (Figure 5.3). The residual axial strain measured by the LVDTs is 0.5%, while 0.47% is assessed from the DVC map. Figures 5.20 and 5.21 show several vertical cross sections of the incremental volumetric strain map, parallel to the YZ and XZ planes respectively. After the plasticity onset, several strain localization bands are identified in the middle and upper part of the sample. These bands have high-angle inclinations with respect to the maximum (in absolute value) principal stress direction. They have a quasi planar shape with a normal vector included in a YZ plane. Their thicknesses vary from 1 to 6 mm (1 to 6 elements). In addition, some boundary effects are observed at both ends of the sample. Indeed, some conjugate shear bands are formed at the top boundary, but they are less developed at the bottom. The compaction evaluated inside these bands can reach 6%, whereas the remaining zones of the sample undergo a very low strain level.

Deformation bands are observed to lay inside more porous zones (mean porosity $\phi = 44\%$), whereas denser zones (mean porosity $\phi = 33\%$) seem to remain undeformed (Figure 5.22). The pattern of strain localization bands is controlled by porosity fluctuations at the scale of one centimeter (Figures 5.24 a, b, c and d). The different orientations of the bands inside the same sample can be linked to the heterogeneity of porosity. When it propagates, a band avoids denser zones and follows a path inside more porous ones, where densification takes place. For instance, a high-porosity zone is selected in Figure 5.22 and the corresponding histograms of porosity before and after loading are shown in Figure 5.23. It is observed that the porosity drops from around 41.5% to about 38.2% after the localization of deformation, a very comparable value to the mean volumetric strain evaluated at 3.5% inside the same zone using Paraview.

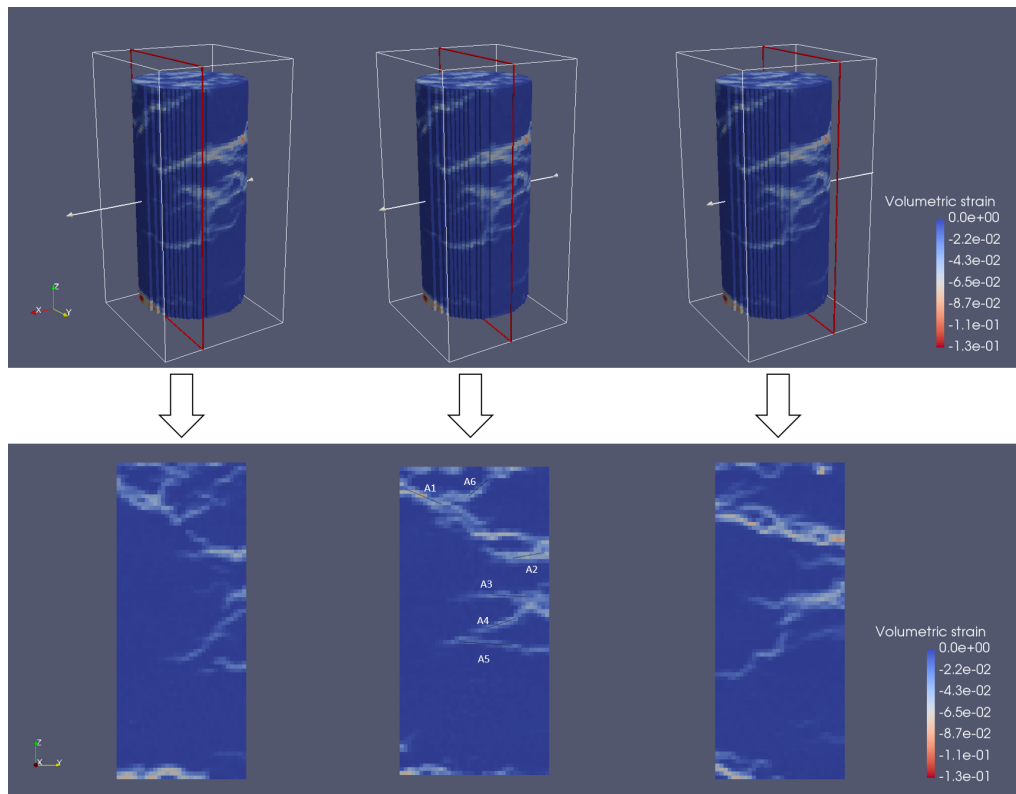


Figure 5.20: The incremental volumetric strain map for the first loading stage of the SML sample tested under high confinement: 3D view and vertical cross sections parallel to the YZ plane. The deformation bands A1 to A6 are selected on the middle section and tangent planes are defined.

A comparison of the XRCT images before and after loading corroborate these observations: a local densification is observed inside the deformation bands (Figure 5.24 g and h), whereas several large pores (up to 3 mm in diameter) remain unchanged (Figure 5.24e-f). Similarly to the observations performed on the sample tested under hydrostatic loading, these pores are present in denser zones and are protected by the rigid matrix of cemented grains around. In conclusion, the porosity heterogeneity at the scale of one centimeter again seems to control the path of deformation bands, whereas the pore size is not observed to have a dominant effect on the strain heterogeneity.

Several deformation bands are selected on the YZ middle section of the DVC map, denoted by A1 to A6 in Figure 5.20. A tangent plane is found for each of these bands and a normal vector is thus defined (for instance, see Figure 4.7 in Chapter 4). Following the steps of the method described in section 4.4.2, the values of the normalized scalar product (*NSP*) of the bands are evaluated. In addition to these results, Table 5.2 summarizes the orientation in absolute value with respect to the maximum principal stress direction (axis of the sample) and the deduced types of the bands. Except for band A6, values of the *NSP* are between -1 and -0.9 indicating that they are of pure compaction type. Their angles with respect to the axial direction are higher than 70°. In contrast, the conic shape, the low angle and

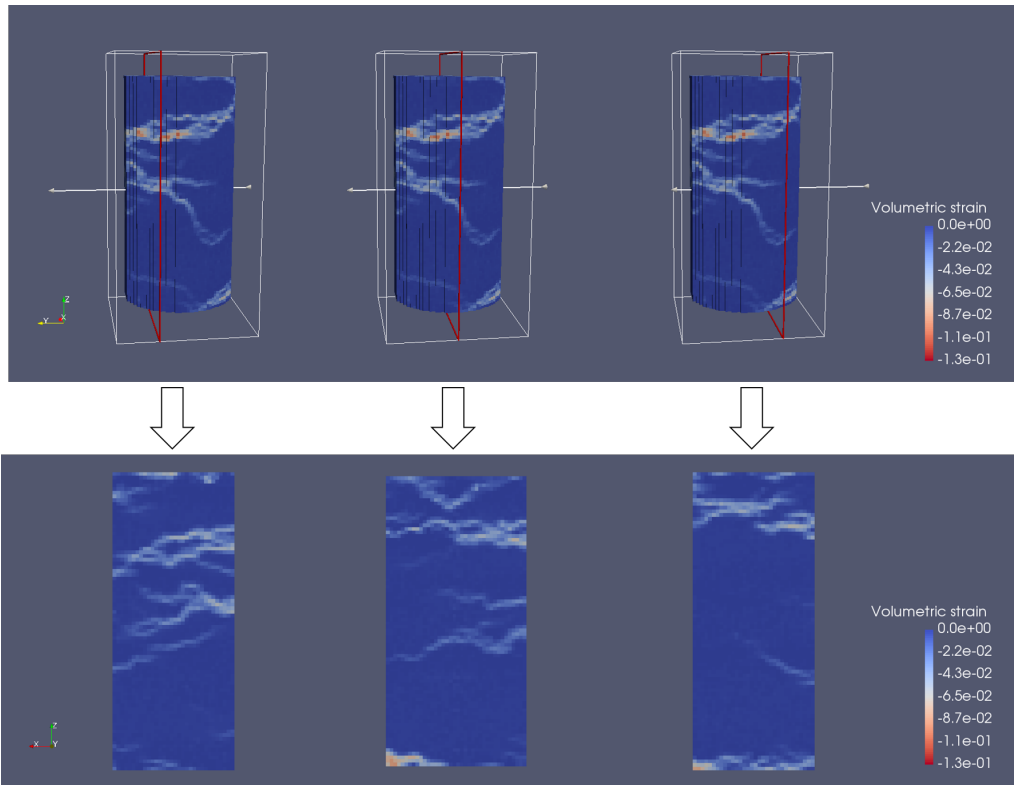


Figure 5.21: The incremental volumetric strain map for the first loading stage of the SML sample tested under high confinement: 3D view and vertical cross sections parallel to the XZ plane.

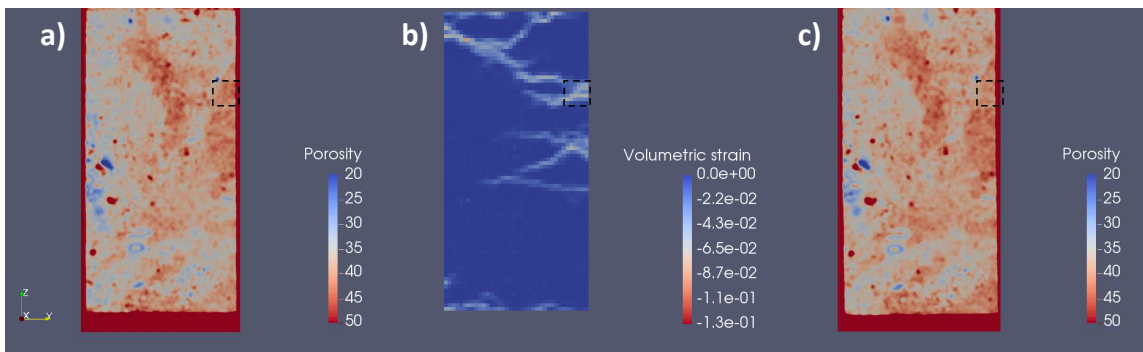


Figure 5.22: Vertical cross-sections at the middle of the SML sample tested under high confining pressure: a)-c) Porosity maps in the initial state and after the first loading stage; b) Incremental volumetric strain.

value of $NSP = -0.82$ suggest that A6 is a compactive shear band and seems to be induced by boundary effects.

5.4.3 Second loading stage

In the second stage, an overall hardening is observed and a residual axial strain of 2.15% is measured from LVDTs (Figure 5.18), while the cumulative average value from the DVC map is 2.1%. Figures 5.25 and 5.26 show the 3D view and vertical cross sections of the

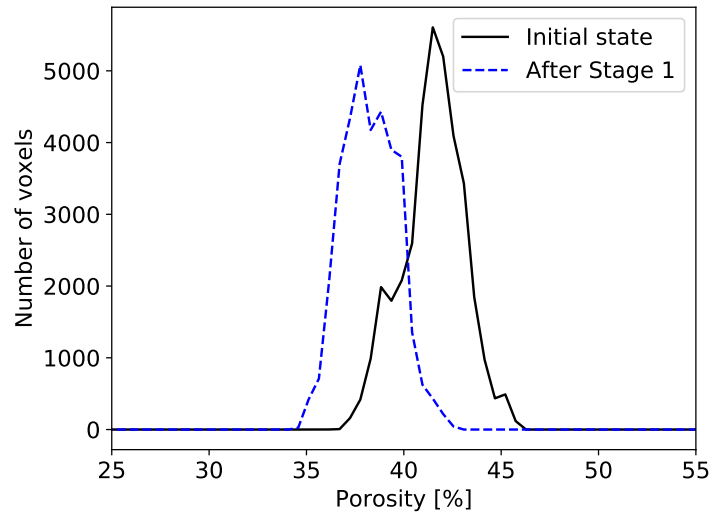


Figure 5.23: Histograms of porosity for the selected zones in Figure 5.22.

Table 5.2: Band types and orientations θ (in absolute value) with respect to the axial direction in the sample tested at high confining pressure (10.5 MPa) after the first and second loading stages.

	Band	NSP^{band}	θ°	Type
After Stage 1 of loading	A1	-0.91	69.9	Compaction band
	A2	-0.91	80.5	Compaction band
	A3	-0.97	84.1	Compaction band
	A4	-0.94	68.2	Compaction band
	A5	-0.94	83.2	Compaction band
	A6	-0.82	48.2	Compactive shear band
After Stage 2 of loading	A7	-0.84	56.3	Compactive shear band
	A8	-0.98	71.6	Compaction band
	A9	-0.94	63.4	Compaction band

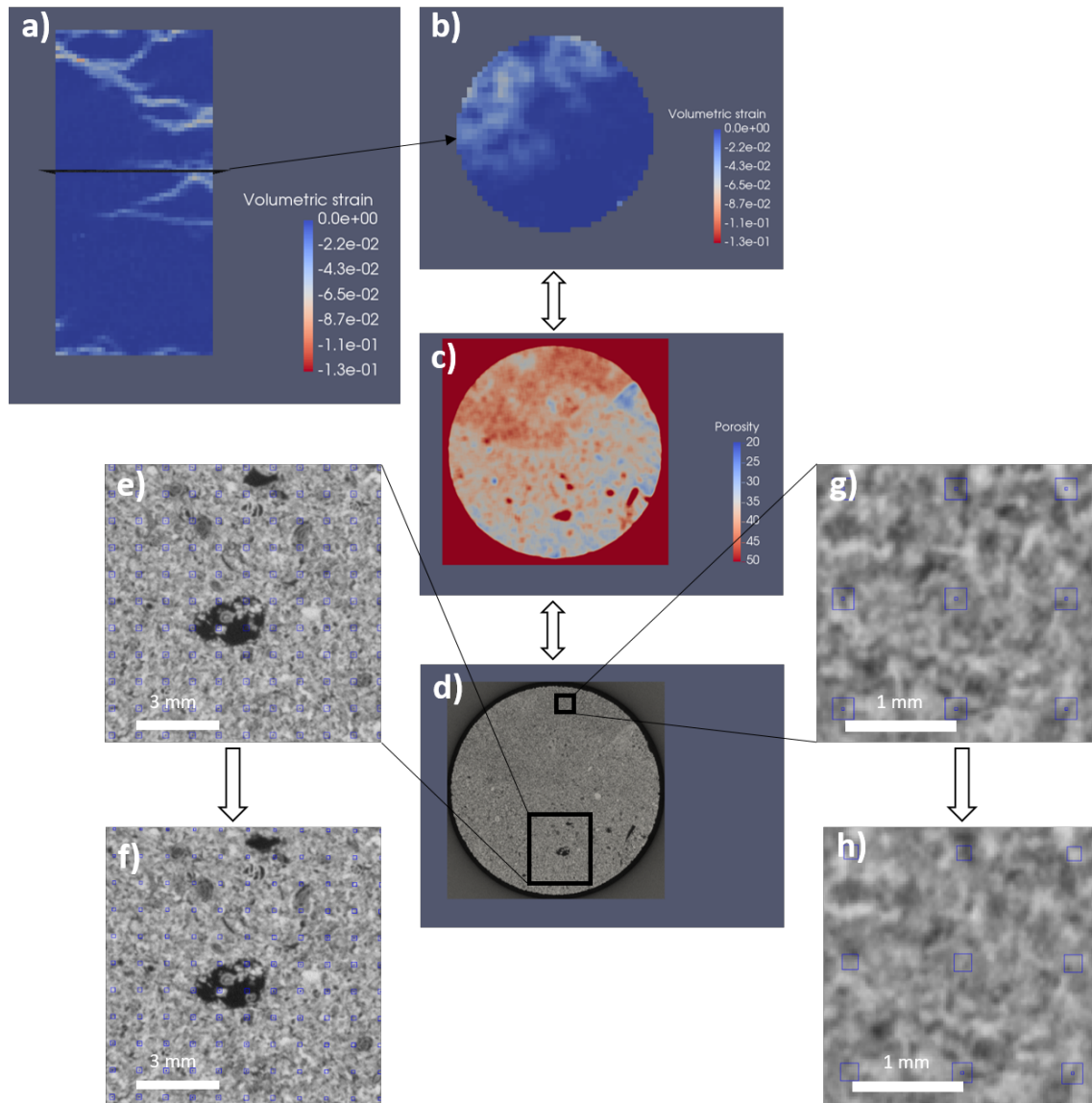


Figure 5.24: The SML sample tested in axisymmetric triaxial loading under high confining pressure: **a)** Vertical cross-section of the incremental volumetric strain map during the first loading stage; **b)-c)-d)** Transverse cross-section showing a heterogeneity of deformation and the corresponding planes of the porosity map and the XRCT image in the initial state; **e)-f)** A large pore laying in a low-porosity zone before and after the first loading stage; **g)-h)** A high-porosity zone in the initial state and after being compacted during the first loading stage.

incremental volumetric strain map, parallel to the YZ and XZ planes respectively. The strain continues to localize inside the previously formed bands (in Stage 1). In addition, the zones of compaction bands become thicker while applying further loading. Several new bands are detected, which coalesce together and form thicker zones of compaction. The new formed bands have the same orientation as in the first stage. At the borders, highly damaged zones are observed where diffuse compaction occurs due to a possible boundary effect in the triaxial experiment. The increment of compaction evaluated inside the deformation bands can reach 7%, whereas the remaining zones of the sample exhibit a very low strain amount (less than 0.5%).

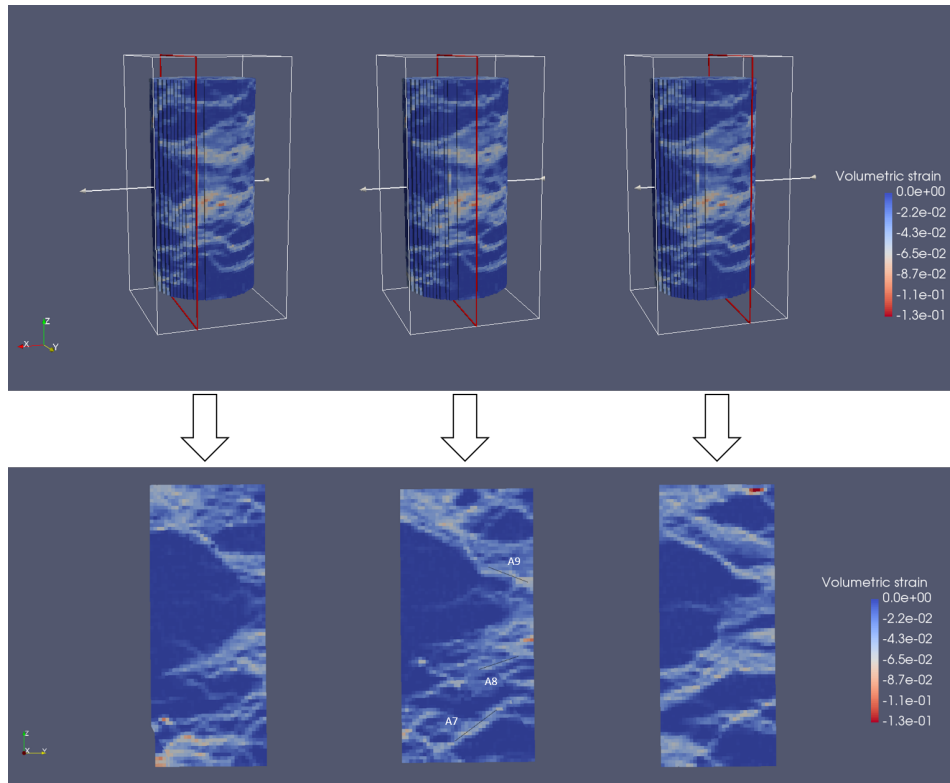


Figure 5.25: The incremental volumetric strain map for the second loading stage of the SML sample tested under high confinement: 3D view and vertical cross sections parallel to the YZ plane. The deformation bands A7 to A9 are selected on the middle section and tangent planes are defined.

Figure 5.27 shows several transverse cross-sections of the incremental volumetric strain and the corresponding initial porosity sections at different levels along the axis of the sample. Figures 5.27 (a, b and c) make evidence of the role of the porosity heterogeneity in controlling the deformation band paths. The bands are observed to propagate inside high-porosity zones, while denser zones remain intact. The same result is obtained when inspecting a section in the bottom part of the sample (Figure 5.27e). The band passes between two low-porosity zones and propagate inside a more porous zone. The elements of the section shown in Figure 5.27c are considered now, where the volumetric strain is plotted against the porosity in the reference state (Figure 5.28). High levels of strain are observed in high-porosity zones, whereas low-porosity zones are almost undeformed. However, a volumetric compaction can be observed in some low-porosity zones, as the band may cross a denser zone in some cases to connect the high-porosity zones.

A vertical cross-section allows to corroborate the previous observations (Figure 5.29). Deformation bands are observed on the right part of the sample, where a high porosity zone is present, despite the existence of many large pores in the denser zones on the left part of the sample. These pores remain intact after loading. The porosity is observed to decrease in high-porosity zones. For instance, the porosity drops from 42% to 38% in the zone marked

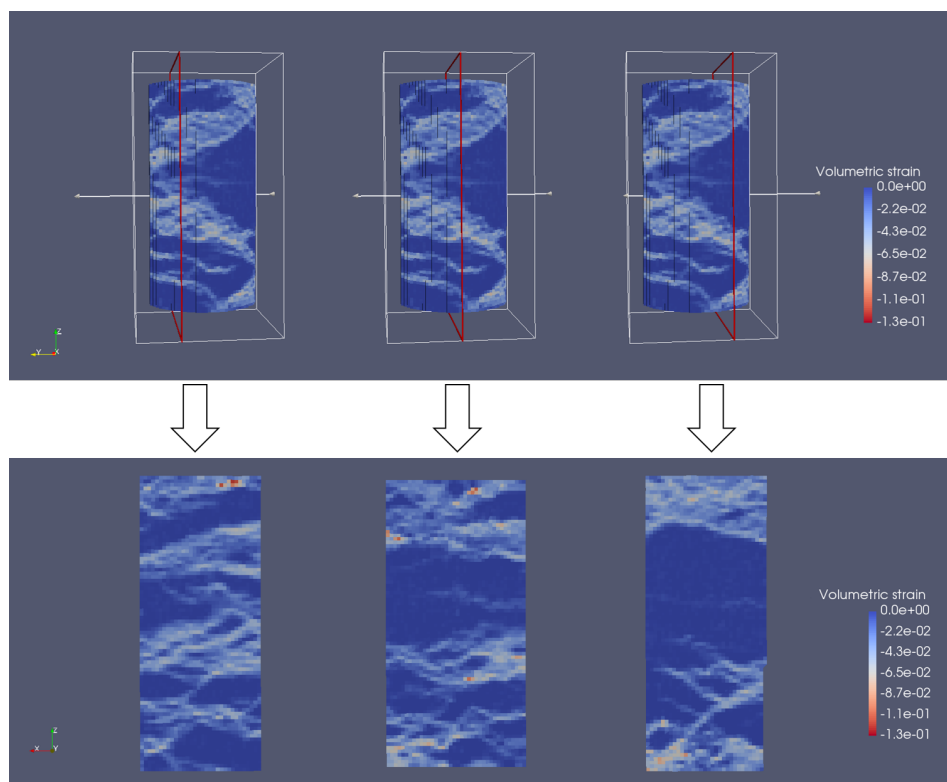


Figure 5.26: The incremental volumetric strain map for the second loading stage of the SML sample tested under high confinement: 3D view and vertical cross sections parallel to the XZ plane.

by a black arrow in Figure 5.29. The porosity reduction is again equivalent to the evaluated volumetric strain on the DVC deformation map.

In Figure 5.30, the microstructure of the rock is presented in two configurations: before and after the second loading stage. The denser zone (at the left part of the section in Figure 5.30c) is undeformed despite the presence of many large pores. An elongated macropore, having one side length of 2 mm is shown in Figure 5.30d before loading. This pore remains undeformed after loading (Figure 5.30e). On the other hand, the deformation bands pass through the high-porosity zones on the right part of the section. Pore size reduction (Figures 5.30 f and g) and global densification (Figures 5.30 h and i) are observed inside these zones.

The type of the deformation bands is then studied. The strain localization bands formed during the first loading stage have been identified as compaction bands, except those near the boundaries. Since the bands have coalesced in the second loading stage and thick zones of localized deformation have formed, it is difficult to define a discrete band. However, three distinct bands have been selected on the middle section parallel to the YZ plane denoted by A7 to A9 in Figure 5.25. Table 5.2 summarizes the analyses performed on these bands. High-angle bands ($\theta > 63^\circ$) are found to be highly compactive ($NSP < -0.9$). On the other hand, A7 has an orientation of 56.3° and has a value of $NSP > -0.9$. A conic shape is also

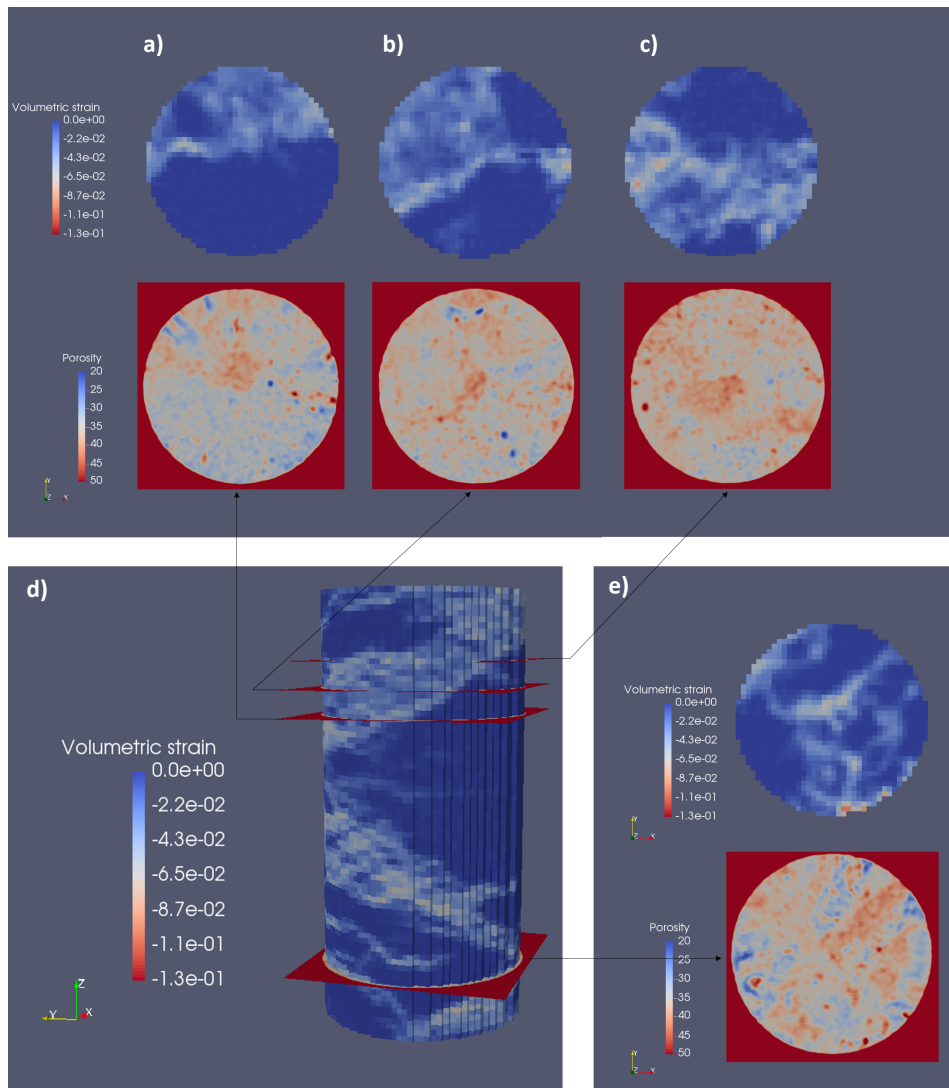


Figure 5.27: Transverse cross-sections showing the initial porosity (after Stage 1 of loading) and the incremental volumetric strain during the second loading stage at different levels along the axis of the SML sample tested under high confinement.

found to appear at the bottom part of the sample (see the middle section in Figure 5.26) suggesting that A7 is a compactive shear band induced by boundary effects. In summary, following the classification presented in Table 5.2, a compaction band is defined when $NSP < -0.9$ and $\theta > 60^\circ$. These bands appear in the central part of the sample, whereas compactive shear bands having a conic shape near the borders are induced by boundary effects.

5.4.4 Thin section observations

Again, a thin section, prepared after the second loading stage, is observed under SEM using the BSE mode. Several zones are selected on the middle vertical cross-section of the

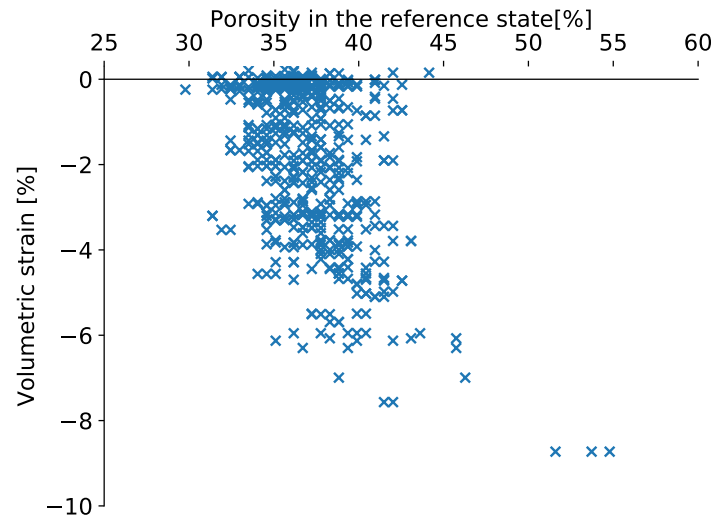


Figure 5.28: Volumetric strain vs porosity in the reference state for all the elements of the section shown in Figure 5.27c.

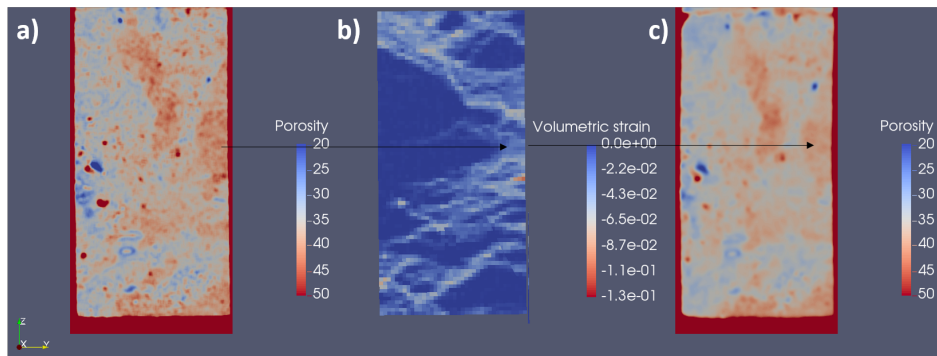


Figure 5.29: Vertical cross-sections at the middle of the sample tested under high confinement: a) Porosity map before the second loading stage b) the incremental volumetric strain map during the second loading stage; c) Porosity map after the second loading stage.

volumetric strain map³ (Figure 5.31a). Figure 5.31b shows the contrast between an intact zone and a compaction band passing through an initial high-porosity zone. A large pore of 200 μm in size is undeformed in the denser zone, whereas a pervasive grain crushing is observed inside compacted zones (see also Figure 5.31c). The large and cemented grains work as barriers to the compaction bands propagation (Figure 5.31 d and f). Inside the compacted zones, calcite grains are crushed, whereas quartz grains remain intact, in consistency with Baud et al. (2017a) observations. A pervasive grain crushing occurs, fine powders of diameters less than 1 μm are formed (Figure 5.31h) and pores are then filled as shown in Figure 5.31g. In conclusion, the porosity reduction observed is due to the calcite grain crushing mechanism and the pore space is reduced by induced fines.

³These selections are qualitative, as the SEM observations may not correspond precisely to the positions marked on the DVC map.

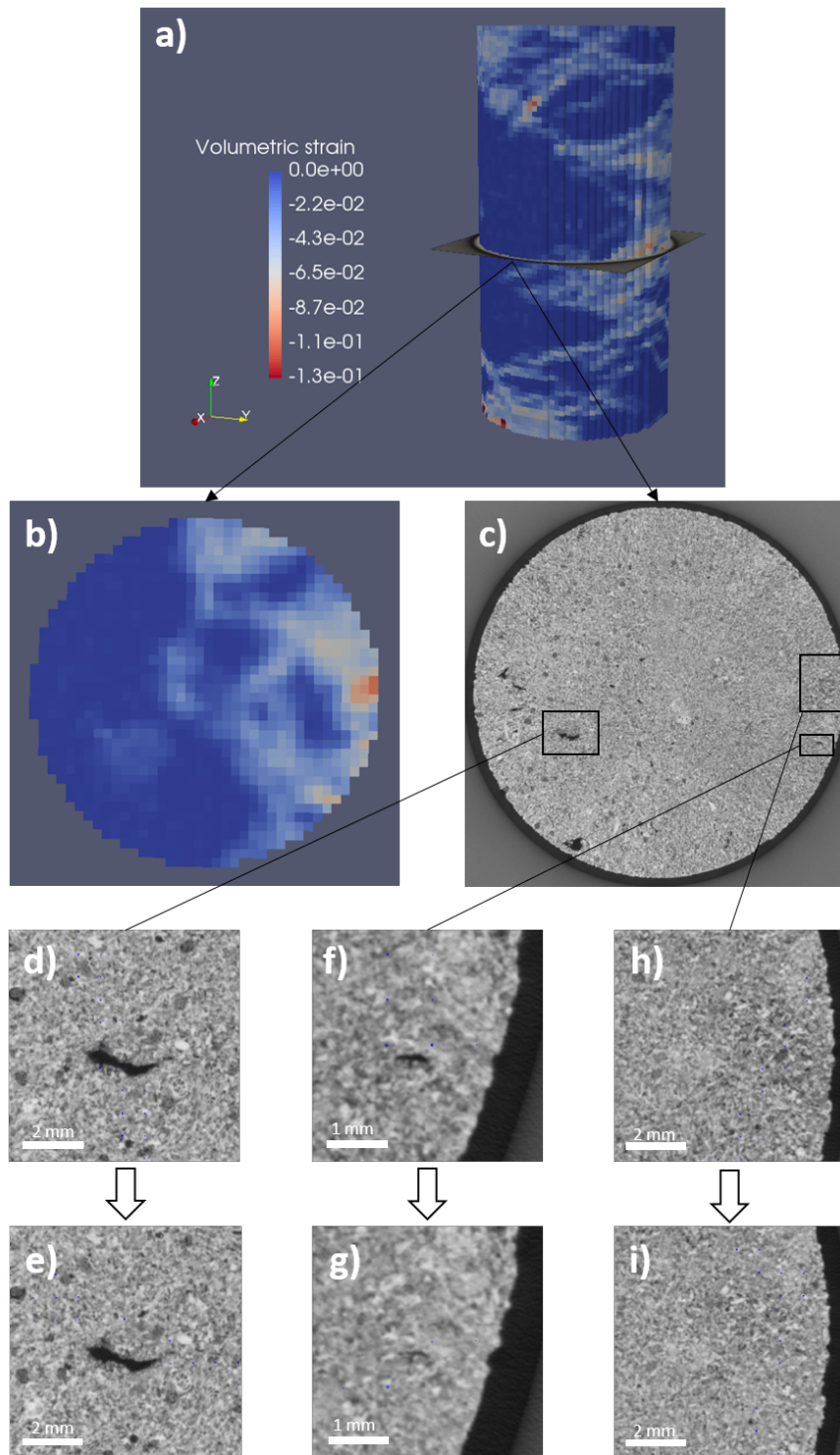


Figure 5.30: The SML sample tested in axisymmetric triaxial loading under high confining pressure: **a)** The incremental volumetric strain map during the second stage of loading; **b)-c)** A transverse cross-section of the volumetric strain map and the corresponding plane of the XRCT image before loading; **d)-e)** A macropore laying in a denser zone before and after the second loading stage; **f)-g)** A macropore in a high-porosity zone before and after the second loading stage; **h)-g)** A high-porosity zone before and after the second loading stage.

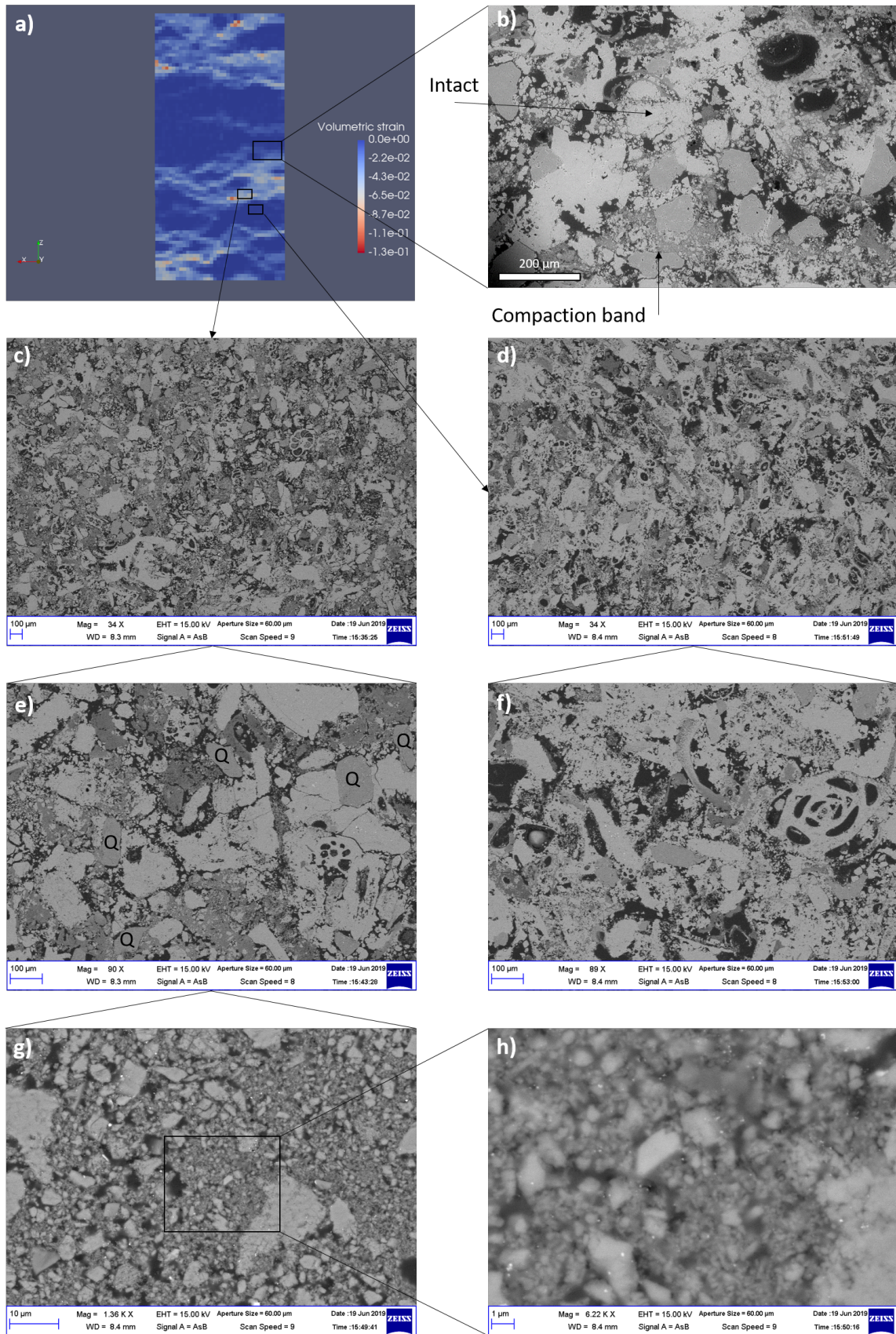


Figure 5.31: The SML sample tested under high confinement: a) Middle cross-section of the incremental volumetric strain map during the second loading stage; b) BSE image showing the contrast between intact and compacted zones; c) Zone of compaction bands; d) Intact zone; e) Zone of compaction bands (Q for quartz grains); f) Intact zone; g) Grain crushing and pore filling; h) Fine powders filling the pores.

5.5 Triaxial test under low confining pressure

A SML sample having an overall porosity of 37.9% is now tested under a relatively low confining pressure of 1.5 MPa. Figure 5.32 presents the shear stress intensity vs axial strain for the two loading stages. The softening occurring after the peak stress is less pronounced in this experiment in comparison with the sample tested under 1 MPa of confining pressure presented in Figure 5.1b.

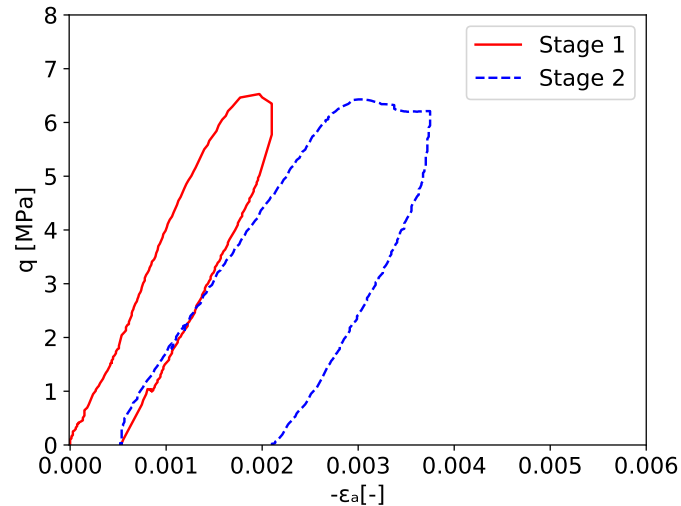


Figure 5.32: A SML sample tested in triaxial conditions under relatively low confining pressure (1.5 MPa).

5.5.1 Initial state

Figure 5.33 shows a vertical cross-section of the 3D XRCT image and its porosity map. The porosity of this sample is more heterogeneous than in previous samples. A zone of high density (20% of porosity) is observed on the upper part of the sample. Several zones of high-porosity (more than 40% and up to 46%) are separated by less porous zones (around 33%) in the sample. The length scale of the porosity heterogeneity is also in the order of one centimeter, similarly to the previously presented samples.

5.5.2 First loading stage

In the first stage, loading is stopped at the peak stress, evaluated at a shear stress intensity $q=6.5$ MPa (equivalent to 12.8 MPa of axial loading) as shown in Figure 5.32. The residual axial strain is evaluated at 0.05% from the LVDTs and at 0.035% from the DVC map. Figure 5.34 shows several vertical cross sections of the incremental shear strain magnitude map

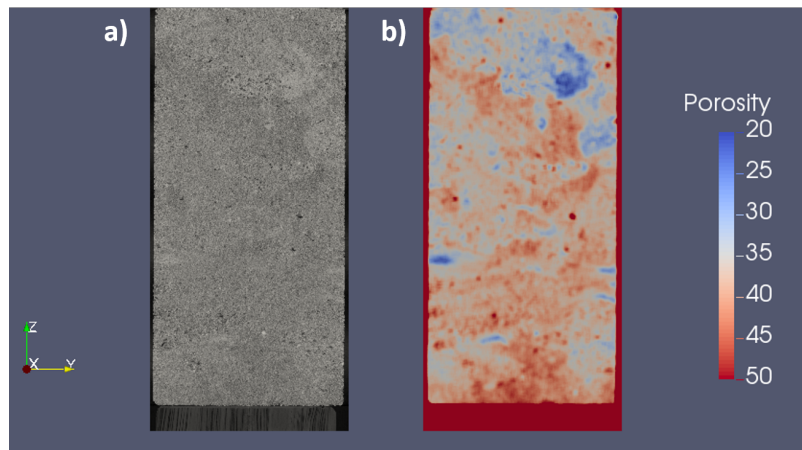


Figure 5.33: A SML sample in the initial state before being tested in axisymmetric triaxial loading under relatively low confining pressure: **a)-b)** YZ middle cross-section of the XRCT image and the corresponding porosity map.

parallel to the XZ plane. The peak stress occurs when two conjugate strain localization bands develop at the bottom of the sample. The two bands, whose thicknesses are around 2 mm, are nearly perpendicular and have orientations of 52.4° and 43.2° with respect to the maximum principal stress direction respectively. The shear strain magnitude inside the bands can go up to 6%, whereas very low strain levels are assessed in the remaining zones of the sample (less than 0.1%).

On the other hand, the volumetric strain map shows a complex kinematic behavior inside the bands. When compared with the shear strain magnitude map, compaction and dilation are found to alternate along a single band (Figure 5.35 b and c). In order to explore a possible role of the porosity in the volumetric strain heterogeneity, a cross-section corresponding to the same plane in the initial state is shown in Figure 5.35a. In contrast to the observations of the two previous loading cases, deformation bands at low confinement are observed to cross both high- and low-porosity zones. Dilation is observed to occur in low-porosity zones (black arrow in Figure 5.35), suggesting a crack opening induced by shearing. However, compactive volumetric strain is observed in more porous zones (white arrow in Figure 5.35). These results are clearly highlighted in Figure 5.36 as several transverse cross-sections are shown. Moreover, the elements having a volumetric strain higher than 1% (in absolute value) in the cross-section shown in Figure 5.36b are selected. Then, the volumetric strain is plotted against the initial porosity in Figure 5.37. Dilatancy is observed in zones where porosity is lower than 40%, whereas high-porosity zones undergo a compactive behavior.

A mechanism of shearing is identified in Figure 5.38, as the zone on the left of the deformation band is moving relative to the zone on its right, in a tangent direction to the band plane. The displacement direction of the zone on the left to the band is marked by three arrows. In Figure 5.38c, the out-of-plane displacement is shown with respect to the

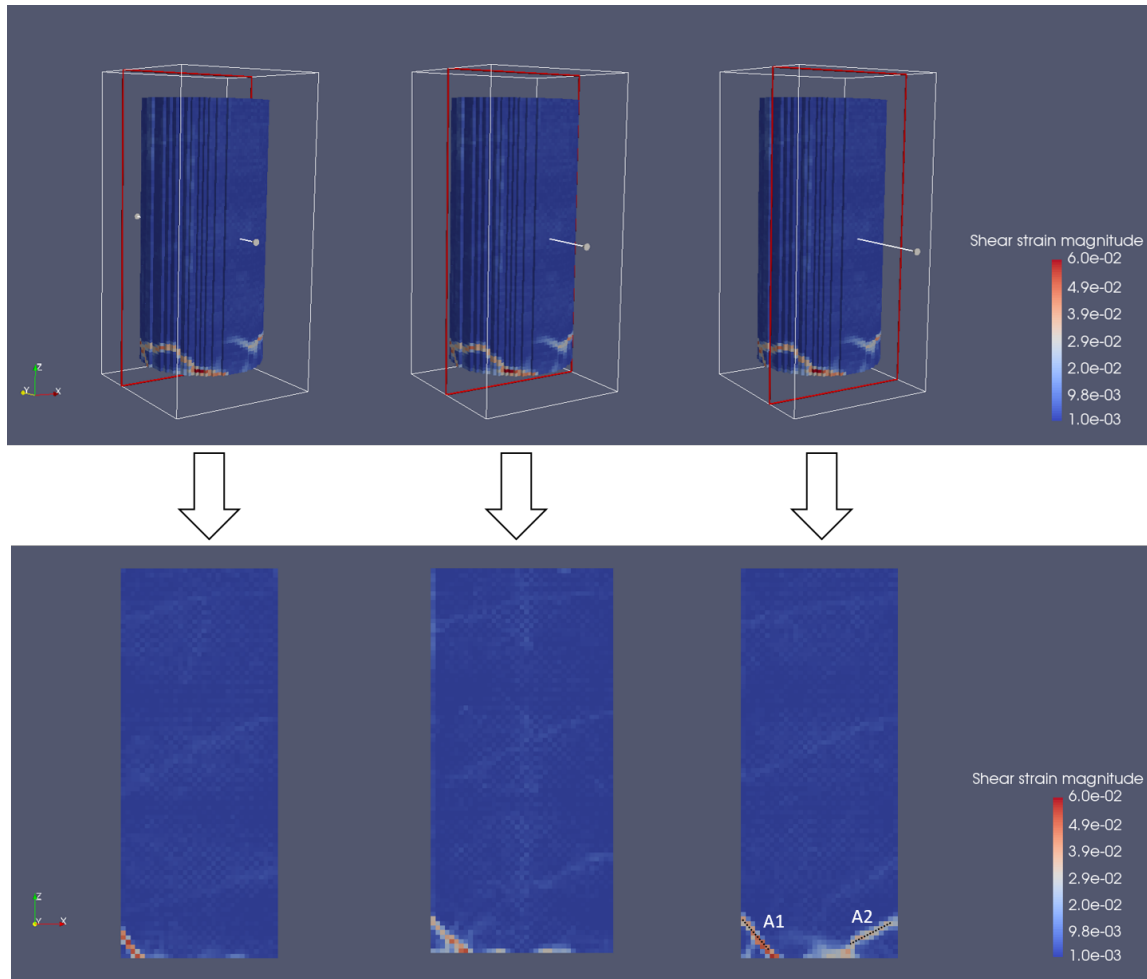


Figure 5.34: The incremental shear strain magnitude map for the first loading stage of the SML sample tested under low confining pressure (1.5 MPa): 3D view and vertical cross sections parallel to the XZ plane. A1 and A2 are two selected deformation bands.

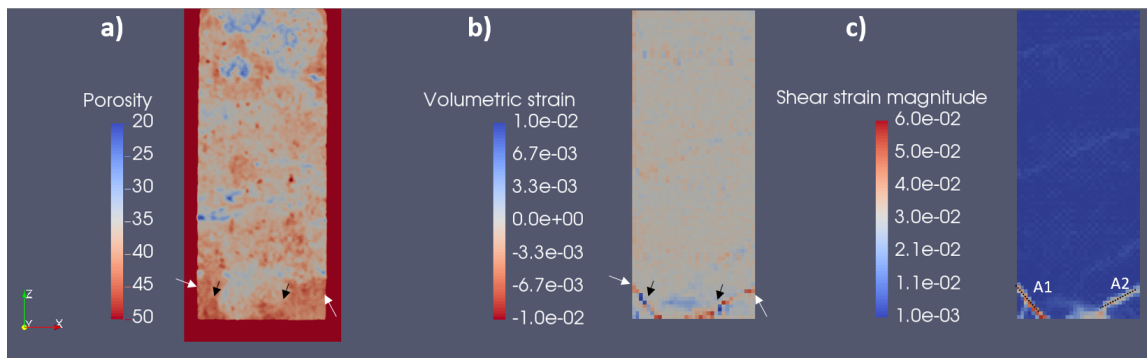


Figure 5.35: Vertical cross-sections parallel to the XZ plane of the SML sample tested under low confining pressure: **a)** Porosity map in the initial state; **b)** Incremental volumetric strain; **c)** Incremental shear strain magnitude.

initial configuration (Figure 5.38b). In addition, a crack with an opening of about 4 voxels (*i.e.* about $100 \mu\text{m}$), can be observed (marked by a white arrow). This crack causes the local dilatancy observed inside the band.

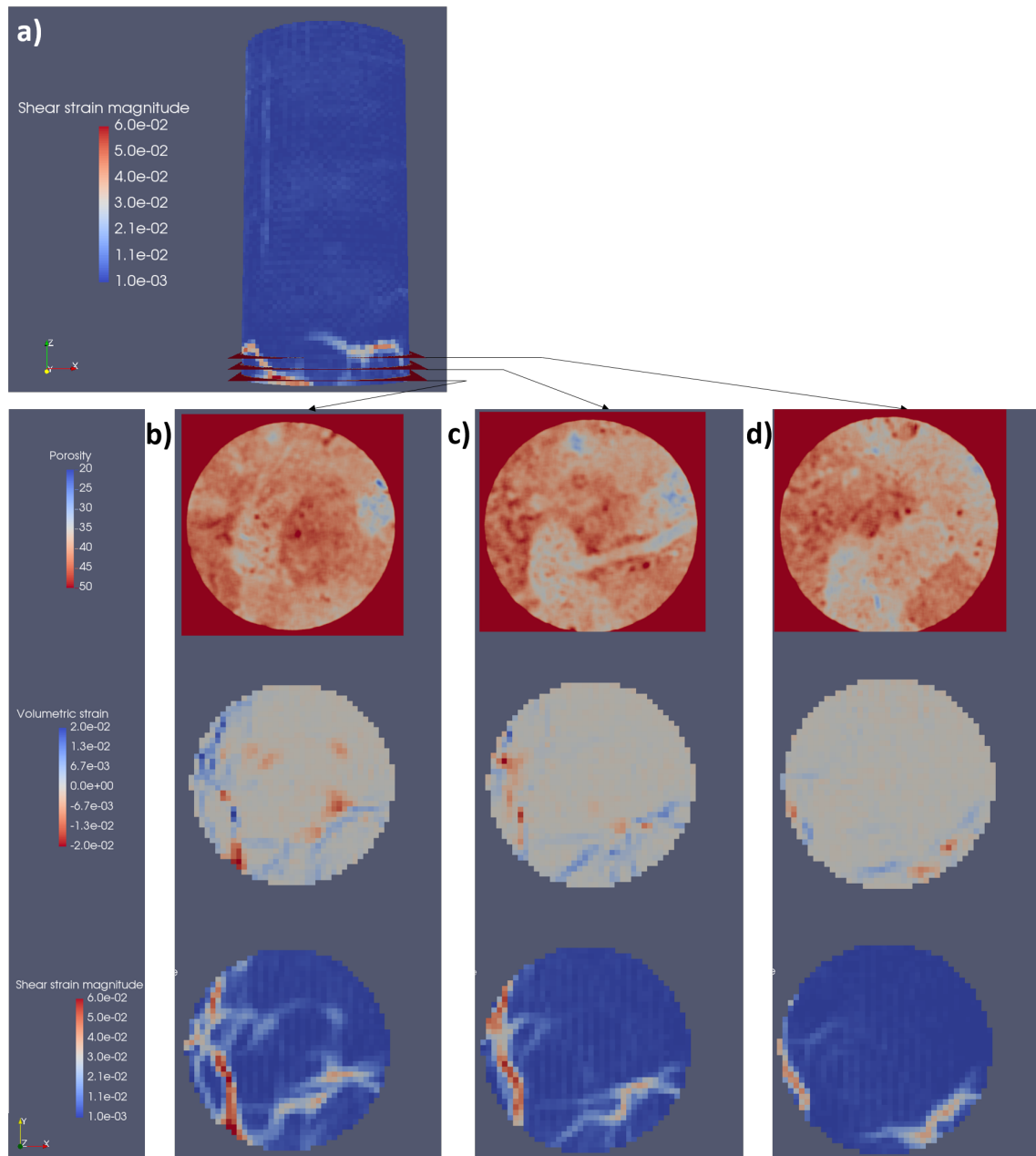


Figure 5.36: a) The incremental shear strain magnitude of the SML sample tested under low confining pressure during the first loading stage; b) - c) - d) Transverse cross-sections of the porosity map in the initial state, the volumetric strain and the shear strain magnitude maps at different levels along the sample axis z .

Two deformation bands are selected after the first loading stage and are denoted by A1 and A2 as shown on the section XZ in Figure 5.34. The type of these bands is studied and results are gathered in Table 5.3. As already mentioned, these two bands are almost perpendicular. The mean value of the NSP over the elements crossed by the black dashed line in band A1 (Figure 5.34) is found to be 0.07. Thus, the band is identified as a pure shear band. However, local compaction and dilation are identified inside this band (Figure 5.35b-c). The NSP evaluated for each element along the central line of the band A1 is depicted in

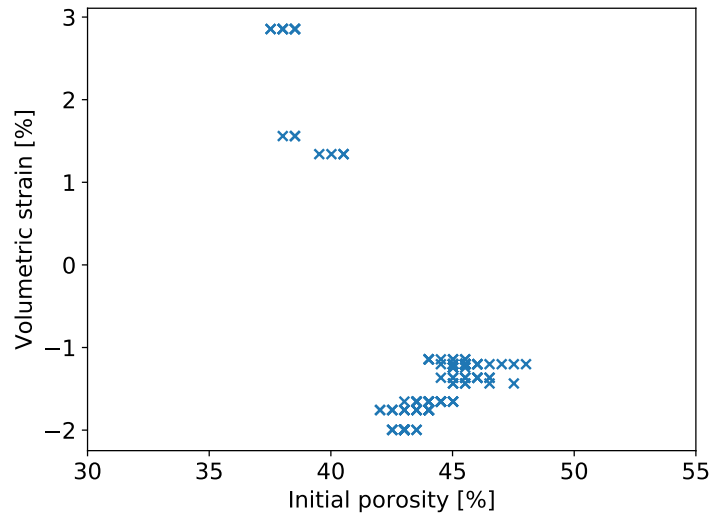


Figure 5.37: Volumetric strain vs initial porosity for some elements of the section shown in Figure 5.36b.

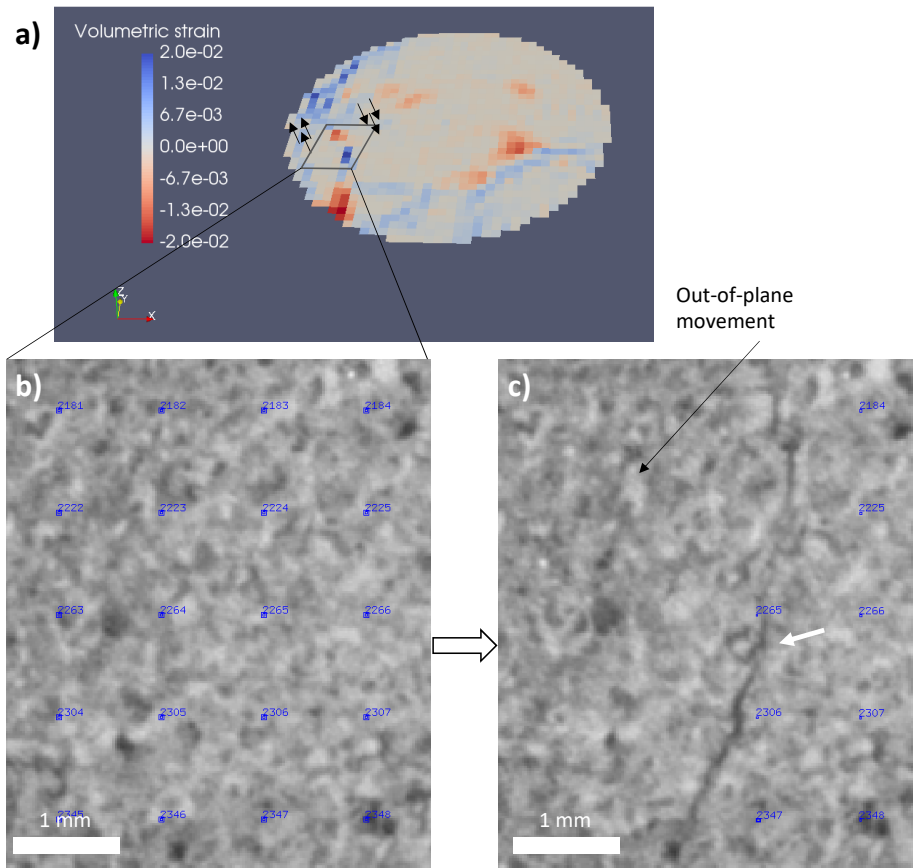


Figure 5.38: The SML sample tested under low confining pressure during the first loading stage: a) Transverse cross-sections showing the volumetric strain map; b)-c) A focus on a zone before and after being crossed by the deformation band: an out-of-plane displacement is identified and a crack is formed (marked by a white arrow).

Table 5.3: Band types and orientations θ (in absolute value) with respect to the axial direction of the sample tested at low confining pressure (1.5 MPa) after the first and second loading stages.

	Band	NSP^{band}	θ°	Type
After Stage 1 of loading	A1	0.07	52.4	Pure shear band
	A2	-0.17	43.2	Compactive shear band
After Stage 2 of loading	A2	-0.19	46.0	Compactive shear band
	A3	0.16	34.6	dilatant shear band

Figure 5.39. The values fluctuate between -0.3 and 0.3 at a wave length of about 5 mm. Therefore, the band changes locally its type from dilatant shear band to compactive shear band once it crosses a high-porosity zone. As for the band A2, the compaction component is more important and the calculated NSP for the elements are more homogeneous (Figure 5.35 - Figure 5.39). The average value over all the elements is about -0.17 and the band A2 is therefore identified as a compactive shear band.

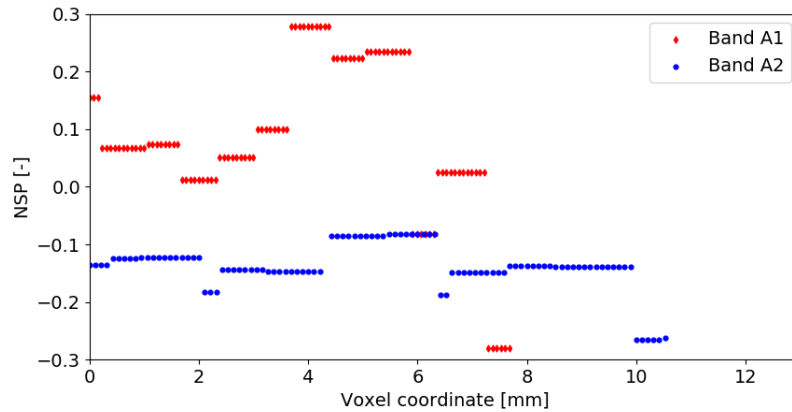


Figure 5.39: NSP calculated for each element along the central line of the deformation bands A1 and A2 in the SML sample tested under low confining pressure during the first loading stage.

5.5.3 Second loading stage

In the second stage, axial loading is resumed and a slight softening is observed to occur after the peak stress as shown in Figure 5.32. When the sample is unloaded, a residual axial strain of 0.2% is measured. It is worthwhile to remind that axial LVDTs cover only 5 cm of height and are disposed around the central zone of the sample. However, the shear bands are formed near the boundaries. Thus, the LVDT measurements do not give a good representation of the sample global deformation. From the DVC map, 0.29% of axial strain is indeed evaluated for this loading stage only, leading to a residual axial strain of 0.33%. Figure 5.40 shows the 3D view with several vertical cross sections of the incremental shear strain magnitude map obtained from DVC analysis, parallel to the XZ plane. Shear strain is still active in the previously formed band A2, which has preserved its thickness of 2 mm (2

elements). Moreover, a small piece under the band A1 has been strongly altered during the second loading stage and came off before imaging the sample by XRCT. These results suggest that a high level of stress - which corresponds to the peak stress in the macroscopic curves - is needed to trigger this strain localization process. Then, once shearing mechanisms are unblocked, sliding becomes easier. This behavior is manifested in the post-peak softening. On the other hand, new bands are detected, with thicknesses varying between 1 and 2 mm. A new band denoted by A3 is shown in Figure 5.40. It has an orientation of 34.6° with respect to the axial direction. The shear strain magnitude inside the bands can go up to 30%. A highly damaged zone is also observed near the bottom boundary, suggesting that stress concentration induced by boundary effects may have triggered the strain localization bands.

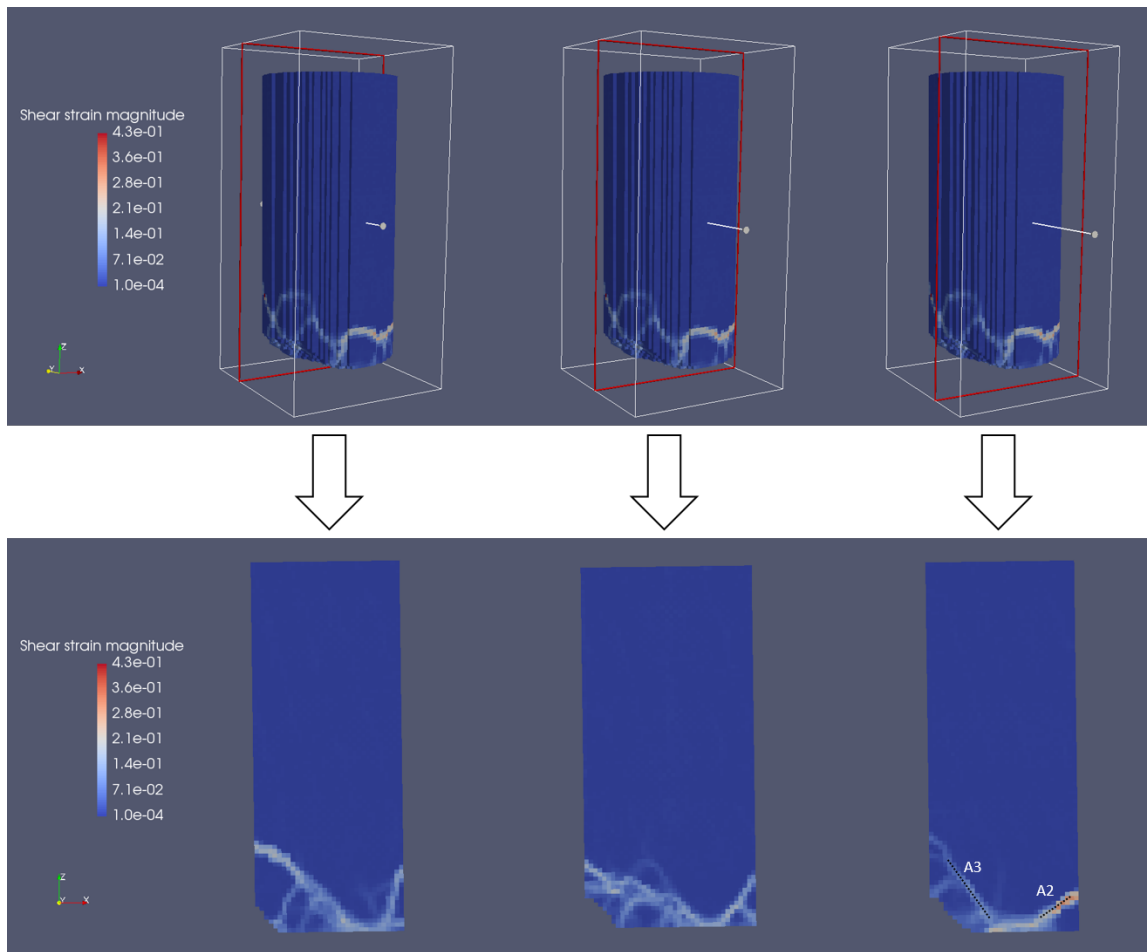


Figure 5.40: The incremental shear strain magnitude map for the second loading stage of the SML sample tested under low confining pressure (1.5 MPa): 3D view and several vertical cross sections parallel to the XZ plane. A2 and A3 are two selected deformation bands.

Again, the volumetric strain map makes evidence of a complex kinematic behavior inside the deformation bands (Figure 5.41 b and c). The role of the porosity in the volumetric strain heterogeneity is again explored, where a cross-section corresponding to the same plane in the initial state is shown in Figure 5.41a. In accordance with the observations

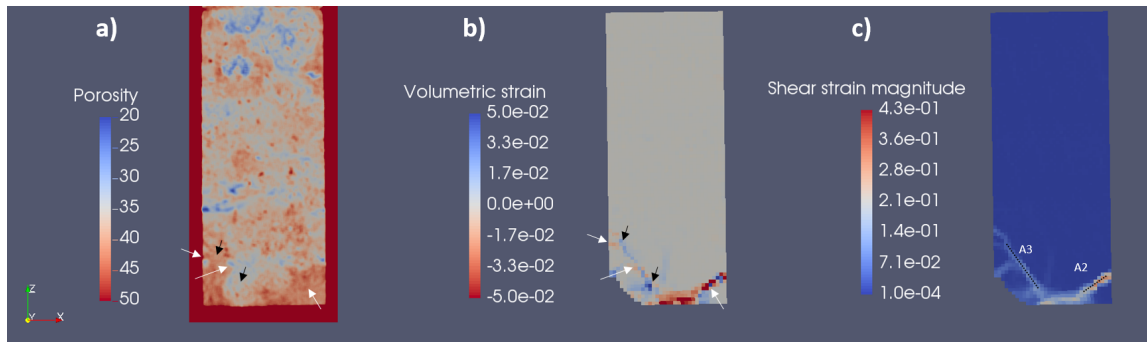


Figure 5.41: Vertical cross-sections parallel to the XZ plane of the SML sample tested under low confining pressure: **a)** Porosity map in the initial state; **b)** Incremental volumetric strain; **c)** Incremental shear strain magnitude. White arrows indicate zones of compaction, whereas black arrows indicate zones of dilation. A2 and A3 are two selected deformation bands.

performed in the first loading stage, deformation bands at low confinement cross both high- and low-porosity zones, where dilation is identified in low-porosity zones (black arrow in Figure 5.41) and compaction is observed in more porous zones (white arrow in Figure 5.41). Transverse cross-sections of the maps, presented in Figure 5.42b-c-d, corroborate the previous observations. The cross-section of the XRCT image after the second loading stage, presented in Figure 5.42f, reveals clearly the formation of many cracks in the low-porosity zones (marked in black arrows). These cracks had not been formed before this stage (Figure 5.42e). However, they disappear in high-porosity zones. Figure 5.42g focuses on the interface between a high- and low-porosity zone before being crossed by a deformation band. A crack, with about 2 voxels (48 μm) in opening, is clearly observed in the denser zone (Figure 5.42h). This crack is in contact with a high-porosity zone, which has been compacted. Similarly to the first stage, the volumetric strain is plotted against the reference porosity for the elements of the section shown in Figure 5.42 and for which the absolute value of volumetric strain is higher than 1%. The results presented in Figure 5.43 show a compactive behavior for zones of porosities higher than 40%, and *vice versa*.

The type of the deformation bands is then studied. Unfortunately, because of the broken piece, the deformation band A1 cannot be identified on the DVC maps during the second loading stage. Two deformation bands are selected: the band A2 (identical to the band selected in the first loading stage) and a band denoted by A3, shown in Figure 5.40. The results are presented in Table 5.3. The band A2 seems to preserve its nature, as a very close *NSP* is obtained (-0.19 in comparison with -0.17 in the first stage), with a very close orientation and thickness. The band A2 is thus still identified as a compactive shear band. Note that for the band A2, the *NSP* values of the elements inside the band are homogeneous (Figure 5.44). As for the band A3, dilation seems to be dominant, and the *NSP* mean value over the band is about 0.16 (Figure 5.41). This band, with an orientation of 34.6° with respect to the sample axis, is identified as a dilatant shear band. However, similarly to the band A1 in the first loading stage, local compaction and dilation are identified inside the band A3 (Figure 5.41b-c). The *NSP* evaluated for each element along the central line of the

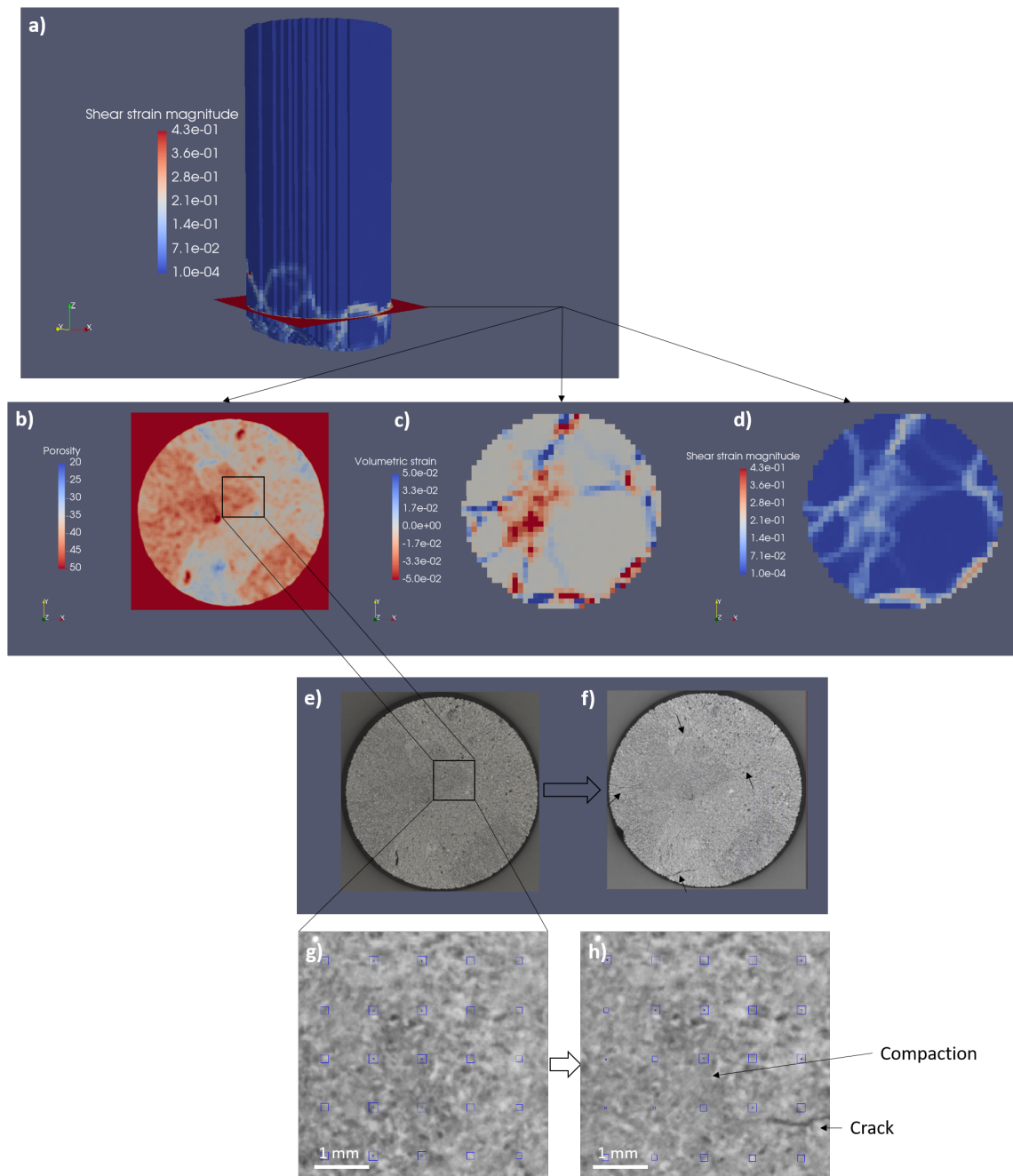


Figure 5.42: a) The incremental shear strain magnitude of the SML sample tested under low confining pressure during the second loading stage; b) - c) - d) Transverse cross-sections of the porosity map in the initial state, the volumetric strain and the shear strain magnitude maps during the second loading stage; e)-f) XRCT images before and after the second loading stage at the same plane; g)-h) Interface between a high- and low-porosity zones crossed by a deformation band before and after the second loading stage.

band A3 is depicted in Figure 5.44. The values fluctuate between -0.2 and 0.5 at a wave length of about 1 cm. The band crosses mainly a low-porosity zone of porosity around 30%, which explains why dilation is dominant in this case.

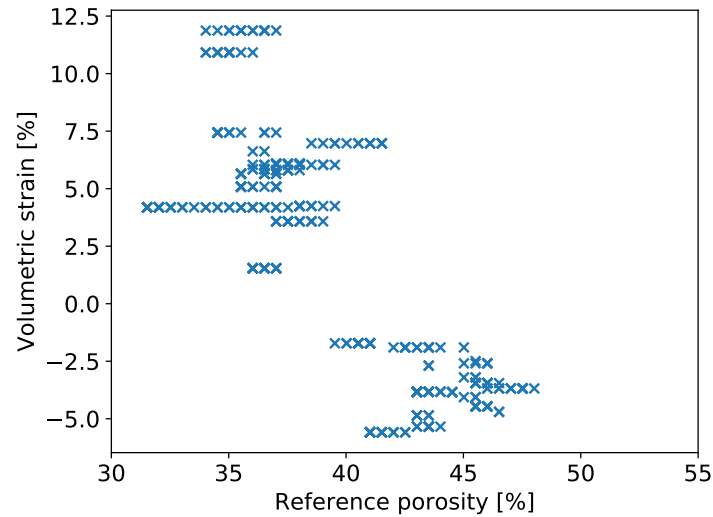


Figure 5.43: Volumetric strain vs reference porosity for some elements of the section shown in Figure 5.42.

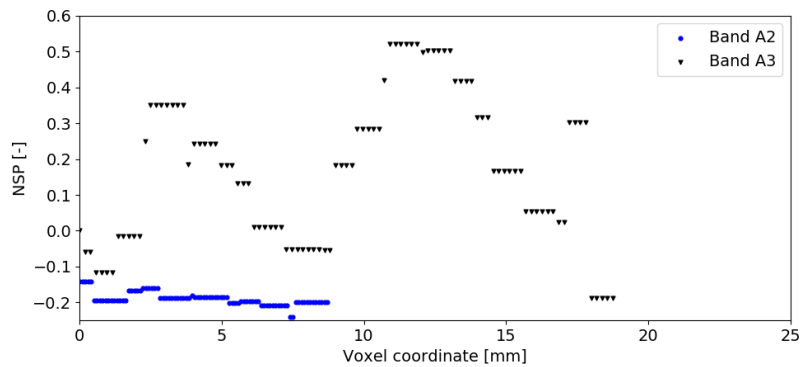


Figure 5.44: NSP calculated for each element along the central line of the deformation bands A2 and A3 in the SML sample tested under low confining pressure during the second loading stage.

5.5.4 Thin section observations

After the second loading stage, a thin section is prepared and observed under SEM using the BSE mode. As already shown, the strain amount at the center of the sample is negligible (Figure 5.45a). This result is verified on microscopic observations, where Figure 5.45b shows a comparison between a high- and low-porosity zones, which are still undeformed after the second loading stage. In addition, Figure 5.45c focuses on an undamaged low-porosity zone at the central part of the sample and shows intact grains, pores and cementation. However, a compactive zone inside the shear band is shown in Figure 5.45d. A pervasive calcite grain crushing is observed, and powders are formed. These fine particles are responsible for a pore filling mechanism and therefore, a reduction in the pore space. On the other hand, Figure 5.45e shows a dilatant zone of the shear band. Figures 5.45 (f and g) make evidence

of a formation of cracks inside the cementation between the grains. Cracks propagate inside this "weaker material" and avoid to cross the grains or the *Miliolidae* shells.

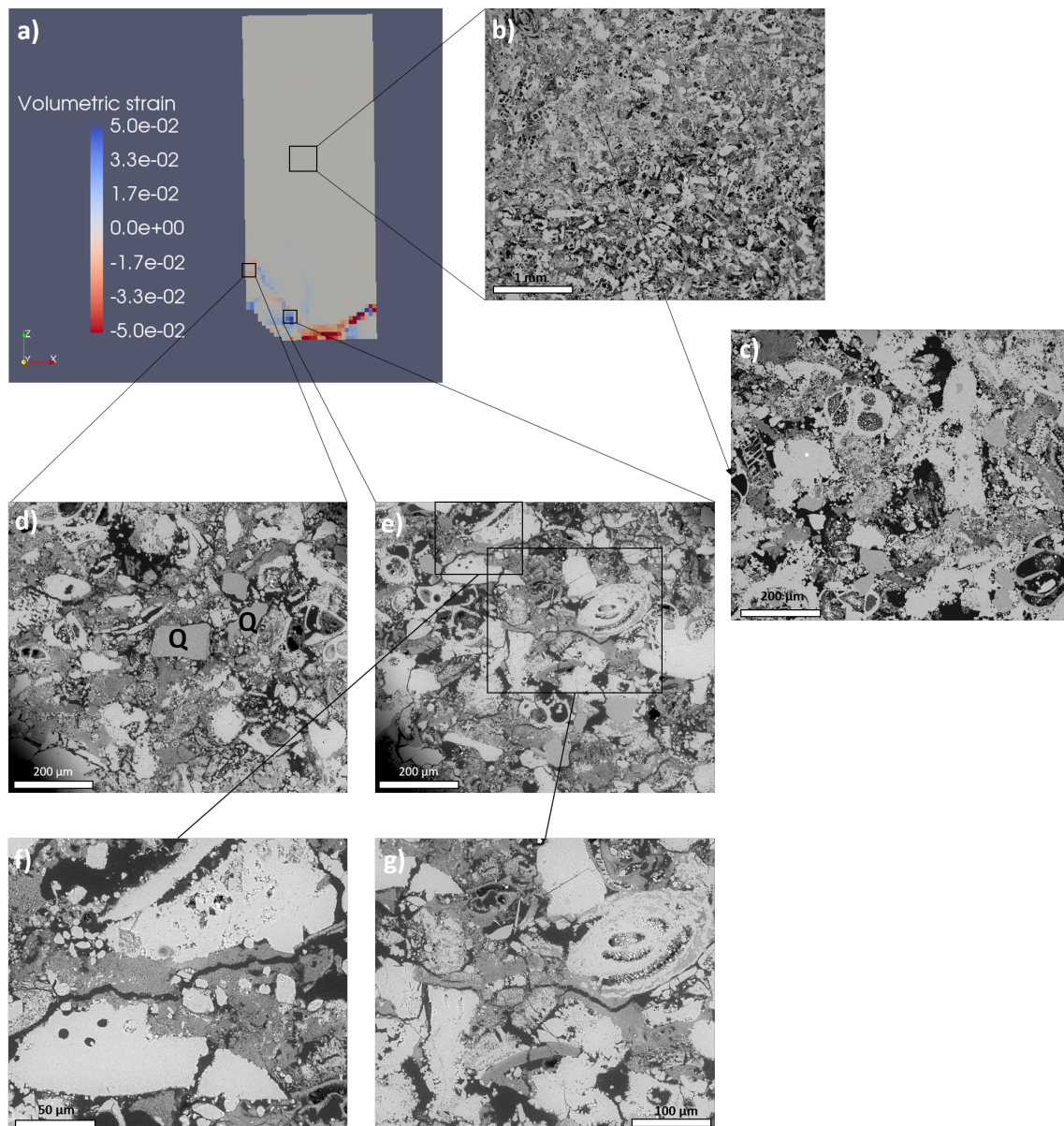


Figure 5.45: The SML sample tested under low confinement: **a)** Vertical cross-section of the incremental volumetric strain map during the second loading stage; **b)** BSE image showing the contrast between high- and low-porosity zones remained undeformed after the two loading stages; **c)** Intact low-porosity zone; **d)** Compactive zone of the shear band (Q for quartz grains); **e)** Dilatant zone of the shear band; **f)-g)** Crack opening in the cementation.

5.6 Triaxial test under intermediate confining pressure

A SML sample with an overall porosity of 38.0% has been tested under an intermediate confining pressure of 6 MPa, which corresponds to the brittle-ductile transitional regime. Again, the sample is imaged by XRCT in the initial state and after two loading stages. Figure 5.46 presents the shear stress intensity vs axial strain measured from LVDTs.

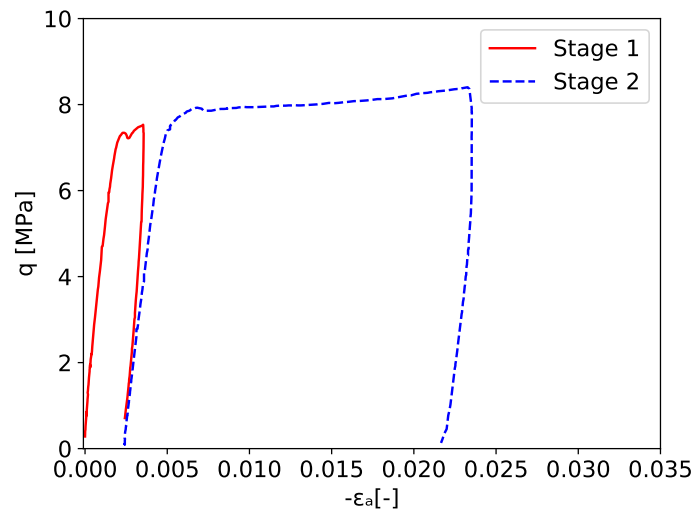


Figure 5.46: A SML sample tested in triaxial conditions under relatively intermediate confining pressure (6 MPa).

5.6.1 Initial state

Figure 5.47 shows a vertical cross-section of the 3D XRCT image and its porosity map in the initial state. The heterogeneity of the porosity is comparable to the one of the samples described previously. A zone of high density (20% of porosity) is observed on the right and above the center of the sample. Several zones of high-porosity (more than 40% and up to 46%) are separated by less porous zones (around 33%). The length scale of the porosity heterogeneity is also in the order of one centimeter, in accordance with the observations presented in sections 5.3.1, 5.4.1 and 5.5.1.

5.6.2 First loading stage

In the first stage, loading is stopped after the plasticity onset, evaluated at a shear stress intensity $q=7.0$ MPa (equivalent to 18.2 MPa of axial loading). The LVDTs measure a residual axial strain of 0.24% (against 0.34% evaluated from the DVC map). Figures 5.48 and 5.49 show the 3D view and vertical cross sections of the incremental shear strain

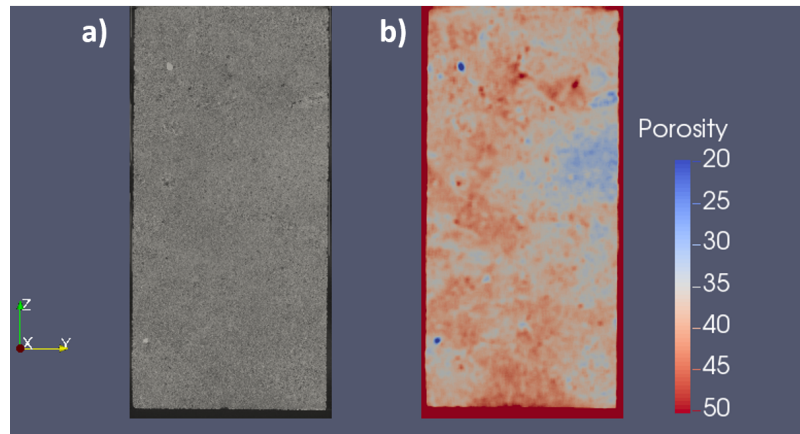


Figure 5.47: A SML sample in the initial state before being tested in axisymmetric triaxial loading under intermediate confining pressure: **a)-b)** YZ middle cross-section of the XRCT image and the porosity map.

magnitude map parallel to the XZ and YZ planes respectively. The sections make evidence of the formation of a deformation band at the plasticity onset. The normal vector to the band plane has no component along the x direction. The band has an orientation of 50.2° with respect to the maximum principal stress direction, with a thickness between 2 and 3 mm (2 to 3 elements). The shear strain magnitude inside the band has a mean value around 10% and can go up to 14%. Some shear strain caused by boundary effects are observed at the lower part of the sample. The induced damage near the boundary may have triggered the deformation band. On the upper part of the sample, the amount of strain is very low in comparison with the bottom part. Some traces of a deformation band begin to appear, but a full strain localization band is not developed yet.

The volumetric strain map is compared to the shear strain magnitude map at the middle YZ cross-section in Figure 5.50. A compactive strain is observed to occur inside the band and can reach a value of 10%. The porosity map at the same cross-section is also presented in Figure 5.50a. The band crosses a zone of a porosity varying between 35% and 40%. Several transverse cross-sections at different levels of the localized zone show that local dilatancy can occur inside the band. Figure 5.51 presents cross-sections of the porosity map in the initial state, the volumetric strain and the shear strain magnitude maps. Negative volumetric strain is dominant inside the band. Nonetheless, some local dilation is detected when the deformation band crosses a low-porosity zone, similarly to the shear bands observed at low confinement. In Figure 5.51b, a 10% of compaction is observed in a zone of 41% of porosity. However, a tiny dilatant band with a dilation around 1% is observed in a low-porosity zone where $\phi = 34\%$. In Figure 5.51c, a dilation between 1% and 1.5% is observed for a zone with porosity around 36%. In contrast, compactive strain between 5% and 8% is evaluated in zones of porosity higher than 40% in Figure 5.51d.

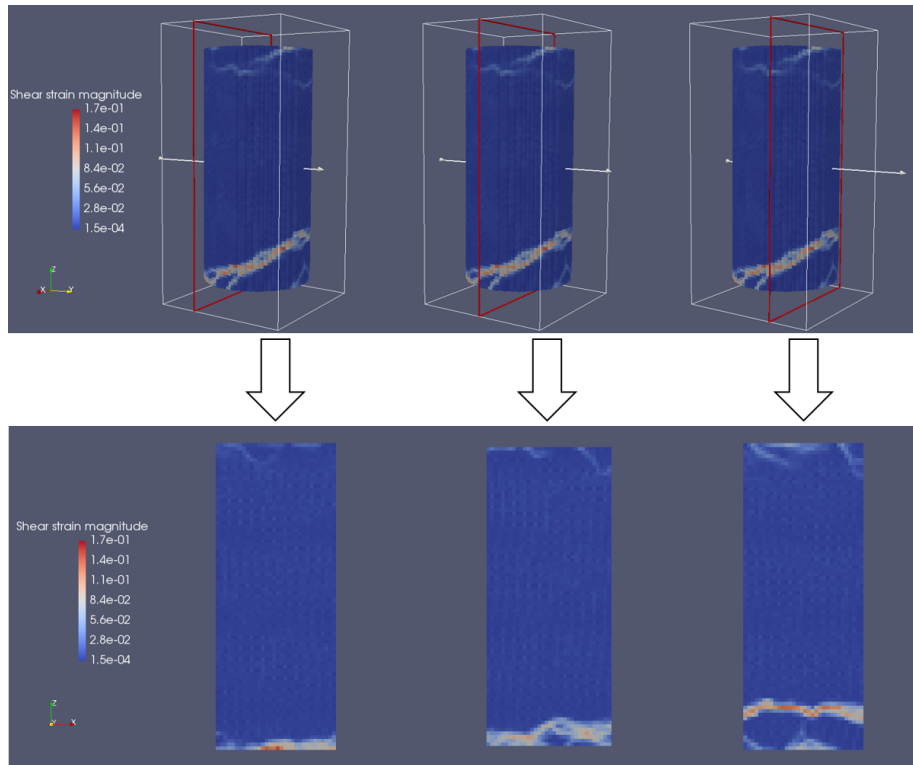


Figure 5.48: The incremental shear strain magnitude map for the first loading stage of the SML sample tested under intermediate confining pressure (6 MPa): 3D view and vertical cross sections parallel to the XZ plane.

The microstructure of the sample is inspected before and after the first loading stage. The cross-section presenting a dilatant behavior in the deformation band is investigated in Figures 5.52 a, c and d (the same section as Figure 5.51c). Despite the dilatancy identified on the DVC map, no crack opening is observed after the first loading stage on the XRCT images. This is due to the current resolution of the XRCT images: for a volumetric dilation less than 1.5% over the finite element, which is of cubic shape with $960 \mu\text{m}$ in side length, the crack opening should be less than $960 \times 0.015 = 14.4 \mu\text{m}$ (if the strain amount in the other directions is assumed to be negligible). This length is lower than the voxel size ($24 \mu\text{m}$), which explains why the cracks have not been observed on the XRCT images in the deformed configuration. However, an out-of-plane movement between the two adjacent zones to the band can be identified. In fact, the centers of the correlation domains are generated on a given horizontal plane in the reference configuration (Figure 5.52c). After applying the DVC, these points are no longer on the same plane. Figure 5.52d shows a horizontal plane passing through the points of the lower zone. In contrast, the points of the upper zone are shifted in the z axis direction of about 0.2 mm. These observations make evidence of shearing inside the deformation band and a rigid block movement of one adjacent zone with respect to the other. On the other hand, a cross-section showing a compactive behavior inside the deformation band is considered in Figures 5.52 b, e and f (the same section in Figure 5.51d). A comparison between the porosity maps before and after the first loading stage highlights the compaction of the high-porosity zones. For

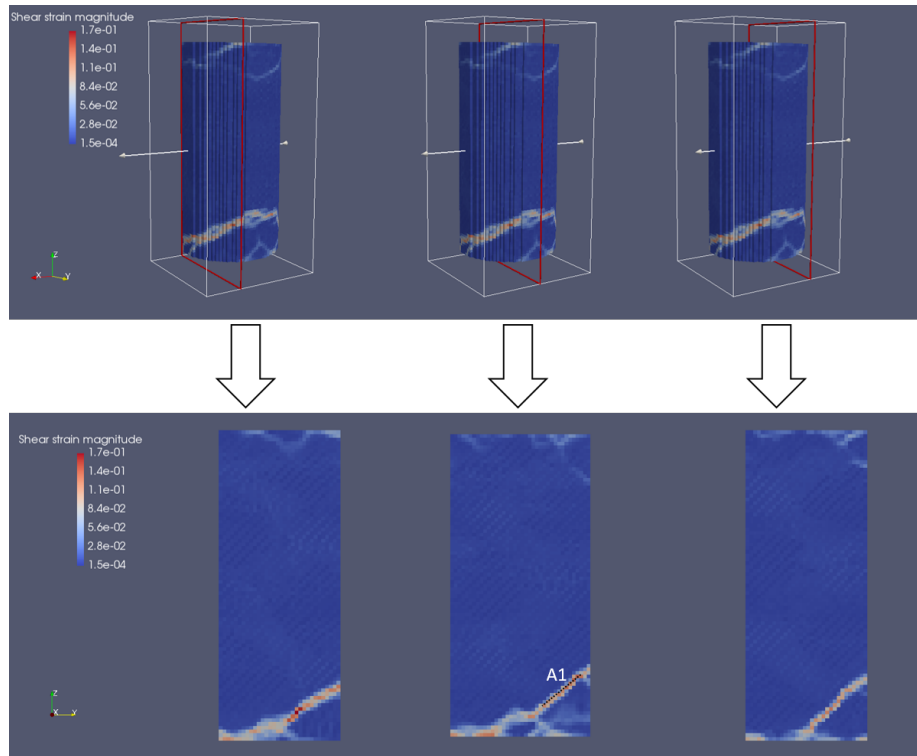


Figure 5.49: The incremental shear strain magnitude map for the first loading stage of the SML sample tested under intermediate confining pressure (6 MPa): 3D view and vertical cross sections parallel to the YZ plane. A1 is the selected deformation band.

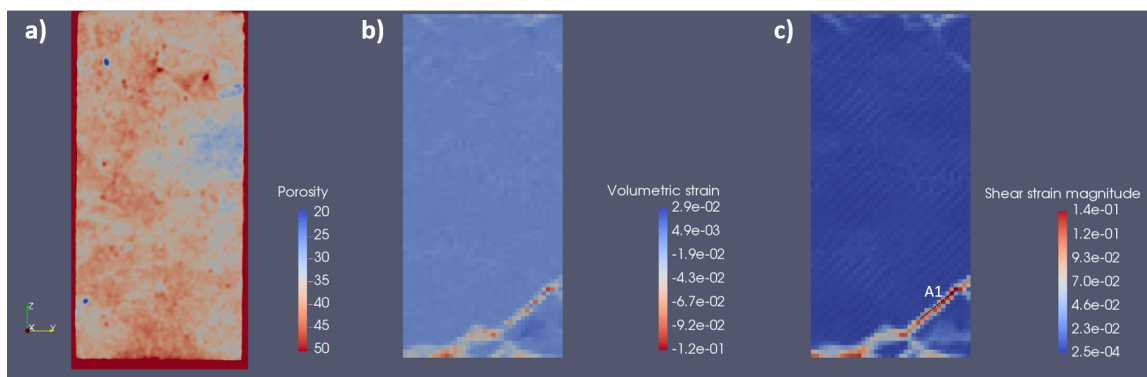


Figure 5.50: Vertical cross-sections parallel to the YZ plane of the SML sample tested under intermediate confining pressure: **a)** Porosity map in the initial state; **b)** Incremental volumetric strain; **c)** Incremental shear strain magnitude. A1 is the selected deformation band.

instance, the deformation band passes through two high-porosity zones (initial porosity $\phi = 41\%$), marked by the arrows in Figure 5.52e. Then, after loading, the porosity is reduced to 34% (Figure 5.52f). From the DVC map, the volumetric compaction is evaluated at 7% in these zones, which corresponds to the porosity reduction.

After the plasticity onset, one deformation band is formed denoted by A1 in Figure 5.49. The band orientation with respect to the axial direction is around 50.2° , an intermediate value between the orientations of compaction bands obtained at high confinement ($> 70^\circ$)

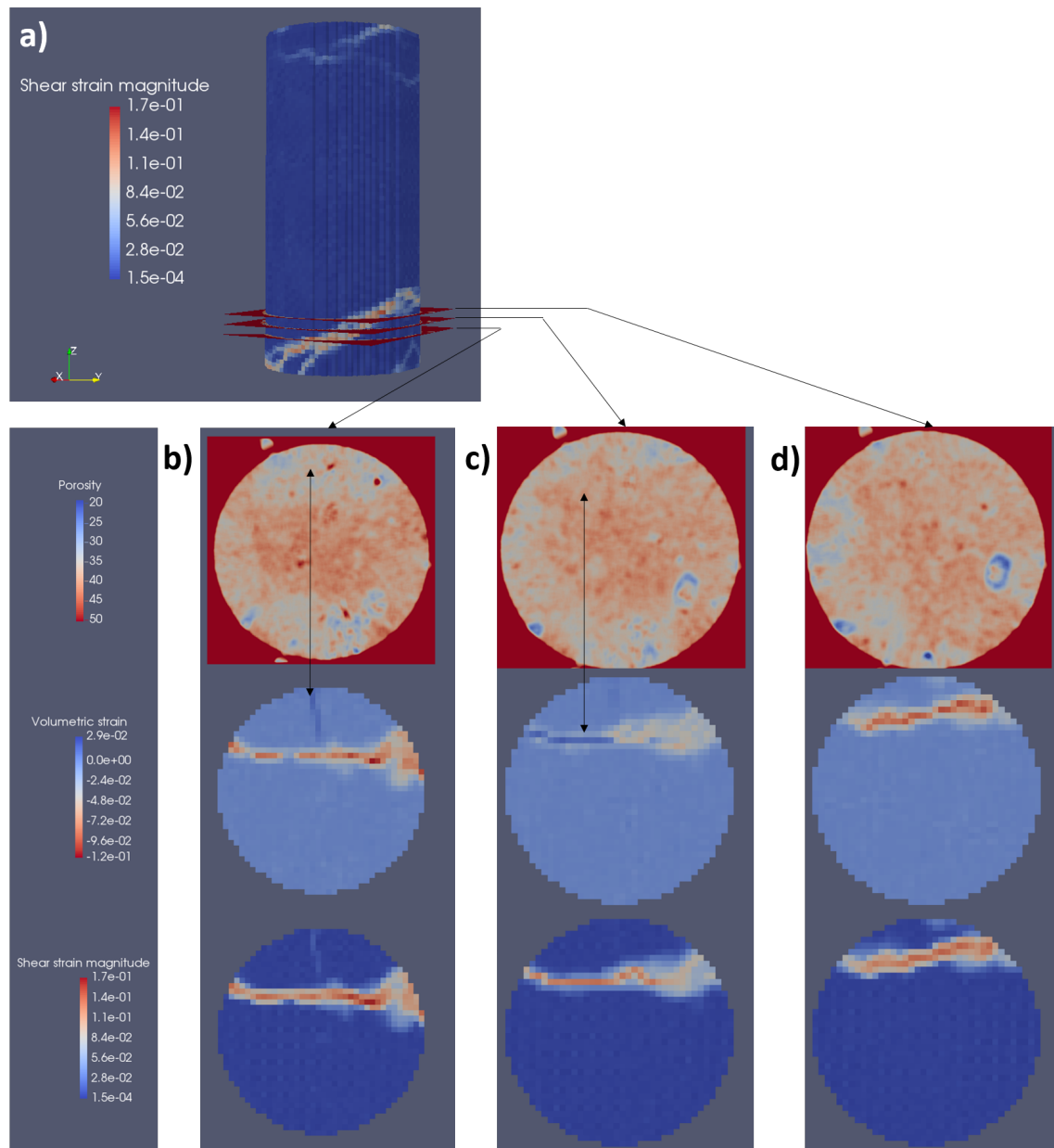


Figure 5.51: a) The incremental shear strain magnitude of the SML sample tested under intermediate confining pressure during the first loading stage; b) - c) - d) Transverse cross-sections of the porosity map in the initial state, the volumetric strain and the shear strain magnitude maps at different levels of the sample axis z .

and those of the shear bands obtained at low confinement, which can reach 30° . The average *NSP* for the band A1 is evaluated at -0.67, suggesting that A1 is a compactive shear band (Table 5.4). The values of the *NSP* along the elements of the band are homogeneous, and the slight dilatancy observed in Figure 5.51c has not a significant impact on the nature of the band.

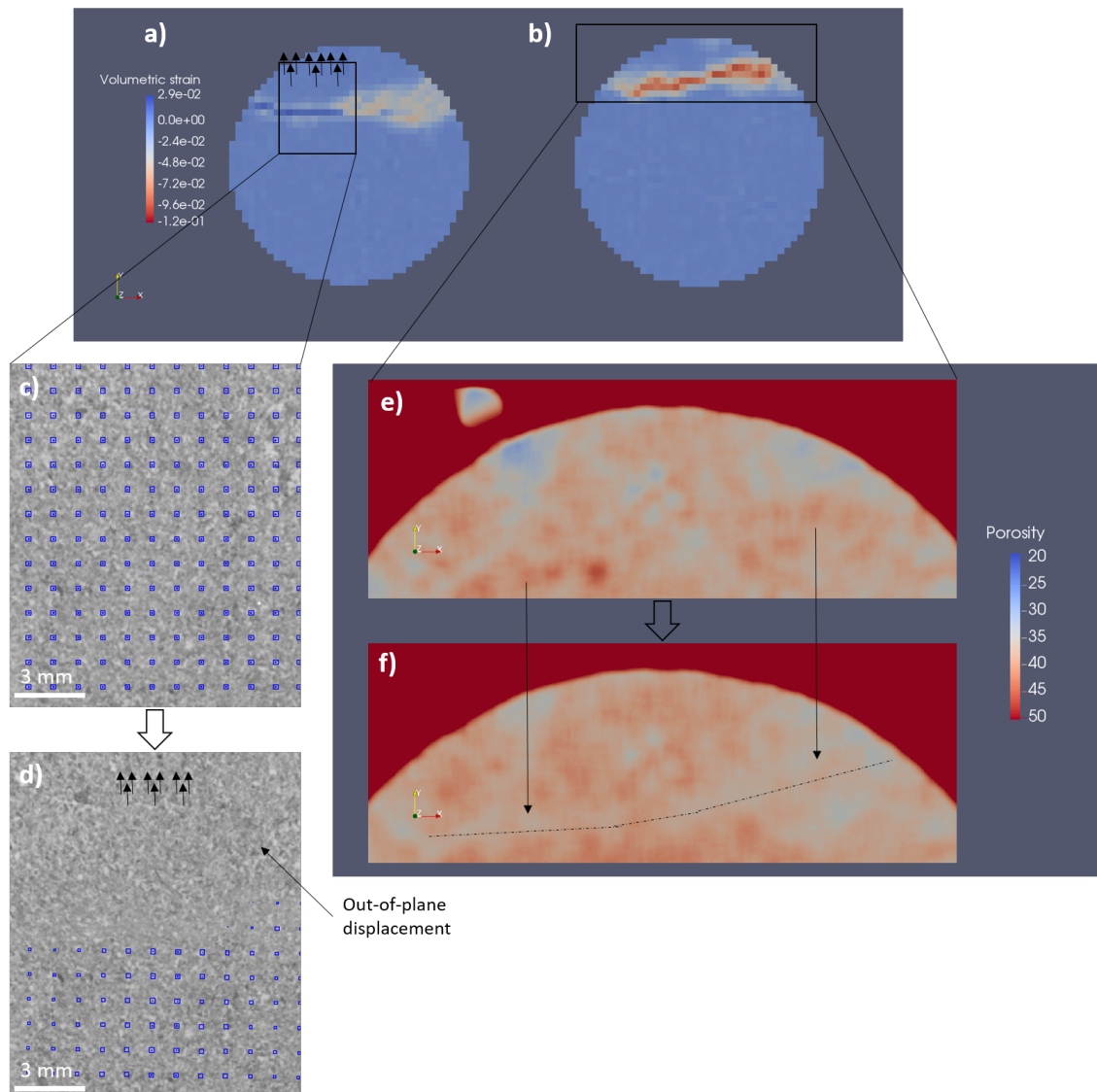


Figure 5.52: The SML sample tested under intermediate confining pressure during the first loading stage: **a)** Transverse cross-section of the volumetric strain map at the level of Figure 5.51c; **b)** Transverse cross-section of the volumetric strain map at the level of Figure 5.51d; **c)** A focus on a zone before being sheared. Each point corresponds the center of a correlation domain; **d)** The same zone after being crossed by the deformation band, where the points represent the correlation domain centers found from DVC: an out-of-plane displacement is identified. ; **e)** Porosity map of a zone before being crossed by the deformation band; **f)** The porosity map of the zone after the first loading stage.

5.6.3 Second loading stage

In the second stage, a plateau is observed in the shear stress intensity vs axial strain curve (Figure 5.46), characterizing a perfectly plastic behavior. The shear stress intensity remains around 8 MPa, and a residual axial strain of 2.2% is obtained by means of the LVDTs after unloading the sample. However, 2.8% of cumulative axial strain is evaluated from DVC maps of both stages. This can be related to the fact that LVDTs do not completely cover the zone where strain is localizing. Figures 5.53 and 5.54 show the middle cross-sections

Table 5.4: Band types and orientations θ (in absolute value) with respect to the axial direction in the sample tested at intermediate confining pressure (6 MPa).

	Band	NSP^{band}	θ°	Type
After Stage 1 of loading	A1	-0.67	50.2	Compactive shear band
After Stage 2 of loading	A1	-0.62	50.2	Compactive shear band
	A2	-0.79	59.5	Compactive shear band
	A3	-0.50	47.7	Compactive shear band

of the reference porosity map, the shear strain magnitude and volumetric strain maps in the direction of the YZ and XZ planes respectively. During this loading stage, compactive shear continues to localize inside the band A1, formed in the first stage. The thickness of the band does not evolve significantly (around 2 to 3 mm). Despite the formation of a thick damaged zone near the bottom boundary, a new deformation band is formed and is denoted by A2 in Figure 5.53. The band has a comparable thickness to A1. Another band is formed just above, but it is difficult to be distinguished because of the damage around. Strain localization is mainly observed in high-porosity zones. Some boundary effects are also present near the upper boundary, where a small cone of localized deformation is identified. However, a deformation band can be selected on the XZ cross-section and is denoted by A3 (Figure 5.54). The thickness of this band is around 2 mm. The shear strain magnitude inside the deformation bands can reach 20 to 25%. As for the volumetric strain, 6 to 10% of compaction are assessed inside the bands.

The volumetric strain maps indicate that compactive strain is dominant inside strain localization bands. However, similarly to the first loading stage and to shear bands at low confinement, a dilatant behavior is again observed in some parts of the deformation bands. A transverse cross-section of the porosity map before loading superimposed on the volumetric strain and shear strain magnitude maps is shown in Figure 5.55 a, b and c. Obviously, the shear strain magnitude map is not sufficient to understand the effect of the porosity heterogeneity on strain localization. The volumetric strain map indicates that compactive shear band are localized in high-porosity zones (around 40%). This observation is similar to the results of compaction banding under high confinements. Moreover, similarly to shear bands, dilation occurs in low-porosity zones. For instance, a local dilation of 6% is found in a zone of 34% in porosity (Figure 5.55 a and b).

Figure 5.55d shows a XRCT image of a low-porosity zone before the current loading stage. Then, a crack with around 50 μm in opening is formed as shown in Figure 5.55e. This result corroborates the dilation of 5% to 6% obtained from DVC analyses (Figure 5.55b). By comparing the porosity maps before and after strain localization in Figures 5.55 f and g, a porosity reduction from 41% to around 34% is evaluated. This porosity reduction is

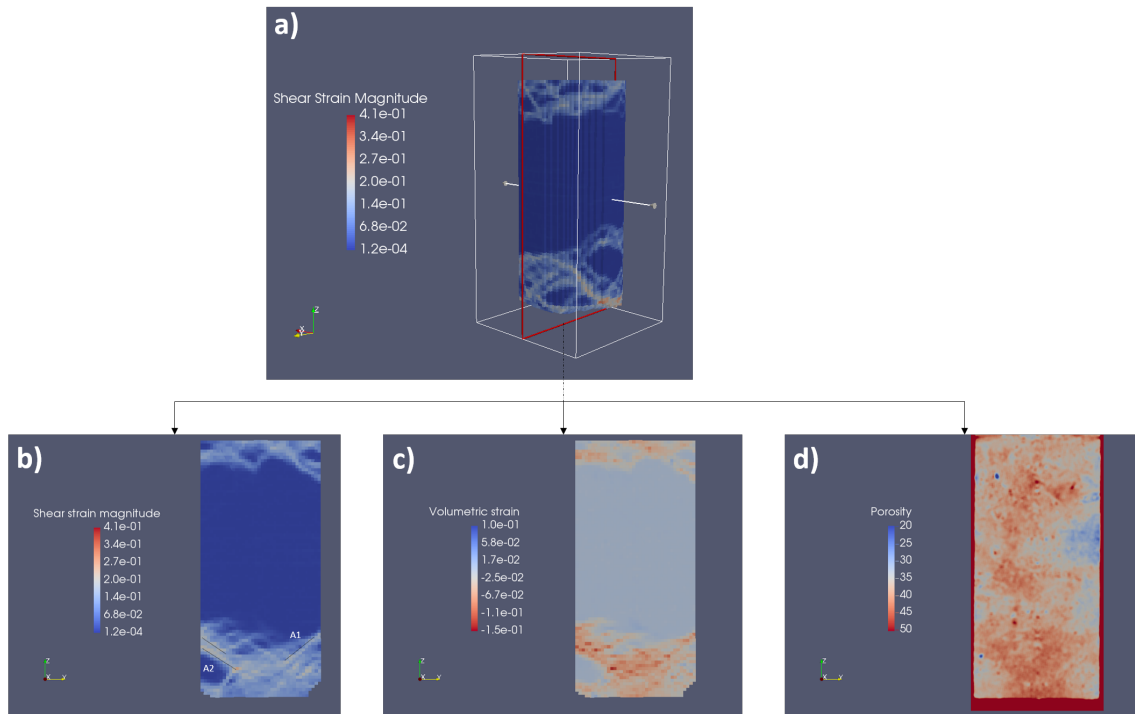


Figure 5.53: The SML sample tested under relatively intermediate confining pressure during the second loading stage: A vertical YZ cross-section at the middle plane showing the incremental shear strain magnitude, the volumetric deformation and the reference porosity maps. A1 and A2 are two selected deformation bands.

comparable with the volumetric compaction obtained from DVC analyses (around 7% in Figure 5.55b).

The type of the bands is then studied and results are summarized in Table 5.4. During the second stage of loading, the band A1 is still a compactive shear band, having a slightly higher amount of shear (the *NSP* increases to -0.62). The two other bands A2 and A3 are also identified as compactive shear bands. The *NSP* of the bands ranges between -0.50 and -0.79. The values of the *NSP* along the elements of the bands are homogeneous, and dilatant behavior does not seem to have a significant impact on the nature of the bands. The band orientations vary between 48° and 60° . The average orientation of the bands with respect to the axial direction is globally higher than those of the SML sample tested at low confining pressure, but lower than those of the SML studied at high confinement.

5.6.4 Thin section observations

In accordance with the analysis done in the previous section, Figure 5.56a shows that compactive shear bands pass through high-porosity zones and avoid low-porosity zones. Significant crushing of calcite grains is observed inside the compactive shear bands and fine powders are formed (Figures 5.56b and d). In addition, some cracked *Miliolidae* shells are

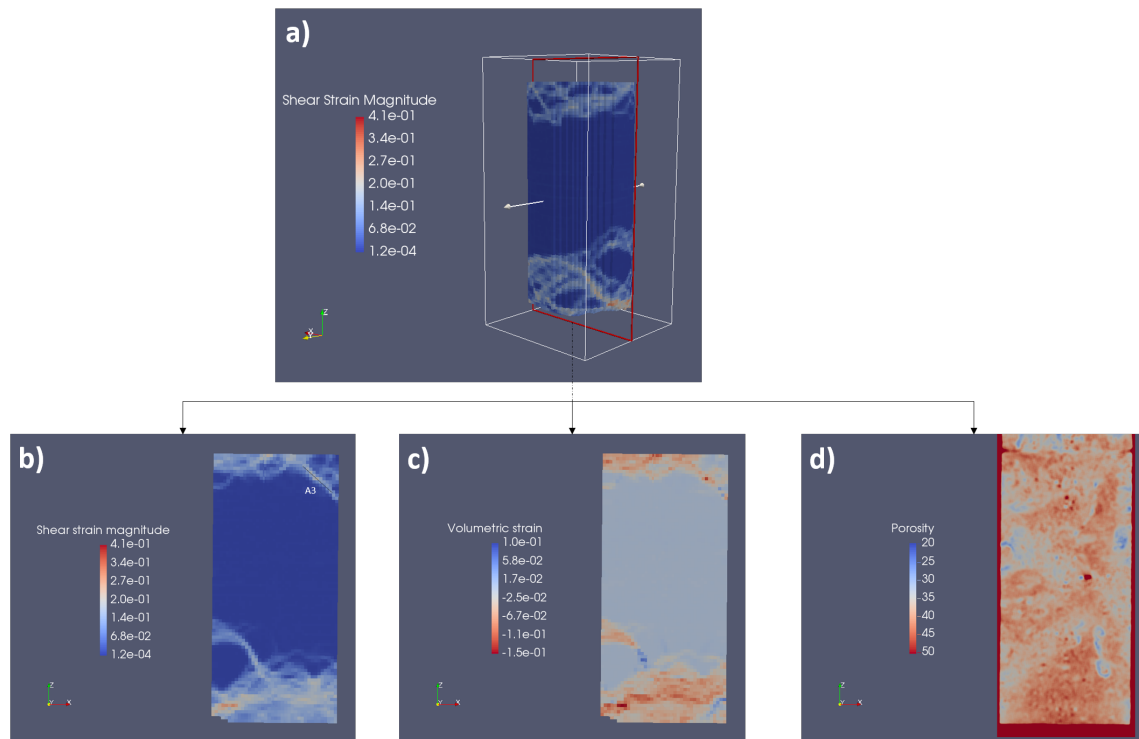


Figure 5.54: The SML sample tested under relatively intermediate confining pressure during the second loading stage: A vertical XZ cross-section at the middle plane showing the incremental shear strain magnitude, the volumetric deformation and the reference porosity maps. A3 is a selected deformation band.

observed inside the compactive band (Figure 5.56c). On the other hand, the compactive shear bands can cross sometimes low porosity zones. Similarly to shear bands, local dilatant behavior can be induced by the intergranular cement cracking. Fractures are observed to form between the grains and the shells as shown in Figure 5.57.

5.7 Conclusions

The mechanical behavior and the deformation mode of a high-porosity carbonate rock is studied in this chapter. DVC technique is successfully applied to identify deformation bands in the SML. The effect of the confining pressure on the deformation mode is studied. In addition, computed porosity maps allow to understand the role played by the porosity heterogeneity in the deformation.

Under hydrostatic loading, diffuse compaction is observed in high-porosity zones. Denser zones present stiff inclusions which remain undeformed. However, due to the stiffness contrast, stresses are redistributed and some shear strain is observed locally. Crushing of calcite grains is identified as the principal micromechanism of deformation. An induced production of fines contributes in a pore space reduction.

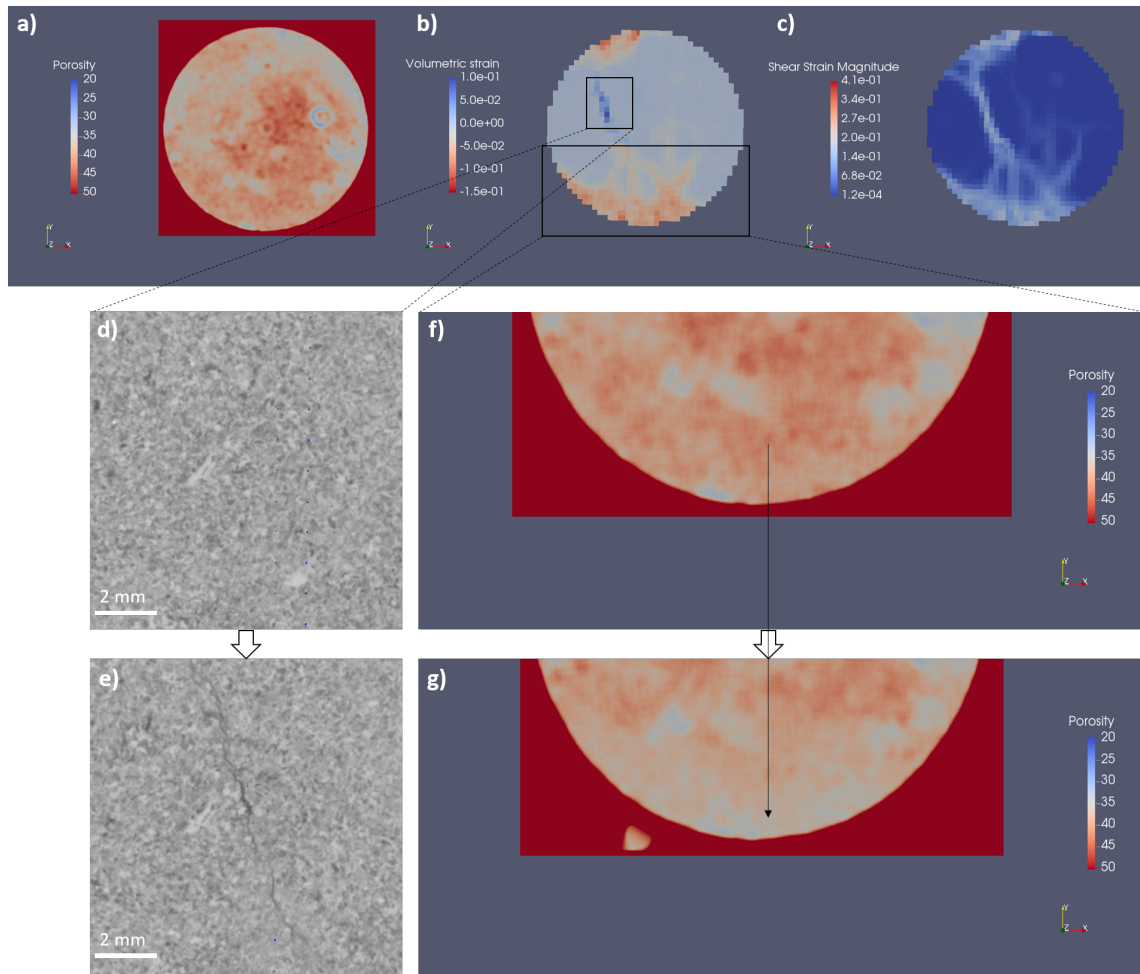


Figure 5.55: The SML sample tested under relatively intermediate confining pressure during the second loading stage: **a) - b) - c)** Transverse cross-sections showing the porosity map before loading, the incremental volumetric strain and shear strain magnitude maps; **d) - e)** A low-porosity zone before and after being crossed by a deformation band; **f) - g)** Porosity maps of a high-porosity zone before and after being crossed by compactive deformation bands.

At relatively high confinements, compaction bands are identified. These bands propagate in high-porosity zones, while denser zones remain intact. A calcite grain crushing is identified as the main micromechanism of deformation. For low confinements, shear bands form at low-angle orientations with respect to the direction of maximum principal stress (in absolute value). The porosity heterogeneity does not play a significant role in the orientation and the path of shear bands, as observed bands may pass through both zones. However, it affects the volumetric strain behavior: shearing a high-porosity zone induces a local compaction due to a calcite grain crushing phenomenon. In contrast, shearing a low-porosity zone induces a local dilation due to the grain cementation fracturing. The brittle-ductile transitional regime is characterized by the formation of compactive shear bands. These bands propagate preferably through high-porosity zones similarly to compaction bands, with significant crushing of calcite grains. But in addition, they may also cross low-porosity zones, where cement microcracking can be observed similarly to shear bands.

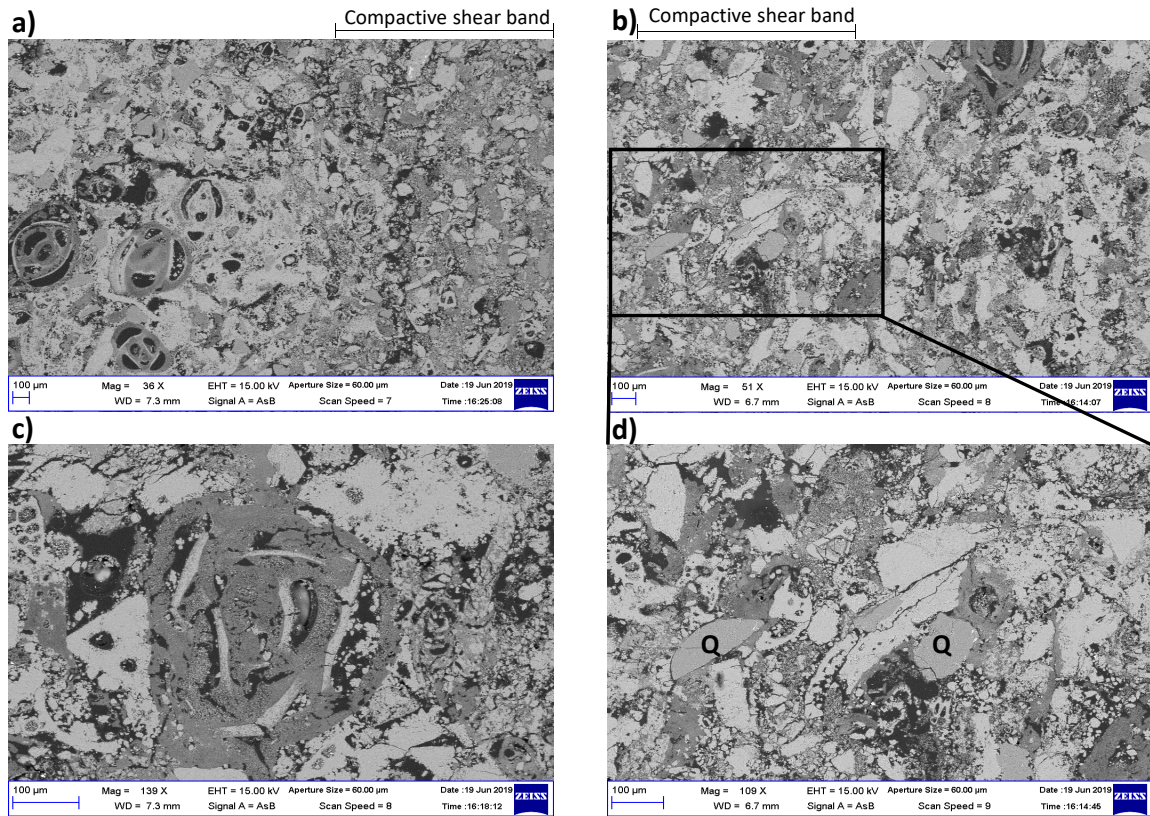


Figure 5.56: BSE images of the SML sample tested under intermediate confinement: **a)** A zone at the interface between a high- and low-porosity zone; **b)-d)** Calcite grain crushing inside compactive shear bands, Q denotes quartz grains; **c)** *Miliolidae* shell cracked inside a compactive shear band.

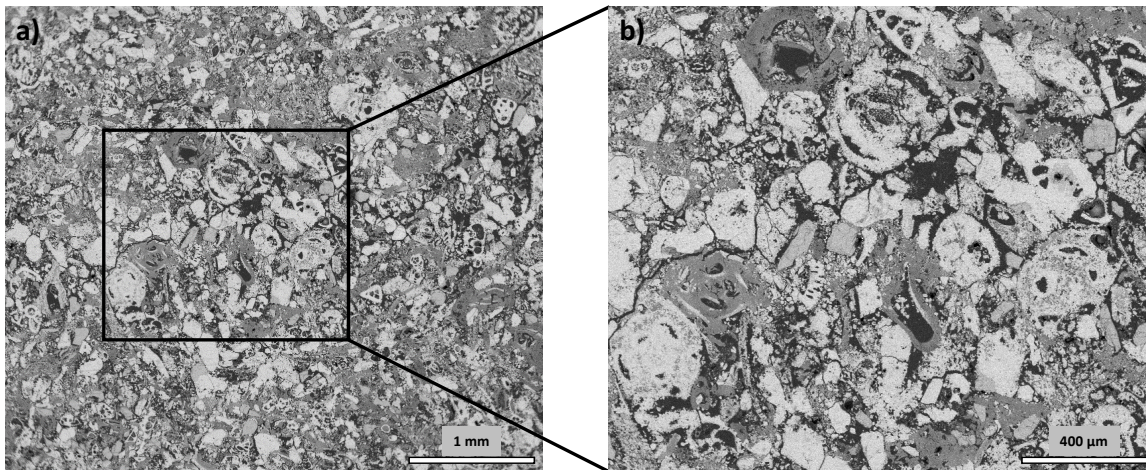


Figure 5.57: BSE images of the SML sample tested under intermediate confinement: Cracks formed between grains in low-porosity zones.

The orientations of deformation bands with respect to the maximum principal stress direction has a positive correlation with respect to the confining pressure. The porosity heterogeneity seems to play a secondary role in the bands orientation: compaction bands have orientations greater than 70° , shear bands have orientations lower than 50° and compactive shear bands have intermediate orientations.

The analyses done in this chapter shows that larger pores do not collapse at first as one may have expected from other observations in literature. Rather, the heterogeneity of porosity at the scale of one centimeter is the dominant quantity that determines the path and the mode of deformation. The properties around a material point plays a role in controlling its deformation state. This observation leads to consider non-local approaches to model compaction banding. The development of such model, its calibration and then its implementation in a finite element code will be the purpose of the next chapter.

A gradient-dependent plasticity model for compaction banding

Résumé L'objectif de ce chapitre est tout d'abord de présenter un modèle de plasticité du second-gradient. En se basant sur les résultats expérimentaux (données mécaniques macroscopiques, images aux rayons X et cartes de déformation), une méthode de calage de ce modèle est ensuite proposée. Finalement, le modèle est implémenté dans un logiciel de calcul aux éléments finis, *Numerical geolab*, afin de simuler la formation des bandes de compaction. Les résultats numériques et expérimentaux sont assez cohérents.

Abstract The objective of this chapter is to present a gradient-dependent plasticity model. Based on the experimental results (macroscopic mechanical data, XRCT images and deformation maps), a calibration procedure of the model is proposed. Finally, the constitutive law is implemented in a Finite Element code, *Numerical geolab*, in order to simulate the formation and evolution of compaction bands. The numerical results are consistent with the experimental data.

6.1 Gradient-dependent plasticity model

As already seen in the previous chapter, large pores do not collapse at first, since they are protected by a surrounding rigid lattice of cemented grains. Moreover, compaction bands have been observed in zones of high-porosity. In a modelling approach, this means that the deformation state at a point does not only depend on the local properties, but it also depends on the properties of the material at the vicinity. This leads to consider non local models, in which the constitutive law depends on a plastic hardening parameter κ and its second gradient $\nabla^2\kappa$ (already presented in Section 2.4.4). The yield surface F depends thus on two hardening parameters as presented in Equation 6.1, where σ_{ij} is the stress tensor.

$$F = F(\sigma_{ij}, \kappa, \nabla^2\kappa) \quad (6.1)$$

Compaction bands are associated with porosity reduction as observed experimentally in Sections 5.4.2 and 5.4.3. This porosity reduction may be induced either by grain crushing as in the case of the SML, or by other micromechanisms (see Section 2.3.3). Therefore, the plastic porosity change ϕ^{pl} can be identified to the plastic hardening parameter κ . If the deformation of the solid matrix is neglected, the plastic porosity change can be approximated by the plastic volumetric strain ϵ_v^{pl} (Coussy, 2011). The validity of this assumption in view of the experimental data will be discussed later in Section 6.3. Consequently, the plastic hardening parameter is considered as:

$$\kappa \equiv \epsilon_v^{pl} \quad (6.2)$$

The consistency equation $\dot{F} = 0$ leads to the following equation:

$$\frac{\partial F}{\partial \sigma_{ij}} \dot{\sigma}_{ij} + \frac{\partial F}{\partial \epsilon_v^{pl}} \dot{\epsilon}_v^{pl} + \frac{\partial F}{\partial \nabla^2 \epsilon_v^{pl}} \nabla^2 \dot{\epsilon}_v^{pl} = 0 \quad (6.3)$$

By considering the elastic law $\dot{\sigma}_{ij} = C_{ijkl}^e (\dot{\epsilon}_{kl} - \dot{\epsilon}_{kl}^{pl})$ and the plastic flow rule $\dot{\epsilon}_{kl}^{pl} = \dot{\lambda} \frac{\partial g}{\partial \sigma_{kl}}$ (g is the plastic potential), and by neglecting the second gradient of the elastic volumetric strain ($\nabla^2 \epsilon_v^{pl} \simeq \nabla^2 \dot{\epsilon}_v$), one can find the expression of the plastic multiplier $\dot{\lambda}$ as:

$$\dot{\lambda} = \frac{b_{kl}^f \dot{\epsilon}_{kl} + \frac{\partial F}{\partial \nabla^2 \epsilon_v} \nabla^2 \dot{\epsilon}_v}{H_1} \quad (6.4)$$

with

$$b_{kl}^f = \frac{\partial F}{\partial \sigma_{ij}} C_{ijkl}^e \quad (6.5)$$

and

$$H_1 = b_{kl}^f \frac{\partial g}{\partial \sigma_{kl}} - \frac{\partial F}{\partial \epsilon_v^{pl}} \frac{\partial g}{\partial p} \quad (6.6)$$

Finally, the constitutive relationship is obtained as:

$$\dot{\sigma}_{ij} = C_{ijkl}^{ep} \dot{\epsilon}_{kl} + A_{ij} \nabla^2 \dot{\epsilon}_v \quad (6.7)$$

where the elastic-plastic matrix is

$$C_{ijkl}^{ep} = C_{ijkl}^e - \langle 1 \rangle \frac{b_{ij}^g b_{kl}^f}{H_1} \quad (6.8)$$

and

$$A_{ij} = -\langle 1 \rangle \frac{b_{ij}^g \frac{\partial F}{\partial \nabla^2 \epsilon_v}}{H_1} \quad (6.9)$$

with

$$b_{ij}^g = C_{ijkl}^e \frac{\partial g}{\partial \sigma_{kl}} \quad (6.10)$$

and $\langle 1 \rangle$ is the McAuley brackets of plasticity theory defined as follows:

$$\langle 1 \rangle = \begin{cases} 1 & \text{If } F = 0 \text{ and } \dot{\lambda} > 0 \\ 0 & \text{If } F < 0 \text{ or } (F = 0 \text{ and } \dot{\lambda} \leq 0) \end{cases} \quad (6.11)$$

A gradient-dependent plasticity model can thus be built. The constitutive law depends on the first and third gradient of the displacement field (second-gradient in terms of strain). In the next section, the link between this gradient-dependent plasticity model and a micromorphic continuum is established.

6.2 Micromorphic continuum

The gradient-dependent plasticity model can be interpreted as a micromorphic continuum. In such continua, a subvolume is attached to each material point leading to introduce additional degrees of freedom (Section 2.4.3). A rigorous mathematical framework is developed in this section for a general micromorphic continuum theory, in order to establish the equilibrium equations, the boundary conditions and define the material parameters. Based on the method of virtual power, higher order strain-gradient continuum theories can be developed (Germain, 1973b).

6.2.1 Internal power density

As presented in Section 2.4.3, the displacement of a point M' of the subvolume in a micromorphic continuum, of coordinate x'_j with respect to its center of mass M , can be expressed as:

$$u'_i = u_i + \chi_{ij} x'_j + \chi_{ijk} x'_j x'_k + \chi_{ijkl} x'_j x'_k x'_l + \dots \quad (6.12)$$

Since the second-gradient of strain is required in the constitutive law (Equation 6.7), a third gradient of displacement is needed. Therefore, a first grade micromorphic continuum of degree 2 should be considered (for a detailed description of micromorphic continuum types, see the Appendix E). The internal power density δw is thus assumed to linearly depend on u_i , χ_{ij} , χ_{ijk} and their first gradients, or equivalently on u_i , $u_{i,j}$, $\eta_{ij} = u_{i,j} - \chi_{ij}$, $\kappa_{ijk} = \chi_{ij,k}$, $\eta_{ijk} = \chi_{ij,k} - \chi_{ijk}$ and $\kappa_{ijkl} = \chi_{ijk,l}$:

$$\delta w = K_i u_i + \sigma_{ij} u_{i,j} + s_{ij} \eta_{ij} + \nu_{ijk} \kappa_{ijk} + s_{ijk} \eta_{ijk} + \zeta_{ijkl} \kappa_{ijkl} \quad (6.13)$$

This expression is an extension from the first to the second degree of the micromorphic continuum expression (Equation 2.17). The micromorphic medium is designated as a first grade continuum of degree 2, because the Taylor series is developed up to the second degree in Equation 6.12 and because the first gradients of each degree of freedom are only considered in the internal power density.

By analogy with the second-gradient theory (Germain, 1973b), the deformation of the subvolume and its first gradient can be identified with the deformation of the general continuum and its gradient. Two restrictions are thus considered:

- Vanishing relative microdisplacement gradient $\eta_{ij} = 0$.
- Vanishing relative microdisplacement second gradient $\eta_{ijk} = 0$.

As discussed in Section 2.4.3, K_i must be zero and σ_{ij} must be a symmetric tensor. Taking into account these conditions and the assumed restrictions, the expression of the internal forces density can be written as:

$$\delta w = \sigma_{ij} u_{i,j} + \nu_{ijk} u_{i,jk} + \zeta_{ijkl} u_{i,jkl} \quad (6.14)$$

6.2.2 Equilibrium equation

To obtain the equilibrium equation, the principle of virtual power is applied:

$$\hat{P}_i + \hat{P}_e = 0 \quad (6.15)$$

where \hat{P}_i is the internal virtual power defined as:

$$\hat{P}_i = - \int_{\mathcal{D}} [\delta \hat{w}] dv \quad (6.16)$$

and \hat{P}_e is the external virtual power, divided into two categories: long range volumic forces \hat{P}_v and contact forces \hat{P}_c :

$$\hat{P}_e = \hat{P}_v + \hat{P}_c \quad (6.17)$$

For simplicity, the hat symbols will be dropped from here. To obtain the equilibrium equation, the terms of volume integrals in Equation 6.15 should be only considered. The volumic external forces are defined as:

$$P_v = \int_{\mathcal{D}} \left[f_i u_i + \Psi_{ij} \chi_{ij} + \xi_{ijk} \chi_{ijk} \right] dv \quad (6.18)$$

where f_i is the volumic force, Ψ_{ij} is a volumic double force and ξ_{ijk} is a higher order volumic force defined by analogy. The contact external power P_c will be defined in the next subsection, since it does not contain volume integrals. After some integration by parts, the integral over the volume from Equation 6.15 can be written as:

$$\int_{\mathcal{D}} \left[\sigma_{ij,j} - \nu_{ijk,kj} + \zeta_{ijkl,lkj} + f_i - \Psi_{ij,j} + \xi_{ijk,kj} \right] u_i dv = 0 \quad (6.19)$$

for any virtual displacement field u_i (the details of integration are presented in Appendices F and H). Thus, the equilibrium equation is given by:

$$\tilde{\tau}_{ij,j} + f_i = 0 \quad (6.20)$$

where a stress tensor is introduced as follows:

$$\tilde{\tau}_{ij} = \sigma_{ij} - \nu_{ijk,k} + \zeta_{ijkl,lk} - \Psi_{ij} + \xi_{ijk,k} \quad (6.21)$$

Note that, by omitting the higher order terms ζ_{ijkl} and ξ_{ijk} , the equilibrium equation degenerates to the one of the second gradient theory as defined by Germain (1973b).

6.2.3 Boundary conditions

Boundary conditions are obtained from the surface integrals of Equation 6.15. On the surface of the domain \mathcal{D} , the displacement field u_i , its first and second normal derivatives DU_i and D^2U_i may be chosen independently. Consequently, the tangential derivations following Mindlin (1964) notations ($D_j U_i$, $D_k D_j U_i$ and $D_j DU_i$) may be computed (definitions are given in Appendix F). The contact external power P_c can be generalized as:

$$P_c = \int_{\partial\mathcal{D}} \left[T_i u_i + M_{ij} u_{i,j} + \mathcal{L}_{ijk} u_{i,jk} \right] dS \quad (6.22)$$

After some integrations by part (see Appendix G), P_c has the following form:

$$P_c = \int_{\partial\mathcal{D}} \left[\tilde{T}_i u_i + \tilde{N}_i D u_i + \tilde{P}_i D^2 u_i \right] dS + \int_{\Gamma} \left[\tilde{R}_i u_i + \tilde{S}_i D u_i \right] ds + \tilde{F}_i u_i \quad (6.23)$$

where

- \tilde{T}_i , \tilde{N}_i and \tilde{P}_i represent respectively: a surface traction, normal double traction and normal triple traction (Extension of \tilde{N}_i to the following order) on the domain surface $\partial\mathcal{D}$.
- \tilde{R}_i and \tilde{S}_i are eventually a line traction and a line normal double traction on a line Γ over the surface $\partial\mathcal{D}$ (if any) where the tangent plane of $\partial\mathcal{D}$ is discontinuous.
- \tilde{F}_i is eventually a punctual traction on a point between two lines of discontinuous tangential vectors.

Note that if the higher order term \mathcal{L}_{ijk} vanishes, all the equations degenerate to the second gradient theory model (as presented by Germain (1973b)). Gathering all the integrals (P_i , P_v and P_c) in Equation 6.15, the following boundary conditions can be obtained by considering the surface integrals only:

$$\begin{aligned} \tilde{T}_i &= \tilde{\tau}_{ij}n_j - (D_l n_l)\xi_{ijk}n_k n_j + D_j(\xi_{ijk}n_k) + D_p n_p(\nu_{ijk} - \zeta_{ijkl,l})n_k n_j \\ &- D_j((\nu_{ijk} - \zeta_{ijkl,l})n_k) + D_p n_p D_s n_s n_k n_j \zeta_{ijkl} n_l - D_p n_p n_j D_k(\zeta_{ijkl} n_l) \\ &- D_j(D_p n_p n_k \zeta_{ijkl} n_l - D_k(\zeta_{ijkl} n_l)) + D_p(n_k \zeta_{ijkl} n_l D_j(n_p)) \end{aligned} \quad (6.24)$$

$$\begin{aligned} \tilde{N}_i &= -(\xi_{ijk} - \nu_{ijk} + \zeta_{ijkl,l})n_k n_j + D_p n_p n_k n_j \zeta_{ijkl} n_l \\ &- D_k(\zeta_{ijkl} n_l)n_j + D_p n_p n_j n_k \zeta_{ijkl} n_l - D_j(n_k \zeta_{ijkl} n_l) \end{aligned} \quad (6.25)$$

$$\tilde{P}_i = \zeta_{ijkl} n_l n_k n_j \quad (6.26)$$

where n_j represents a unit outward normal vector to a boundary.

6.2.4 Gradient-dependent plasticity model interpreted as a restricted micromorphic continuum

The enhanced kinematics considered in the first grade micromorphic continuum of degree two introduces 39 degrees of freedom: 3 components of the displacement field u_i , 9 components of the relative displacement gradient χ_{ij} and 27 components of the relative displacement second gradient χ_{ijk} . However, the gradient-dependent constitutive law formulated in Section 6.1 contains 4 degrees of freedom only: the displacement field u_i and the second-gradient of the volumetric strain $\nabla^2 \epsilon_v$. Thus, some assumptions should be taken in the formulation of the micromorphic medium to establish an equivalence with the gradient-dependent plasticity model. Raude et al. (2015) have presented the formulation of a second gradient dilation model, where the only additional degree of freedom is the gradient of the volumetric strain. In this section, a similar approach will be presented,

but for a "third gradient" dilation model. To do so, only the volumetric quantities of the higher-order stresses and kinematic variables should be considered. Hence, the following relations are defined:

- $s_{ij} = \delta_{ij}s$ and $\eta_{ij} = \frac{1}{3}\delta_{ij}\eta$
- $\nu_{ijk} = \delta_{ij}\nu_k$ and $\chi_{ij} = \frac{1}{3}\delta_{ij}\chi$
- $s_{ijk} = \delta_{ij}s_k$ and $\eta_{ijk} = \frac{1}{3}\delta_{ij}\eta_k$
- $\zeta_{ijkl} = \delta_{ij}\delta_{kl}\zeta$ and $\chi_{ijk} = \frac{1}{3}\delta_{ij}\chi_k$

The internal work density can thus be written as follows:

$$\delta w = \sigma_{ij}u_{i,j} + s\eta + \nu_k\chi_{,k} + s_k\eta_k + \zeta\chi_{k,k} \quad (6.27)$$

In addition, if the restrictions are considered:

$$\eta = u_{i,i} - \chi = 0 \quad \text{and} \quad \eta_k = \chi_{,k} - \chi_k = 0 \quad (6.28)$$

the internal work density expression is simplified to:

$$\delta w = \sigma_{ij}u_{i,j} + \nu_k\chi_{,k} + \zeta\chi_{k,k} \quad (6.29)$$

and the equilibrium equation becomes:

$$\sigma_{ij,j} - \delta_{ij}\nu_{k,kj} + \delta_{ij}\delta_{kl}\zeta_{,lkj} + f_i = 0 \quad (6.30)$$

where the higher order volumic external forces have been neglected (Ψ_{ij} and ξ_{ijk}).

6.2.5 Constitutive modelling

The yield surface is supposed to depend on the Cauchy stress state, the scalar stress state ζ (which is conjugated to the tensor of third gradient of displacement) and the hardening parameter e_v^{pl} :

$$F(\sigma_{ij}, \zeta, e_v^{pl}) = 0 \quad (6.31)$$

In addition, isotropic linear elastic behaviors are assumed for the higher-order stresses:

$$\dot{\nu}_k = AL^2\dot{\chi}_{,k} \quad (6.32)$$

and

$$\dot{\zeta} = BL^4\dot{\chi}_{k,k} \quad (6.33)$$

where A and B are additional higher-order elastic moduli and L is an internal length of the material. Since the first gradient of the volumetric strain is not considered in the developed gradient-dependent plasticity model, the modulus A can be taken equal to zero. The consistency equation $\dot{F} = 0$ leads to the following equation:

$$\frac{\partial F}{\partial \sigma_{ij}} \dot{\sigma}_{ij} + \frac{\partial F}{\partial \zeta} \dot{\zeta} + \frac{\partial F}{\partial \epsilon_v^{pl}} \dot{\epsilon}_v^{pl} = 0 \quad (6.34)$$

Following the steps described in Section 6.1 and considering the elastic law (Equation 6.33), the plastic multiplier can be expressed as:

$$\dot{\lambda} = \frac{b_{kl}^f \dot{\epsilon}_{kl} + \frac{\partial F}{\partial \zeta} BL^4 \dot{\chi}_{k,k}}{H_1} \quad (6.35)$$

and the following constitutive law is obtained:

$$\dot{\sigma}_{ij} = \left(C_{ijkl}^e - \langle 1 \rangle \frac{b_{ij}^g b_{kl}^f}{H_1} \right) \dot{\epsilon}_{kl} - \langle 1 \rangle \frac{b_{ij}^g \frac{\partial F}{\partial \zeta} BL^4}{H_1} \dot{\chi}_{k,k} \quad (6.36)$$

which is equivalent to the gradient-dependent plasticity constitutive law (Equation 6.7), since $\frac{\partial F}{\partial \zeta} BL^4 = \frac{\partial F}{\partial \nabla^2 \epsilon_v}$ and $\chi_{k,k} = u_{i,ikk} = \nabla^2 \epsilon_v$. The dependence of the yield surface on the higher-order stress state ζ is defined once its evolution with the second gradient of the volumetric strain is characterized. Notice that, if zero higher-order stresses are applied on the boundaries ($\nu_k = 0$ and $\zeta = 0$), the standard boundary conditions are obtained: $\tilde{T}_i = \sigma_{ij} n_j$, $\tilde{N}_i = 0$ and $\tilde{P}_i = 0$.

6.3 Calibration of the constitutive model

The constitutive law of the gradient-dependent plasticity model (Equations 6.33 and 6.36) can be seen as an expansion of a constitutive law in the Cauchy formulation. The calibration procedure of this enhanced model is thus done in several steps illustrated in Figure 6.1. A full characterization of this model requires a calibration of:

- The Cauchy continuum component, where the standard parameters are calibrated using the macroscopic mechanical data averaged over the samples.
- The internal length L , which is done by means of the Fast Fourier Transformation (FFT), applied on the porosity map in the initial state of the SML sample tested under relatively high confining pressure.
- The dependence of the yield surface on the second gradient of porosity which is considered as an internal variable, or equivalently on the higher order stress: $\frac{\partial F}{\partial \zeta}$. In this step, the second-gradient of porosity is evaluated from XRCT images at several

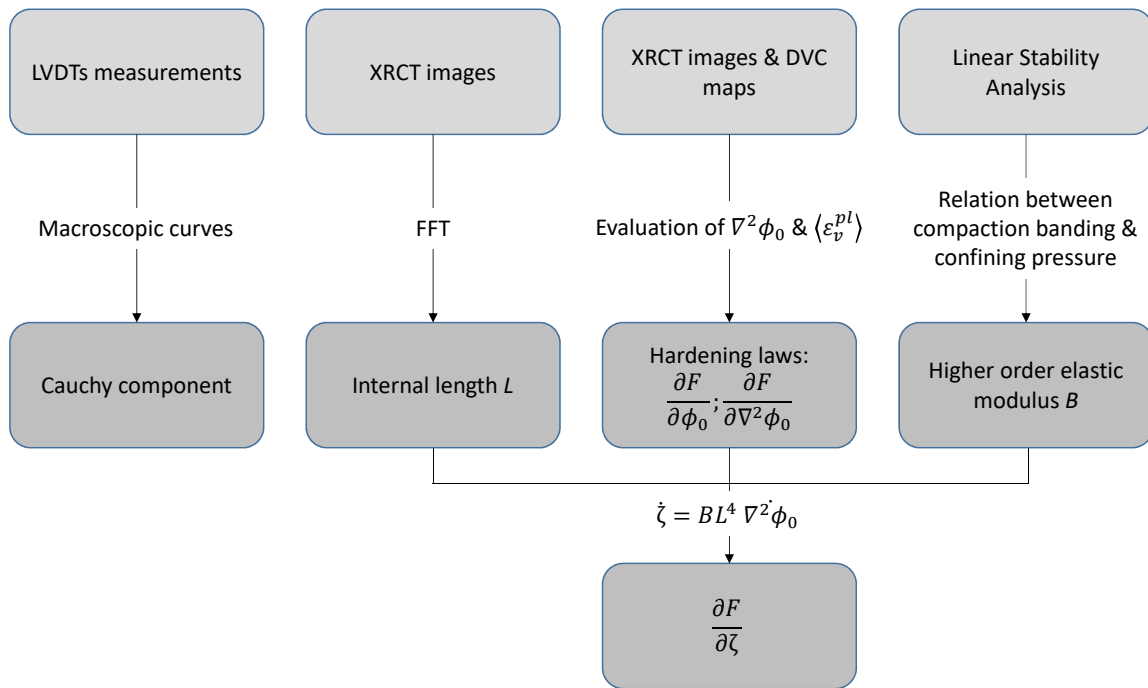


Figure 6.1: Calibration procedure of the gradient-dependent plasticity model.

states of deformation and the mean plastic volumetric strain is calculated from the DVC maps. The full procedure is explained in detail later.

- The higher order elastic modulus B , which is assessed by means of a Linear Stability Analysis (LSA) performed on the stress states of the yield surface in the initial state. The range of confining pressures, for which compaction bands can occur at the plasticity onset in axisymmetric triaxial loading, leads to an evaluation of the modulus B value.

Each of the following 4 sections is devoted to one of the steps stated above.

6.3.1 Calibration of the Cauchy component

Based on the measurements of the 6 LVDTs disposed around the samples and the stress sensors of the triaxial machine, stresses and strains are averaged at the scale of the samples and a standard calibration of the Cauchy parameters is performed:

Elastic parameters

The isotropic elastic behavior is characterized by two material parameters: the Young modulus E and the bulk modulus K . Going back to the Hooke law, one can easily demonstrate that:

- $\dot{p} = K \dot{\epsilon}_v^{el}$
- $\dot{q} = -\frac{E}{3} \dot{\epsilon}_a^{el}$

In absence of data on unloading/reloading cycles, the elastic moduli are simply evaluated on the initial linear part of the stress strain curves. The fitted parameters are: $E = 6230$ MPa and $K = 2810$ MPa (Figure 6.2).

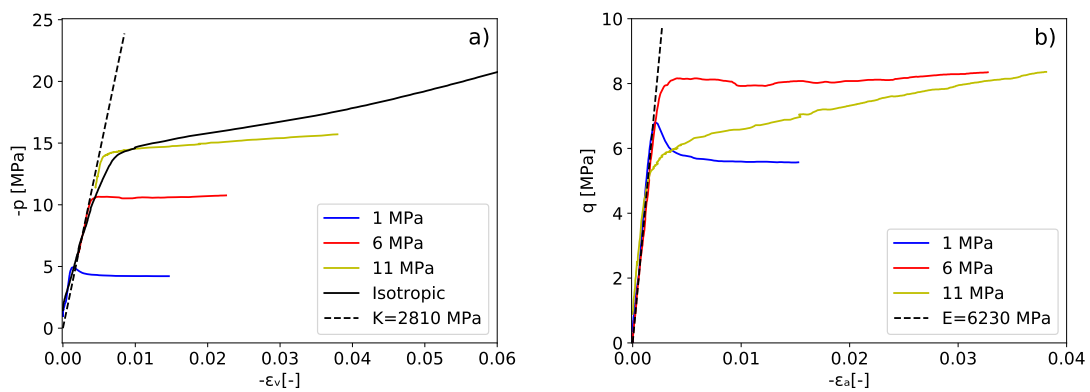


Figure 6.2: Fitting of elastic parameters.

Yield surface

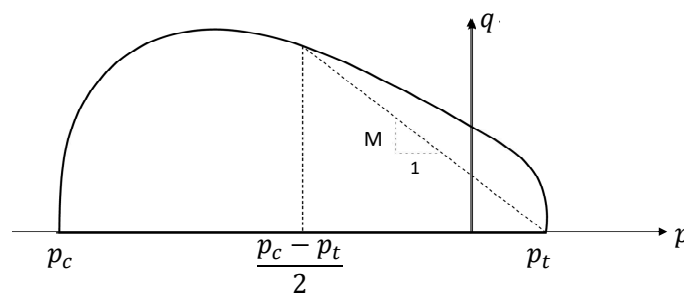


Figure 6.3: Schematic representation of the ACC yield surface.

The Asymmetric Cam-Clay (ACC) model seems to better fit the yield stresses presented in Figure 5.3. The complete derivation of this model is given in the Phd Thesis of Samudio (2017). The ACC model, which is an extension of the classical Modified Cam-Clay

(MCC) model (Roscoe et al. (1958), Schofield and Wroth (1968)), is more flexible and allows a displacement of the hardening-softening threshold. Figure 6.3 shows a schematic representation of the yield surface, whose expression is the following:

$$F = q^2 e^{kx} + M^2(p - p_c)(p + p_t) \quad (6.37)$$

where k is the hardening-softening threshold, p_c and p_t are the compression and traction isotropic yield stresses and $x = \frac{2p+p_t-p_c}{p_t+p_c}$ is the normalized mean stress with respect to the isotropic axis domain size. For $p = p_c$, x takes the value of 1 and for $p = -p_t$, x is equal to -1. In order to characterize the yield surface, 4 parameters should be evaluated: k , M , p_t and p_c . Note that for $k = 0$ and $p_t = 0$, the MCC model is recovered. Moreover, the ACC model is better adapted to numerical implementation since its expression (Equation 6.37) always takes real values and remains continuous in the real domain.

To fit the yield surface, the Orthogonal Distance Regression method from the `scipy.odr` python module is used. The method consists in minimizing the orthogonal distance between experimental data and the model curve. It has an advantage over the standard linear regression for a better fitting of points near vertical slopes. The values of the fitted parameters are given in Table 6.1 and the corresponding yield surface is plotted together with the yield stresses in Figure 6.4.

Table 6.1: Values of fitted parameters.

k [-]	M [-]	p_c [MPa]	p_t [MPa]
-0.7	0.92	-15.4	-0.7

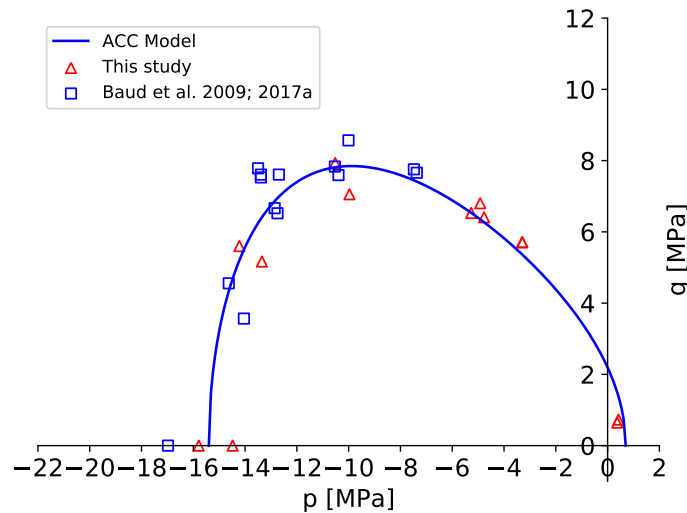


Figure 6.4: ACC yield surface fitted to the yield stresses data in the deviatoric vs mean stress plane: red triangles represent the data of this study & blue squares for Baud et al. (2009); Baud et al. (2017a) data.

Hardening laws

After the characterization of the initial yield surface, it is important to assess its evolution with accumulated plastic strain. A hardening is observed in hydrostatic loading experiments and in triaxial experiments at relatively high-confining pressures. On the other hand, a slight softening is observed at low confining pressures, whereas a perfectly plastic behavior occurs in the transitional regime. To describe these stress-dependent hardening/softening behaviors and to model the yield surface evolution, the two variables p_c and M are simply supposed to linearly evolve with the plastic internal variable ϵ_v^{pl} , whereas the variables p_t and k are assumed to remain constant. An increase of the parameter p_c (in absolute value) is responsible for a global hardening, whereas a decrease of the parameter M induces a softening mainly at low and intermediate confining pressures. The hardening laws are assumed to have the following forms:

$$\dot{p}_c = h_1 \dot{\epsilon}_v^{pl} \quad (6.38)$$

$$\dot{M} = h_2 \dot{\epsilon}_v^{pl} \quad (6.39)$$

The plastic volumetric deformation can be calculated from the total volumetric strain data along the experiments, since $\epsilon_v^{pl} = \epsilon_v^{total} - \epsilon_v^{el}$. For each experiment, the stress state is evaluated at several levels of ϵ_v^{pl} . Then, the hardening variables are calibrated as shown in Figure 6.5 and the corresponding hardening moduli are obtained:

$$h_1 = 1.53 \times 10^2 \text{ MPa} \quad (6.40)$$

$$h_2 = 4.21 \quad (6.41)$$

Although the softening behavior is slightly underestimated by the calibrated model, the hardening laws seem to give a very good representation for hydrostatic loading and for intermediate/high confinement triaxial tests. To improve the calibration, an evolution of one additional variable (p_t or k) can be considered. However, since modelling compaction bands is the objective of this study, the simple hardening laws given in Equations 6.38 and 6.39 are sufficient here.

Plastic potential

A simple Drucker-Prager plastic potential is used here:

$$g = \beta p + q \quad (6.42)$$

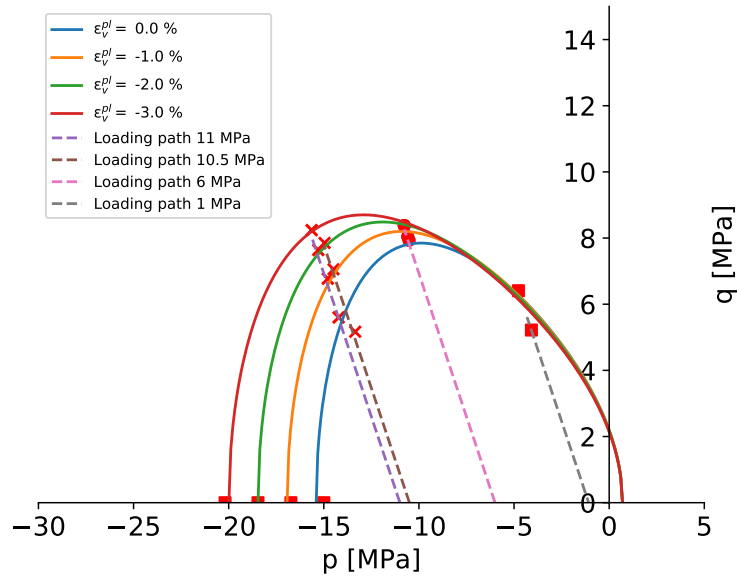


Figure 6.5: The yield surface evolution is calibrated on the stress states at different levels of hardening and for several confining pressures.

Noticing the flow rule ($\dot{\epsilon}_v^{pl} = \dot{\lambda} \frac{\partial g}{\partial p}$; $\dot{\gamma}^{pl} = \dot{\lambda} \frac{\partial g}{\partial q}$), the dilatancy parameter β links the rate of the plastic volumetric strain to the rate of the plastic shear strain magnitude as follows:

$$\beta = \frac{\dot{\epsilon}_v^{pl}}{\dot{\gamma}^{pl}} \quad (6.43)$$

This parameter is calculated for each experiment, since the quantities ϵ_v^{pl} and γ^{pl} can be evaluated at any loading state from the LVDTs measurements and the fitted elastic law. The experimental data of the plastic volumetric strain are plotted against the plastic shear strain magnitude for three different confining pressures in Figure 6.6. The black dashed line shows the model prediction for $\beta = -0.75$, which is retained in this study. In conclusion, the dilatancy parameter is assumed to be constant and independent on the stress state neither on the hardening level.

6.3.2 Internal length identification

The porosity of the SML evaluated at the scale of the cylindrical samples has been observed to be quite homogeneous with a mean value of 37.85% (Figure 3.2). In addition, the XRCT images recorded on four different samples in the initial state show the existence of two alternated high- and low-porosity zones at the centimetric scale (Sections 5.3.1; 5.4.1; 5.5.1 and 5.6.1). For instance, a histogram of porosity is computed on the upper part of the sample tested under high confining pressure, where compaction bands will be the most developed after loading (dashed domain in Figure 5.19). Figure 6.7 presents the results. The initial porosity can be subdivided into two families with mean values around 42% and

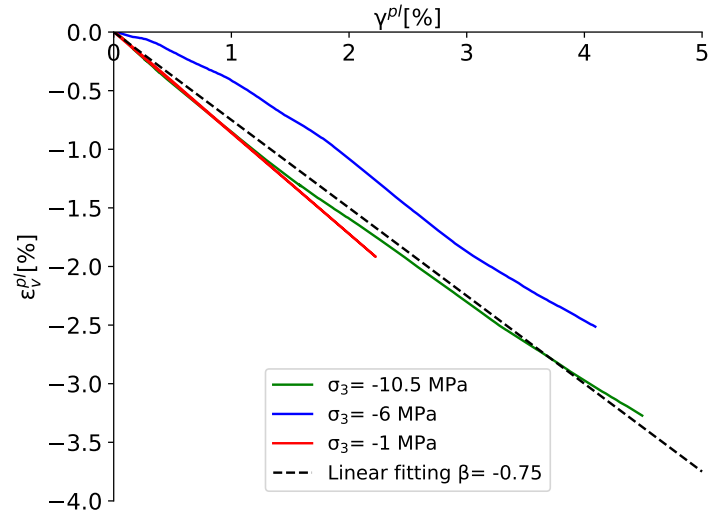


Figure 6.6: Plastic volumetric strain vs plastic shear strain magnitude for 3 different confining pressures. The dashed line represents the model prediction for $\beta = -0.75$.

35%. From these observations, the porosity heterogeneity can be schematically represented as a periodic pattern of high- and low-porosity cubic zones as shown in Figure 6.8. An elementary cell with side length L centered over a cube of high-porosity is defined as the primitive cell of the periodic lattice. Notice that the choice is not unique, but this elementary cell is appropriate to account for the second gradient of the porosity. In the frame of the gradient-dependent plasticity, this primitive cell is considered as the Representative Elementary Volume (REV) over which the porosity and its second gradient are evaluated and over which compaction banding is studied. In addition, for the sake of simplicity, the material in this study is assumed to have only one internal length L .

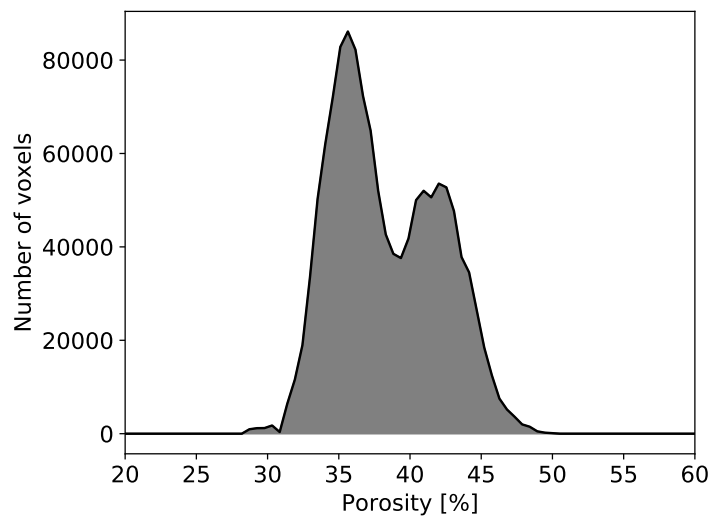


Figure 6.7: Porosity histogram computed over the selected heterogeneous domain in Figure 5.19.

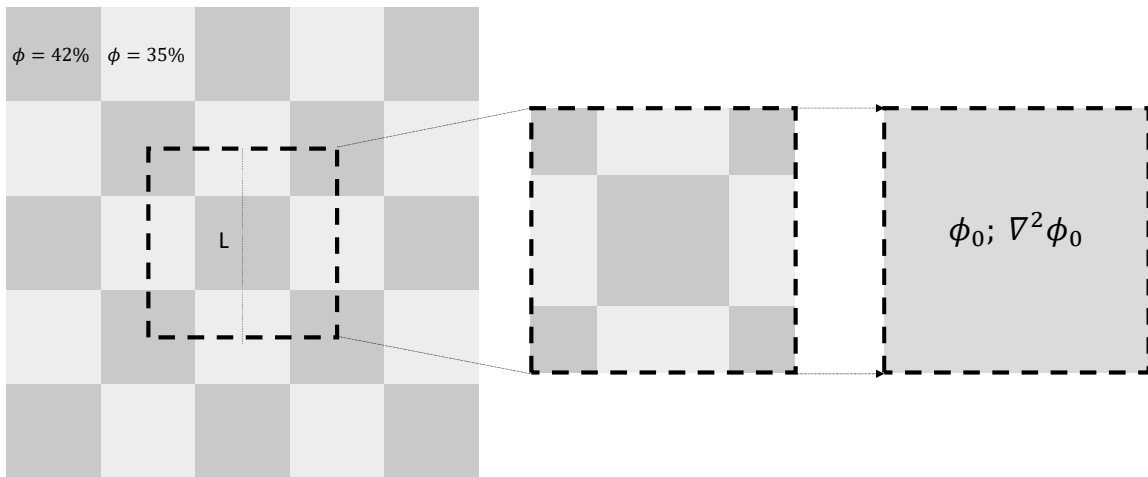


Figure 6.8: A schematical 2D representation of the assumed porosity heterogeneity. Darker areas represent high-porosity zones ($\phi=42\%$) and brighter areas represent low-porosity zones ($\phi=35\%$). A cubic elementary cell centered over a high-porosity zone is chosen as the primitive cell of the periodic lattice and over which the central porosity and its second-gradient are evaluated.

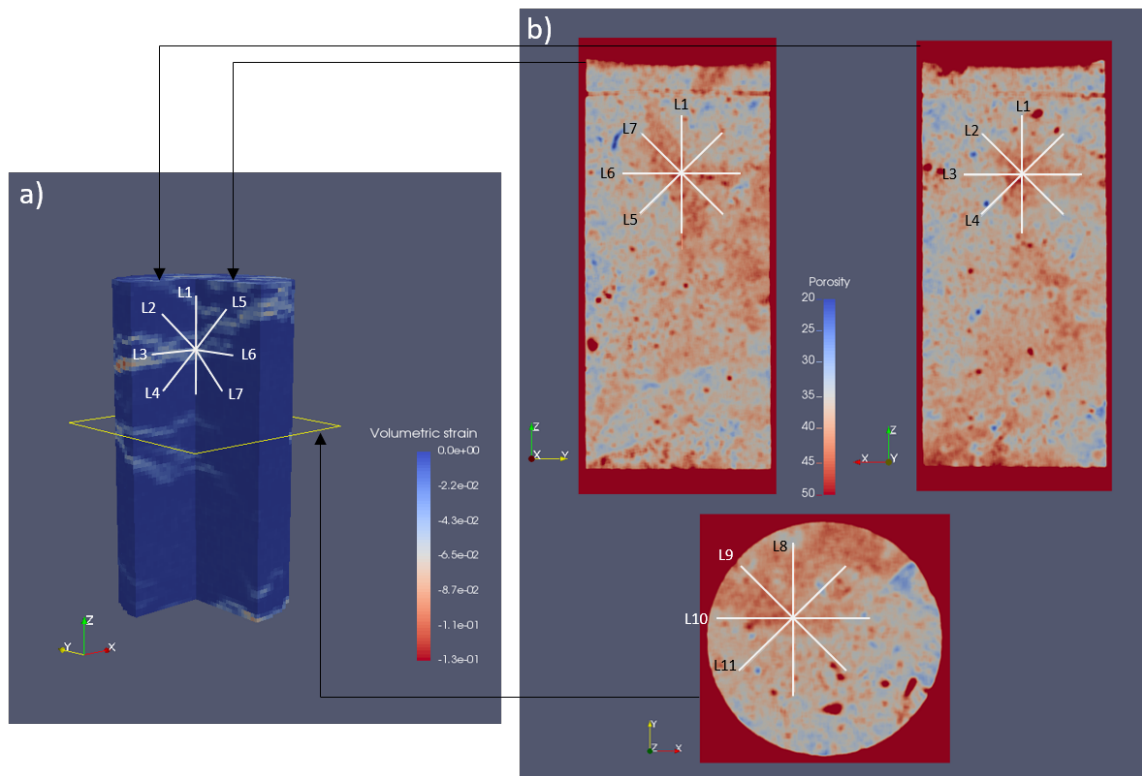


Figure 6.9: Definition of the lines over which porosity profiles are plotted.

In order to evaluate this internal length, a 3D FFT applied on volumic domains selected in the porosity maps may be applied. However, this tool is not yet implemented in FIJI. Therefore, a 1D FFT is simply applied in this study. The transformation is performed over several lines with different orientations defined in the porosity map in the initial state.

The objective of this study is not to fully characterize the porosity heterogeneity of the SML, but rather to study the effect of this heterogeneity on compaction banding. Therefore, the lines over which the porosity profiles are plotted, are intentionally chosen centered over high-porosity zones where compaction bands occur (Figure 6.9). In total, 11 lines are shown in three different planes: L1 to L4 in a XZ cross-section, L5 to L7 in a YZ cross-section. In addition, lines L8 to L11 are defined in a XY cross-section in the middle part of the sample.

Figure 6.10 shows all the plots of the porosity profiles over these lines. Between high- and low-porosity zones, the heterogeneity wavelength goes from around 18 to 25 mm. Then, the FFT is applied on these plots in order to select the dominant frequencies (Figure 6.11). For all the lines, except L5 and L11, the dominant frequency is 0.0417 mm^{-1} , which corresponds to a wavelength of 24 mm. However, for the lines L5 and L11, the dominant frequency is 0.083 mm^{-1} , which corresponds to a wavelength of 12 mm. This indicates, that the porosity distribution is not perfectly isotropic. But for the sake of simplicity, it will be considered as isotropic in this study, and the selected internal length is finally taken as $L = 24 \text{ mm}$.

6.3.3 Enhanced hardening laws

A comparison between the classical (Cauchy) constitutive law and the enhanced gradient-dependent plasticity model is presented in Table 6.2. The yield surface and the hardening laws for the Cauchy continuum formulation have been given in Section 6.3.1. Mean values of strains at the scale of the samples have been considered. However, in the gradient-dependent plasticity formulation, the REV (of cubic shape with side length L defined in Figure 6.8) is described by two internal variables: the porosity and its second gradient ($\nabla^2 \phi_0$ whose equivalency with $\chi_{k,k}$ has been shown in Section 6.2.5). Therefore, the yield surface should depend on these two internal variables, or equivalently on the higher order stress state ζ (Section 6.2.5).

In this section, the dependence of the yield surface on the higher order stress state ζ is sought. The yield surface is assumed to have the same expression as the one of the Cauchy formulation, with the same initial parameters presented in Table 6.1. Moreover, since the evolutions of the variables p_c and M are linear in terms of the mean plastic volumetric strain

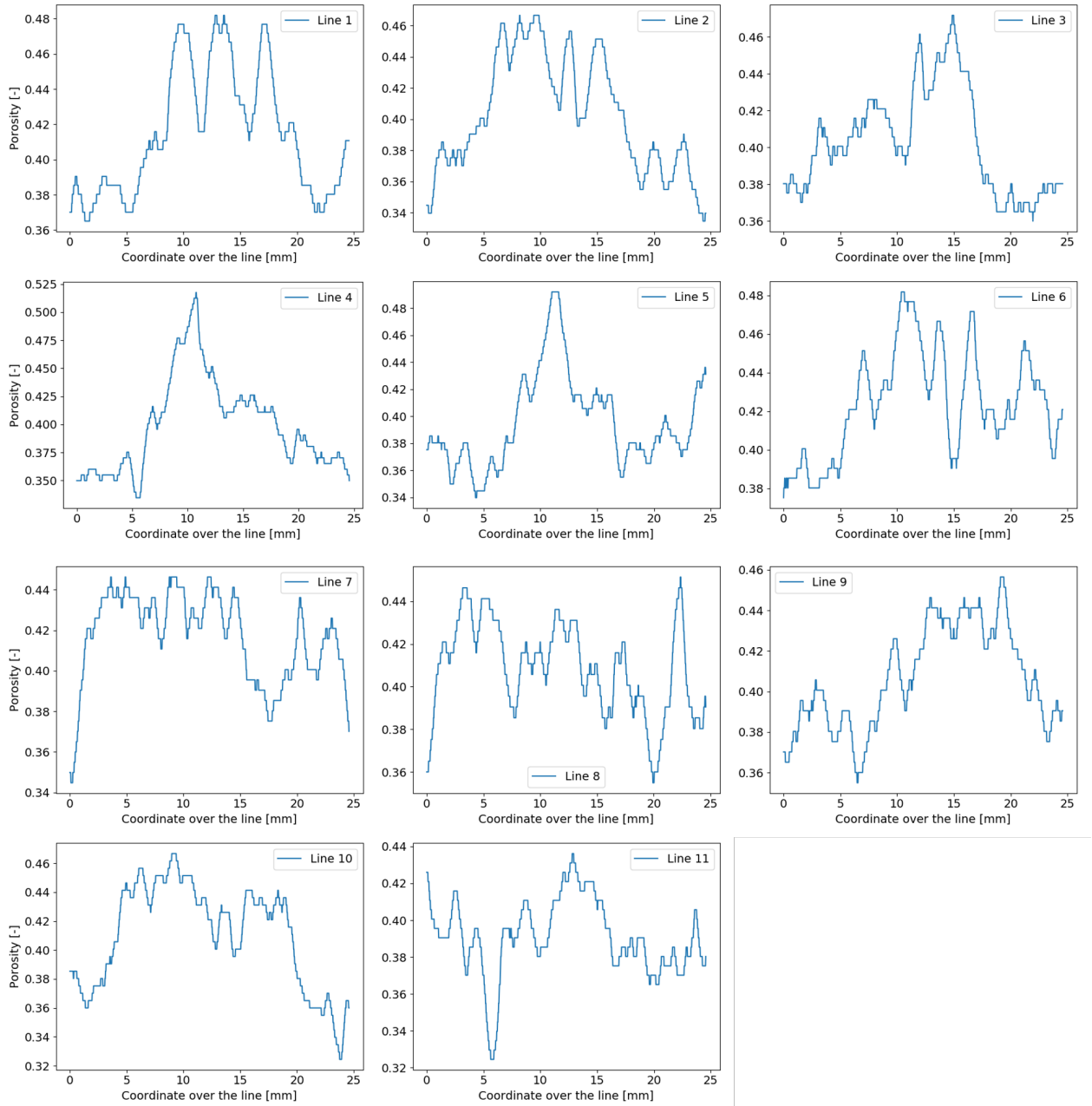


Figure 6.10: Porosity profiles plotted over the lines L1 to L11.

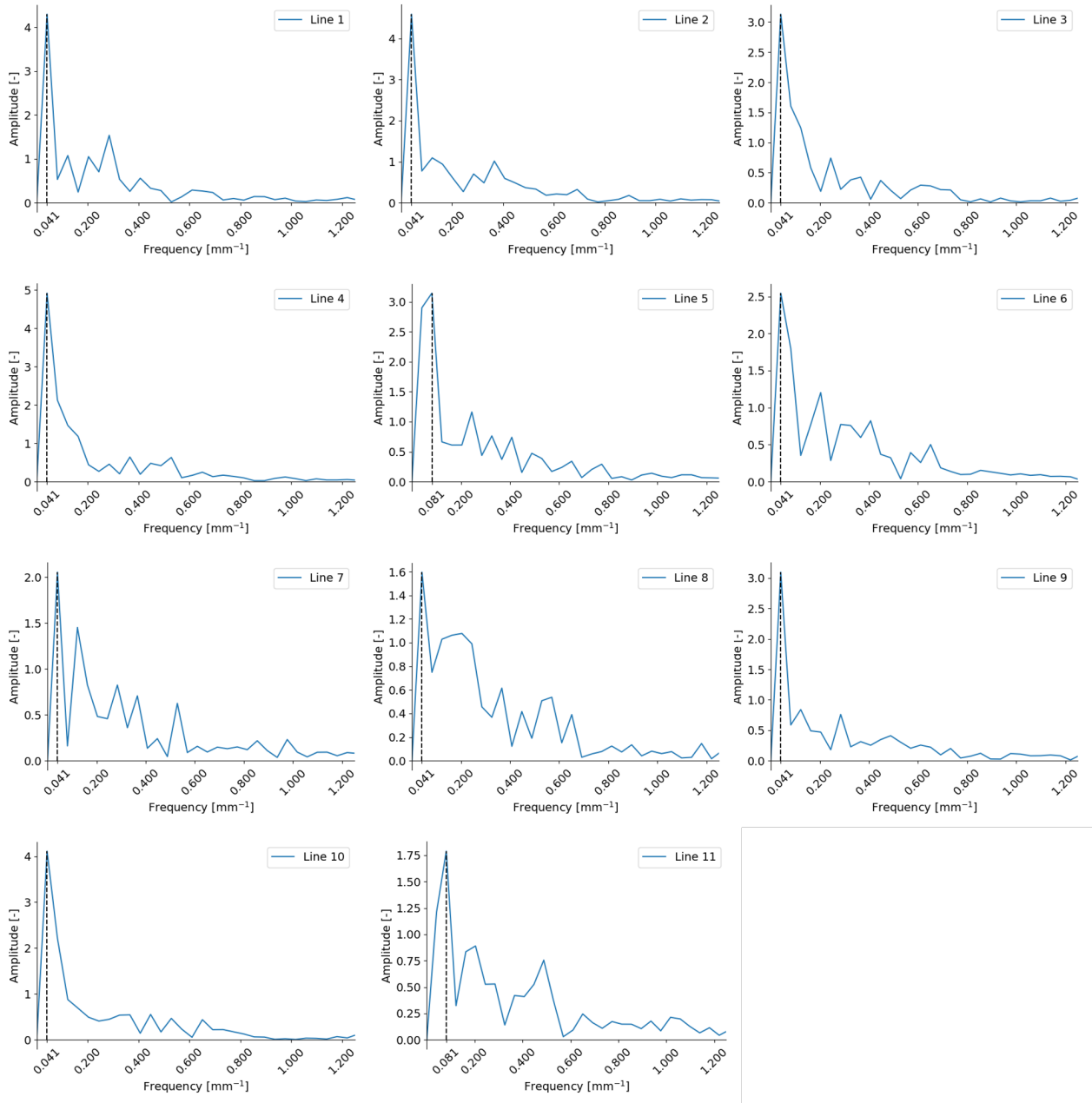


Figure 6.11: FFT applied on the porosity profiles over the lines L1 to L11.

in the Cauchy formulation, it would be reasonable to assume that the enhanced hardening laws are:

$$\dot{p}_c = \alpha_1(\dot{\phi}_0 + \frac{L^2}{24}\nabla^2\dot{\phi}_0) \quad (6.44)$$

$$\dot{M} = \alpha_2(\dot{\phi}_0 + \frac{L^2}{24}\nabla^2\dot{\phi}_0) \quad (6.45)$$

as the mean plastic volumetric deformation is approximated by the mean plastic porosity change $\langle \epsilon_v^{pl} \rangle \simeq \langle \phi^{pl} \rangle$, which is evaluated from the XRCT images by $\dot{\phi}_0 + \frac{L^2}{24}\nabla^2\dot{\phi}_0$ on a cubic element of side length equal to L (see Section 4.6). α_1 and α_2 are new hardening moduli that should be calibrated on the tests data.

Table 6.2: Comparison of the Cauchy and the gradient-dependent plasticity formulation.

	Cauchy formulation	Gradient-dependent plasticity formulation
Constitutive law	$\dot{\sigma}_{ij} = C_{ijkl}^{ep}\dot{\epsilon}_{kl}$	$\dot{\sigma}_{ij} = C_{ijkl}^{ep}\dot{\epsilon}_{kl} - \langle 1 \rangle \frac{b_{ij}^g \frac{\partial F}{\partial \zeta} BL^4}{H_1} \dot{\chi}_{k,k}$ $\dot{\zeta} = BL^4 \dot{\chi}_{k,k}$
Internal variables	$\langle \epsilon_v^{pl} \rangle$ $F(\sigma_{ij}, \langle \epsilon_v^{pl} \rangle)$	$\phi_0; \nabla^2\phi_0 \equiv \chi_{k,k}$ $F(\sigma_{ij}, \phi_0, \nabla^2\phi_0)$ or $F(\sigma_{ij}, \zeta, \phi_0)$
Yield surface	$q^2 e^{kx} + M^2(p - p_c)(p + p_t)$	$q^2 e^{kx} + M^2(p - p_c)(p + p_t)$
Hardening laws	$\dot{p}_c = h_1 \langle \dot{\epsilon}_v^{pl} \rangle$ $\dot{M} = h_2 \langle \dot{\epsilon}_v^{pl} \rangle$	$\dot{p}_c = \alpha_1(\dot{\phi}_0 + \frac{L^2}{24}\nabla^2\dot{\phi}_0)$ $\dot{M} = \alpha_2(\dot{\phi}_0 + \frac{L^2}{24}\nabla^2\dot{\phi}_0)$
Plastic potential	$g = \beta p + q$	$g = \beta p + q$

The procedure followed to calibrate the moduli α_1 and α_2 is presented in Figure 6.12. For a loading stage from the State i to the State $i + 1$, the porosity and its second gradient on a selected cubic domain can be evaluated from the porosity maps as presented in Section 4.6.2. On the other hand, the mean plastic volumetric strain can be evaluated over the same domain from the DVC map using the software Paraview. This allows to calculate the increments of p_c and M based on the macroscopic hardening laws given in Equations 6.38 and 6.39. This procedure can be repeated for different selected cubic domain in the same cylindrical sample and for several loading stages. In this way, the moduli α_1 and α_2 can be fitted as shown in the following.

The sample tested under high confining pressure (see Section 5.4) is considered thereafter. Two cubic domains, centered over high-porosity zones, are selected inside the sample as shown in Figure 6.13. The porosity and its second-gradient are evaluated for each REV in

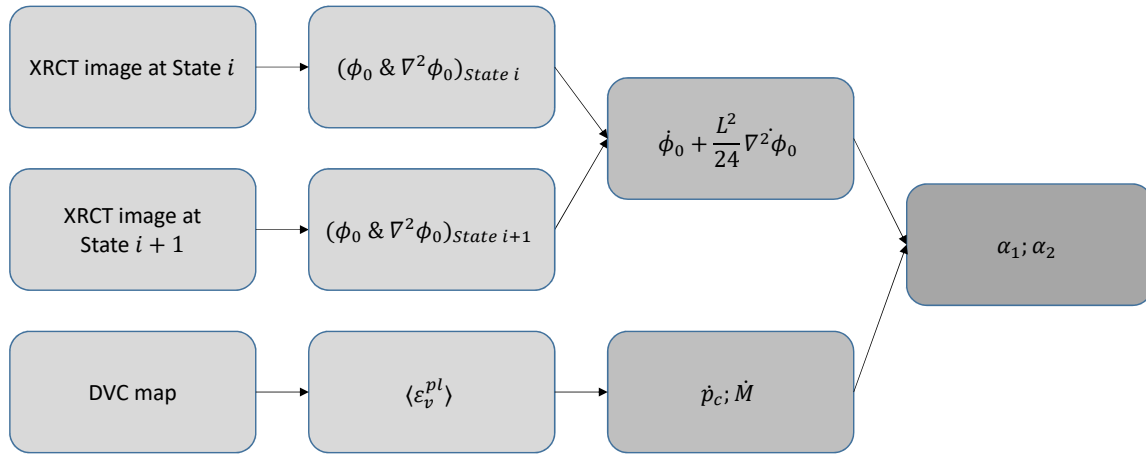


Figure 6.12: Procedure followed to calibrate the hardening moduli α_1 and α_2 for a loading stage from State i to $i + 1$.

the initial state and after the first and second loading stages. The values are gathered in Table 6.3 and plotted in Figure 6.14. It is observed that during the compaction banding phenomenon, both internal variables are decreasing (in absolute value) which indicates that the material is becoming more homogeneous and less porous in accordance with the observations described in the previous chapter. The plastic volumetric strain is averaged over each REV for each loading stage and the values are given in Table 6.4. Figure 6.15 shows the calculated data with the fitted values $\alpha_1 = 150.9$ MPa and $\alpha_2 = 4.15$.

These fitted moduli are very close to those obtained for the macroscopic hardening laws (Equations 6.38 and 6.39). In other words, the mean value of the plastic porosity reduction measured from the XRCT images is very close to the mean plastic volumetric deformation measured by means of the LVDTs or the DVC maps. This confirms that the solid matrix plastic deformation can be ignored with respect to the porosity evolution and corroborates the assumption made in Section 6.1.

Furthermore, it is important to note that the REVs are assumed to preserve their cubic shapes when ϕ_0 and $\nabla^2 \phi_0$ are calculated, even in the deformed states. This assumption, which is adopted to simplify the calibration procedure, is acceptable due to the low deformation levels of the REVs (in the order of 2 to 3% as presented in Table 6.4). In addition, the high confining pressure test is found to be sufficient to calibrate the gradient-dependent model, since several REVs can be selected inside the sample. The size of the REVs are considered large enough to have the same stress states as the ones evaluated for the cylindrical sample¹. Moreover, the plastic potential for this enhanced model is supposed to be identical to the one of the underlying Cauchy continuum (Equation 6.42). This means, that the second-gradient of the porosity change is purely elastic since $\dot{\chi}_{k,k}^{pl} = \dot{\lambda} \frac{\partial g}{\partial \zeta} = 0$.

¹The largest cube that lays inside a cylinder of 4 cm in diameter has a side length $= \frac{4}{\sqrt{2}} = 2.8$ cm. The considered cubic domains have comparable dimensions ($L = 2.4$ cm).

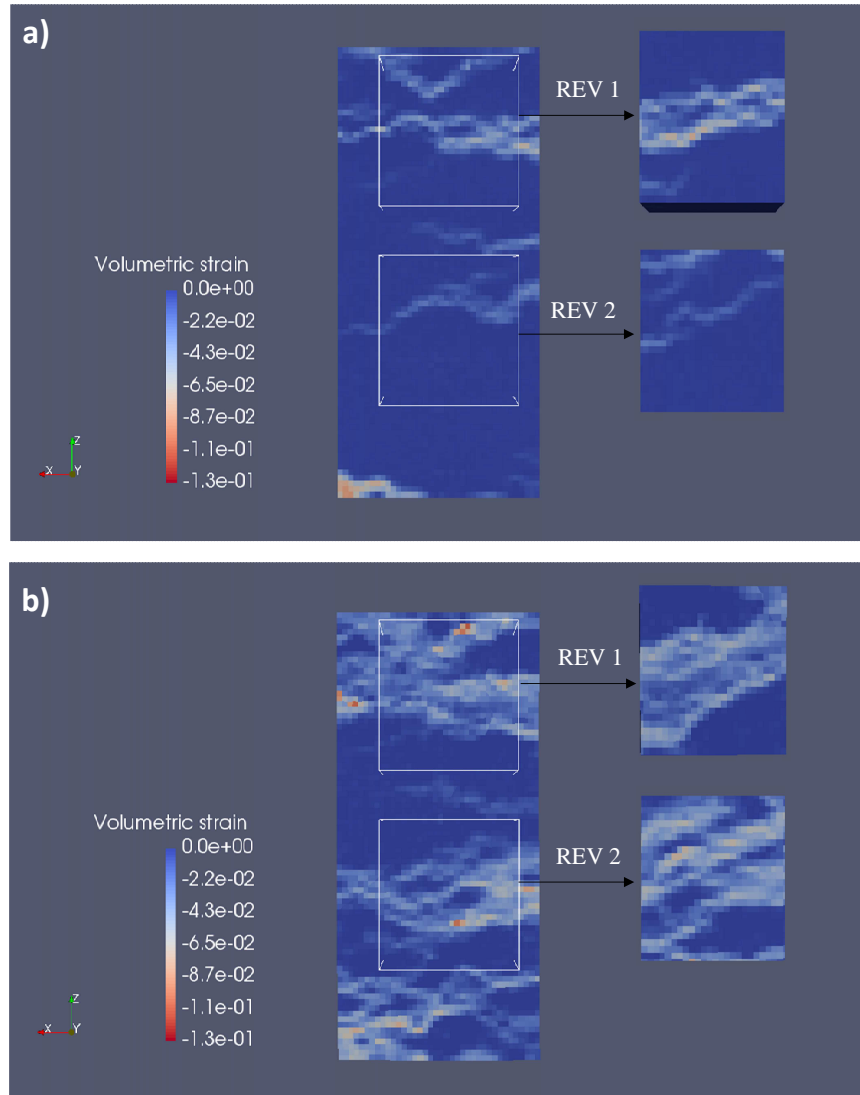


Figure 6.13: Two selected cubic elements, over which the mean plastic volumetric deformation and the internal variables are evaluated: **a)** during the first loading stage; **b)** during the second loading stage.

Table 6.3: Values of ϕ_0 and $\nabla^2\phi_0$ over the two selected REV's in the initial state and after each stage of loading.

REV	State	ϕ_0 [%]	$\nabla^2\phi_0 \times 10^4$ [mm^{-2}]
1	Initial	39.48	-7.28
1	After Stage 1	37.91	-4.82
1	After Stage 2	36.70	-4.33
2	Initial	38.86	-2.80
2	After Stage 1	37.84	-1.65
2	After Stage 2	36.74	-0.72

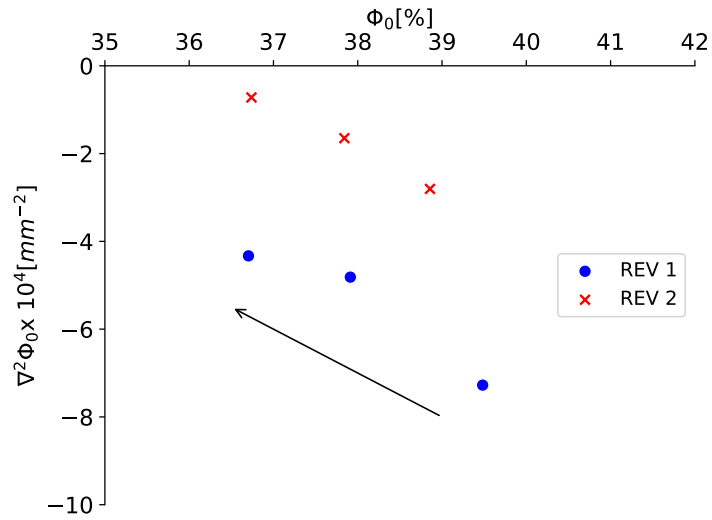


Figure 6.14: Evolution of ϕ_0 and $\nabla^2\phi_0$ for each REV from the initial state, to the states after the first and second loading stages. The arrow shows the direction of the evolution with loading.

Table 6.4: Mean plastic volumetric strain for each REV in each loading stage.

REV	Loading Stage	$\langle \epsilon_v^{pl} \rangle$ [%]
1	1	-0.74
1	2	-1.44
2	1	-0.24
2	2	-1.54

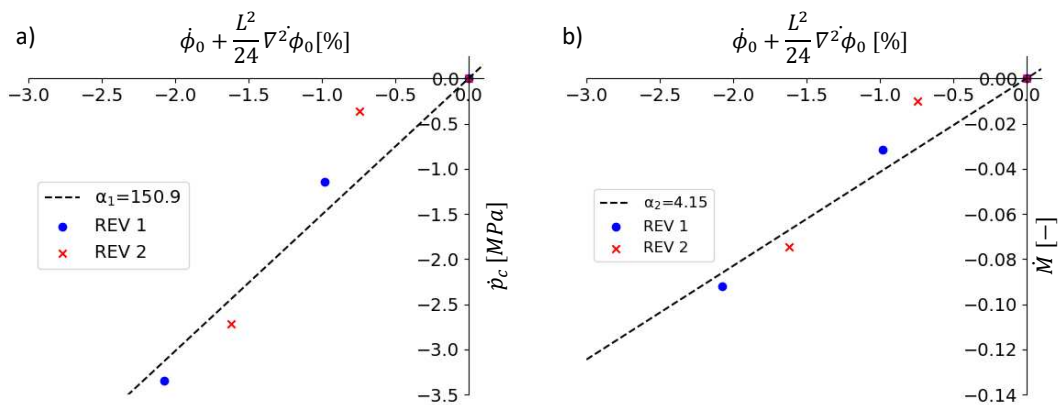


Figure 6.15: Evolution of \bar{p}_c and \dot{M} vs $\phi_0 + \frac{L^2}{24}\nabla^2\phi_0$. The dashed lines represent the fitted hardening laws obtained with the following moduli $\alpha_1 = 150.9$ MPa and $\alpha_2 = 4.15$.

Yield surface dependence on the higher order stress

The yield surface dependence on the porosity and its second gradient has been established. Taking into account the elastic law for the higher order stress (Equation 6.33), the new yield surface can be characterized easily:

$$F = q^2 e^{kx_1} + M^2 \left(p - \frac{\alpha_1}{24} \frac{\zeta}{BL^2} - p_c \right) (p + p_t) + \left[\left(\frac{\alpha_2}{24} \frac{\zeta}{BL^2} \right)^2 + \frac{\alpha_2 M}{12} \frac{\zeta}{BL^2} \right] \left(p - \frac{\alpha_1}{24} \frac{\zeta}{BL^2} - p_c \right) (p + p_t) = 0 \quad (6.46)$$

with

$$x_1 = \frac{2p - \frac{\alpha_1}{24} \frac{\zeta}{BL^2} - p_c + p_t}{\frac{\alpha_1}{24} \frac{\zeta}{BL^2} + p_c + p_t} \quad (6.47)$$

where $p_t = -0.7$ MPa and $k = -0.7$ are supposed to remain constant and:

$$p_c = -15.4 + 1.51 \times 10^2 \dot{\phi}_0 \quad (6.48)$$

and

$$M = 0.92 + 4.15 \dot{\phi}_0 \quad (6.49)$$

6.3.4 Linear stability analysis - Calibration of the parameter B

To have a complete characterization of the model, the higher-order elastic modulus B must be evaluated. As it will be shown in the following, this parameter plays a role on the onset of compaction bands. Therefore, a LSA of the triaxial test is performed to back analyze the experiments and calibrate this parameter. The principles of the analysis have been introduced in Section 2.4.2. For the homogeneous solution, the equilibrium equation can be written as:

$$\sigma_{ij,j}^* + \delta_{ij} \delta_{kl} \zeta_{,lkj}^* = 0 \quad (6.50)$$

Considering the constitutive law for a small perturbation of the system (Equations 6.33 and 6.36), the momentum balance can be written as:

$$\left(C_{ijkl}^e - \langle 1 \rangle \frac{b_{ij}^g b_{kl}^f}{H_1} \right) \Delta u_{k,lj} - \langle 1 \rangle \frac{b_{ij}^g \frac{\partial F}{\partial \zeta} L^2}{H_1} \Delta u_{p,pkkj} + \delta_{ij} \delta_{kl} B L^4 \Delta u_{p,prrrjkl} = \rho \Delta \ddot{u}_i \quad (6.51)$$

The formation of compaction bands with a normal vector oriented in the direction 1 is investigated. Thus, the perturbation applied to the equilibrium solution u_i^* is assumed to take the following form:

$$\Delta u_i = U_i e^{i \frac{2\pi}{\lambda} x_1 + st} \quad (6.52)$$

with $U_2 = U_3 = 0$. After some algebraic manipulations, the following characteristic equation is obtained:

$$\left[-\left(\frac{2\pi}{\lambda}\right)^2 C_{1111}^{ep} - \left(\frac{2\pi}{\lambda}\right)^4 \langle 1 \rangle \frac{b_{11}^g \frac{\partial F}{\partial \frac{\zeta}{BL^2}} L^2}{H_1} - \left(\frac{2\pi}{\lambda}\right)^6 BL^4 - \rho s^2 \right] U_1 e^{i\frac{2\pi}{\lambda} x_1 + st} = 0 \quad (6.53)$$

Cauchy continuum

At first, a Cauchy continuum is considered. The characteristic equation in this case is reduced to the following form:

$$\left[-\left(\frac{2\pi}{\lambda}\right)^2 C_{1111}^{ep} - \rho s^2 \right] U_1 e^{i\frac{2\pi}{\lambda} x_1 + st} = 0 \quad (6.54)$$

Non trivial solutions exist for $s = \pm \frac{2\pi}{\lambda} \sqrt{\frac{-C_{1111}^{ep}}{\rho}}$. In addition, these solutions are unstable, if the real part of s takes positive values. It is obvious, that if C_{1111}^{ep} is positive, s is purely imaginary. This is the case in the elastic domain because $C_{1111}^{ep} = C_{1111}^e = K + \frac{4}{3}G$ can only take positive values, where G and K are the elastic shear and bulk moduli. Then, the sign of this component on the yield surface is inspected with respect to the confining pressure for axisymmetric compression loading (Table 6.5). The initial yield surface (i.e. for zero accumulated plastic volumetric strain) is considered here. In other words, the possibility of instability when the stress state first reaches the yield surface is inspected. It is found that for confining pressures greater than 11.9 MPa (in absolute value), the sign of C_{1111}^{ep} is negative and compaction banding can occur. The growth coefficient is plotted in Figure 6.16 against the perturbation wavelength for an axisymmetric compression under 12 MPa of confining pressure. A typical result of the Cauchy continuum is observed, where the smallest wavelength is the dominant one.

Table 6.5: The component C_{1111}^{ep} evaluated at the plasticity onset of axisymmetric triaxial compressions under different confining pressures. The last column indicates if a compaction band (CB) is formed or not.

σ_3 [MPa]	C_{1111}^{ep} [MPa]	CB formation
-15.0	-175.24	Yes
-14.0	-109.72	Yes
-13.0	-55.83	Yes
-12.0	-5.69	Yes
-11.9	-0.72	Yes
-11.8	4.27	No
-11.0	44.67	No
-10.0	97.87	No
-9.0	155.98	No

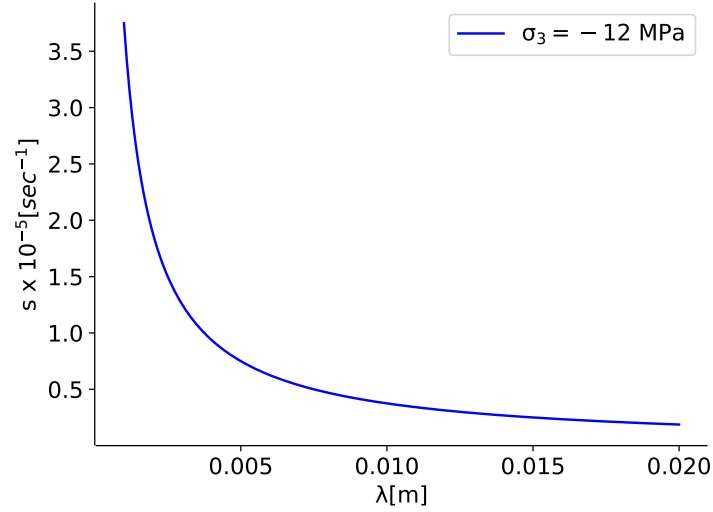


Figure 6.16: The growth coefficient s plotted against the perturbation wavelength λ in a Cauchy continuum for a confining pressure of $\sigma_3 = -12$ MPa. ρ is taken equal to 1600 kg/m^3 .

Comparison with Issen and Rudnicki (2000) criterion for compaction banding In their paper, Issen and Rudnicki (2000) have considered an elastic-plastic constitutive law of the form:

$$L_{ijkl}^{ep} = L_{ijkl}^{el} - \frac{(G \frac{s_{ij}}{q} + \beta K \delta_{ij})(G \frac{s_{kl}}{q} + \mu K \delta_{kl})}{h + G + \mu \beta K} \quad (6.55)$$

In the frame of the bifurcation theory, they have given the conditions for which compaction bands can form in axisymmetric compression loading:

$$h < h_{cr} = \left(-\frac{1 + \nu}{3(1 - \nu)} \left(1 + \frac{2}{\sqrt{3}} \mu \right) \left(1 + \frac{2}{\sqrt{3}} \beta \right) \right) G \quad (6.56)$$

and for $\beta + \mu < -\sqrt{3}$. The critical hardening modulus can be easily evaluated at a stress state on the yield surface. However, the expression of the elastic-plastic matrix (Equation 6.8) should be re-written in order to define the appropriate hardening modulus. Noticing that $\frac{\partial p}{\partial \sigma_{ij}} = \frac{1}{3} \delta_{ij}$ and $\frac{\partial q}{\partial \sigma_{ij}} = \frac{s_{ij}}{2q}$, one can show that the elastic-plastic matrix (Equation 6.8) can be re-written in the following form:

$$C_{ijkl}^{ep} = C_{ijkl}^{el} - \frac{(G \frac{s_{ij}}{q} + \beta K \delta_{ij})(G \frac{s_{kl}}{q} + \mu K \delta_{kl})}{G + \mu \beta K - \beta \frac{\partial F}{\partial \epsilon_v^{pl}} \frac{1}{\frac{\partial F}{\partial q}}} \quad (6.57)$$

By identification with the constitutive law of Issen and Rudnicki (2000), the hardening modulus can be defined as:

$$h = -\beta \frac{\partial F}{\partial \epsilon_v^{pl}} \frac{1}{\frac{\partial F}{\partial q}} \quad (6.58)$$

Finally, the hardening modulus can be evaluated from the macroscopically calibrated model. These data with the critical moduli of Issen and Rudnicki (2000) are gathered in Table 6.6. In accordance with the results shown previously, compaction bands can only form for

axisymmetric compression under confining pressures greater than 11.9 MPa (in absolute value).

Table 6.6: Hardening modulus evaluated from the Cauchy constitutive law and compared to the critical values given by Issen and Rudnicki (2000) for several confining pressures. The last column indicates if a compaction band (CB) is formed or not.

σ_3 [MPa]	h [MPa]	h_{cr} [MPa]	$\beta + \mu + \sqrt{3}$	CB formation
-15.0	2326	3632	-19.6	Yes
-14.0	693	969	-5.13	Yes
-13.0	401	493	-2.55	Yes
-12.0	271	278	-1.39	Yes
-11.9	262	263	-1.31	Yes
-11.8	253	248	-1.22	No
-11.0	194	150	-0.69	No
-10.0	142	60	-0.21	No
-9.0	104	-6	0.15	No

Micromorphic continuum

The higher-order terms are now considered in the characteristic equation. The growth coefficient s , corresponding to non-trivial solutions, is calculated in terms of the normalized wavelength $\lambda^* = \frac{\lambda}{L}$ at any stress state of the yield surface:

$$s = \pm \frac{1}{L\sqrt{\rho}} \sqrt{-(2\pi)^2 C_{1111}^{ep} \frac{1}{\lambda^{*2}} - (1)(2\pi)^4 b_{11}^g \frac{\partial F}{\partial \frac{\zeta}{BL^2}} \frac{1}{H_1} \frac{1}{\lambda^{*4}} - (2\pi)^6 B \frac{1}{\lambda^{*6}}} \quad (6.59)$$

Notice that the quantity $\frac{\partial F}{\partial \frac{\zeta}{BL^2}}$ is independent of both B and L at the onset of strain localization, since $\zeta = 0$ for the homogeneous solution². This is done in order to study the effects of the two parameters. It is obvious that when the internal length tends towards zero, the growth coefficient takes the same expression as in the Cauchy continuum case ($s = \pm \frac{2\pi}{\lambda} \sqrt{\frac{-C_{1111}^{ep}}{\rho}}$). The effect of the elastic modulus B is explored in Figure 6.17 for a stress state on the yield surface which corresponds to an axisymmetric compression under 12 MPa of confinement. When B tends towards zero, the dominant perturbation wavelength λ_{max} tends to be zero, similarly to the Cauchy continuum. However, when B vanishes with a non-zero internal length L , the micromorphic continuum does not degenerate to a Cauchy continuum, since the second term under the square root in Equation 6.59 does not vanish. The impact of this observation will be discussed in the next paragraph. With increasing

²The expression of the yield surface F is given in Equation 6.46. For $\zeta = 0$, the derivative $\frac{\partial F}{\partial \frac{\zeta}{BL^2}} = q^2 k \frac{-\frac{\alpha_1}{24}(2p+2p_t)}{p_c+p_t} e^{kx_1} + M^2(-\frac{\alpha_1}{24})(p+p_t) + \frac{\alpha_2 M}{12}(p-p_c)(p+p_t)$ is independent of both B and L .

values of B , the dominant wavelength tends to increase. Consequently, the band thickness³ $d = \frac{\lambda_{max}}{2}$ becomes greater.

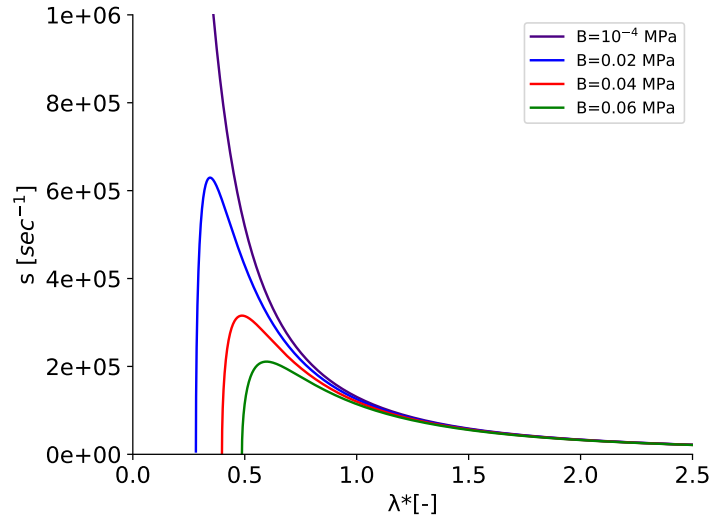


Figure 6.17: Growth coefficient s vs the normalized perturbation wavelength λ^* in the micromorphic continuum at the stress state corresponding to an axisymmetric compression under 12 MPa of confining pressure. ρ is taken equal to 1600 kg/m³ and L equal to 24 mm.

Effect of the confining pressure on compaction banding

In case of a Cauchy continuum, it is observed that compaction bands can form at the plasticity onset for axisymmetric compression under confinements greater than 11.9 MPa. It is interesting to explore to what extent compaction bands can form in the micromorphic continuum. Figure 6.18 shows the plots of the growth coefficient under several confining pressures in two cases: for $B = 0.08$ MPa and $B = 0.02$ MPa. In the first case, compaction bands are observed to occur for confinements higher than 9.2 MPa. However, for a lower value of B (0.02 MPa), the range of confining pressures allowing compaction banding is larger (confining pressure greater than 7.2 MPa). Notice that, when B tends towards zero, compaction bands occur at the plasticity onset for all the possible confining pressures. This result reflects the difference between the micromorphic continuum with vanishing value of B and the Cauchy continuum.

In addition, it appears that the internal length does not contribute in controlling the range of confining pressures for which compaction bands can occur. In the plane (s vs λ^*), the internal length only scales the dominant wavelength. Indeed, it does not affect the range of perturbation wavelengths corresponding to positive s for a given confinement as shown in

³At the band boundaries, the displacement field should be continuous. Thus, if the perturbation has the form $\Delta u_1(x_1) = U_1 \cos(\frac{2\pi}{\lambda} x_1) e^{st}$, the boundary conditions lead to $\Delta u_1(\pm \frac{d}{2}) = 0$, where d is the band thickness. Hence, $d = \frac{\lambda}{2}$.

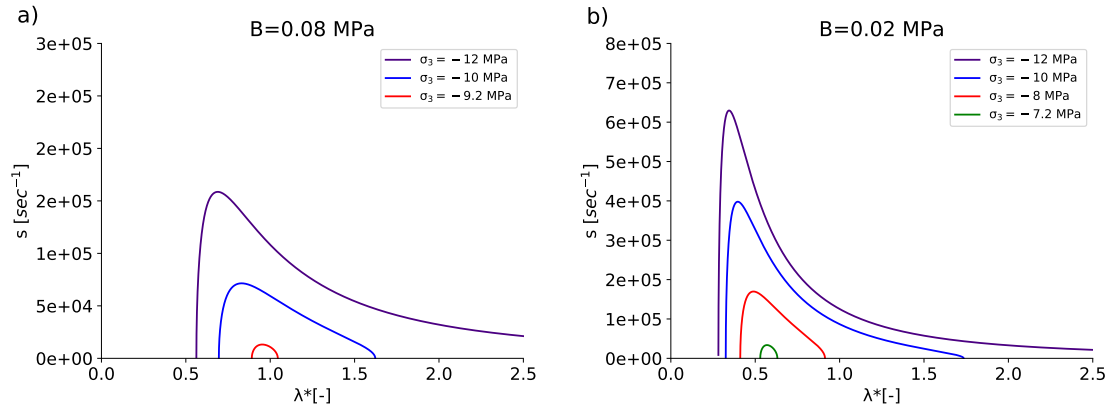


Figure 6.18: Growth coefficient s vs the normalized perturbation wavelength λ^* under several confining pressures for a) $B=0.08$ MPa; b) $B=0.02$ MPa. ρ is taken equal to 1600 kg/m^3 and L equal to 24 mm.

Figure 6.19. For several confinements and values of B , an internal length of 40 mm induces a scaling ratio of 0.5 with respect to the results with an internal length of 20 mm.

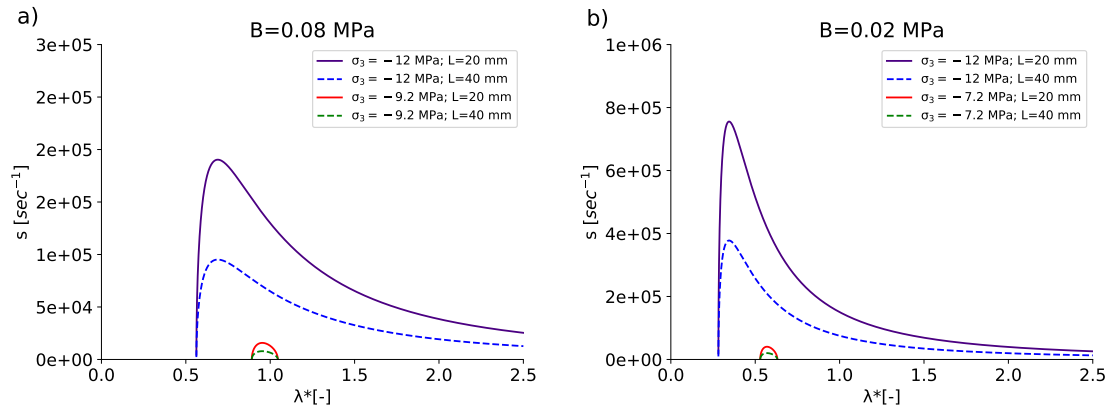


Figure 6.19: Growth coefficient s vs the normalized perturbation wavelength λ^* under several confining pressures and for different internal lengths ($L = 20$ mm and $L = 40$ mm) in two cases: a) $B=0.08$ MPa; b) $B=0.02$ MPa. ρ is taken equal to 1600 kg/m^3 .

Accordingly, the elastic modulus B is the only higher-order parameter that controls the range of confining pressures for which compaction bands occur at the plasticity onset. Figure 6.20 shows the effect of B on the range extension. For instance, if $B = 0.008$ MPa, compaction bands can form for confinements higher than 6 MPa. Based on the experimental observations performed in the previous chapter, compaction bands are identified in the sample tested at 10.5 MPa of confinement. However, no compaction bands are observed in the sample tested at 6 MPa of confinement. In addition, Baud et al. (2017a) have shown by means of acoustic emission measurements that compaction bands can form in a SML sample tested at 9 MPa of confining pressure in dry condition. Assuming that the confining pressure threshold for the formation of compaction bands is at the mid-point of these two values (i.e.

7.5 MPa), the corresponding value of the parameter B would be 0.025 MPa, which will be retained for the numerical modelling.

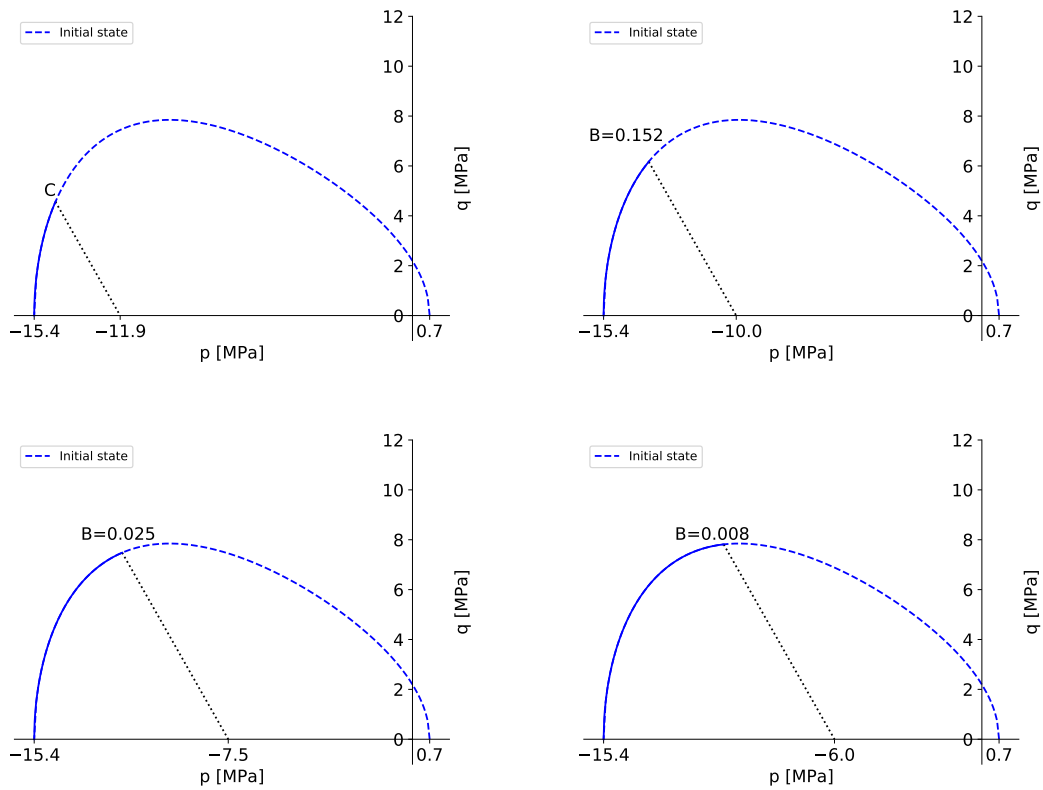


Figure 6.20: Ranges of confining pressures that allow compaction banding in the Cauchy continuum (C) and in the micromorphic continuum (for several values of B). The solid lines indicate the stress states for which compaction bands occur. L is taken equal to 24 mm.

6.4 Numerical implementation

The above constitutive model is implemented in the finite element code, *Numerical Geolab* (Stefanou, 2018), as a general micromorphic continuum in order to simulate the formation of compaction bands and follow their evolution. This platform uses the Fenics library for finite element generation and the volume is meshed using tetrahedral elements with linear interpolation shape functions and using reduced integration. 1D simulations are performed on parallelepipedic samples with a height equal to the internal length L and a width of $L/10$. Looking for 1D deformation modes, the sample is discretized in the axial direction whereas only one element is considered in the lateral directions. Triaxial compression tests are simulated, where a confining pressure is imposed on the lateral boundaries and controlled axial displacement is imposed on the upper boundary. As a first step, the results of the Cauchy formulation implementation are presented and compared with results of the previous section. Then, the micromorphic continuum is considered.

6.4.1 Cauchy continuum

Using one element in the axial direction, triaxial compression is applied under several confining pressures. In addition, a homogeneous semi-analytic solution is developed using the Mathematica platform. The results are superimposed with the experimental data in Figure 6.21 in the p vs ϵ_v and q vs γ planes. For all the loading cases (hydrostatic and triaxial loading under 11, 6 and 1 MPa of confinement), the numerical results are identical to the predicted homogeneous solution, which validates the implementation of the model for the Cauchy continuum. On the other hand, the model is observed to well reproduce the experimental data for intermediate and high confining pressures and for hydrostatic loading, but underestimates the softening behavior for low confining pressures.

The possibility of compaction bands formation is investigated. A cubic solid of 1 unit in side length (meter in this case) is meshed using 10 tetrahedral elements in the z -direction. A slight imperfection on the material properties is applied in order to trigger strain localization: the initial value of the variable p_c is reduced by 0.5% on two elements. Four confining pressures are considered and the results are presented in Figure 6.22. When $\sigma_3 \leq -11.9$ MPa, compaction bands are formed at the plasticity onset, in accordance with the LSA performed for the Cauchy continuum in Section 6.3.4. On the other hand, a quasi-homogeneous deformation is observed for $\sigma_3 \geq -11.8$ MPa, from the plasticity onset up to an axial strain of 2%. The profiles of the plastic axial strain for the two extreme cases are presented in Figure 6.23. Strain localization is observed over one element in the case of $\sigma_3 = -13$ MPa. In contrast, no localization occurs in the case of $\sigma_3 = -10$ MPa. A homogeneous plastification occurs in the whole sample, with slight additional amounts in the central part due to the material imperfection.

Finally, several mesh sizes have been considered in order to show the mesh-dependency character of the band thickness. In Figure 6.24, the sample is meshed with 8, 16 and 24 elements over the loading direction. Under 13 MPa of confinement, the compaction band is observed to form over one element. These results make evidence of the limitation of the Cauchy continuum and its deficiency for a robust assessment of the band thickness.

6.4.2 Micromorphic medium implementation

The gradient-dependent plasticity model is implemented in the *Numerical Geolab* code as a general micromorphic continuum of degree 2. The restrictions ($\eta = 0$ and $\eta_k = 0$) are introduced indirectly, by means of two penalty moduli defined as follows:

$$\begin{aligned}\dot{s} &= P_1 \dot{\eta} \\ \dot{s}_k &= P_2 L^2 \dot{\eta}_k\end{aligned}\tag{6.60}$$

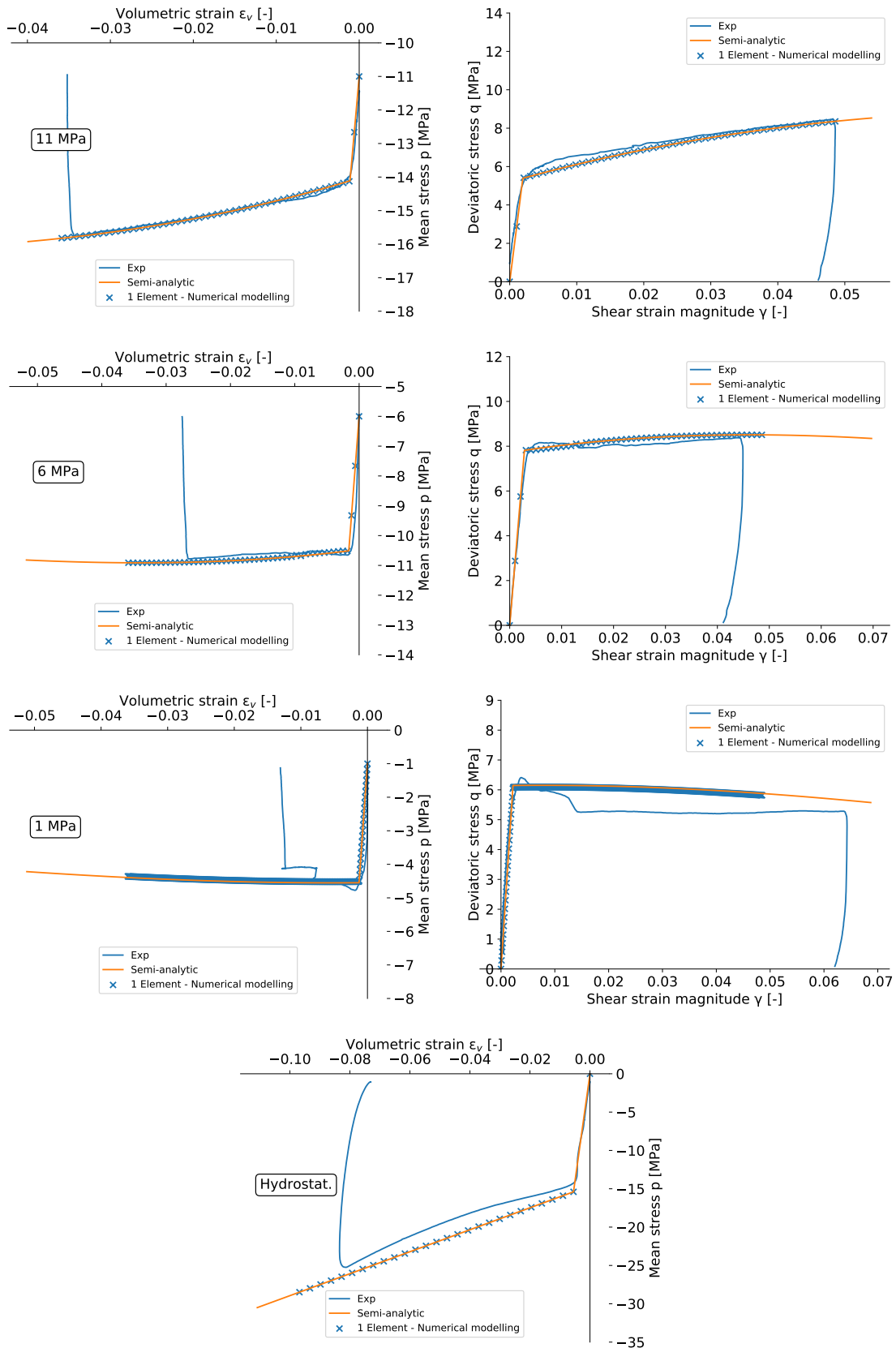


Figure 6.21: Numerical code validation: Plots of the semi-analytic homogeneous solutions and the numerical simulations in Cauchy continuum considering one element are superimposed to the experimental data for different loading conditions.

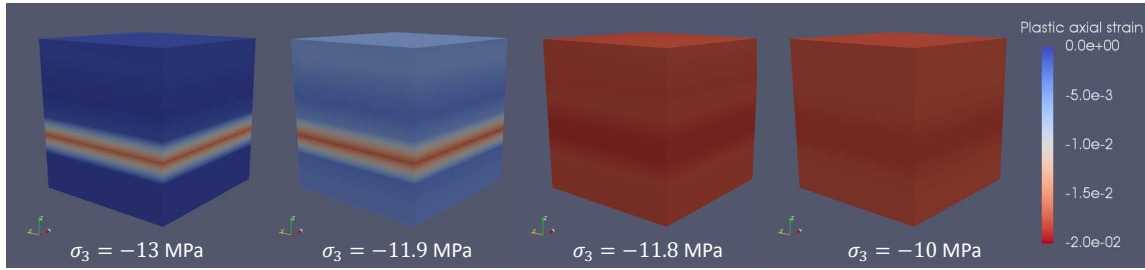


Figure 6.22: Cauchy continuum: Numerical modelling of samples tested under different confining pressures. Compaction bands form at the plasticity onset for confinements $\sigma_3 \leq -11.9$ MPa, whereas a quasi-homogeneous deformation is observed for confinements $\sigma_3 > -11.9$ MPa up to 2% of applied axial strain.

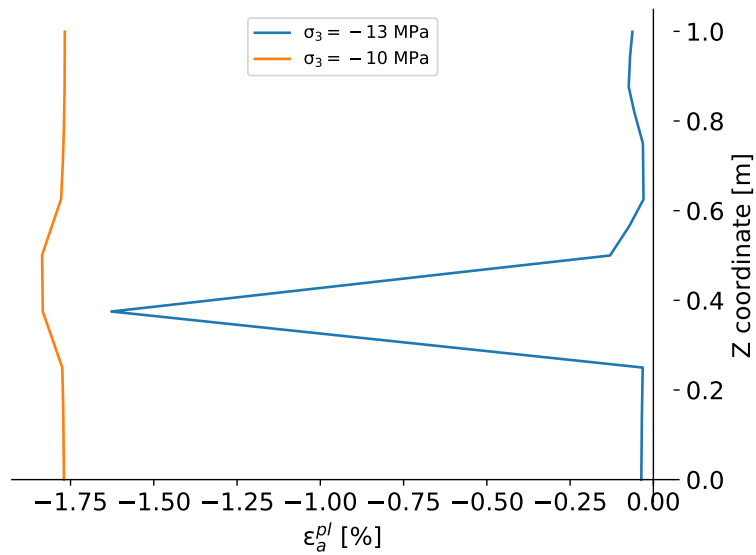


Figure 6.23: Cauchy continuum: Profile of the plastic axial strain over the z -axis for the numerical simulations performed under 10 and 13 MPa of confining pressures.

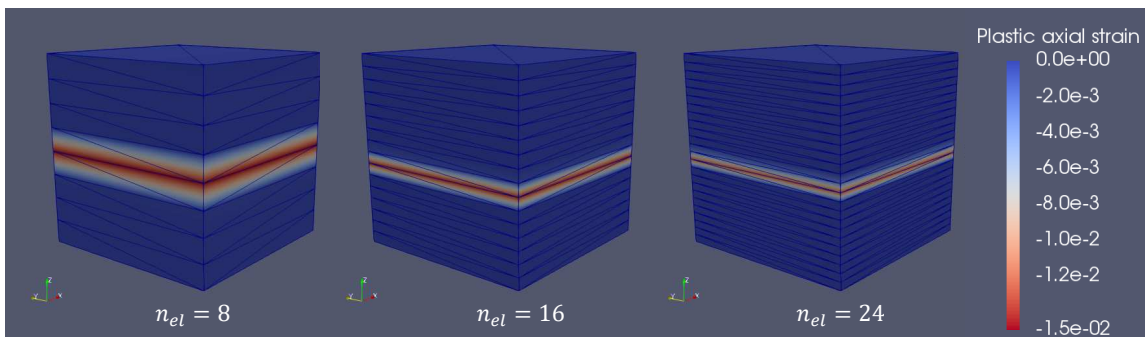


Figure 6.24: Cauchy continuum: Mesh-dependency of the compaction band thickness for a sample tested under 13 MPa of confining pressure.

For very high values of P_1 and P_2 , the degrees of freedom are constrained as required. A LSA for this micromorphic is performed. For $P_1 = 10^9$ MPa and $P_2 = 10^9$ MPa, identical results to those presented in Section 6.3.4 are obtained (the development is given in Appendix I). Therefore, these values are retained for the numerical modelling.

In order to validate the implementation, a numerical simulation is performed over one unit cubic element in true triaxial compression under 6 and 11 MPa of confining pressures. The curves of p vs ϵ_v and q vs γ are compared to those of the Cauchy numerical simulation in Figure 6.25. Results are consistent, since strain localization is forbidden and the higher order degrees of freedom are not activated for a single element mesh.

Considering now different meshes with different number of elements, the mesh-dependency problem is investigated. A numerical simulation of a sample tested under 10.5 MPa of confining pressure is performed for several mesh sizes: 25, 40, 50 and 70 elements along the loading direction. The height of the sample is taken equal to the internal length $L = 24$ mm. The plastic axial strain maps and their profiles over a vertical line passing through the center of the sample are presented in Figure 6.26. The amount of the mesh-dependency of these quantities becomes negligible from the case of 50 elements. This mesh-size (tetrahedral elements with 0.48 mm height each) is retained for the numerical simulations discussed in the following.

Sensitivity analysis

The effect of the parameter B on compaction banding is firstly investigated in this paragraph. A sample is again tested under 10.5 MPa of confining pressure up to 0.25% of total axial strain for an internal length $L = 24$ mm. Three cases are presented, where B is taken equal to 0.025, 0.035 and 0.045 MPa. Figure 6.27 presents the plastic axial strain maps and the corresponding profiles over the loading direction. For the lowest value of B , the compaction band is observed to have the smallest thickness. When B takes greater values, the band becomes larger for the same level of the applied axial strain. However, compaction bands are observed to accumulate greater plastic strain amounts for lower values of B , as the plastic axial strain is of -0.36% in the middle of the compaction band for $B = 0.025$ MPa, and is only of -0.27% for $B = 0.035$ MPa.

In addition, the effect of the internal length L on compaction banding is also investigated. Similarly to the previous tests, the sample is loaded at 10.5 MPa of confinement up to 0.25% of axial loading. Three cases are considered: $L = 16, 20$ and 24 mm, where B takes the value of 0.025 MPa. The plastic axial strain maps and their profiles over a vertical line are shown in Figure 6.28. The effect of the parameter L is similar to the one of B . When L takes smaller values, compaction bands become thinner and the amounts of plastic strains

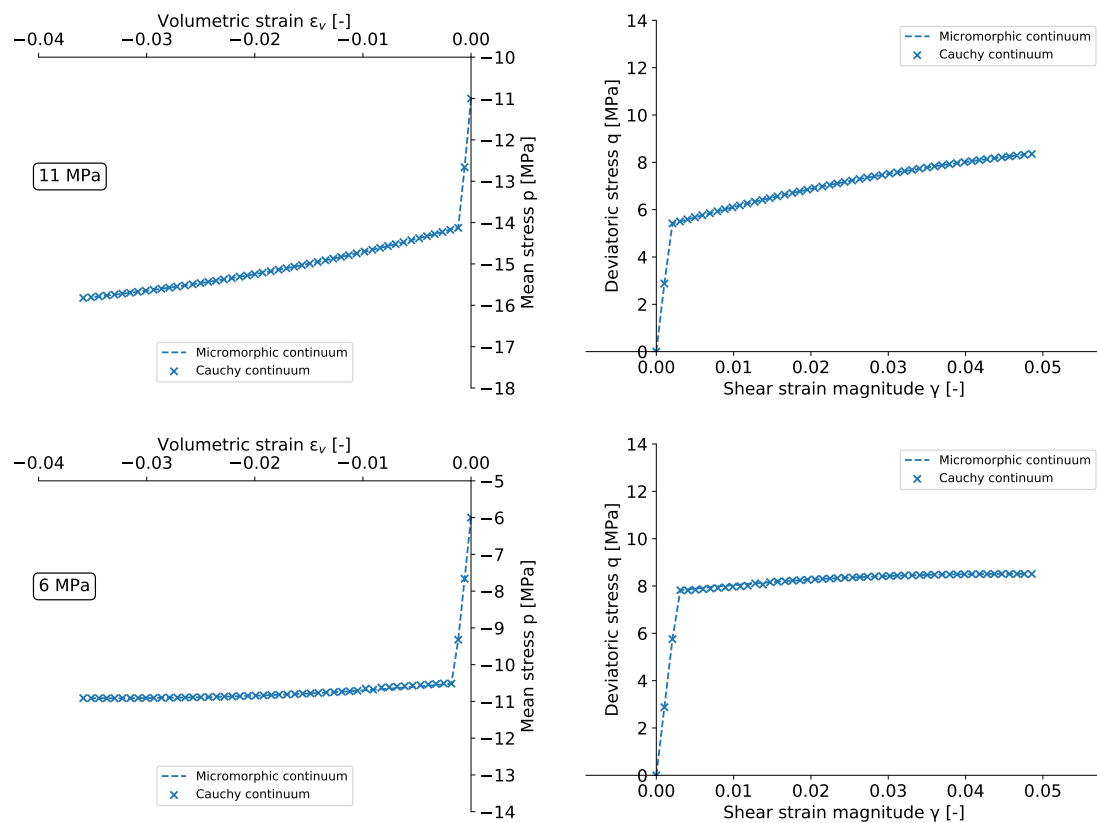


Figure 6.25: Numerical code validation in the micromorphic formulation: A comparison with the numerical results with Cauchy formulation by considering one element tested in two loading cases.

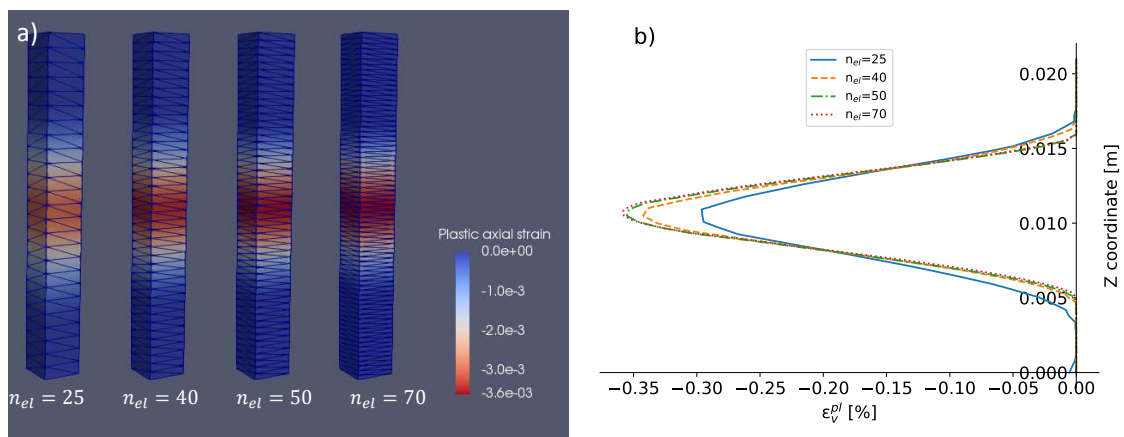


Figure 6.26: Mesh-independency of the compaction band thickness in the micromorphic formulation: **a)** Numerical modelling of a sample tested under 10.5 MPa of confining pressure up to 0.25% of applied axial strain for different mesh sizes; **b)** Vertical profiles of the plastic axial strain.

in the band become greater. For instance, -0.57% of plastic axial strain is obtained in the middle of the compaction band for $L = 16$ mm, while only -0.44% is obtained when $L = 20$ mm at the same level of axial loading.

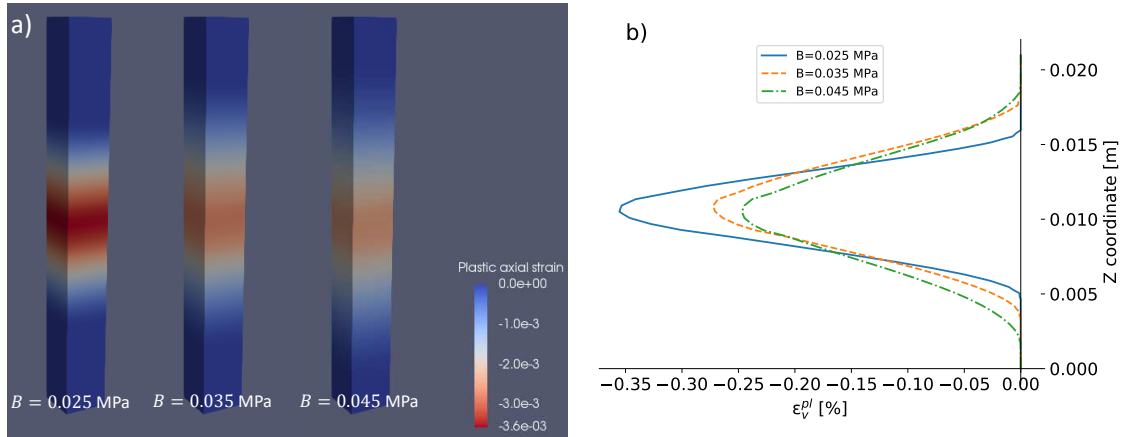


Figure 6.27: Effect of the modulus B on compaction banding: **a)** Numerical modelling of a sample tested under 10.5 MPa of confining pressure for different values of B ; **b)** Vertical profiles of the plastic axial strain. The internal length is taken $L = 24$ mm.

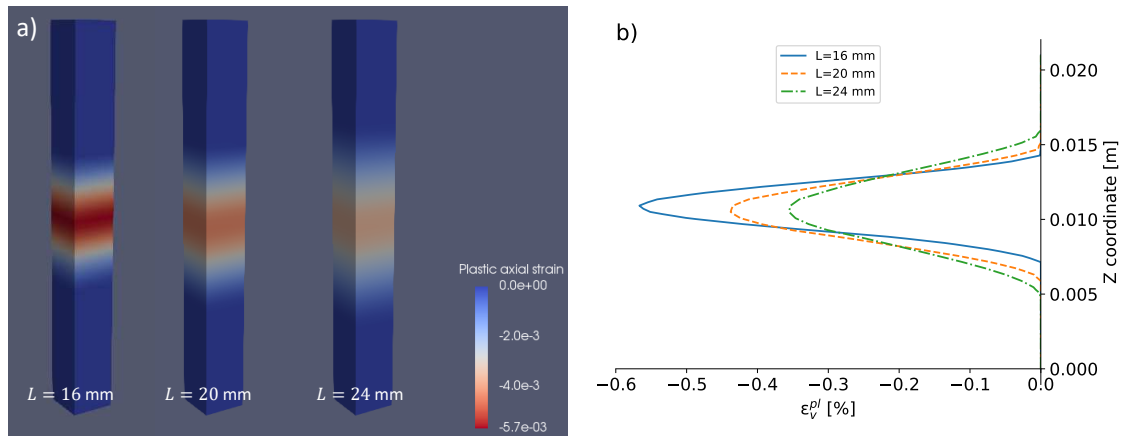


Figure 6.28: Effect of the internal length L on compaction banding: **a)** Numerical modelling of a sample tested under 10.5 MPa of confining pressure for different values of L ; **b)** Vertical profiles of the plastic axial strain. The modulus B is taken $B = 0.025$ MPa.

6.4.3 High confinement triaxial loading

In this section, the numerical modelling of a true triaxial compression loading under 10.5 MPa of confining pressure is performed in the frame of the micromorphic continuum. The objective of this section is to study compaction banding at relatively high confining pressure. In the next section, these results will be compared to the experimental data presented in Section 5.4. The plastic volumetric strain maps at different levels of loading are shown in Figure 6.29. An imperfection is introduced in the middle of the sample in order to enhance the strain localization: the initial value of the variable p_c is reduced by 2% over 3 mm (6 elements). A compaction band is formed at the plasticity onset, in accordance with the experimental observations. Then, the band thickness is observed to increase with loading

and the plastic strain continues to localize inside the band: -1.3% of plastic volumetric strain is found inside the band for -0.6% of imposed total axial strain. The plastic strain amount continues to increase inside the band and finally -5.6% of plastic volumetric strain is reached for -2.4% of imposed total axial strain.

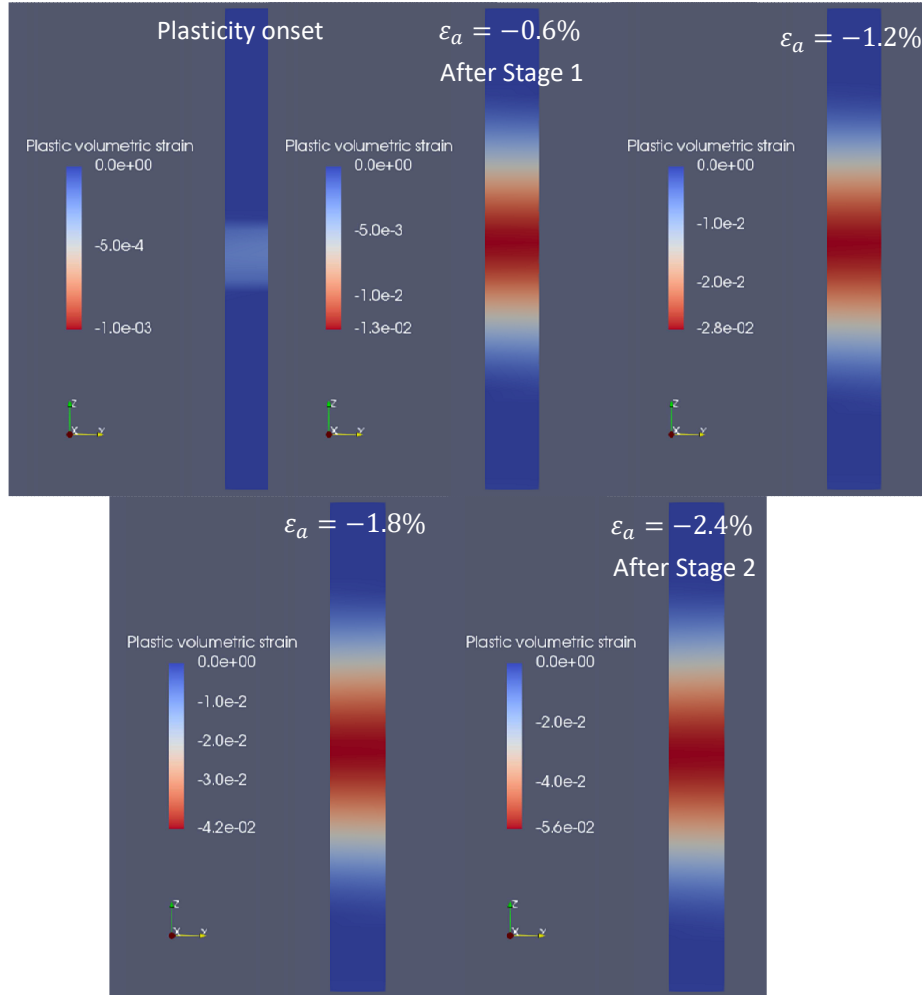


Figure 6.29: Accumulated plastic volumetric strain maps are shown at different loading levels.

Band thickness

In order to evaluate the band thickness evolution, the profiles of the accumulated plastic volumetric strain over the loading direction are considered (Figure 6.30). By analogy with the method used to evaluate a shear band thickness in Rattiez et al. (2018), the compaction band thickness is estimated here by fitting a trigonometric interpolating function $f(z)$ with the vertical profiles of the plastic volumetric strain:

$$f(z) = \frac{a_1}{2} \cdot \Omega_{[a_2 - \frac{a_3}{2}; a_2 + \frac{a_3}{2}]}(z) \cdot \left[\cos\left(2\pi \frac{z - a_2}{a_3}\right) + 1 \right] \quad (6.61)$$

where a_1 is the maximum plastic volumetric strain, a_2 is the position of the band center, a_3 is the wavelength of the cosine function and $\Omega_{[a_2 - \frac{a_3}{2}; a_2 + \frac{a_3}{2}]}(z)$ is a rectangular function defined as:

$$\Omega_{[a_2 - \frac{a_3}{2}; a_2 + \frac{a_3}{2}]}(z) = \begin{cases} 1 & \text{if } z \in [a_2 - \frac{a_3}{2}; a_2 + \frac{a_3}{2}] \\ 0 & \text{if } z \notin [a_2 - \frac{a_3}{2}; a_2 + \frac{a_3}{2}] \end{cases} \quad (6.62)$$

The wavelength is interpreted as the band thickness $d = a_3$. The function $f(z)$ is fitted successively with the vertical profiles and the results are presented with black dashed lines in Figure 6.30. Then, the compaction band thickness evolution with respect to the imposed total axial strain is depicted in Figure 6.31. The initial thickness of the band at the plasticity onset is evaluated at 4.42 mm. This thickness increases rapidly with loading to reach around 12 mm for -0.3% of imposed total axial strain. Then, the band continues to expand slowly and reaches a thickness of 15.4 mm for an imposed total axial strain of -2.4%.

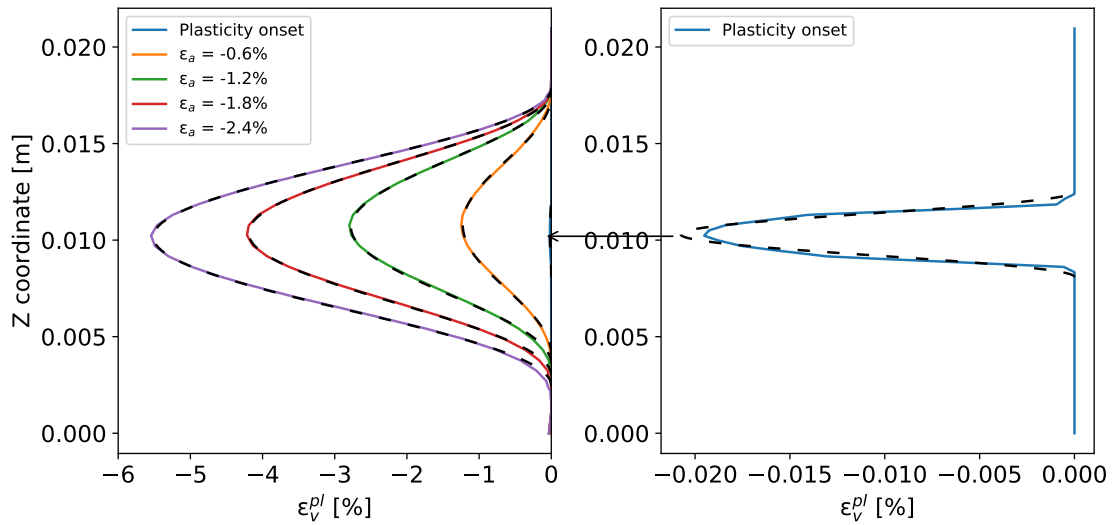


Figure 6.30: Vertical profiles of the accumulated plastic volumetric strain. Dashed lines represent the fitted curves of $f(z)$. The plot on the right shows a zoom on the profile at the plasticity onset.

In order to better understand the band thickness evolution, the plastic volumetric strain rates are explored (each rate corresponds to an imposed total axial strain rate of $\dot{\epsilon}_a = -0.15\%$). For 3 close loading states ($\epsilon_a = -1.159\%$, -1.177% and -1.195%), the plastic volumetric strain rate maps and their vertical profiles are presented in Figures 6.32 and 6.33. At the state of $\epsilon_a = -1.159\%$, additional strain localization occurs at the lower part of the band, where the rate of the plastic volumetric strain is evaluated as $\dot{\epsilon}_v^{pl} = -0.02\%$. Later, additional plastic strain with a similar amplitude is observed to occur in the middle of the band. In the third state $\epsilon_a = -1.195\%$, the rate of the plastic volumetric strain is again translated to the upper part of the band. Zones of plastic strain rate surges - that take place in due course of the loading - are observed to have a quasi constant thickness and to oscillate along the already formed compaction band (*i.e.* the zone of localized accumulated plastic strain). This can be related to the fact that the system has not a unique solution and strain localization

takes place in several positions inside the existing band. In addition, the system may harden in a place and therefore the surrounding material is easier to compact, but then it hardens leading to a wave-like oscillation motion. The localized zone of plastic strain rate may occur in the middle of the sample and thus, leads to an increase in the amount of accumulated plastic strain in the localized zone (Figure 6.29). In addition, when the localized zone of plastic strain rate occurs at the boundaries, it contributes in an enlargement of the localized zone of accumulated plastic strain.

Similarly to the approach adopted to evaluate the band thickness from the accumulated plastic volumetric strain profiles, the profiles of the zones of localized plastic strain rate are fitted with the function $f(z)$ and the results are presented in Figure 6.32. At the beginning of the strain localization, plastic volumetric strain occurs in the middle of the sample and the thickness evaluated from both profiles are identical. Then, when the thickness of localized zones of plastic strain rate reaches a value of 7.5 mm, it becomes constant and the oscillation phenomenon occurs. This leads to slower expansion of the thickness of localized zones of accumulated plastic volumetric strain.

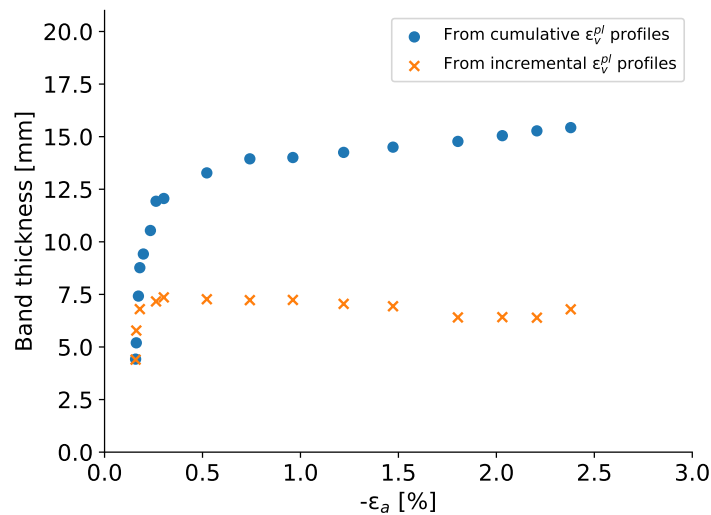


Figure 6.31: Evolution of compaction band thickness evaluated from accumulated and rates of plastic volumetric strain profiles (each plastic volumetric strain rate corresponds to an imposed total axial strain rate of $\dot{\epsilon}_a = -0.15\%$).

Size effect

The size effect is now explored. Two additional samples having a height $H = 48$ mm ($2 \times L$) and 72 mm ($3 \times L$) respectively are considered under the same loading conditions (10.5 MPa of confining pressure). The same mesh size is considered for the various samples and 2.4% of total axial loading is imposed (which corresponds to the loading level applied the experiment). The corresponding plastic axial strain maps are shown at several loading

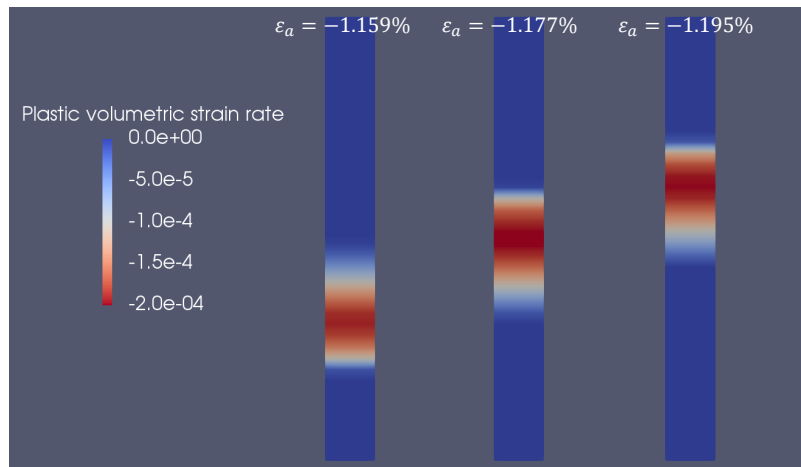


Figure 6.32: Plastic volumetric strain rate maps at different loading levels (each plastic volumetric strain rate corresponds to an imposed total axial strain rate of $\dot{\epsilon}_a = -0.15\%$).

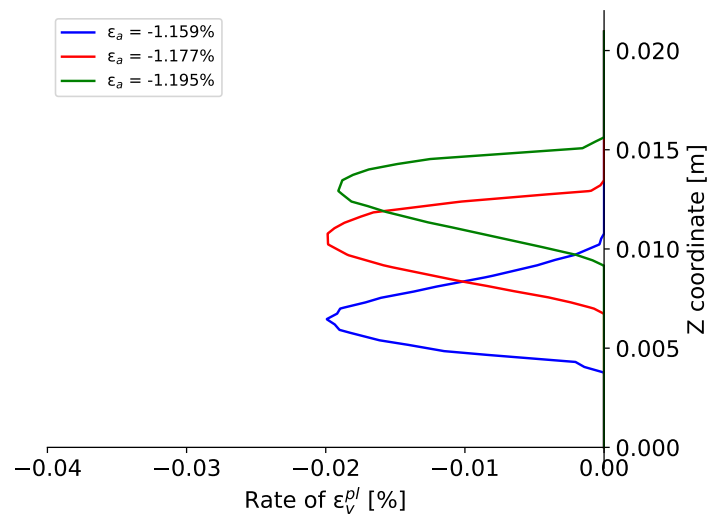


Figure 6.33: Vertical profiles of plastic volumetric strain rates at different loading levels (each plastic volumetric strain rate corresponds to an imposed total axial strain rate of $\dot{\epsilon}_a = -0.15\%$).

states in Figure 6.34. It is observed that for higher specimens, the number of compaction bands increases, as three bands form for $H=48$ mm (denoted by M1 to M3) and five form for $H=72$ mm (denoted by N1 to N5). The first band to develop is located where the imperfection is placed (98% of the parameter p_c in the middle of the sample). This band appears at the plasticity onset whereas the other bands appear later and simultaneously at a total imposed axial strain $\epsilon_a^{tot} = -0.19\%$ in both cases $H = 48$ mm and $H = 72$ mm.

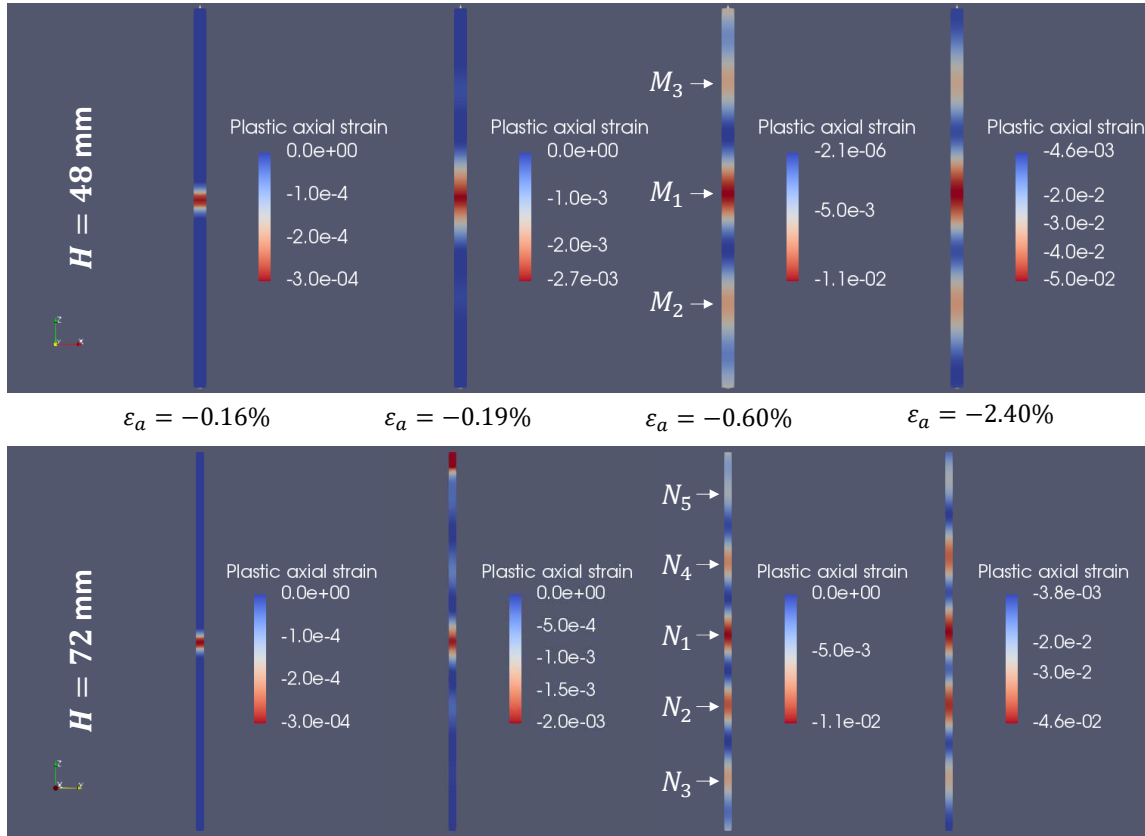


Figure 6.34: Accumulated plastic axial strain maps at several loading states for the cases $H=48$ mm and 72 mm.

The profiles of the plastic axial strain at several loading states are plotted and compared with the 24-mm height sample results in Figure 6.35. Again, the trigonometric function $f(z)$ is fitted for each band and two information can be deduced: the band thickness identified with the parameters a_3 as before and the band spacing deduced from the parameters a_2 which are interpreted as the positions of the band centers. The bands thicknesses are thus evaluated along loading and are compared with the case $H = 24$ mm (Figure 6.36). The results indicate that the band thickness is independent on the sample height and is not affected by the number of bands developed. In addition, a regular spacing between the centers of the bands is observed. This spacing is comparable to the band thicknesses, as the ratio between the band spacing over the central band thickness is close to 1 (Figure 6.37). Moreover, the amount of the plastic strain in the central bands in both cases $H = 48$ mm and $H = 72$ mm are similar at the same level of loading. These amounts are slightly

lower than the evaluated plastic axial strain obtained in the single band formed for the case $H = 24$ mm at the ultimate loading level.

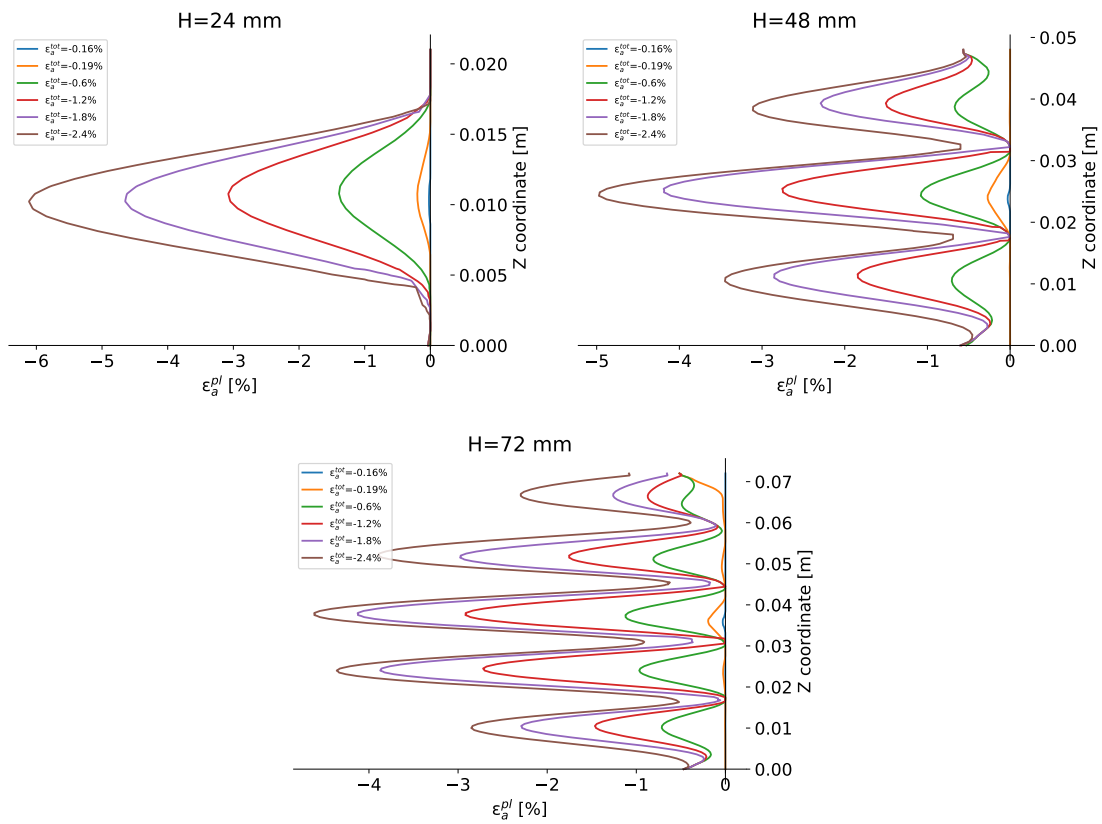


Figure 6.35: Profiles of accumulated plastic axial strain.

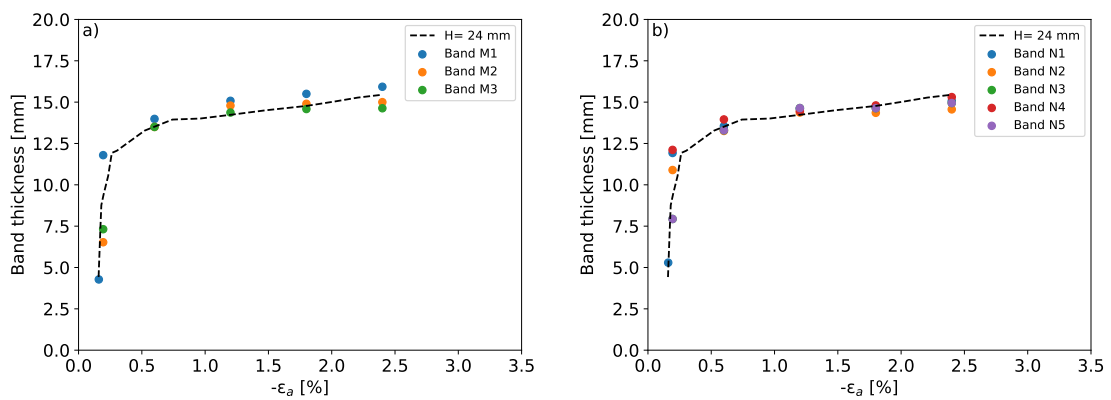


Figure 6.36: Band thicknesses evolution with imposed axial loading and compared to the thickness evaluated for $H = 24$ mm: a) Case of $H = 48$ mm; b) Case of $H = 72$ mm.

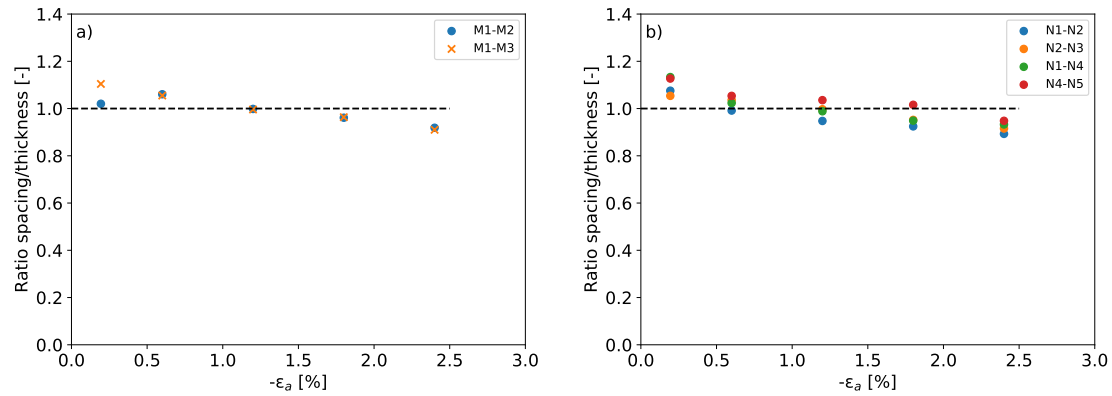


Figure 6.37: Evolution of the ratio of band spacing over central band thickness: **a)** Case of $H = 48$ mm; **b)** Case of $H = 72$ mm.

6.4.4 Comparison with the experimental results

In this section, the numerical modelling of the sample tested under 10.5 MPa of confining pressure is compared to the experimental results of the SML tested under the same condition:

- In both experimental and numerical tests, compaction bands are formed at the plasticity onset.
- The initial band thickness in the numerical modelling is evaluated at 4.42 mm. On the other hand, a LSA conducted at the plasticity onset, with $B = 0.025$ MPa and $L = 24$ mm, leads to the growth coefficient s vs λ^* curve presented in Figure 6.38. The dominant wavelength perturbation is estimated at $\lambda_{max} = 0.427 \times L = 0.427 \times 24 = 10.25$ mm. The initial band thickness is thus $d = \frac{\lambda_{max}}{2} = 5.12$ mm, very close to the predicted value of the numerical simulation.
- Two DVC have been performed on the SML sample tested under 10.5 MPa of confining pressure (Section 5.4). The REV 1 (Figure 6.13) is considered here where compaction bands are the most developed in comparison to other zones. Then, the plastic volumetric strain in both stages is plotted over two lines defined in the normal direction to the bands (Figure 6.39). The obtained band thicknesses are: 8.2 mm after the first stage and 13.4 mm after the second stage. On the other hand, the thicknesses predicted in the numerical modelling are 13.0 mm after the first stage and 15.4 mm after the second loading stage. Therefore, the numerical results are consistent with the experimental data. Notice that, at the scale of the REV, each compacted zone is considered as one compaction band. However, this band may also be seen as the combination of several thinner bands at smaller scales of porosity heterogeneity. This could be further explored in future studies.

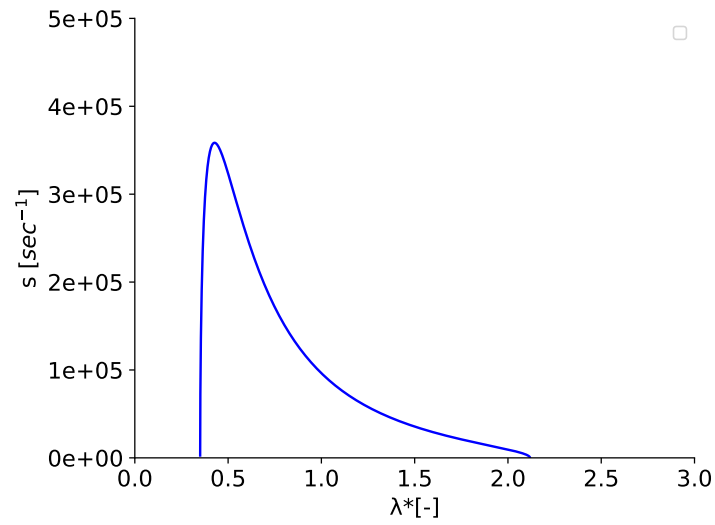


Figure 6.38: LSA conducted at the plasticity onset of a sample tested under 10.5 MPa of confining pressure: The growth coefficient vs the normalized wavelength perturbation.

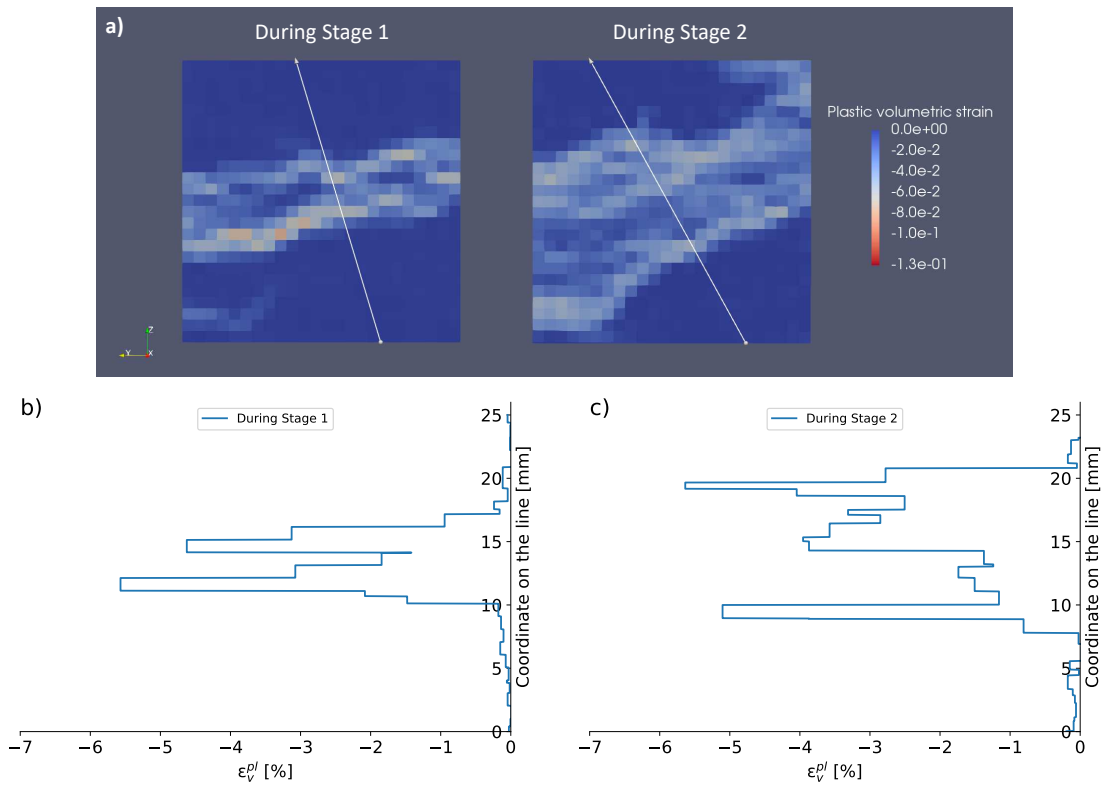


Figure 6.39: REV 1: Plastic volumetric strain profiles over the two lines defined on the DVC maps.

Table 6.7: Cumulative plastic volumetric strain evaluated after each loading stage: in the numerical modelling and in the REV 1 selected inside the SML sample tested under 10.5 MPa of confining pressure.

	Triaxial test	Numerical modelling
ϵ_v^{pl} after Stage 1	-2.9%	-1.3%
ϵ_v^{pl} after Stage 2	-5.5%	-5.6%

- The amount of the plastic volumetric strain inside the band is also investigated. The mean value of the incremental plastic volumetric strain inside the compacted zone of the REV 1 is evaluated from the profiles shown in Figure 6.39 (one increment corresponds to a loading stage) and the results are gathered in Table 6.7. A very good consistency between the numerical and experimental results is obtained, where -5.5% of plastic volumetric strain is assessed in the experiment after the second loading stage, which is very close to the value obtained in the numerical modelling (-5.6%).

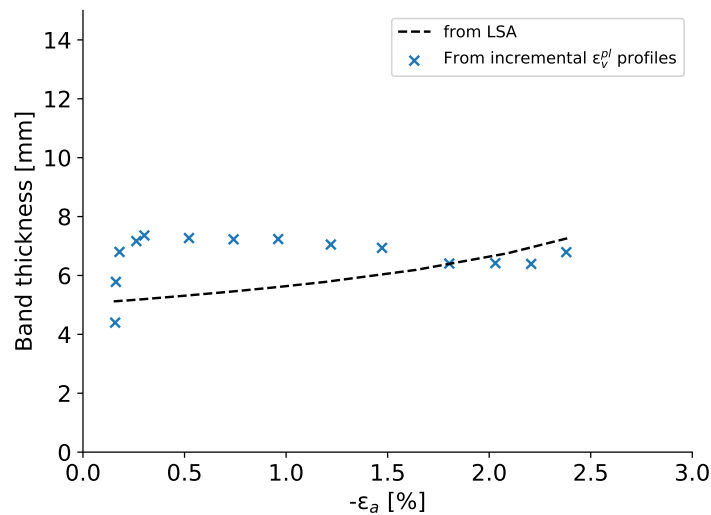


Figure 6.40: Compaction band thickness evaluated from the incremental plastic volumetric strain profiles and from the LSA applied on an equivalent homogenized material.

- The band thickness evaluated from the plastic volumetric strain rates $\dot{\epsilon}_v^{pl}$ of the numerical modelling can be compared to the thickness predicted by the LSA. For that, an associated homogenized system is defined for each axial strain level, where the average of the plastic volumetric strain is computed and the higher order stress is assumed to vanish $\zeta = 0$. The LSA is thus performed, and the band thickness is evaluated along the axial loading (Figure 6.40). The thickness predicted from the LSA is found close to that calculated from the increments of the plastic volumetric strain obtained in the numerical modelling.

6.5 Conclusions

In this chapter, a gradient-dependent plasticity model has been presented. The experimental observations have shown the need of a non-local approach to model the compaction phenomenon. In such a model, porosity and its second-gradient have been identified as two independent hardening parameters. The constitutive law has been interpreted as a micromorphic continuum of degree 2, which can be seen as an extension of the second-gradient theory.

In addition to the standard elastic-plastic parameters, the proposed model introduces three additional parameters: the internal length L , an enhancement of the hardening laws, where the second-gradient of porosity is considered as an additional internal variable and a higher order elastic modulus B linking the higher order stress with the second gradient of volumetric strain (the porosity change is identified with the plastic volumetric strain). The adopted procedure of calibration has been performed based on XRCT images recorded at several deformation states, on DVC deformation maps and on a LSA applied at the plasticity onset at relatively high confining pressures.

The porosity heterogeneity has been schematically represented by alternated high- and low-porosity zones of cubic shapes. The FFT applied on 1D porosity profiles has permitted to identify the wavelength of the porosity heterogeneity. This length, evaluated at 2.4 cm, constitutes the size of the domain over which the porosity and its second gradient are evaluated. Then, two domains in which compaction bands have been experimentally observed, have been considered inside the SML sample tested under high confining pressure. In addition, plastic volumetric strain has been evaluated over these domains which has permitted to calibrate the enhanced hardening moduli. Finally, a linear stability analysis performed on the enhanced constitutive laws has shown that the remaining elastic modulus controls the confining pressure range for which compaction bands may form at the plasticity onset. From the experimental results presented in this work and from the data provided by Baud et al. (2017a), the threshold of confining pressure is estimated at 7.5 MPa. The corresponding modulus B is evaluated at 0.025 MPa.

Finally, a numerical modelling of the triaxial test under 10.5 MPa of confining pressure has been performed in order to validate the model with the experimental results. First, some results have shown the limitation of the Cauchy formulation in modelling the compaction banding problem. Then, the constitutive law has been implemented as a general micromorphic continuum of degree two where the kinematic restrictions are introduced indirectly by means of penalty moduli. A sensitivity analysis of both the elastic modulus B and the internal length L shows that when their values are smaller, compaction bands become thinner and strain localization becomes more accentuated for a given level of loading. A

triaxial compression test under 10.5 MPa of confining pressure has been thereafter simulated. The numerical results are consistent with experimental data in terms of compaction banding onset, band thickness evolution and the plastic strain amount inside the band. In addition, compaction bands spacing has been studied by considering higher samples, and has been found very close to the bands thickness. This result is consistent with the linear stability analysis which considers the perturbation as a sinusoidal function.

Conclusions and Perspectives

7.1 General conclusions

Understanding the compaction banding phenomenon is of high importance in rock mechanics. In this thesis, the formation of compaction bands in porous limestones has been investigated by laboratory testing. In addition, a constitutive modelling in the frame of higher-order continuum mechanics has been presented in order to predict their evolution.

The Saint-Maximin limestone has been selected due to its high porosity (38%). X-Ray Computed Tomography, microscopic observations on thin sections and mercury intrusion porosimetry tests have revealed complex microstructural features of the selected carbonate rock. The porosity, evaluated at the scale of 1 mm, is observed to fluctuate between 30% and 45% at the centimetric scale. Large and cemented grains are observed in low-porosity zones, whereas it appears that calcite dissolution may be responsible for the higher porosity in other zones.

Based on XRCT images recorded before and after several loading stages, the Digital Volume Correlation technique has been applied and strain localization bands have been identified in axisymmetric triaxial tests under different confining pressures. The mode of deformation inside the bands has been studied and a simple method to identify their types has been proposed. In addition, 3D porosity maps have been computed in the initial and deformed configurations in order to study the effect of porosity heterogeneity on strain localization and to follow its evolution with loading.

High-angle compaction bands of several millimeters in thickness have been identified at relatively high confining pressure. These bands are triggered at the plasticity onset in the more porous zones. Zones of compaction bands become thicker with increasing load, as new bands form and coalesce with previously developed bands. Calcite grain crushing has been identified as the main micromechanism involved in compaction banding. It creates fines which fill the pore space. Despite their presence in the low-porosity zones, many large pores remain undeformed, as they are protected by the surrounding rigid microstructure.

At low confinements, low-angle pure shear bands are observed at the peak stress. These bands keep a constant thickness of around 2 mm along loading. Porosity heterogeneity

does not control the shear band orientations, as they cross both low- and high-porosity zones. However, porosity heterogeneity affects the volumetric behavior of shear bands: local dilation is observed in low-porosity zones, whereas local compaction is found in high-porosity zones. Again, calcite grain crushing is found to be the responsible mechanism for the compactive behavior. On the other hand, cracking of intergranular cement is found to induce dilatancy in low-porosity zones.

An intermediate behavior is identified at the brittle-ductile transition. Compactive shear bands, with orientations between those of compaction and shear bands are observed at the plasticity onset. Similarly to compaction bands, compactive shear bands become thicker with increasing load. Moreover, porosity heterogeneity is found to control the volumetric behavior of compactive shear bands, as the same micromechanisms involved in shear banding are again identified.

In contrast, deformation bands do not form in hydrostatic loading. The plasticity onset is characterized by a slight compaction occurring in a high-porosity zone. Then, the plastic regime is characterized by the compaction of all high-porosity zones. Denser zones present stiff inclusions that remain undeformed, but induce some shearing at their boundaries. Calcite grain crushing and powders pore filling are responsible for the compactive behavior.

The experimental observations performed on the tested samples have led to adopt the non-local approach in order to model the material behavior. Thus, a gradient-dependent plasticity model has been proposed, where the constitutive law depends not only on the porosity, but also on its second gradient. A theoretical development of a micromorphic continuum of degree two¹ has been conducted to define a rigorous mathematical framework of the model. This higher order continuum introduces several additional parameters whose calibration requires an enhanced procedure.

The first step of the calibration procedure relies on a standard macroscopic calibration based on the LVDTs measurements. Therefore, the elastic parameters, the initial yield surface, the hardening laws and the plastic potential have been identified. Then, the calibration of the additional parameters has been conducted as follows:

- The internal length L : The porosity heterogeneity of the material has been schematically represented by a periodic pattern of high- and low-porosity zones of cubic shapes. The internal length, which is by definition the side length of the cubic domain over which the second-gradient of the porosity must be calculated, is given by the dominant wavelength of the porosity heterogeneity. To identify this length, a porosity map of

¹Following the definition of Germain (1973b)

a SML sample at the initial state has been considered. Then, the Fast Fourier Transformation has been applied on several porosity profiles plotted over lines in different orientations inside the sample. The dominant wavelength L of the heterogeneity that stands out is 24 mm.

- The dependence of the yield surface on the second gradient of the porosity has been studied thereafter. Cubic domains centered over high-porosity zones (where compaction bands have taken place) have been selected inside the sample tested under high confining pressure, at the initial state and the subsequently deformed states. On these cubes, the second gradient of the porosity has been evaluated. By means of the macroscopic hardening laws and the DVC deformation maps, the hardening laws in the enhanced model have been established.
- Finally, to have a full characterization of the model, a higher order elastic modulus B requires to be calibrated. To do so, a linear stability analysis has been performed on the homogeneous solution at the plasticity onset at different states on the yield surface. The modulus B is found to influence the range of confining pressures, for which compaction bands occur at the plasticity onset in axisymmetric triaxial loading. Based on the experimental observations, the value of the parameter B is chosen as 0.025 MPa, which corresponds to a formation of compaction bands for confining pressures higher than 7.5 MPa (in absolute value).

The constitutive model has been implemented in the Finite Element Code, *Numerical geolab*, in order to simulate the formation and evolution of compaction bands. First, some results in the Cauchy formulation have been presented to validate the implementation and show the mesh-dependent character of strain localization. Then, numerical modelling in the micromorphic continuum has been studied. A triaxial compression loading has been simulated at the same conditions of the SML sample that has shown the formation of compaction bands. Similarly to the experimental observations, compaction banding is identified at the plasticity onset, of a very close thickness to that predicted by the linear stability analysis. It has been shown that the numerical results are consistent with the experimental data in terms of the band thickness evolution and the amount of the accumulated plastic volumetric strain inside the bands.

In conclusion, identifying compaction bands in laboratory tested carbonate rocks has been a challenge over the past years. It is shown that the Digital Volume Correlation technique can meet this challenge. In addition, the influence of the microstructural features on compaction banding, which is a primordial topic, has been partly clarified in this thesis. XRCT images recorded on several deformed states have shed the light on the porosity role in strain localization. On the other hand, higher order continuum media, which are required to model strain localization phenomena, have an issue concerning the calibration

of their additional parameters. A back-analysis of the deformation band thickness is usually performed in order to identify the internal length of the material. In this study, a new calibration method of the additional parameters has been proposed independently on band thickness assessments. This model permits a consistent simulation of the compaction banding phenomenon in high-porosity carbonate rocks.

7.2 Suggestions for future research

The work presented in this thesis can be pursued and extended in several directions:

- The experimental and modelling work in this thesis has been performed at room temperature in dry conditions and has focused on the mechanisms of deformation without considering multiphysical couplings. However, these factors are present in underground conditions and cannot be ignored. For instance, a water effect on the strength of different sedimentary rocks is usually reported (David et al., 2015; Baud et al., 2015; Baud et al., 2017a), but not on others (Nicolas et al., 2016). Moreover, fluids can chemically interact with rocks leading to some instabilities (Stefanou and Sulem, 2014). Therefore, it would be interesting to explore the fluid effects on the deformation modes of sedimentary rocks by means of X-Ray imaging and 3D volume correlation and to extend the constitutive law to take them into consideration.
- In addition, high temperatures can be encountered during many geosystem operations: for instance, temperature can exceed 100°C in some geothermal fields (Barbier, 2002). A high temperature is observed to lower the brittle-ductile transition and may affect the rock deformation modes (Paterson and Wong, 2005). It can also induce anisotropic deformation inside the geomaterials due to the discrepancy between the thermal expansion of different minerals (Somerton, 1992; Lion, 2004). Thus, it would be interesting to investigate the temperature effect and to consider it in the modelling. The experimental procedure can be similar to the one followed in this work, since the triaxial machine in the Navier laboratory is equipped with a heating system able to prescribe high temperatures up to 200°C.
- The mechanical compaction of sedimentary rocks and carbonate rocks in particular, is quite complex. Homogeneous deformation is reported for some rocks and localized strain in the form of compaction bands are observed for others (usually in high-porosity rocks, but not always). These observations are questionable, since compaction bands can form but may not be identified due to the reasons discussed in the literature review. In this study, the Saint-Maximin limestone has been chosen due to its high-porosity and the high probability of forming compaction bands. However, it would be interesting to revisit the deformation modes of different carbonate rocks, in which

homogeneous compaction has been reported in the literature. The Digital Volume Correlation presents a promising technique for this purpose.

- In the modelling approach, the porosity heterogeneity is simply represented by introducing one wavelength and compaction bands have been thus studied at one scale (2.4 cm), which is the scale of the cylindrical laboratory sample. However, the compaction banding phenomenon has a multiscale character: one compaction band at a given scale can be seen as a zone of many compaction bands at lower scales. In this case, further analyses on the internal length scale are required. Local tomography can be used in order to focus on some subdomains inside the sample along the loading process, with a better resolution in comparison to the current one (24 $\mu\text{m}/\text{voxel}$). Moreover, the proposed approach could be extended to large scale problems. From geophysical surveys, porosity maps can be constructed at larger scales and the internal length of the gradient model can be assessed from the dominant wavelength. In this way, numerical computations at the scale of a reservoir could be performed.
- The present work has been essentially devoted to the modelling of compaction bands based on considering hardening parameters related to the volumetric response. The proposed model needs to be further tested on its capacity to predict compactive and pure shear banding.

Appendices

A Limestones classifications

Based on calcite grain size (Figure 8.1a), four families can be defined (Lezin et al., 2009; Flügel, 2013):

1. Micrite: It is an abbreviation for microcrystalline calcite which is the finest constituent of carbonate rocks. The crystal size is lower than 4 μm .
2. Microsparite: It is a constituent of the rock matrix, having sizes ranging from 5 to 10 μm .
3. Sparite: Larger cement crystal ranging up to 20 μm .
4. Grains: Identifiable particles larger than 20 μm . They can have different shapes (spherical, angular) and origins (organic fragment, etc..).

Two main classifications exist for limestones: Dunham (1962) and Folk (1962) classifications which are based on depositional texture and are briefly presented in the next two subsections.

A.1 Dunham classification

It is the most widely used classification. It can be applied to either field's investigation of cores or in laboratory studies. Dunham (1962) have distinguished between carbonates whose original components are organically bound (Boundstone) or not (Figure 8.1b). In the second group, a separation is done between rocks that are matrix-supported or grain-supported. Mudstone are matrix-supported carbonate rocks which have less than 10% of grains with respect to the volume, whereas wackestones are constituted by more than 10% of grains. In these kinds of rocks, micrite is abundant and micro-porosity is dominant. Note that the nomenclature of mudstone can cause some ambiguity because it is also used for rocks constituted by silicate silt and clay material. Grain-supported carbonate rocks which do not contain mud are called grainstone, whereas others are called wackestone. In these rocks, porosity is generally bimodal and macro-porosity is sometimes dominant. For

instance, from the cited carbonate rocks in Table 2.2, Solnhofen is classified as a mudstone, whereas Majella and Saint-Maximin are considered as grainstones.

A.2 Folk classification

Since it needs microscopic observations on thin sections, Folk classification is more used in laboratory studies than in field. Folk (1962) has defined three end-members: **Allochems** which are discrete carbonate grains; **Microcrystalline**, which refers to micrite and constitutes the matrix; **Sparry calcite**, which refers to sparite and constitutes the cement. Based on the relative proportions of each constituent, three categories are defined:

1. Sparry allochemical rocks: where grains are cemented by sparry calcite cement.
2. Microcrystalline allochemical rocks: where a microcrystalline matrix exists with various amounts of grains.
3. Microcrystalline rocks: where a microcrystalline matrix is dominant with few or no grains.

The two classifications are quite similar. Grainstones from the Dunham classification are equivalent to sparry allochemical limestones from Folk classification. Mudstones are equivalent to microcrystalline rocks as well.

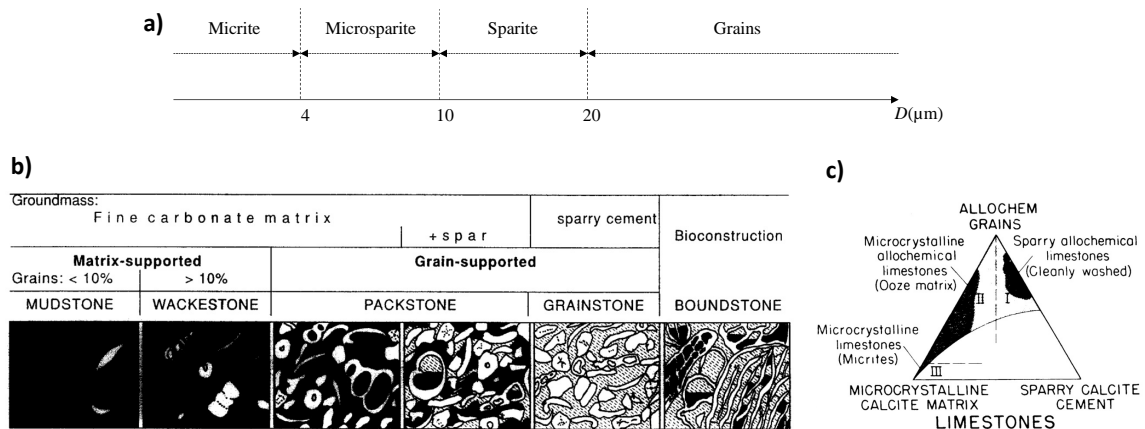


Figure 8.1: a) Carbonate rocks constituents; b) Dunham classification for limestones; c) Folk classification for limestones (from Flügel, 2013).

B Microstructural features of several limestones

The microstructural features of several limestones are gathered in this appendix. These rocks are mainly in France and have been characterized and studied in several publications.

B.1 Lavoux limestone

It is an oolitic grainstone from the Dogger formation of the Parisian Basin (Zinsmeister, 2013; Borgomano et al., 2017). Several facies of this limestone exist: A coarse-grained and a fine-grained one. The porosity of this rock is around 24% and is divided into macro- (45%) and micro-porosity (55%). In coarse-grained Lavoux (Figure 8.2a), grains are micro-porous and subspherical of 500 μm of diameter. Cementation is rare and microstructure is quite homogeneous. In fine-grained facies, grains are also micro-porous, but are poorly sorted (Figure 8.2b). Cementation is more present and microstructure is heterogeneous.

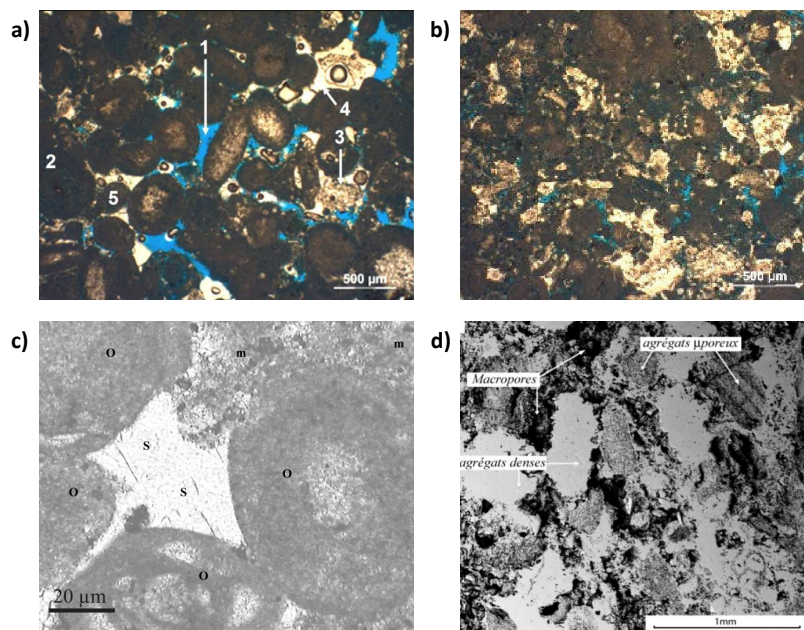


Figure 8.2: a) Coarse-grained Lavoux limestone; b) Fine-grained Lavoux limestone (Zinsmeister, 2013); c) Anstrude limestone (o: oolitic grains; s: sparite cement; m: micrite) (Lion, 2004); d) Estailades limestone (Dautriat, 2009).

B.2 Anstrude limestone

It is a monomineral limestone purely constituted by calcite (Lion, 2004), with a homogeneous microstructure. Oolitic micro-porous grains and sparite cement are dominant and few micrite zones are observed. The cement fills macro-pores among the grains which are

spherical and ranging between 0.1 and 1 mm (Figure 8.2c). No macro-porosity exists and the micro-porosity lays inside the grains. Thus, the porosity which is evaluated at 20% is unimodal and the pore diameter is uniform (around 0.4 μm).

B.3 Estailades limestone

Its microstructure is heterogeneous, composed by dense and micro-porous grains, with a porosity varying between 24 and 30% (Dautriat, 2009). It is a monomineral limestone formed by calcite (99%) and composed of subangular grains (Figure 8.2d) and sparite crowns surrounding micro-porous grains. Micro-porosity presents one third of the total bimodal porosity. Micro-pore diameters are around 0.2 μm , whereas macro-pores are 10 μm in diameter.

B.4 Euville limestone

It is a mono-mineral limestone formed by calcite (Nguyen, 2012). Grains are either dense or micro-porous, ranging between 0.1 and 1 mm. Porosity is around 17%, composed of a macro-porosity (55%) and a micro-porosity (45%). Pore diameters are around 0.5 μm and 20 μm .

B.5 Chamesson limestone

Chamesson limestone is composed of oolitic grains having diameters less than 1 mm and sparite cement (Saad, 2011). Porosity is around 17.4% and is constituted by micro-pores of 0.2 μm in diameter.

B.6 Lens limestone

Lens limestone is composed of oolitic grains and sparite cement with some voids surrounding the grains. Two pore diameter families exist: one of 0.2 μm and another of 0.85 μm forming a total porosity of 13.9% (Saad, 2011). Macro-porosity does not exist in this rock.

B.7 Vilhonneur limestone

It is formed by oolitic grains of around 1 mm in diameter and sparite cement which fills the macro-pores. Three facies of this rock exist: the first one contains voids around the

grains, the second contains voids around some grains and the third does not contain voids. The total porosity is around 11%.

B.8 Chauvigny limestone

It is a monomineral limestone from the Dogger formation of the Parisian Basin, purely composed by calcite (Fortin et al., 2009b). Its porosity is around 17% of which more than two thirds is constituted by micro-pores. Cement is present and fills macro-pores.

B.9 Other limestones

Several limestones have been presented previously in section 2.3.2 (see Table 2.2). Solnhofen is a mudstone whose porosity is too low (3%). Tavel limestone has a 10% of porosity and its grains are small. Furthermore, Indiana has higher porosity (16%) and its grains are larger (300 μm in diameter). Majella and Saint-Maximin are grainstones which show the formation of compaction bands in laboratory. Their porosities are higher than 30%. The microstructure of Saint-Maximin is quite homogeneous and grains have 150 μm in diameter. Leitha limestone is a porous rock presenting several facies, whose porosities vary between 18% and 31%. Micro-pores are negligible in all facies. In addition, according to Lezin et al. (2009), Pillar limestone is a mudstone composed by calcite (between 75 and 94%). The grains are rare and constitute less than 18.5%. Its porosity is unimodal and varies between 9% and 22%. In addition, Bouye is a limestone that can be classified as a mudstone or a wackestone in the Dunham classification since the grains proportion varies between 0% and 62%. Its porosity is less than 14% and is completely composed of micro-pores.

C Thin rod preparation

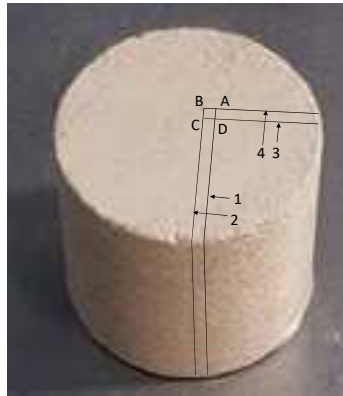


Figure 8.3: A schematic showing the adopted way to extract a thin rod from a porous material using a diamond wire saw.

The way in which the rod is cored should be emphasized. In fact, a preparation of a very thin specimen in such a highly porous rock is extremely difficult. Several specific saws and core drills at the Navier laboratory have been used to cut a such thin specimen. However, all the attempts have failed since the specimens have been broken while coring either by friction with the core drill or under their own weight. Finally, the diamond wire saw has been used to extract the thin rod. A schematic of the sample before cutting is shown in Figure 8.3. To core the rod with $ABCD$ as a square base, the sample is sawed first along the plane (1) until the point A. Then, a new section is created along the plane (2) up to the point B. Similarly, sections along the plane (3) then (4) are performed. Finally, the rod is simply extracted, as the lateral friction helps to preserve it from the breakage due to its own weight.

D Python script to calculate the porosity and its second gradient

```
import numpy as np

#This script allows to calculate porosity and
#its second gradient on a cubic volume

#Image_size in voxels
nb_raws=1722
nb_columns=1722

# For memory capacity reasons, the file is opened in packets.
#The number of packets should be an integer

#Each packet contains a Max_nb_slices_to_read of slices.
Max_nb_slices_to_read=100

#Cube_size in voxels
nb_raws_cube=1000
nb_columns_cube=1000
nb_slices_cube=1000

#Center coordinates of the cube
X0=802
Y0=858
Z0=1392

#Starting point: The left lower vertex of the cube
X=X0-(nb_raws_cube-1)/2
Y=Y0-(nb_columns_cube-1)/2
Z=Z0-(nb_slices_cube-1)/2

#Open the raw file (porosity map)
#Mode: Read (r) and Binary (b)
fileContent=open('filepath...\\filename.raw', 'rb')

#For memory problem reasons, the raw file is opened in packets.
packet_number=nb_slices_cube/Max_nb_slices_to_read
Mean=0.
SOSM=0.
```

```

k_initial=0
for k in range(packet_number):
Starting_voxel=(Z+k_initial-1)*nb_columns*nb_rows

# Shift to the first point, at which we begin reading
#the file
fileContent.seek(Starting_voxel)
Vector_length=Max_nb_slices_to_read*nb_rows*nb_columns

# Total number of voxels to read
GV = np.fromfile(fileContent, dtype=np.uint8,
count=Vector_length)

#Reshape the GV vector by creating an array for each
#slice, each slice array is an array of raw arrays.
#The dimension is nb_slices x nb_rows x nb_columns
GV = GV.reshape((Vector_length/nb_rows/nb_columns,
nb_rows,nb_columns))

#extract the grey levels of voxels in the cube
#from the image.
GV=GV[0:Max_nb_slices_to_read,X:X+nb_rows_cube,
Y:Y+nb_columns_cube]

#Calculate the mean value
Mean=Mean+np.mean(GV)*float(Max_nb_slices_to_read)
/float(nb_slices_cube)

#Form the matrix of square distances (in the plane).
#It is a weight matrix
Weight_matrix=np.array([[[(X+j-X0)**2+(Y+i-Y0)**2
for j in range(nb_columns_cube)]
for i in range(nb_rows_cube)])

#Calculate the distance square dot porosity for each
#plane
X2GV=np.full((Max_nb_slices_to_read,nb_rows_cube,
nb_columns_cube),1)
for i in range(len(GV)):
X2GV[i]=np.multiply(GV[i],Weight_matrix)+GV[i]
*float((Z+i+k_initial-Z0)**2)

```

```

#Calculate the second order statistical moment
SOSM=SOSM+np.mean(X2GV)*float(Max_nb_slices_to_read)
/float(nb_slices_cube)
print SOSM

#Increment
k_initial=k_initial+Max_nb_slices_to_read
print k_initial
GV=[]
Weight_matrix=[]
X2GV=[]

print "Mean=", Mean
print "SOSM=", SOSM

#Calculate the porosity at the center of the cube & its
#second gradient
Second_gradient_g=360./float(nb_rows_cube**4)*
(SOSM-float(nb_rows_cube**2)/4.*Mean)
g_0=Mean-float(nb_rows_cube**2)/24.*Second_gradient_g

print "g0=", g_0
print "Second_gradient_g=", Second_gradient_g

```

E m-grade of micromorphic continuum of degree n

Germain (1973b) has applied the method of virtual power to develop the equations of motion of general micromorphic medium. In these continuous media with microstructure, the material point is no longer a rigid point, but instead, it is a microvolume that may deform. Let M be the center of mass of the subvolume and u_i its displacement vector. The displacement of a point M' of the subvolume of coordinate x'_j with respect to the center of mass can be approximated using the Taylor expansion by:

$$u'_i = u_i + \chi_{ij} \cdot x'_j + \chi_{ijk} \cdot x'_j \cdot x'_k + \chi_{ijkl} \cdot x'_j \cdot x'_k \cdot x'_l \dots \quad (8.1)$$

where χ_{ij} is equivalent to a gradient of the relative displacement, χ_{ijk} is equivalent to a second gradient of the relative displacement and so on. The density of internal forces δw is postulated to be a linear combination of the degrees of freedom and their derivatives. If the density is a function of u_i and its first gradient $u_{i,j}$, then the continuum is called a first grade of a micromorphic medium of degree zero. If the density depends also on the second gradient of the displacement field $u_{i,jk}$, then the continuum is called a second grade of a micromorphic of degree zero. On the other hand, if the density depends on the displacement field u_i and the tensor χ_{ij} with their first gradients, the medium is a first grade of micromorphic of degree one. Figure 8.4 highlights the generalization of the definitions of Germain (1973b).

Grade \ Degree	Degree 0	Degree 1	Degree 2
1	$\delta w(u_i, u_{i,j})$	$\delta w(u_i, u_{i,j}, \chi_{ij}, \chi_{ij,k})$	$\delta w(u_i, u_{i,j}, \chi_{ij}, \chi_{ij,k}, \chi_{ijk}, \chi_{ijk,l})$
2	$\delta w(u_i, u_{i,j}, u_{i,jk})$	$\delta w(u_i, u_{i,j}, u_{i,jk}, \chi_{ij}, \chi_{ij,k}, \chi_{ij,kl})$	$\delta w(u_i, u_{i,j}, u_{i,jk}, \chi_{ij}, \chi_{ij,k}, \chi_{ij,kl}, \chi_{ijk}, \chi_{ijk,l}, \chi_{ijk,lm})$
3	$\delta w(u_i, u_{i,j}, u_{i,jk}, u_{i,jkl})$	$\delta w(u_i, u_{i,j}, u_{i,jk}, u_{i,jkl}, \chi_{ij}, \chi_{ij,k}, \chi_{ij,kl}, \chi_{ij,klm})$...

Figure 8.4: Density of internal forces for a m-grade micromorphic media of degree n. Cells in blue and green highlight a second and third gradient theories respectively when restrictions (Equations 8.2 and 8.3) are applied.

A second gradient theory may be obtained from a restriction on the first grade micromorphic medium of degree one, when assuming that the subvolume is subjected to the same deformation as the general continuum:

$$u_{i,j} = \chi_{ij} \quad (8.2)$$

An equivalence can be thus established among the following micromorphic media (highlighted in blue on Figure 8.4):

- First grade of micromorphic of degree one
- Second grade of micromorphic of degree zero

Since the intended non-local model is a third-gradient dependent model, the restriction of Germain (1973b) can be generalized to the following higher degree:

$$u_{i,j} = \chi_{ij} \quad \text{and} \quad \chi_{ij,k} = \chi_{ijk} \quad (8.3)$$

Or, in terms of the relative microdisplacement gradient $\eta_{ij} = U_{i,j} - \chi_{ij}$ and its extension $\eta_{ijk} = \chi_{ij,k} - \chi_{ijk}$ proposed in this study:

$$\eta_{ij} = 0 \quad \text{and} \quad \eta_{ijk} = 0 \quad (8.4)$$

For this restriction, where the subvolume gradients of deformation are identified with the general continuum gradients of deformation, an equivalence between the following micromorphic media (highlighted in green on Figure 8.4) can be made:

- Third grade of micromorphic of degree zero
- Second grade of micromorphic of degree one
- First grade of micromorphic of degree two

The internal work density δw can be written in terms of u_i , $u_{i,j}$ and $u_{i,jk}$ as:

$$\delta w = \sigma_{ij} u_{i,j} + \nu_{ijk} u_{i,jk} + \zeta_{ijkl} u_{i,jkl} \quad (8.5)$$

F Calculation of P_v

This appendix presents the integral calculations that lead to the expression of the virtual power of external volumic forces P_v , which is defined as:

$$P_v = \int_{\mathcal{D}} \left[f_i \cdot u_i + \Psi_{ij} \cdot \chi_{ij} + \xi_{ijk} \cdot \chi_{ijk} \right] dv \quad (8.6)$$

Using the restrictions of Equation 8.3, the previous virtual power can be rewritten then decomposed to three distinct integrals as:

$$P_v = \int_{\mathcal{D}} \left[f_i \cdot u_i + \Psi_{ij} \cdot u_{i,j} + \xi_{ijk} \cdot u_{i,jk} \right] dv = I_1 + J_1 + J_2 \quad (8.7)$$

Calculation of J_1 An integration by parts leads to:

$$J_1 = \int_{\partial\mathcal{D}} \Psi_{ij} n_j u_i dS - \int_{\mathcal{D}} \Psi_{ij,j} u_i dv \quad (8.8)$$

Where $\partial\mathcal{D}$ represents the boundary on the volume \mathcal{D} .

Calculation of J_2 Again, an integration by parts leads to:

$$J_2 = \int_{\partial\mathcal{D}} \xi_{ijk} n_k u_{i,j} dS - \int_{\mathcal{D}} \xi_{ijk,k} u_{i,j} dv \quad (8.9)$$

The second term of J_2 is analogous to J_1 . Thus J_2 can be rewritten as:

$$J_2 = \int_{\partial\mathcal{D}} \xi_{ijk} n_k u_{i,j} dS - \int_{\partial\mathcal{D}} \xi_{ijk,k} n_j u_i dS + \int_{\mathcal{D}} \xi_{ijk,kj} u_i dv \quad (8.10)$$

More developments must be done on the first term of J_2 . The solution of this integral is given in Germain (1973b) when they have presented the second gradient theory. Following the definitions of Mindlin (1964), $D_j K_i$ and DK_i are the tangential and normal derivatives of the vector field K_i on the surface $\partial\mathcal{D}$:

$$K_{i,j} = D_j K_i + n_j DK_i \quad \text{with} \quad DK_i = n_k K_{i,k}$$

Notice that

$$\begin{aligned} M_{ij} u_{i,j} &= (M_{ij} u_i)_{,j} - M_{ij,j} u_i \\ &= D_j (M_{ij} u_i) + M_{ij} n_j D u_i - (D_j M_{ij}) u_i \end{aligned} \quad (8.11)$$

On the other hand, the divergence theorem for an open subdomain Σ of $\partial\mathcal{D}$ gives:

$$\int_{\Sigma} D_j q_j dS = \int_{\Sigma} (D_l n_l) n_j q_j dS + \int_{\partial\Sigma} v_j q_j ds \quad (8.12)$$

where t_i is the unit tangent vector to $\partial\Sigma$, $v_j = \epsilon_{jml} \cdot t_m \cdot n_l$ is the unit normal vector to $\partial\Sigma$, tangent to $\partial\mathcal{D}$ and ϵ_{jml} is the Levi-Civita symbol:

$$\epsilon_{jml} = \begin{cases} +1, & \text{if } (j, m, l) \in \{(1, 2, 3); (3, 1, 2); (2, 3, 1)\} \\ -1, & \text{if } (j, m, l) \in \{(1, 3, 2); (3, 2, 1); (2, 1, 3)\} \\ 0, & \text{if } j = m \text{ or } m = l \text{ or } j = l \end{cases} \quad (8.13)$$

Thus:

$$\begin{aligned} \int_{\partial\mathcal{D}} M_{ij} u_{i,j} dS &= \int_{\partial\mathcal{D}} [((D_k n_k) M_{ij} n_j - D_j M_{ij}) u_i + M_{ij} n_j D u_i] dS \\ &+ \int_{\Gamma} [[M_{ij} v_j]] u_i ds \end{aligned} \quad (8.14)$$

where the notation $[[K_i]]$ marks a discontinuity of the vector field K_i and Γ represents a line on $\partial\mathcal{D}$ (if any) where the tangent plane of $\partial\mathcal{D}$ is discontinuous. Finally, the first term of J_2 is expressed similarly to the previous equation, where $\xi_{ijk} n_k$ replaces M_{ij} . Therefore, the expression of J_2 is:

$$\begin{aligned} J_2 &= \int_{\partial\mathcal{D}} [((D_l n_l) \xi_{ijk} n_k n_j - D_j (\xi_{ijk} n_k)) u_i + \xi_{ijk} n_k n_j D u_i] dS \\ &+ \int_{\Gamma} [[\xi_{ijk} n_k v_j]] u_i ds \\ &- \int_{\partial\mathcal{D}} \xi_{ijk, k} n_j u_i dS + \int_{\mathcal{D}} \xi_{ijk, kj} u_i dv \end{aligned} \quad (8.15)$$

Gathering all the results, the virtual power of the external volumic forces can be written as:

$$\begin{aligned} P_v &= \int_{\mathcal{D}} [f_i - \Psi_{ij,j} + \xi_{ijk, kj}] u_i dv \\ &+ \int_{\partial\mathcal{D}} [\Psi_{ij} n_j - \xi_{ijk, k} n_j + (D_l n_l) \xi_{ijk} n_k n_j - D_j (\xi_{ijk} n_k)] u_i dS \\ &+ \int_{\partial\mathcal{D}} \xi_{ijk} n_k n_j D u_i dS \\ &+ \int_{\Gamma} [[\xi_{ijk} n_k v_j]] u_i ds \end{aligned} \quad (8.16)$$

G Calculation of P_c

This appendix presents the integral calculations that lead to the expression of the virtual power of external contact forces P_c , which is defined as:

$$P_c = \int_{\partial\mathcal{D}} \left[T_i u_i + M_{ij} \chi_{ij} + \mathcal{L}_{ijk} \chi_{ijk} \right] dS \quad (8.17)$$

Using the restrictions of Equation 8.3, the previous virtual power can be rewritten then decomposed to three distinct integrals as:

$$P_c = \int_{\partial\mathcal{D}} \left[T_i u_i + M_{ij} u_{i,j} + \mathcal{L}_{ijk} u_{i,jk} \right] dS = I_2 + J_3 + K_1 \quad (8.18)$$

Calculation of J_3 The calculation of this term has been exposed in appendix F (Equation 8.14).

$$\begin{aligned} J_3 &= \int_{\partial\mathcal{D}} M_{ij} u_{i,j} dS \\ &= \int_{\partial\mathcal{D}} \left[((D_k n_k) M_{ij} n_j - D_j M_{ij}) u_i + M_{ij} n_j D u_i \right] dS \\ &\quad + \int_{\Gamma} [[M_{ij} v_j]] u_i ds \end{aligned} \quad (8.19)$$

Calculation of K_1

$$K_1 = \int_{\partial\mathcal{D}} \mathcal{L}_{ijk} u_{i,jk} dS$$

Similarly to Equation 8.11, notice that:

$$\begin{aligned} \mathcal{L}_{ijk} u_{i,jk} &= (\mathcal{L}_{ijk} u_{i,j})_{,k} - \mathcal{L}_{ijk,k} u_{i,j} \\ &= D_k (\mathcal{L}_{ijk} u_{i,j}) + n_k \mathcal{L}_{ijk} D(u_{i,j}) - D_k (\mathcal{L}_{ijk}) u_{i,j} \end{aligned}$$

Thus, K_1 can be decomposed to three integrals after applying the divergence theorem to its first term:

$$\begin{aligned} K_1 &= \int_{\partial\mathcal{D}} \left[D_k (\mathcal{L}_{ijk} u_{i,j}) + n_k \mathcal{L}_{ijk} D(u_{i,j}) - D_k (\mathcal{L}_{ijk}) u_{i,j} \right] dS \\ &= \int_{\partial\mathcal{D}} \left[(D_l n_l n_k \mathcal{L}_{ijk} - D_k (\mathcal{L}_{ijk})) u_{i,j} + n_k \mathcal{L}_{ijk} D(u_{i,j}) \right] dS \\ &\quad + \int_{\Gamma} [[v_k \mathcal{L}_{ijk}]] u_{i,j} ds \\ &= L_1 + L_2 + L_3 \end{aligned} \quad (8.20)$$

Calculation of L_1 Similarly to J_3 , L_1 can be deduced by replacing M_{ij} by $D_l n_l n_k \mathcal{L}_{ijk} - D_k(\mathcal{L}_{ijk})$:

$$\begin{aligned}
L_1 &= \int_{\partial \mathcal{D}} (D_l n_l n_k \mathcal{L}_{ijk} - D_k(\mathcal{L}_{ijk})) u_{i,j} dS \\
&= \int_{\partial \mathcal{D}} \left[[D_p n_p D_l n_l n_k n_j \mathcal{L}_{ijk} - D_p n_p n_j D_k(\mathcal{L}_{ijk}) \right. \\
&\quad \left. - D_j(D_l n_l n_k \mathcal{L}_{ijk} - D_k(\mathcal{L}_{ijk})) \right] u_i \\
&\quad + [D_l n_l n_k n_j \mathcal{L}_{ijk} - D_k(\mathcal{L}_{ijk}) n_j] D u_i \Big] dS \\
&\quad + \int_{\Gamma} [(D_l n_l n_k \mathcal{L}_{ijk} v_j - D_k(\mathcal{L}_{ijk}) v_j)] u_i ds
\end{aligned} \tag{8.21}$$

Calculation of L_2

$$L_2 = \int_{\partial \mathcal{D}} n_k \mathcal{L}_{ijk} D(u_{i,j}) dS \tag{8.22}$$

However,

$$\begin{aligned}
D(u_{i,j}) &= n_p u_{i,jp} = n_p u_{i,pj} \\
&= (n_p u_{i,p})_{,j} - n_{p,j} u_{i,p} \\
&= (D u_i)_{,j} - n_{p,j} u_{i,p} \\
&= D_j(D u_i) + n_j D^2 u_i - n_{p,j} u_{i,p}
\end{aligned}$$

The last term can be written as:

$$n_{p,j} u_{i,p} = [D_j(n_p) + n_j D(n_p)] \cdot [D_p(u_i) + n_p D(u_i)]$$

Noticing that

•

$$n_p n_p = 1 \quad \text{then} \quad D(n_p n_p) = 0 \quad \text{then} \quad D(n_p) n_p = 0$$

•

$$\begin{aligned}
D_j(n_p) n_p &= D_j(n_p n_p) - D_j(n_p) n_p = D_j(1) - D_j(n_p) n_p = -D_j(n_p) n_p \\
&\text{then} \quad D_j(n_p) n_p = 0
\end{aligned}$$

•

$$D(n_p) \cdot D_p(U_i) = 0 \quad (\text{By definition, they are orthogonal})$$

Therefore, the last term can be written as:

$$n_{p,j} u_{i,p} = D_j(n_p) \cdot D_p(u_i)$$

This result was given by Mindlin, 1965, but without a proof. Going back to L_2 , it can be written as:

$$L_2 = \int_{\partial\mathcal{D}} n_k \mathcal{L}_{ijk} \left[D_j(Du_i) + n_j D^2 u_i - D_j(n_p) D_p(u_i) \right] dS \quad (8.23)$$

Noticing that

$$n_k \mathcal{L}_{ijk} D_j(Du_i) = D_j(n_k \mathcal{L}_{ijk} Du_i) - D_j(n_k \mathcal{L}_{ijk}) Du_i$$

and

$$n_k \mathcal{L}_{ijk} D_j(n_p) D_p(u_i) = D_p(n_k \mathcal{L}_{ijk} D_j(n_p) u_i) - D_p(n_k \mathcal{L}_{ijk} D_j(n_p)) u_i$$

L_2 can be split into 5 integrals:

$$\begin{aligned} L_2 &= \int_{\partial\mathcal{D}} \left[D_j(n_k \mathcal{L}_{ijk} Du_i) - D_j(n_k \mathcal{L}_{ijk}) Du_i + n_k \mathcal{L}_{ijk} n_j D^2 u_i \right. \\ &\quad \left. - D_p(n_k \mathcal{L}_{ijk} D_j(n_p) u_i) + D_p(n_k \mathcal{L}_{ijk} D_j(n_p)) u_i \right] dS \\ &= N_1 - N_2 + N_3 - N_4 + N_5 \end{aligned}$$

To determine L_2 , the divergence theorem must be applied on N_1 and N_4 :

$$\begin{aligned} N_1 &= \int_{\partial\mathcal{D}} D_j(n_k \mathcal{L}_{ijk} Du_i) dS \\ &= \int_{\partial\mathcal{D}} D_l n_l n_j n_k \mathcal{L}_{ijk} Du_i dS + \int_{\Gamma} [[v_j n_k \mathcal{L}_{ijk}]] Du_i ds \end{aligned}$$

$$\begin{aligned} N_4 &= \int_{\partial\mathcal{D}} D_p(n_k \mathcal{L}_{ijk} D_j(n_p) u_i) dS \\ &= \int_{\partial\mathcal{D}} \cancel{D_l n_l n_p n_k \mathcal{L}_{ijk} D_j(n_p) u_i} dS + \int_{\Gamma} [[v_p n_k \mathcal{L}_{ijk} D_j(n_p)]] u_i ds \end{aligned}$$

The first term of N_4 is nil since $D_j(n_p) n_p = 0$ as showed previously.

Calculation of L_3

$$L_3 = \int_{\Gamma} [[v_k \mathcal{L}_{ijk}]] u_{i,j} ds$$

Similarly to Equation 8.11, notice that:

$$[[v_k \mathcal{L}_{ijk}]] u_{i,j} = D_j([[v_k \mathcal{L}_{ijk}]] u_i) + n_j [[v_k \mathcal{L}_{ijk}]] Du_i - D_j([[v_k \mathcal{L}_{ijk}]] u_i)$$

After applying the divergence theorem to the first term, L_3 is written as:

$$\begin{aligned} L_3 &= \int_{\Gamma} \left[D_j([[v_k \mathcal{L}_{ijk}]] u_i) + n_j [[v_k \mathcal{L}_{ijk}]] Du_i - D_j([[v_k \mathcal{L}_{ijk}]] u_i) \right] ds \\ &= \int_{\Gamma} \left[\left[D_l n_l n_j [[v_k \mathcal{L}_{ijk}]] - D_j([[v_k \mathcal{L}_{ijk}]] \right) u_i + n_j [[v_k \mathcal{L}_{ijk}]] Du_i \right] ds \\ &\quad + \left[[t_j [[v_k \mathcal{L}_{ijk}]]] \right] u_i \end{aligned}$$

Where t_j is the tangent to the ridge Γ and $\left[\left[t_j \left[v_k \mathcal{L}_{ijk} \right] \right] \right]$ represents eventually a contact force on the intersection of two ridges of discontinuous tangents. Gathering all the results, the virtual power of the external contact forces can be written as the sum of the integrals:

$$\begin{aligned}
P_c &= I_2 + J_3 + K_1 \\
&= I_2 + J_3 + L_1 + L_2 + L_3 \\
&= I_2 + J_3 + L_1 + N_1 - N_2 + N_3 - N_4 + N_5 + L_3
\end{aligned} \tag{8.24}$$

Finally, P_c has the following form:

$$\boxed{
\begin{aligned}
P_c &= \int_{\partial\mathcal{D}} \left[\tilde{T}_i u_i + \tilde{N}_i D u_i + \tilde{P}_i D^2 u_i \right] dS \\
&\quad + \int_{\Gamma} \left[\tilde{R}_i u_i + \tilde{S}_i D u_i \right] ds \\
&\quad + \tilde{F}_i u_i
\end{aligned}
} \tag{8.25}$$

Where \tilde{T}_i is a surface traction:

$$\begin{aligned}
\tilde{T}_i &= T_i + (D_k n_k) M_{ij} n_j - D_j M_{ij} + D_p n_p D_l n_l n_k n_j \mathcal{L}_{ijk} \\
&\quad - D_p n_p n_j D_k (\mathcal{L}_{ijk}) - D_j (D_l n_l n_k \mathcal{L}_{ijk} - D_k (\mathcal{L}_{ijk})) \\
&\quad + D_p (n_k \mathcal{L}_{ijk} D_j (n_p))
\end{aligned} \tag{8.26}$$

\tilde{N}_i is a normal double traction:

$$\begin{aligned}
\tilde{N}_i &= M_{ij} n_j + D_l n_l n_k n_j \mathcal{L}_{ijk} - D_k (\mathcal{L}_{ijk}) n_j \\
&\quad + D_l n_l n_j n_k \mathcal{L}_{ijk} - D_j (n_k \mathcal{L}_{ijk})
\end{aligned} \tag{8.27}$$

\tilde{P}_i is a normal triple traction (generalization of \tilde{N}_i to the next higher order):

$$\tilde{P}_i = n_k \mathcal{L}_{ijk} n_j \tag{8.28}$$

\tilde{R}_i is eventually a line traction:

$$\begin{aligned}
\tilde{R}_i &= [[M_{ij} v_j]] + [[(D_l n_l n_k \mathcal{L}_{ijk} v_j - D_k (\mathcal{L}_{ijk}) v_j)]] \\
&\quad - [[v_p n_k \mathcal{L}_{ijk} D_j (n_p)]] + D_l n_l n_j [[v_k \mathcal{L}_{ijk}]] - D_j ([[v_k \mathcal{L}_{ijk}]])
\end{aligned} \tag{8.29}$$

\tilde{S}_i is eventually a line normal double traction:

$$\tilde{S}_i = [[v_j n_k \mathcal{L}_{ijk}]] + n_j [[v_k \mathcal{L}_{ijk}]] \tag{8.30}$$

\tilde{F}_i is eventually a punctual traction:

$$\tilde{F}_i = \left[\left[t_j \left[v_k \mathcal{L}_{ijk} \right] \right] \right] \tag{8.31}$$

H Calculation of P_i

This appendix presents the integral calculations that lead to the expression of the virtual power of internal forces P_i , which is defined as:

$$P_i = - \int_{\mathcal{D}} \left[\sigma_{ij} u_{i,j} + \nu_{ijk} u_{i,jk} + \zeta_{ijkl} u_{i,jkl} \right] dv \quad (8.32)$$

An integration by parts applied on the last term leads to:

$$\begin{aligned} P_i &= - \int_{\mathcal{D}} \left[\sigma_{ij} u_{i,j} + (\nu_{ijk} - \zeta_{ijkl,l}) u_{i,jk} \right] dv - \int_{\partial\mathcal{D}} \zeta_{ijkl} n_l u_{i,jk} dS \\ &= -J_4 - J_5 - K_2 \end{aligned} \quad (8.33)$$

Calculation of J_4 J_4 is simply obtained by an integration by parts:

$$\begin{aligned} J_4 &= \int_{\mathcal{D}} \sigma_{ij} u_{i,j} dv \\ &= \int_{\partial\mathcal{D}} \sigma_{ij} n_j u_i dS - \int_{\mathcal{D}} \sigma_{ij,j} u_i dv \end{aligned} \quad (8.34)$$

Calculation of J_5 An integration by parts is first applied, then the integral is split into two parts:

$$\begin{aligned} J_5 &= \int_{\mathcal{D}} (\nu_{ijk} - \zeta_{ijkl,l}) u_{i,jk} dv \\ &= \int_{\partial\mathcal{D}} (\nu_{ijk} - \zeta_{ijkl,l}) n_k u_{i,j} dS - \int_{\mathcal{D}} (\nu_{ijk,k} - \zeta_{ijkl,lk}) u_{i,j} dv \\ &= L_4 - L_5 \end{aligned} \quad (8.35)$$

Calculation of L_4 This integral is similar to the integral in Equation 8.14, where M_{ij} is replaced by $(\nu_{ijk} - \zeta_{ijkl,l}) n_k$:

$$\begin{aligned} L_4 &= \int_{\partial\mathcal{D}} (\nu_{ijk} - \zeta_{ijkl,l}) n_k u_{i,j} dS \\ &= \int_{\partial\mathcal{D}} \left[D_p n_p (\nu_{ijk} - \zeta_{ijkl,l}) n_k n_j - D_j ((\nu_{ijk} - \zeta_{ijkl,l}) n_k) \right] u_i \\ &\quad + (\nu_{ijk} - \zeta_{ijkl,l}) n_k n_j D u_i dS \\ &\quad + \int_{\Gamma} [(\nu_{ijk} - \zeta_{ijkl,l}) n_k v_j] u_i ds \end{aligned} \quad (8.36)$$

Calculation of L_5 L_5 is simply obtained by an integration by parts:

$$\begin{aligned} L_5 &= \int_{\mathcal{D}} (\nu_{ijk,k} - \zeta_{ijkl,lk}) u_{i,j} dv \\ &= \int_{\partial\mathcal{D}} (\nu_{ijk,k} - \zeta_{ijkl,lk}) n_j u_i dS - \int_{\mathcal{D}} (\nu_{ijk,kj} - \zeta_{ijkl,lkj}) u_i dv \end{aligned} \quad (8.37)$$

Calculation of K_2 K_2 is similar to K_1 , presented in Appendix G, where \mathcal{L}_{ijk} is replaced by $\zeta_{ijkl} n_l$. Therefore, P_i can be written as:

$$\begin{aligned} P_i &= \int_{\mathcal{D}} \left[\sigma_{ij,j} - \nu_{ijk,kj} + \zeta_{ijkl,lkj} \right] u_i dv \\ &+ \int_{\partial\mathcal{D}} \left[-\sigma_{ij} n_j - D_p n_p (\nu_{ijk} - \zeta_{ijkl,l}) n_k n_j \right. \\ &+ D_j ((\nu_{ijk} - \zeta_{ijkl,l}) n_k) + (\nu_{ijk,k} - \zeta_{ijkl,lk}) n_j \\ &- D_p n_p D_s n_s n_k n_j \zeta_{ijkl} n_l + D_p n_p n_j D_k (\zeta_{ijkl} n_l) \\ &\left. + D_j (D_p n_p n_k \zeta_{ijkl} n_l - D_k (\zeta_{ijkl} n_l)) - D_p (n_k \zeta_{ijkl} n_l D_j (n_p)) \right] u_i dS \\ &+ \int_{\partial\mathcal{D}} \left[-(\nu_{ijk} - \zeta_{ijkl,l}) n_k n_j - D_p n_p n_k n_j \zeta_{ijkl} n_l \right. \\ &\left. + D_k (\zeta_{ijkl} n_l) n_j - D_p n_p n_j n_k \zeta_{ijkl} n_l + D_j (n_k \zeta_{ijkl} n_l) \right] D u_i dS \\ &+ \int_{\partial\mathcal{D}} \left[-n_k \zeta_{ijkl} n_l n_j \right] D^2 u_i dS \\ &+ \int_{\Gamma} \left[[-(\nu_{ijk} - \zeta_{ijkl,l}) n_k v_j - D_p n_p n_k \zeta_{ijkl} n_l v_j + D_k (\zeta_{ijkl} n_l) v_j \right. \\ &+ v_p n_k \zeta_{ijkl} n_l D_j (n_p)] - D_p n_p n_j [[v_k \zeta_{ijkl} n_l]] + D_j ([[v_k \zeta_{ijkl} n_l]]) \left. \right] u_i ds \\ &+ \int_{\Gamma} \left[-[[v_j n_k \zeta_{ijkl} n_l]] - n_j [[v_k \zeta_{ijkl} n_l]] \right] D u_i ds \\ &- \left[[t_j [[v_k \zeta_{ijkl} n_l]]] \right] u_i \end{aligned} \quad (8.38)$$

I Penalty moduli identification

The gradient-dependent plasticity model is implemented in the *Numerical geolab* code as a general micromorphic continuum of degree two. The restrictions ($\eta = 0$ and $\eta_k = 0$) are introduced indirectly, by means of two penalty moduli defined as following:

$$\begin{aligned}\dot{s} &= P_1 \dot{\eta} \\ \dot{s}_k &= P_2 L^2 \dot{\eta}_k\end{aligned}\quad (8.39)$$

For very high values of P_1 and P_2 , the restrictions above are obtained. To identify the values of these moduli, a linear stability analysis is applied on the general micromorphic continuum (without restrictions), the results are compared to those of the micromorphic continuum presented in Section 6.3.4. The equilibrium equations for the micromorphic continuum of degree two without restrictions have been given by Germain (1973b):

$$\begin{aligned}\sigma_{ij,j}^* + s_{ij,j}^* &= 0 \\ s_{ij}^* + \nu_{ijk,k}^* + s_{ijk,k}^* &= 0 \\ s_{ijk}^* + \zeta_{ijkl,l}^* &= 0\end{aligned}\quad (8.40)$$

In this study, only the volumetric quantities of the higher-order stresses are considered ($s_{ij} = \delta_{ij}s$; $\nu_{ijk} = \delta_{ij}\nu_k$; $s_{ijk} = \delta_{ij}s_k$; $\zeta_{ijkl} = \delta_{ij}\delta_{kl}\zeta$). Hence, the new equilibrium equations become:

$$\begin{aligned}\sigma_{ij,j}^* + \delta_{ij}s_{,j}^* &= 0 \\ \delta_{ij}s^* + \delta_{ij}\nu_{k,k}^* + \delta_{ij}s_{k,k}^* &= 0 \\ \delta_{ij}s_k^* + \delta_{ij}\delta_{kl}\zeta_{,l}^* &= 0\end{aligned}\quad (8.41)$$

A perturbation is applied on the homogeneous solution, and is linked to the kinematic quantities via the following constitutive law:

$$\begin{aligned}\tilde{\sigma}_{ij} &= C_{ijkl}^{ep} \tilde{u}_{k,l} - \langle 1 \rangle \frac{b_{ij}^g \frac{\partial F}{\partial \zeta} BL^4}{H_1} \tilde{\chi}_{k,k} \\ \tilde{s} &= P_1 \tilde{\eta} = P_1 (\tilde{u}_{i,i} - \tilde{\chi}) \\ \tilde{\nu}_k &= AL^2 \tilde{\chi}_{,k} \\ \tilde{s}_k &= P_2 L^2 \tilde{\eta}_k = P_2 L^2 (\tilde{\chi}_{,k} - \tilde{\chi}_k) \\ \tilde{\zeta} &= BL^4 \tilde{\chi}_{k,k}\end{aligned}\quad (8.42)$$

The perturbations of the seven degrees of freedom are assumed to be in the direction 1 and have thus the following forms:

$$\begin{aligned}\tilde{u}_i &= U_i e^{st + \frac{2\pi}{\lambda} ix_1} \\ \tilde{\chi} &= X e^{st + \frac{2\pi}{\lambda} ix_1} \\ \tilde{\chi}_k &= X_k e^{st + \frac{2\pi}{\lambda} ix_1}\end{aligned}\quad (8.43)$$

In addition, the perturbation must respect the momentum balance:

$$\begin{aligned}
 \tilde{\sigma}_{ij,j} + \delta_{ij}\tilde{s}_{,j} &= \rho\ddot{u}_i \\
 \delta_{ij}\tilde{s} + \delta_{ij}\tilde{\nu}_{k,k} + \delta_{ij}\tilde{s}_{k,k} &= 0 \\
 \delta_{ij}\tilde{s}_k + \delta_{ij}\delta_{kl}\tilde{\zeta}_{,l} &= 0
 \end{aligned}
 \tag{8.44}$$

where the micro-inertia terms are neglected here. Finally, by injecting the constitutive relations in the momentum balance, one can obtain the governing equations (Equation 8.45 on the following page). The non-trivial solution is obtained when the determinant of the matrix vanishes. The results of the linear stability analysis applied on the material with restrictions (Section 6.3.4) and the material without restrictions for $P_1 = 10^9$ MPa and $P_2 = 10^9$ MPa are compared at several points on the yield surface and identical results are obtained. For instance, Figure 8.5 shows the consistency between the results at the plasticity onset in axisymmetric triaxial loading under 10.5 MPa of confining pressure. In conclusion, the values $P_1 = 10^9$ MPa and $P_2 = 10^9$ MPa are retained for the numerical implementation.

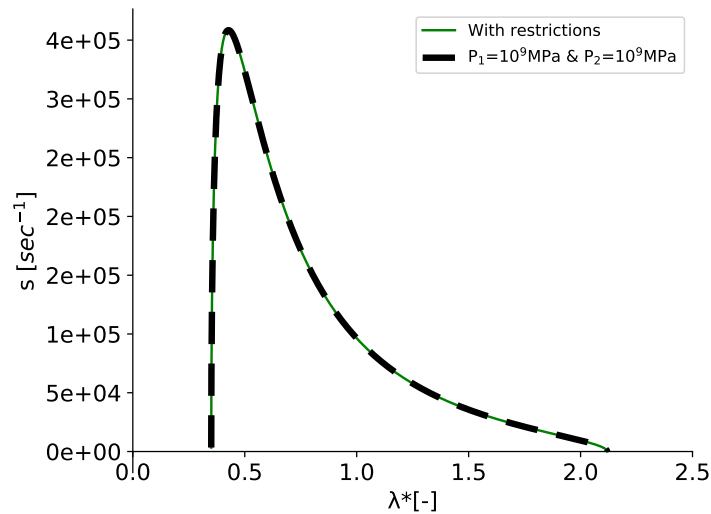


Figure 8.5: Growth coefficient s vs the normalized perturbation wavelength λ^* at the plasticity onset in an axisymmetric triaxial loading under 10.5 MPa of confining pressure. Two cases are presented: with restrictions and without restrictions, where $P_1 = 10^9$ MPa and $P_2 = 10^9$ MPa. In both cases, $\rho = 1600$ Kg/m³, $L = 24$ mm and $B = 0.025$ MPa.

Bibliography

- Allis, R., Zhan, X., and Clotworthy, A. (1998). „Predicting Future Subsidence Wairakei Field, New Zealand“. In: *TRANSACTIONS-GEOTHERMAL RESOURCES COUNCIL*, pp. 43–48 (cit. on p. 2).
- Antonellini, M. A., Aydin, A., and Pollard, D. D. (1994). „Microstructure of deformation bands in porous sandstones at Arches National Park, Utah“. In: *Journal of structural geology* 16.7, pp. 941–959 (cit. on pp. 11–13, 26).
- Araujo, R. E., Bezerra, F. H., Nogueira, F. C., Balsamo, F., Carvalho, B. R., Souza, J. A., Sanglard, J. C., de Castro, D. L., and Melo, A. C. (2018). „Basement control on fault formation and deformation band damage zone evolution in the Rio do Peixe Basin, Brazil“. In: *Tectonophysics* 745, pp. 117–131 (cit. on p. 11).
- Ayachit, U. (2015). *The paraview guide: a parallel visualization application*. Kitware, Inc. (cit. on p. 63).
- Aydin, A., Borja, R. I., and Eichhubl, P. (2006). „Geological and mathematical framework for failure modes in granular rock“. In: *Journal of Structural Geology* 28.1, pp. 83–98 (cit. on pp. 11, 26).
- Barbier, E. (2002). „Geothermal energy technology and current status: an overview“. In: *Renewable and sustainable energy reviews* 6.1-2, pp. 3–65 (cit. on pp. 1, 2, 176).
- Bathurst, R. G. (1972). *Carbonate sediments and their diagenesis*. Vol. 12. Elsevier.
- Baud, P., Vinciguerra, S., David, C., Cavallo, A., Walker, E., and Reuschlé, T. (2009). „Compaction and failure in high porosity carbonates: Mechanical data and microstructural observations“. In: *Pure and Applied Geophysics* 166.5-7, pp. 869–898 (cit. on pp. 14, 19, 20, 41, 80, 81, 137).
- Baud, P., Schubnel, A., and Wong, T.-f. (2000). „Dilatancy, compaction, and failure mode in Solnhofen limestone“. In: *Journal of Geophysical Research: Solid Earth* 105.B8, pp. 19289–19303 (cit. on pp. 9, 14, 16, 19, 41).
- Baud, P., Klein, E., and Wong, T.-f. (2004). „Compaction localization in porous sandstones: spatial evolution of damage and acoustic emission activity“. In: *Journal of Structural Geology* 26.4, pp. 603–624 (cit. on pp. 14–19, 23).
- Baud, P., Vajdova, V., and Wong, T. F. (2006). „Shear-enhanced compaction and strain localization: Inelastic deformation and constitutive modeling of four porous sandstones“. In: *Journal of Geophysical Research: Solid Earth* 111.12, pp. 1–17 (cit. on p. 14).
- Baud, P., Reuschlé, T., Ji, Y., Cheung, C. S., and Wong, T.-f. (2015). „Mechanical compaction and strain localization in Bleurswiller sandstone“. In: *Journal of Geophysical Research: Solid Earth* 120.9, pp. 6501–6522 (cit. on pp. 7, 14–17, 176).

- Baud, P., Schubnel, A., Heap, M., and Rolland, A. (2017a). „Inelastic Compaction in High-Porosity Limestone Monitored Using Acoustic Emissions“. In: *Journal of Geophysical Research: Solid Earth* 122.12, p. 9989 (cit. on pp. 3, 14, 21, 23, 44, 69, 78, 80, 81, 88, 101, 137, 154, 171, 176).
- Baud, P., Exner, U., Lommatzsch, M., Reuschlé, T., and Wong, T.-f. (2017b). „Mechanical behavior, failure mode, and transport properties in a porous carbonate“. In: *Journal of Geophysical Research: Solid Earth* 122.9, pp. 7363–7387 (cit. on pp. 9, 14, 18, 19, 21, 22, 25, 27, 41).
- Baxevanis, T., Papamichos, E., Flornes, O., and Larsen, I. (2006). „Compaction bands and induced permeability reduction in Tuffeau de Maastricht calcarenite“. In: *Acta Geotechnica* 1.2, pp. 123–135 (cit. on pp. 14, 19, 20).
- Bazant, Z. P. and Pijaudier-Cabot, G. (1988). „Nonlocal continuum damage, localization instability and convergence“. In: *Journal of applied mechanics* 55.2, pp. 287–293 (cit. on p. 37).
- Bertani, R. (2016). „Geothermal power generation in the world 2010–2014 update report“. In: *Geothermics* 60, pp. 31–43 (cit. on p. 1).
- Bésuelle, P. and Lanatà, P. (2017). „Emergence of Strain Localization in Porous Rocks Characterized by Full-Field Measurement in Plane Strain Condition“. In: *International Workshop on Bifurcation and Degradation in Geomaterials*. Springer, pp. 25–31 (cit. on p. 20).
- Bésuelle, P. and Rudnicki, J. W. (2004). „Localization: shear bands and compaction bands“. In: *INTERNATIONAL GEOPHYSICS SERIES*. 89, pp. 219–322 (cit. on pp. 10, 28).
- Borgomano, J., Pimienta, L., Fortin, J., and Guéguen, Y. (2017). „Dispersion and attenuation measurements of the elastic moduli of a dual-porosity limestone“. In: *Journal of Geophysical Research: Solid Earth* 122.4, pp. 2690–2711 (cit. on p. 181).
- Bornert, M., Chaix, J.-M., Doumalin, P., Dupré, J.-C., Fournel, T., Jeulin, D., Maire, E., Moreaud, M., and Moulinec, H. (2004). „Mesure tridimensionnelle de champs cinématiques par imagerie volumique pour l'analyse des matériaux et des structures“. In: *Instrumentation, Mesure, Métrologie* 4.3-4, pp. 43–88 (cit. on pp. 60, 62).
- Cashman, S. and Cashman, K. (2000). „Cataclasis and deformation-band formation in unconsolidated marine terrace sand, Humboldt County, California“. In: *Geology* 28.2, pp. 111–114 (cit. on p. 20).
- Chambon, R., Caillerie, D., and Matsushima, T. (2001). „Plastic continuum with microstructure, local second gradient theories for geomaterials: localization studies“. In: *International Journal of Solids and Structures* 38.46-47, pp. 8503–8527 (cit. on p. 36).
- Charalampidou, E.-M., Hall, S. A., Stanchits, S., Lewis, H., and Viggiani, G. (2011). „Characterization of shear and compaction bands in a porous sandstone deformed under triaxial compression“. In: *Tectonophysics* 503.1-2, pp. 8–17 (cit. on p. 23).
- Charalampidou, E.-M., Hall, S. A., Stanchits, S., Viggiani, G., and Lewis, H. (2014). „Shear-enhanced compaction band identification at the laboratory scale using acoustic and full-field methods“. In: *International Journal of Rock Mechanics and Mining Sciences* 67, pp. 240–252 (cit. on p. 23).
- Chateau, C., Nguyen, T. T., Bornert, M., and Yvonnet, J. (2018). „DVC-based image subtraction to detect microcracking in lightweight concrete“. In: *Strain*, e12276 (cit. on p. 83).
- Cheung, C. S., Baud, P., and Wong, T.-f. (2012). „Effect of grain size distribution on the development of compaction localization in porous sandstone“. In: *Geophysical Research Letters* 39.21 (cit. on pp. 3, 26, 27).
- Choquette, P. W. and Pray, L. C. (1970). „Geologic nomenclature and classification of porosity in sedimentary carbonates“. In: *AAPG bulletin* 54.2, pp. 207–250 (cit. on pp. 3, 22).

- Ciantia, M. and Hueckel, T (2013). „Weathering of submerged stressed calcarenites: chemo-mechanical coupling mechanisms“. In: *Géotechnique* 63.9, pp. 768–785 (cit. on p. 11).
- Cilona, A., Baud, P., Tondi, E., Agosta, F., Vinciguerra, S., Rustichelli, A., and Spiers, C. J. (2012). „Deformation bands in porous carbonate grainstones: Field and laboratory observations“. In: *Journal of Structural Geology* 45, pp. 137–157 (cit. on p. 22).
- Cilona, A., Faulkner, D. R., Tondi, E., Agosta, F., Mancini, L., Rustichelli, A., Baud, P., and Vinciguerra, S. (2014). „The effects of rock heterogeneity on compaction localization in porous carbonates“. In: *Journal of Structural Geology* 67, pp. 75–93 (cit. on pp. 11, 14, 18–20, 41, 74).
- Cosserat, E. and Cosserat, F. (1909). „Théorie des corps déformables“. In: (cit. on p. 36).
- Coussy, O. (2004). *Poromechanics*. John Wiley & Sons (cit. on p. 74).
- Coussy, O. (2011). *Mechanics and physics of porous solids*. John Wiley & Sons (cit. on p. 128).
- Dautriat, J. (2009). „Comportement hydromécanique de roches réservoir sous contraintes: relations entre évolution de perméabilité des mécanismes d'endommagement“. PhD thesis. Palaiseau, Ecole polytechnique (cit. on pp. 41, 181, 182).
- Dautriat, J., Gland, N., Dimanov, A., and Raphanel, J. (2011). „Hydromechanical behavior of heterogeneous carbonate rock under proportional triaxial loadings“. In: *Journal of Geophysical Research: Solid Earth* 116.1, pp. 1–26 (cit. on p. 7).
- David, C, Dautriat, J, Sarout, J, Delle Piane, C, Menéndez, B, Macault, R, and Bertauld, D (2015). „Mechanical instability induced by water weakening in laboratory fluid injection tests“. In: *Journal of Geophysical Research: Solid Earth* 120.6, pp. 4171–4188 (cit. on p. 176).
- De Borst, R. and Mühlhaus, H.-B. (1992). „Gradient-dependent plasticity: formulation and algorithmic aspects“. In: *International Journal for Numerical Methods in Engineering* 35.3, pp. 521–539 (cit. on pp. 37, 74).
- Dixon, J., Marek, B., et al. (1990). „The effect of bimodal-pore size distribution on electrical properties of some middle eastern limestones“. In: *SPE Annual Technical Conference and Exhibition*. Society of Petroleum Engineers (cit. on p. 49).
- Doumalin, P. and Bornert, M. (2000). „Micromechanical applications of digital image correlation techniques“. In: *Interferometry in Speckle Light*. Springer, pp. 67–74 (cit. on p. 62).
- Du Bernard, X., Eichhubl, P., and Aydin, A. (2002). „Dilation bands: A new form of localized failure in granular media“. In: *Geophysical Research Letters* 29.24, pp. 29–1 (cit. on pp. 12, 14, 30).
- Dunham, R. J. (1962). „Classification of carbonate rocks according to depositional textures“. In: (cit. on pp. 3, 40, 179).
- Eichhubl, P., Hooker, J. N., and Laubach, S. E. (2010). „Pure and shear-enhanced compaction bands in Aztec Sandstone“. In: *Journal of Structural Geology* 32.12, pp. 1873–1886 (cit. on pp. 11–13).
- El Bied, A., Sulem, J., and Martineau, F. (2002). „Microstructure of shear zones in Fontainebleau sandstone“. In: *International Journal of Rock Mechanics and Mining Sciences* 39.7, pp. 917–932 (cit. on p. 14).
- El Moustapha, K. (2014). „Identification d'une loi de comportement enrichie pour les géomatériaux en présence d'une localisation de la déformation“. PhD thesis. Université de Grenoble (cit. on p. 38).

- Esin, M, Dyskin, A., Pasternak, E, and Xu, Y (2017). „Mode I crack in particulate materials with rotational degrees of freedom“. In: *Engineering Fracture Mechanics* 172, pp. 181–195 (cit. on p. 38).
- Feldkamp, L. A., Davis, L., and Kress, J. W. (1984). „Practical cone-beam algorithm“. In: *Josa a* 1.6, pp. 612–619 (cit. on p. 60).
- Flügel, E. (2013). *Microfacies of carbonate rocks: analysis, interpretation and application*. Springer Science & Business Media (cit. on pp. 3, 40, 45, 179, 180).
- Folk, R. L. (1962). „Spectral subdivision of limestone types“. In: (cit. on pp. 40, 179, 180).
- Follet, H., Bruyère-Garnier, K., Peyrin, F., Roux, J.-P., Arlot, M., Burt-Pichat, B., Rumelhart, C, and Meunier, P. (2005). „Relationship between compressive properties of human os calcis cancellous bone and microarchitecture assessed from 2D and 3D synchrotron microtomography“. In: *Bone* 36.2, pp. 340–351 (cit. on p. 23).
- Fortin, J., Stanchits, S., Dresen, G., and Guéguen, Y. (2006). „Acoustic emission and velocities associated with the formation of compaction bands in sandstone“. In: *Journal of Geophysical Research: Solid Earth* 111.B10 (cit. on pp. 3, 14–16).
- Fortin, J., Stanchits, S., Dresen, G., and Gueguen, Y. (2009a). „Acoustic emissions monitoring during inelastic deformation of porous sandstone: comparison of three modes of deformation“. In: *Pure and Applied Geophysics* 166.5-7, pp. 823–841 (cit. on p. 14).
- Fortin, J., Stanchits, S., Dresen, G., and Guéguen, Y. (2009b). „Micro-mechanisms involved during inelastic deformation of porous carbonate rocks.“ In: (cit. on pp. 41, 183).
- Fossen, H., Schultz, R. A., and Torabi, A. (2011). „Conditions and implications for compaction band formation in the Navajo Sandstone, Utah“. In: *Journal of Structural Geology* 33.10, pp. 1477–1490 (cit. on pp. 11, 13, 25, 26).
- Fredrich, J. T., Evans, B., and Wong, T.-F. (1989). „Micromechanics of the brittle to plastic transition in Carrara marble“. In: *Journal of Geophysical Research: Solid Earth* 94.B4, pp. 4129–4145 (cit. on p. 17).
- Fronteau, G., Moreau, C., Thomachot-Schneider, C., and Barbin, V. (2010). „Variability of some Lutetian building stones from the Paris Basin, from characterisation to conservation“. In: *Engineering Geology* 115.3-4, pp. 158–166 (cit. on p. 42).
- Gaye, A. (2015). „Analyse multiéchelle des mécanismes de déformation du sel gemme par mesures de champs surfaciques et volumiques“. PhD dissertation. Paris Est (cit. on pp. 60, 62).
- Germain, P. (1973a). „La méthode des puissances virtuelles en mécanique des milieux continus“. In: *J. Mécanique* 12, pp. 236–274 (cit. on p. 35).
- Germain, P. (1973b). „The method of virtual power in continuum mechanics. Part 2: Microstructure“. In: *SIAM Journal on Applied Mathematics* 25.3, pp. 556–575 (cit. on pp. 35, 36, 129–132, 174, 188–190, 198).
- Grgic, D (2011). „Influence of CO₂ on the long-term chemomechanical behavior of an oolitic limestone“. In: *Journal of Geophysical Research: Solid Earth* 116.B7 (cit. on p. 11).
- Hadamard, J. (1903). *Leçons sur la propagation des ondes et les équations de l'hydrodynamique*. A. Hermann (cit. on p. 33).

- Hall, S. A., Desrues, J., Viggiani, G., Bésuelle, P., and Andò, E. (2012). „Experimental characterisation of (localised) deformation phenomena in granular geomaterials from sample down to inter- and intra-grain scales“. In: *Procedia Iutam* 4, pp. 54–65 (cit. on p. 38).
- Hill, R. (1962). „Acceleration waves in solids“. In: *Journal of the Mechanics and Physics of Solids* 10.1, pp. 1–16 (cit. on p. 65).
- Holcomb, D., Rudnicki, J. W., Issen, K. A., and Sternlof, K. (2007). „Compaction localization in the Earth and the laboratory: state of the research and research directions“. In: *Acta Geotechnica* 2.1, pp. 1–15 (cit. on p. 11).
- Homand, F. and Duffaut, P. (2000). *Manuel de mécanique des roches*. Vol. 1. Presses des MINES (cit. on p. 6).
- Issen, K. and Rudnicki, J. W. (2000). „Conditions for compaction bands in porous rock“. In: *Journal of Geophysical Research: Solid Earth* 105.B9, pp. 21529–21536 (cit. on pp. 31, 32, 151, 152).
- Jenkins, D. and Luterbacher, H. (1992). „Paleogene stages and their boundaries (Introductory remarks)“. In: *Neues Jahrbuch für Geologie und Paläontologie, Abhandlungen* 186.1, pp. 1–5 (cit. on p. 42).
- Ji, Y., Hall, S. A., Baud, P., and Wong, T.-f. (2014). „Characterization of pore structure and strain localization in Majella limestone by X-ray computed tomography and digital image correlation“. In: *Geophysical Journal International* 200.2, pp. 701–719 (cit. on pp. 14, 18, 23, 41).
- Laplaige, P. and Lemale, J. (2008). „Géothermie“. In: *Energies Métier : ingénieur territorial* 2, pp. 1–27 (cit. on p. 1).
- Lemaitre, J., Chaboche, J.-L., Benallal, A., and Desmorat, R. (2009). *Mécanique des matériaux solides-3eme édition*. Dunod (cit. on p. 33).
- Lenoir, N., Bornert, M., Desrues, J., Bésuelle, P., and Viggiani, G. (2007). „Volumetric digital image correlation applied to X-ray microtomography images from triaxial compression tests on argillaceous rock“. In: *Strain* 43.3, pp. 193–205 (cit. on pp. 23, 60).
- Lezin, C., Odonne, F., Massonnat, G. J., and Escadeillas, G. (2009). „Dependence of joint spacing on rock properties in carbonate strata“. In: *AAPG bulletin* 93.2, pp. 271–290 (cit. on pp. 41, 179, 183).
- Lion, M. (2004). „Influence de la température sur le comportement poromécanique ou hydraulique d’une roche carbonatée et d’un mortier . Etudes expérimentales“. PhD thesis (cit. on pp. 7, 41, 176, 181).
- Louis, L., Wong, T.-f., Baud, P., and Tembe, S. (2006). „Imaging strain localization by X-ray computed tomography: discrete compaction bands in Diemelstadt sandstone“. In: *Journal of Structural Geology* 28.5, pp. 762–775 (cit. on p. 23).
- Lucia, F. J. (1995). „Rock-fabric/ petrophysical classification of carbonate pore space for reservoir characterization“. In: *AAPG bulletin* 79.9, pp. 1275–1300 (cit. on p. 22).
- Lyapunov, A. M. (1992). „The general problem of the stability of motion“. In: *International journal of control* 55.3, pp. 531–534 (cit. on p. 32).
- Mair, K., Main, I., and Elphick, S. (2000). „Sequential growth of deformation bands in the laboratory“. In: *Journal of Structural Geology* 22.1, pp. 25–42 (cit. on pp. 13, 14).

- Melikoglu, M. (2017). „Geothermal energy in Turkey and around the World: a review of the literature and an analysis based on Turkey’s Vision 2023 energy targets“. In: *Renewable and Sustainable Energy Reviews* 76, pp. 485–492 (cit. on p. 1).
- Mindlin, R. D. (1964). „Micro-structure in linear elasticity“. In: *Archive for Rational Mechanics and Analysis* 16.1, pp. 51–78 (cit. on pp. 35, 131, 190).
- Mindlin, R. D. (1965). „Second gradient of strain and surface-tension in linear elasticity“. In: *International Journal of Solids and Structures* 1.4, pp. 417–438 (cit. on p. 194).
- Mühlhaus, H. and Vardoulakis, I (1987). „The thickness of shear bands in granular materials“. In: *Geotechnique* 37.3, pp. 271–283 (cit. on p. 36).
- Mutti, M (1995). „Porosity development and diagenesis in the Orfento Supersequence and its bounding unconformities (Upper Cretaceous, Montagna della Maiella, Italy)“. In: (cit. on p. 40).
- Nguyen, M. T. (2012). „Caractérisation géomécanique de la dégradation des roches sous l’effet de l’injection de gaz acides“. PhD thesis. Université Paris-Est (cit. on pp. 41, 182).
- Nicchio, M. A., Nogueira, F. C., Balsamo, F., Souza, J. A., Carvalho, B. R., and Bezerra, F. H. (2018). „Development of cataclastic foliation in deformation bands in feldspar-rich conglomerates of the Rio do Peixe Basin, NE Brazil“. In: *Journal of Structural Geology* 107, pp. 132–141 (cit. on p. 11).
- Nicolas, A, Fortin, J, Regnet, J., Dimanov, A, and Guéguen, Y (2016). „Brittle and semi-brittle behaviours of a carbonate rock: influence of water and temperature“. In: *Geophysical Journal International* 206.1, pp. 438–456 (cit. on p. 176).
- Olsson, W., Holcomb, D., and Rudnicki, J. (2002). „Compaction localization in porous sandstone: Implications for reservoir mechanics“. In: *Oil & Gas Science and Technology* 57.5, pp. 591–599 (cit. on pp. 3, 11).
- Olsson, W. A. (1999). „Theoretical and experimental investigation of compaction bands in porous rock“. In: *Journal of Geophysical Research: Solid Earth* 104.B4, pp. 7219–7228 (cit. on p. 31).
- Otani, J., Mukunoki, T., and Sugawara, K. (2005). „Evaluation of particle crushing in soils using X-ray CT data“. In: *Journal of the Japanese Geotechnical Society: soils and foundation* 45.1, pp. 99–108 (cit. on p. 23).
- Pamin, J. K. (1996). „Gradient-dependent plasticity in numerical simulation of localization phenomena.“ In: (cit. on p. 37).
- Papazoglou, A, Shahin, G, Marinelli, F, Dano, C., Buscarnera, G., and Viggiani, G (2017). „Localized Compaction in Tuffeau de Maastricht: Experiments and Modeling“. In: *International Workshop on Bifurcation and Degradation in Geomaterials*. Springer, pp. 481–488 (cit. on pp. 14, 23, 24).
- Paterson, M. S. and Wong, T.-f. (2005). *Experimental rock deformation-the brittle field*. Springer Science & Business Media (cit. on pp. 10, 176).
- Pontes, C. C., Nogueira, F. C., Bezerra, F. H., Balsamo, F., Miranda, T. S., Nicchio, M. A., Souza, J. A., and Carvalho, B. R. (2019). „Petrophysical properties of deformation bands in high porous sandstones across fault zones in the Rio do Peixe Basin, Brazil“. In: *International Journal of Rock Mechanics and Mining Sciences* 114, pp. 153–163 (cit. on p. 11).
- Rath, A., Exner, U., Tschegg, C., Grasemann, B., Laner, R., and Draganits, E. (2011). „Diagenetic control of deformation mechanisms in deformation bands in a carbonate grainstone“. In: *AAPG bulletin* 95.8, pp. 1369–1381 (cit. on pp. 2, 11–13, 21, 25, 27).

- Rattez, H., Stefanou, I., Sulem, J., Veveakis, M., and Poulet, T. (2018). „The importance of Thermo-Hydro-Mechanical couplings and microstructure to strain localization in 3D continua with application to seismic faults. Part II: Numerical implementation and post-bifurcation analysis“. In: *Journal of the Mechanics and Physics of Solids* 115, pp. 1–29 (cit. on pp. 36, 162).
- Raude, S., Giot, R., Foucault, A., and Fernandes, R. (2015). „An identification method to calibrate higher-order parameters in local second-gradient models“. In: *Comptes Rendus Mécanique* 343.7-8, pp. 443–456 (cit. on pp. 38, 132).
- Rice, J. and Rudnicki, J. (1980). „A note on some features of the theory of localization of deformation“. In: *International Journal of solids and structures* 16.7, pp. 597–605 (cit. on p. 31).
- Roscoe, K. H., Schofield, A., and Wroth, C. (1958). „On the yielding of soils“. In: *Geotechnique* 8.1, pp. 22–53 (cit. on p. 137).
- Rotevatn, A., Thorsheim, E., Bastesen, E., Fossmark, H. S., Torabi, A., and Sælen, G. (2016). „Sequential growth of deformation bands in carbonate grainstones in the hangingwall of an active growth fault: implications for deformation mechanisms in different tectonic regimes“. In: *Journal of Structural Geology* 90, pp. 27–47 (cit. on p. 11).
- Rudnicki, J. W. and Rice, J. (1975). „Conditions for the localization of deformation in pressure-sensitive dilatant materials“. In: *Journal of the Mechanics and Physics of Solids* 23.6, pp. 371–394 (cit. on pp. 3, 29, 31).
- Rustichelli, A., Tondi, E., Agosta, F., Cilona, A., and Giorgioni, M. (2012). „Development and distribution of bed-parallel compaction bands and pressure solution seams in carbonates (Bolognano Formation, Majella Mountain, Italy)“. In: *Journal of Structural Geology* 37, pp. 181–199 (cit. on pp. 11, 12, 25, 26).
- Rutqvist, J. (2012). „The geomechanics of CO₂ storage in deep sedimentary formations“. In: *Geotechnical and Geological Engineering* 30.3, pp. 525–551 (cit. on pp. 1, 11).
- Saad, A. (2011). „Influence du changement climatique et des conditions extrêmes sur les massifs fracturés: rôle des fluides (H₂O, CO₂) dans leur processus d’altération“. PhD thesis. Paris Est (cit. on pp. 41, 49, 182).
- Samudio, M. (Dec. 2017). „Modelling of an oil well cement paste from early age to hardened state : hydration kinetics and poromechanical behaviour“. PhD dissertation. Paris Est (cit. on p. 136).
- Santerre, Y. (2010). „Influence de la diagenèse précoce et de la dynamique sédimentaire sur la distribution des propriétés pétrophysiques dans les réservoirs carbonatés“. PhD thesis. Aix-Marseille 1.
- Schindelin, J., Arganda-Carreras, I., Frise, E., Kaynig, V., Longair, M., Pietzsch, T., Preibisch, S., Rueden, C., Saalfeld, S., Schmid, B., et al. (2012). „Fiji: an open-source platform for biological-image analysis“. In: *Nature methods* 9.7, p. 676 (cit. on pp. 50, 51).
- Schofield, A. and Wroth, P. (1968). *Critical state soil mechanics*. Vol. 310. McGraw-Hill London (cit. on p. 137).
- Shimada, M., Cho, A., and Yukutake, H. (1983). „Fracture strength of dry silicate rocks at high confining pressures and activity of acoustic emission“. In: *Tectonophysics* 96.1-2, pp. 159–172 (cit. on p. 10).
- Somerton, W. H. (1992). *Thermal properties and temperature-related behavior of rock/fluid systems*. Vol. 37. Elsevier (cit. on p. 176).

- Stefanou, I. (2018). *Numerical Geolab: Multiscale Finite Elements platform for multiphysics and generalized continua* (cit. on p. 155).
- Stefanou, I. and Alevizos, S. (2016). „Fundamentals of bifurcation theory and stability analysis“. In: *Modelling of instabilities and bifurcation in Geomechanics, 26th ALERT Doctoral School 725* (cit. on pp. 32, 34).
- Stefanou, I. and Sulem, J. (2014). „Chemically induced compaction bands: Triggering conditions and band thickness“. In: *Journal of Geophysical Research: Solid Earth* 119.2, pp. 880–899 (cit. on pp. 2, 11, 176).
- Sternlof, K. R., Rudnicki, J. W., and Pollard, D. D. (2005). „Anticrack inclusion model for compaction bands in sandstone“. In: *Journal of Geophysical Research: Solid Earth* 110.B11 (cit. on pp. 12, 13).
- Sulem, J. and Ouffroukh, H. (2006). „Shear banding in drained and undrained triaxial tests on a saturated sandstone: Porosity and permeability evolution“. In: *International journal of rock mechanics and mining sciences* 43.2, pp. 292–310 (cit. on pp. 14, 15).
- Thiery, C. (2013). „Tomographie à rayons X“. In: *Techniques de l'ingénieur CND : méthodes globales et volumiques* base documentaire : TIB585DUO.ref. article : p950. fre (cit. on p. 58).
- Tondi, E, Cilona, A, Agosta, F, Aydin, A, Rustichelli, A, Renda, P, and Giunta, G (2012). „Growth processes, dimensional parameters and scaling relationships of two conjugate sets of compactive shear bands in porous carbonate grainstones, Favignana Island, Italy“. In: *Journal of Structural Geology* 37, pp. 53–64 (cit. on p. 13).
- Tondi, E. (2007). „Nucleation, development and petrophysical properties of faults in carbonate grainstones: evidence from the San Vito Lo Capo peninsula (Sicily, Italy)“. In: *Journal of Structural Geology* 29.4, pp. 614–628 (cit. on pp. 11, 27).
- Tondi, E., Antonellini, M., Aydin, A., Marchegiani, L., and Cello, G. (2006). „The role of deformation bands, stylolites and sheared stylolites in fault development in carbonate grainstones of Majella Mountain, Italy“. In: *Journal of structural geology* 28.3, pp. 376–391 (cit. on pp. 11–13, 22, 26).
- Tucker, M. E. and Wright, V. P. (2009). *Carbonate sedimentology*. John Wiley & Sons.
- Turner, F. J., T GRIGGS, D., and Heard, H. (1954). „Experimental deformation of calcite crystals“. In: *Geological Society of America Bulletin* 65.9, pp. 883–934 (cit. on p. 21).
- Vajdova, V., Baud, P., and Wong, T.-f. (2004). „Compaction, dilatancy, and failure in porous carbonate rocks“. In: *Journal of Geophysical Research: Solid Earth* 109.B5 (cit. on pp. 8, 10, 14, 17, 19, 23, 40, 41).
- Vajdova, V., Zhu, W., Chen, T.-M. N., and Wong, T.-f. (2010). „Micromechanics of brittle faulting and cataclastic flow in Tavel limestone“. In: *Journal of Structural Geology* 32.8, pp. 1158–1169 (cit. on pp. 14, 17).
- Vardoulakis, I and Aifantis, E. (1991). „A gradient flow theory of plasticity for granular materials“. In: *Acta mechanica* 87.3-4, pp. 197–217 (cit. on pp. 37, 74).
- Vardoulakis, I and Sulem, J (1995). *Bifurcation analysis in geomechanics*. Chapman & Hall (cit. on pp. 3, 30, 36).
- Walsh, J. B. (1965). „The effect of cracks on the compressibility of rock“. In: *Journal of Geophysical Research* 70.2, p. 381 (cit. on p. 7).

- Wang, K., Sun, W., Salager, S., Na, S., and Khaddour, G. (2016). „Identifying material parameters for a micro-polar plasticity model via X-ray micro-computed tomographic (CT) images: lessons learned from the curve-fitting exercises“. In: *International Journal for Multiscale Computational Engineering* 14.4 (cit. on p. 38).
- Washburn, E. W. (1921). „The dynamics of capillary flow“. In: *Physical review* 17.3, p. 273 (cit. on p. 49).
- Weitkamp, T, Scheel, M, Giorgetta, J., Joyet, V, Le Roux, V, Cauchon, G, Moreno, T, Polack, F, Thompson, A, and Samama, J. (2017). „The tomography beamline ANATOMIX at Synchrotron SOLEIL“. In: *Journal of Physics: Conference Series*. Vol. 849. 1. IOP Publishing, p. 012037 (cit. on p. 44).
- Wilkinson, B. H., McElroy, B. J., Kesler, S. E., Peters, S. E., and Rothman, E. D. (2009). „Global geologic maps are tectonic speedometers—Rates of rock cycling from area-age frequencies“. In: *Geological Society of America Bulletin* 121.5-6, pp. 760–779 (cit. on p. 6).
- Wong, T.-f. and Baud, P. (2012). „The brittle-ductile transition in porous rock: A review“. In: *Journal of Structural Geology* 44, pp. 25–53 (cit. on pp. 7, 9, 10, 22).
- Wong, T.-f., David, C., and Zhu, W. (1997). „The transition from brittle faulting to cataclastic flow in porous sandstones: Mechanical deformation“. In: *Journal of Geophysical Research: Solid Earth* 102.B2, pp. 3009–3025 (cit. on pp. 8, 9, 16, 26, 80).
- Wu, X. Y., Baud, P, and Wong, T.-f. (2000). „Micromechanics of compressive failure and spatial evolution of anisotropic damage in Darley Dale sandstone“. In: *International Journal of Rock Mechanics and Mining Sciences* 37.1-2, pp. 143–160 (cit. on p. 23).
- Yin, H. and Dvorkin, J. (1994). „Strength of cemented grains“. In: *Geophysical Research Letters* 21.10, pp. 903–906 (cit. on p. 28).
- Zhang, J., Wong, T.-F., and Davis, D. M. (1990). „Micromechanics of pressure-induced grain crushing in porous rocks“. In: *Journal of Geophysical Research: Solid Earth* 95.B1, pp. 341–352 (cit. on p. 22).
- Zhu, W., Baud, P., and Wong, T.-f. (2010). „Micromechanics of cataclastic pore collapse in limestone“. In: *Journal of Geophysical Research: Solid Earth* 115.B4 (cit. on pp. 10, 14, 21, 22, 25, 49, 83).
- Zinsmeister, L. (2013). „Étude de l'évolution hydromécanique d'un carbonate après altération chimique. Application des méthodes de corrélation d'images 2D et 3D à la mesure des champs locaux de déformation lors d'essais mécaniques à différentes échelles“. PhD thesis. Palaiseau, Ecole polytechnique (cit. on pp. 7, 23, 41, 60, 181).

List of Figures

1.1	A schematic of a geothermal system (from Barbier, 2002).	2
2.1	Typical Mean pressure vs Volumetric strain plot for a hydrostatic loading (Vajdova et al., 2004).	8
2.2	Typical results for triaxial loading at different confining pressures. a) Differential stress versus axial strain; b) Mean stress versus volumetric strain (Vajdova et al., 2004).	8
2.3	Typical yield stresses (black squares and circles), dilatancy thresholds (black squares and triangles) and brittle failure envelope (hollow squares) of carbonate rocks (From Baud et al. (2000)).	9
2.4	Porosity effect on yield stresses of limestones (From Vajdova et al. (2004)). . .	10
2.5	Field observations of: a) Conjugated shear bands at the millimetric scale in the Navajo sandstone (Fossen et al., 2011); b) Shear band of 3 meters thickness in the Navajo Sandstone (Antonellini et al., 1994); c) A single shear band at the millimetric scale in a porous carbonate grainstone (Tondi et al., 2012); d) Thick zone of shear bands in the same carbonate rock field (Tondi et al., 2012); e) Pure compaction bands in Aztec sandstone (Eichhubl et al., 2010); f) Pure compaction band at the centimeter scale in Aztec sandstone (Sternlof et al., 2005); g) Pure compaction band of millimetric thickness in Majella limestone (Tondi et al., 2006); h) Pure compaction band of centimetric thickness in Saint Margarethen limestone (Rath et al., 2011).	13
2.6	Field observation of a dilation band in a poorly consolidated sand where pore space is impregnated by blue epoxy and clay cement has a dark color (from Du Bernard et al., 2002).	14
2.7	Photomicrographs of shear bands formed in Fontainebleau sandstone samples tested at relatively low confinements: a) in drained conditions; b) in undrained conditions (from Sulem and Ouffroukh, 2006).	15
2.8	Sub-horizontal compaction bands formed in Bleurswiller sandstone sample tested at 80 MPa of effective confining pressure (from Fortin et al., 2006): a) Eye inspection of the sample surface; b) Inferred from acoustic emission measurements.	16
2.9	Photographs of deformation bands on tested Bleurswiller sandstone samples at different confinements (from Baud et al., 2015).	17

2.10	Sub-horizontal compaction bands formed at the boundaries and propagating towards the center of Bentheim sandstone samples (from Baud et al., 2004).	17
2.11	Differential stress and acoustic emission rate plots versus the applied axial strain for a Bentheim sandstone sample tested at 120 MPa of confining pressure (from Baud et al., 2004).	18
2.12	Effective mean pressure vs porosity change for: a) Rothbach sandstone samples; b) Berea sandstone samples; c) Darley Dale sandstone samples. (from Baud et al., 2004).	18
2.13	Spatial distribution of specific surface area (due to grain crushing) in Berea sandstone samples: a) Conjugate shear bands at 75 MPa of confinement; b) Compaction bands at 200 MPa of confinement. (from Baud et al., 2004).	19
2.14	Mean stress vs volumetric strain for samples tested under several confining pressures: a) Majella limestone; b) Saint-Maximin limestone (from Baud et al., 2009).	20
2.15	Photographs of deformation bands on Majella limestone samples tested under several confining pressure (from Cilona et al., 2014).	20
2.16	Deformation modes of two facies of Leitha limestone (from Baud et al., 2017b).	21
2.17	a) Radiated cracks from a grain contact in Boise sandstone (Zhang et al., 1990); b) Grain sliding and rotation in a Majella limestone field compaction band (Tondi et al., 2006); c) A pore surrounded by a halo of cataclastic damage in Tavel limestone (Zhu et al., 2010); d) Pore collapse in Indiana limestone (Zhu et al., 2010); e) Twin lamellae observed in a triaxially deformed sample of Indiana limestone (Wong and Baud, 2012); f) Pressure solution process at the grain contacts in the Majella limestone field (Cilona et al., 2012).	22
2.18	Strain localization in a Maastricht carbonate sample obtained from Digital Volume Correlation (Papazoglou et al., 2017).	24
2.19	a) Grain size distribution in Bleurswiller, Bentheim, Diemelstadt and Boise sandstones; b) Yield stresses for Boise and Bleurswiller sandstones (Cheung et al., 2012).	27
2.20	Backscattered scanning electron micrograph of: a) a discrete compaction band in a Bleurswiller sample; b) cataclastic deformation without localization in a boise sample (Cheung et al., 2012).	27
2.21	Porosity change vs confining pressure for a cemented and non-cemented granular media (Yin and Dvorkin, 1994).	28
2.22	Factors that prohibit, allow and are neutral to compaction banding in sedimentary rocks.	29
2.23	A planar deformation band.	29
2.24	Three reference types of strain localization: compaction, shear and dilation bands (from Du Bernard et al., 2002).	30

2.25	Critical hardening modulus h_{cr} for deformation bands onset in terms of the yield surface slope μ and the dilatancy parameter β . The angle θ represents the orientation of band normal vector with respect to the most compressive principal stress direction (from Issen and Rudnicki (2000)).	32
2.26	An example of mesh-dependent shear band in a rate-independent constitutive law in Cauchy continuum (from Stefanou and Alevizos, 2016).	34
2.27	A schematic of the degrees of freedom considered for: a) a material point in the Cauchy continuum; b) a microvolume in the micromorphic continuum of degree 1.	35
3.1	A schematic of the sample water saturation procedure.	43
3.2	Histogram of the global porosity distribution evaluated for 72 samples.	43
3.3	A SML rod specimen imaged by XRCT at SOLEIL synchrotron.	44
3.4	A transverse cross-section of XRCT image of the SML specimen.	45
3.5	A typical transverse cross-section of XRCT image recorded on cylindrical SML samples.	46
3.6	Transverse cross-sections of the XRCT image recorded on a SML sample in initial condition showing: a) a section of the specimen D1; b) a section of specimen D2; c) a section of specimen D3; d) a section of specimen P1.	47
3.7	SML Specimens: From coring to MIP tests.	47
3.8	a) Typical transverse cross-section of the specimen P1 in a high-porosity zone; b) Zoomed image showing grains and intergranular pores in high-porosity zones; c) Typical transverse cross-section of a specimen in a low-porosity zone; d) Zoomed image showing grains and intergranular pores in low-porosity zones.	48
3.9	Pore throat diameter distribution for the four cored specimens: D1, D2, D3 in denser zones and P1 in more porous zones.	50
3.10	Porosity distribution over 4 cylindrical samples of 4 cm diameter and 8 cm height.	52
3.11	Optical microscopic observation showing the contrast between more porous and denser zones.	53
3.12	a) Optical microscopy observation showing a low-porosity zone; b) Optical microscopy observation showing a high-porosity zone.	53
3.13	Backscattered Electron Microscopy observation showing the contrast between low- and high-porosity zones.	54
3.14	Backscattered Electron Microscopy observation showing a calcite grain, intact at the center and dissolved at the boundaries in a high-porosity zone.	54
3.15	Backscattered Electron Microscopy observations showing: a) a mesopore surrounded by altered calcite; b) A macropore surrounded by altered calcite in high-porosity zones.	54
3.16	Microporosity inside calcite grains.	55
3.17	Backscattered Electron Microscopy observation showing a microporous miliolidae.	55
4.1	Schematic of the triaxial machine and LVDTs disposition.	59

4.2	Details of a XRCT scanning of a SML sample.	60
4.3	DVC principles: Mesh points on the reference image (on the left) and their homologous points on the deformed image (on the right).	62
4.4	Typical DVC applied on the reference sample: (a) Volumetric deformation map; (b) Shear strain magnitude map.	65
4.5	Typical DVC applied on the reference sample: (a) The probability density of volumetric strain with a fitted normal distribution; (b) The probability density of shear strain magnitude with a fitted log-normal distribution.	65
4.6	A schematic representation of the displacement gradient discontinuity across a deformation band (or equivalently, the strain tensor discontinuity).	66
4.7	a) Definition of the plane of a localization band. The displacement vector for each element along the black solid line is evaluated, where GL is the gauge length; b) Cross-section of the DVC map in the plane of the band.	67
4.8	a) A typical transverse cross-section of the reference sample in the 8-bit reference configuration; b) Histogram of the grey level distribution inside the selection in the 8-bit image; c) The same cross-section in the 16-bit deformed configuration before calibration; d) Histogram of the grey level distribution inside the selection in the 16-bit image; e) The same cross-section after adjusting the grey levels; f) Histogram of the grey level distribution inside the selection in the rescaled 8-bit image.	70
4.9	The transmittance coefficient evolution with respect to the source energy over a material length of 0.96 mm for both quartz and calcite minerals.	71
4.10	From XRCT image to porosity map computation: Local porosity evaluation over a subvolume of radius R	72
4.11	A transverse cross-section of a XRCT image.	73
4.12	The profile of the porosity evaluated for different subvolume diameters over the line shown in Figure 4.11.	73
4.13	A transverse cross-section of the porosity map corresponding to the section shown in Figure 4.11.	74
4.14	A line of pixels over which the second gradient of the porosity is evaluated.	75
4.15	A grid of voxels over which the second gradient of the porosity is evaluated.	75
5.1	Typical triaxial test results in dry conditions for several confining pressures (a) Mean pressure vs volumetric deformation; (b) Shear stress intensity vs axial strain; (c) Two SML samples tested under uniaxial loading.	79
5.2	a) SML sample tested under hydrostatic condition; b) Conjugate shear bands on the surface of a sample tested at low confinement $\sigma_3 = -1\text{MPa}$; c) Deformation bands observed on the surface of a sample tested at high confinement $\sigma_3 = -11\text{MPa}$; d) Brazilian test performed on a sample.	79
5.3	Yield stresses of SML samples: solid red triangles for samples studied with XRCT, empty red triangles for the preliminary experiments & blue squares for data from Baud et al. (2009); Baud et al. (2017a).	81

5.4	A SML sample tested in dry condition under hydrostatic loading.	82
5.5	A SML sample in the initial state before being tested under hydrostatic loading conditions: a)-b) XZ middle cross-section of the XRCT image and the corresponding computed porosity map.	82
5.6	The incremental volumetric strain map for the first loading stage of the SML sample tested under hydrostatic loading conditions: 3D view and three vertical cross sections parallel to the XZ plane.	84
5.7	Vertical cross-sections at the middle of the sample of: a) the porosity map in the initial state; b) the incremental volumetric strain; c) the porosity map after the first stage of loading.	84
5.8	Histograms of porosity for the selected zones in Figure 5.7.	85
5.9	The SML sample, tested under hydrostatic loading conditions: a) Volumetric strain map after the first stage of loading; b) A transverse cross-section showing a heterogeneity of deformation; c) A transverse cross-section at the corresponding plane of the XRCT image in the initial state; d)-e) A large pore laying inside a low-porosity zone in the initial state and after the first loading stage; f)-g) A high-porosity zone at the initial state which is compacted after the first loading stage.	86
5.10	Incremental volumetric strain map after the second loading stage: three vertical cross sections parallel to the XZ plane.	87
5.11	Vertical cross-sections at the middle of the sample of: a)-d) the porosity maps before and after the second loading stage; b)-c) the incremental shear strain magnitude and volumetric strain maps during the second loading stage. Zones A correspond to high-porosity zones ($\phi > 40\%$), zones B are low-porosity zones ($\phi < 35\%$) and zones C correspond to interface regions between zones A and B.	88
5.12	Porosity histograms of the three zones (A; B & C) selected in Figure 5.11a before and after the second loading stage.	89
5.13	The SML sample, tested under hydrostatic loading condition: examples of two undeformed large pores observed before the second loading stage (a & c) and after the second loading stage (b & d).	89
5.14	The SML sample, tested under hydrostatic loading condition: a) Volumetric strain map during the second stage of loading; b)-c)-d) A transverse cross-section of the XRCT image before loading and the corresponding planes of the volumetric strain & shear strain magnitude maps; e)-f) A zoom on the XRCT image showing the contrast between high- and low-porosity zones before and after the second loading stage.	90
5.15	Large pore laying in a high porosity zone (41%): a)-b) XRCT image and the porosity map in the initial state; c)-d) A zoom on the pore before and after the second loading stage.	91
5.16	BSE image of the SML sample, tested under hydrostatic loading: a) Contrast between high- and low-porosity zones; b) Pervasive calcite grain crushing and pore filling.	91

5.17	BSE image of the SML sample, tested under hydrostatic loading: a) Pervasive calcite grain crushing and pore filling with intact quartz grains in high-porosity zones; b) Contrast between high-porosity and low-porosity zones; c) Undeformed microstructure in low-porosity zones.	92
5.18	A SML sample tested in triaxial conditions under 10.5 MPa of confining pressure.	92
5.19	The SML sample imaged before being tested in axisymmetric triaxial loading under 10.5 MPa of confining pressure: YZ middle cross-section of the XRCT image and the porosity map. The dashed window represents the zone over which the porosity histogram will be computed in next chapter.	93
5.20	The incremental volumetric strain map for the first loading stage of the SML sample tested under high confinement: 3D view and vertical cross sections parallel to the YZ plane. The deformation bands A1 to A6 are selected on the middle section and tangent planes are defined.	94
5.21	The incremental volumetric strain map for the first loading stage of the SML sample tested under high confinement: 3D view and vertical cross sections parallel to the XZ plane.	95
5.22	Vertical cross-sections at the middle of the SML sample tested under high confining pressure: a)-c) Porosity maps in the initial state and after the first loading stage; b) Incremental volumetric strain.	95
5.23	Histograms of porosity for the selected zones in Figure 5.22.	96
5.24	The SML sample tested in axisymmetric triaxial loading under high confining pressure: a) Vertical cross-section of the incremental volumetric strain map during the first loading stage; b)-c)-d) Transverse cross-section showing a heterogeneity of deformation and the corresponding planes of the porosity map and the XRCT image in the initial state; e)-f) A large pore laying in a low-porosity zone before and after the first loading stage; g)-h) A high-porosity zone in the initial state and after being compacted during the first loading stage.	97
5.25	The incremental volumetric strain map for the second loading stage of the SML sample tested under high confinement: 3D view and vertical cross sections parallel to the YZ plane. The deformation bands A7 to A9 are selected on the middle section and tangent planes are defined.	98
5.26	The incremental volumetric strain map for the second loading stage of the SML sample tested under high confinement: 3D view and vertical cross sections parallel to the XZ plane.	99
5.27	Transverse cross-sections showing the initial porosity (after Stage 1 of loading) and the incremental volumetric strain during the second loading stage at different levels along the axis of the SML sample tested under high confinement.	100
5.28	Volumetric strain vs porosity in the reference state for all the elements of the section shown in Figure 5.27c.	101

5.29	Vertical cross-sections at the middle of the sample tested under high confinement: a) Porosity map before the second loading stage b) the incremental volumetric strain map during the second loading stage; c) Porosity map after the second loading stage.	101
5.30	The SML sample tested in axisymmetric triaxial loading under high confining pressure: a) The incremental volumetric strain map during the second stage of loading; b)-c) A transverse cross-section of the volumetric strain map and the corresponding plane of the XRCT image before loading; d)-e) A macropore laying in a denser zone before and after the second loading stage; f)-g) A macropore in a high-porosity zone before and after the second loading stage; h)-g) A high-porosity zone before and after the second loading stage.	102
5.31	The SML sample tested under high confinement: a) Middle cross-section of the incremental volumetric strain map during the second loading stage; b) BSE image showing the contrast between intact and compacted zones; c) Zone of compaction bands; d) Intact zone; e) Zone of compaction bands (Q for quartz grains); f) Intact zone; g) Grain crushing and pore filling; h) Fine powders filling the pores.	103
5.32	A SML sample tested in triaxial conditions under relatively low confining pressure (1.5 MPa).	104
5.33	A SML sample in the initial state before being tested in axisymmetric triaxial loading under relatively low confining pressure: a)-b) YZ middle cross-section of the XRCT image and the corresponding porosity map.	105
5.34	The incremental shear strain magnitude map for the first loading stage of the SML sample tested under low confining pressure (1.5 MPa): 3D view and vertical cross sections parallel to the XZ plane. A1 and A2 are two selected deformation bands.	106
5.35	Vertical cross-sections parallel to the XZ plane of the SML sample tested under low confining pressure: a) Porosity map in the initial state; b) Incremental volumetric strain; c) Incremental shear strain magnitude.	106
5.36	a) The incremental shear strain magnitude of the SML sample tested under low confining pressure during the first loading stage; b) - c) - d) Transverse cross-sections of the porosity map in the initial state, the volumetric strain and the shear strain magnitude maps at different levels along the sample axis z	107
5.37	Volumetric strain vs initial porosity for some elements of the section shown in Figure 5.36b.	108
5.38	The SML sample tested under low confining pressure during the first loading stage: a) Transverse cross-sections showing the volumetric strain map; b)-c) A focus on a zone before and after being crossed by the deformation band: an out-of-plane displacement is identified and a crack is formed (marked by a white arrow).	108

5.39	<i>NSP</i> calculated for each element along the central line of the deformation bands A1 and A2 in the SML sample tested under low confining pressure during the first loading stage.	109
5.40	The incremental shear strain magnitude map for the second loading stage of the SML sample tested under low confining pressure (1.5 MPa): 3D view and several vertical cross sections parallel to the XZ plane. A2 and A3 are two selected deformation bands.	110
5.41	Vertical cross-sections parallel to the XZ plane of the SML sample tested under low confining pressure: a) Porosity map in the initial state; b) Incremental volumetric strain; c) Incremental shear strain magnitude. White arrows indicate zones of compaction, whereas black arrows indicate zones of dilation. A2 and A3 are two selected deformation bands.	111
5.42	a) The incremental shear strain magnitude of the SML sample tested under low confining pressure during the second loading stage; b) - c) - d) Transverse cross-sections of the porosity map in the initial state, the volumetric strain and the shear strain magnitude maps during the second loading stage; e)-f) XRCT images before and after the second loading stage at the same plane; g)-h) Interface between a high- and low-porosity zones crossed by a deformation band before and after the second loading stage.	112
5.43	Volumetric strain vs reference porosity for some elements of the section shown in Figure 5.42.	113
5.44	<i>NSP</i> calculated for each element along the central line of the deformation bands A2 and A3 in the SML sample tested under low confining pressure during the second loading stage.	113
5.45	The SML sample tested under low confinement: a) Vertical cross-section of the incremental volumetric strain map during the second loading stage; b) BSE image showing the contrast between high- and low-porosity zones remained undeformed after the two loading stages; c) Intact low-porosity zone; d) Compactive zone of the shear band (Q for quartz grains); e) Dilatant zone of the shear band; f)-g) Crack opening in the cementation.	114
5.46	A SML sample tested in triaxial conditions under relatively intermediate confining pressure (6 MPa).	115
5.47	A SML sample in the initial state before being tested in axisymmetric triaxial loading under intermediate confining pressure: a)-b) YZ middle cross-section of the XRCT image and the porosity map.	116
5.48	The incremental shear strain magnitude map for the first loading stage of the SML sample tested under intermediate confining pressure (6 MPa): 3D view and vertical cross sections parallel to the XZ plane.	117
5.49	The incremental shear strain magnitude map for the first loading stage of the SML sample tested under intermediate confining pressure (6 MPa): 3D view and vertical cross sections parallel to the YZ plane. A1 is the selected deformation band.	118

5.50	Vertical cross-sections parallel to the YZ plane of the SML sample tested under intermediate confining pressure: a) Porosity map in the initial state; b) Incremental volumetric strain; c) Incremental shear strain magnitude. A1 is the selected deformation band.	118
5.51	a) The incremental shear strain magnitude of the SML sample tested under intermediate confining pressure during the first loading stage; b) - c) - d) Transverse cross-sections of the porosity map in the initial state, the volumetric strain and the shear strain magnitude maps at different levels of the sample axis z	119
5.52	The SML sample tested under intermediate confining pressure during the first loading stage: a) Transverse cross-section of the volumetric strain map at the level of Figure 5.51c; b) Transverse cross-section of the volumetric strain map at the level of Figure 5.51d; c) A focus on a zone before being sheared. Each point corresponds the center of a correlation domain; d) The same zone after being crossed by the deformation band, where the points represent the correlation domain centers found from DVC: an out-of-plane displacement is identified. ; e) Porosity map of a zone before being crossed by the deformation band; f) The porosity map of the zone after the first loading stage.	120
5.53	The SML sample tested under relatively intermediate confining pressure during the second loading stage: A vertical YZ cross-section at the middle plane showing the incremental shear strain magnitude, the volumetric deformation and the reference porosity maps. A1 and A2 are two selected deformation bands.	122
5.54	The SML sample tested under relatively intermediate confining pressure during the second loading stage: A vertical XZ cross-section at the middle plane showing the incremental shear strain magnitude, the volumetric deformation and the reference porosity maps. A3 is a selected deformation band.	123
5.55	The SML sample tested under relatively intermediate confining pressure during the second loading stage: a) - b) - c) Transverse cross-sections showing the porosity map before loading, the incremental volumetric strain and shear strain magnitude maps; d) - e) A low-porosity zone before and after being crossed by a deformation band; f) - g) Porosity maps of a high-porosity zone before and after being crossed by compactive deformation bands.	124
5.56	BSE images of the SML sample tested under intermediate confinement: a) A zone at the interface between a high- and low-porosity zone; b)-d) Calcite grain crushing inside compactive shear bands, Q denotes quartz grains; c) <i>Miliolidae</i> shell cracked inside a compactive shear band.	125
5.57	BSE images of the SML sample tested under intermediate confinement: Cracks formed between grains in low-porosity zones.	125
6.1	Calibration procedure of the gradient-dependent plasticity model.	135
6.2	Fitting of elastic parameters.	136
6.3	Schematic representation of the ACC yield surface.	136

6.4	ACC yield surface fitted to the yield stresses data in the deviatoric vs mean stress plane: red triangles represent the data of this study & blue squares for Baud et al. (2009); Baud et al. (2017a) data.	137
6.5	The yield surface evolution is calibrated on the stress states at different levels of hardening and for several confining pressures.	139
6.6	Plastic volumetric strain vs plastic shear strain magnitude for 3 different confining pressures. The dashed line represents the model prediction for $\beta=-0.75$	140
6.7	Porosity histogram computed over the selected heterogeneous domain in Figure 5.19.	140
6.8	A schematical 2D representation of the assumed porosity heterogeneity. Darker areas represent high-porosity zones ($\phi=42\%$) and brighter areas represent low-porosity zones ($\phi=35\%$). A cubic elementary cell centered over a high-porosity zone is chosen as the primitive cell of the periodic lattice and over which the central porosity and its second-gradient are evaluated.	141
6.9	Definition of the lines over which porosity profiles are plotted.	141
6.10	Porosity profiles plotted over the lines L1 to L11.	143
6.11	FFT applied on the porosity profiles over the lines L1 to L11.	144
6.12	Procedure followed to calibrate the hardening moduli α_1 and α_2 for a loading stage from State i to $i + 1$	146
6.13	Two selected cubic elements, over which the mean plastic volumetric deformation and the internal variables are evaluated: a) during the first loading stage; b) during the second loading stage.	147
6.14	Evolution of ϕ_0 and $\nabla^2\phi_0$ for each REV from the initial state, to the states after the first and second loading stages. The arrow shows the direction of the evolution with loading.	148
6.15	Evolution of \dot{p}_c and \dot{M} vs $\dot{\phi}_0 + \frac{L^2}{24}\nabla^2\phi_0$. The dashed lines represent the fitted hardening laws obtained with the following moduli $\alpha_1 = 150.9$ MPa and $\alpha_2 = 4.15$	148
6.16	The growth coefficient s plotted against the perturbation wavelength λ in a Cauchy continuum for a confining pressure of $\sigma_3 = -12$ MPa. ρ is taken equal to 1600 kg/m ³	151
6.17	Growth coefficient s vs the normalized perturbation wavelength λ^* in the micromorphic continuum at the stress state corresponding to an axisymmetric compression under 12 MPa of confining pressure. ρ is taken equal to 1600 kg/m ³ and L equal to 24 mm.	153
6.18	Growth coefficient s vs the normalized perturbation wavelength λ^* under several confining pressures for a) B=0.08 MPa; b) B=0.02 MPa. ρ is taken equal to 1600 kg/m ³ and L equal to 24 mm.	154
6.19	Growth coefficient s vs the normalized perturbation wavelength λ^* under several confining pressures and for different internal lengths ($L = 20$ mm and $L = 40$ mm) in two cases: a) B=0.08 MPa; b) B=0.02 MPa. ρ is taken equal to 1600 kg/m ³	154

6.20	Ranges of confining pressures that allow compaction banding in the Cauchy continuum (C) and in the micromorphic continuum (for several values of B). The solid lines indicate the stress states for which compaction bands occur. L is taken equal to 24 mm.	155
6.21	Numerical code validation: Plots of the semi-analytic homogeneous solutions and the numerical simulations in Cauchy continuum considering one element are superimposed to the experimental data for different loading conditions. .	157
6.22	Cauchy continuum: Numerical modelling of samples tested under different confining pressures. Compaction bands form at the plasticity onset for confinements $\sigma_3 \leq -11.9$ MPa, whereas a quasi-homogeneous deformation is observed for confinements $\sigma_3 > -11.9$ MPa up to 2% of applied axial strain.	158
6.23	Cauchy continuum: Profile of the plastic axial strain over the z -axis for the numerical simulations performed under 10 and 13 MPa of confining pressures.	158
6.24	Cauchy continuum: Mesh-dependency of the compaction band thickness for a sample tested under 13 MPa of confining pressure.	158
6.25	Numerical code validation in the micromorphic formulation: A comparison with the numerical results with Cauchy formulation by considering one element tested in two loading cases.	160
6.26	Mesh-independency of the compaction band thickness in the micromorphic formulation: a) Numerical modelling of a sample tested under 10.5 MPa of confining pressure up to 0.25% of applied axial strain for different mesh sizes; b) Vertical profiles of the plastic axial strain.	160
6.27	Effect of the modulus B on compaction banding: a) Numerical modelling of a sample tested under 10.5 MPa of confining pressure for different values of B ; b) Vertical profiles of the plastic axial strain. The internal length is taken $L = 24$ mm.	161
6.28	Effect of the internal length L on compaction banding: a) Numerical modelling of a sample tested under 10.5 MPa of confining pressure for different values of L ; b) Vertical profiles of the plastic axial strain. The modulus B is taken $B = 0.025$ MPa.	161
6.29	Accumulated plastic volumetric strain maps are shown at different loading levels.	162
6.30	Vertical profiles of the accumulated plastic volumetric strain. Dashed lines represent the fitted curves of $f(z)$. The plot on the right shows a zoom on the profile at the plasticity onset.	163
6.31	Evolution of compaction band thickness evaluated from accumulated and rates of plastic volumetric strain profiles (each plastic volumetric strain rate corresponds to an imposed total axial strain rate of $\dot{\epsilon}_a = -0.15\%$).	164
6.32	Plastic volumetric strain rate maps at different loading levels (each plastic volumetric strain rate corresponds to an imposed total axial strain rate of $\dot{\epsilon}_a = -0.15\%$).	165

6.33	Vertical profiles of plastic volumetric strain rates at different loading levels (each plastic volumetric strain rate corresponds to an imposed total axial strain rate of $\dot{\epsilon}_a = -0.15\%$).	165
6.34	Accumulated plastic axial strain maps at several loading states for the cases $H=48$ mm and 72 mm.	166
6.35	Profiles of accumulated plastic axial strain.	167
6.36	Band thicknesses evolution with imposed axial loading and compared to the thickness evaluated for $H = 24$ mm: a) Case of $H = 48$ mm; b) Case of $H = 72$ mm.	167
6.37	Evolution of the ratio of band spacing over central band thickness: a) Case of $H = 48$ mm; b) Case of $H = 72$ mm.	168
6.38	LSA conducted at the plasticity onset of a sample tested under 10.5 MPa of confining pressure: The growth coefficient vs the normalized wavelength perturbation.	169
6.39	REV 1: Plastic volumetric strain profiles over the two lines defined on the DVC maps.	169
6.40	Compaction band thickness evaluated from the incremental plastic volumetric strain profiles and from the LSA applied on an equivalent homogenized material.	170
8.1	a) Carbonate rocks constituents; b) Dunham classification for limestones; c) Folk classification for limestones (from Flügel, 2013).	180
8.2	a) Coarse-grained Lavoux limestone; b) Fine-grained Lavoux limestone (Zinsmeister, 2013); c) Anstrude limestone (o: oolitic grains; s: sparite cement; m: micrite) (Lion, 2004); d) Estailades limestone (Dautriat, 2009).	181
8.3	A schematic showing the adopted way to extract a thin rod from a porous material using a diamond wire saw.	184
8.4	Density of internal forces for a m-grade micromorphic media of degree n. Cells in blue and green highlight a second and third gradient theories respectively when restrictions (Equations 8.2 and 8.3) are applied.	188
8.5	Growth coefficient s vs the normalized perturbation wavelength λ^* at the plasticity onset in an axisymmetric triaxial loading under 10.5 MPa of confining pressure. Two cases are presented: with restrictions and without restrictions, where $P_1 = 10^9$ MPa and $P_2 = 10^9$ MPa. In both cases, $\rho = 1600$ Kg/m ³ , $L = 24$ mm and $B = 0.025$ MPa.	199

List of Tables

2.1	Petrophysical properties of some sandstones	16
2.2	Petrophysical properties of many limestones.	19
2.3	Petrophysical properties of Majella limestone facies studied by Rustichelli et al. (2012). The presence of compaction bands is investigated by naked eye and thin section observations.	25
3.1	Summary of several limestones microstructural properties.	41
3.2	Porosity of the four cored samples estimated from: the MIP tests, the mean grey level (GL) and the mass to volume ratio (M/V) evaluations. The micro- and macro-porosities are evaluated from the MIP tests, considering that $0.6 \mu\text{m}$ is the threshold size between the two families.	51
3.3	Microstructural main features of high- and low-porosity zones.	56
4.1	Band types depending on the normalized scalar product value.	67
5.1	Mean values of volumetric and shear strain magnitude of the 3 domains selected in Figure 5.11 during the second loading stage.	87
5.2	Band types and orientations θ (in absolute value) with respect to the axial direction in the sample tested at high confining pressure (10.5 MPa) after the first and second loading stages.	96
5.3	Band types and orientations θ (in absolute value) with respect to the axial direction of the sample tested at low confining pressure (1.5 MPa) after the first and second loading stages.	109
5.4	Band types and orientations θ (in absolute value) with respect to the axial direction in the sample tested at intermediate confining pressure (6 MPa). . .	121
6.1	Values of fitted parameters.	137
6.2	Comparison of the Cauchy and the gradient-dependent plasticity formulation.	145
6.3	Values of ϕ_0 and $\nabla^2\phi_0$ over the two selected REV in the initial state and after each stage of loading.	147
6.4	Mean plastic volumetric strain for each REV in each loading stage.	148
6.5	The component C_{1111}^{ep} evaluated at the plasticity onset of axisymmetric triaxial compressions under different confining pressures. The last column indicates if a compaction band (CB) is formed or not.	150

6.6	Hardening modulus evaluated from the Cauchy constitutive law and compared to the critical values given by Issen and Rudnicki (2000) for several confining pressures. The last column indicates if a compaction band (CB) is formed or not.	152
6.7	Cumulative plastic volumetric strain evaluated after each loading stage: in the numerical modelling and in the REV 1 selected inside the SML sample tested under 10.5 MPa of confining pressure.	170

